Nanospectroscopy of thiacyanine dye molecules adsorbed on silver nanoparticle clusters

Uroš Ralević [a], Goran Isić [a],[*], Dragana Vasić Anicijević [b], Bojana Laban [c], Una Bogdanović [b], Vladimir M. Lazović [d], Vesna Vodnik [b], Radoš Gajić [a]

[a] Graphene Laboratory of Center for Solid State Physics and New Materials, Institute of Physics, University of Belgrade, Pregrevica 118, 11080 Belgrade, Serbia
[b] Vinča Institute of Nuclear Sciences, University of Belgrade, P.O. Box 522, Belgrade, Serbia
[c] Faculty of Natural Sciences and Mathematics, University of Priština, 38200 Kosovska Mitrovica, Serbia
[d] Institute of Physics, University of Belgrade, Pregrevica 118, 11080 Belgrade, Serbia

ARTICLE INFO

ABSTRACT

The adsorption of thiacyanine dye molecules on citrate-stabilized silver nanoparticle clusters drop-cast onto freshly cleaved mica or highly oriented pyrolytic graphite surfaces is examined using colocalized surface-enhanced Raman spectroscopy and atomic force microscopy. The incidence of dye Raman signatures in photoluminescence hotspots identified around nanoparticle clusters is considered for both citrate- and borate-capped silver nanoparticles and found to be substantially lower in the former case, suggesting that the citrate anions impede the efficient dye adsorption. Rigorous numerical simulations of light scattering on random nanoparticle clusters are used for estimating the electromagnetic enhancement and elucidating the hotspot formation mechanism. The majority of the enhanced Raman signal, estimated to be more than 90%, is found to originate from the nanogaps between adjacent nanoparticles in the cluster, regardless of the cluster size and geometry.

1. Introduction

Dye coated metallic nanoparticles (NPs) exhibit interesting optical properties provided by the interaction between the metal core and dye shell. Depending on the interaction mechanism between the two, the optical properties of dye molecules and NPs can be changed separately or jointly within the adsorbate–NP complex [1]. For example, the NP surface plasmon frequency can be changed by the presence of adsorbate while the dye fluorescence can be quenched or enhanced by the NP [2,3]. Ultimately, under special conditions, these complexes can exhibit unique characteristics different than those of either isolated dye molecules or NPs. Owing to the variety of mechanisms by which dyes can interact with metalic NPs, dye–NP complexes can lead to applications ranging from nanoscale sensing [4] to advanced composite materials for novel active and nonlinear optical devices [5].

Many of the recent studies have been focused on dyes which are able to self-assemble in highly oriented structures called J-aggregates on the surface of the NPs [6–14]. J-aggregates have a strong and narrow excitonic absorption band that is red-shifted with respect to the monomer absorption band [15]. The special way of molecular stacking, responsible for the formation of Frenkel excitons, has been extensively studied [16–24] as these aggregates are the most famous spectral sensitizers of silver halides for the photographic industry [25]. On the other hand, it has been shown that the combination of J-aggregates and silver or gold NPs provides a platform for the fundamental studies of excitons and their interaction with high electromagnetic fields, as well as a way to utilize optical properties of such a hybrid system for nanoscale optical devices.

A necessary condition for the interaction to occur is that the dye molecules are adsorbed on the surface of the NPs. Therefore, the adsorption process plays one of the key roles in these systems. The most common way in which the dye–NP hybrid systems are prepared is by mixing the appropriate colloid and dye solutions and letting the resulting mixture reach its metastabile or stabile state in which the NPs have dye molecules adsorbed on their surface. The dynamics of the adsorption process is quite complex as it the depends on various factors including the target concentration of the constituents, affinity of the dye molecules to bind to the NP surface and the type of capping anions protecting the surface of the NPs. For instance, the spectrophotometric studies of thiacyanine (TC) dye coated silver nanoparticles (AgNPs) in Refs. [26,12–14]

show that the capping anions can influence the mechanism of the adsorption process and therefore its efficiency.

The influence of capping anions on the adsorption process can be studied on a nanoscopic level by exploiting very strong localized plasmonic fields at the NP surface and employing surface-enhanced Raman scattering (SERS) [27,28]. SERS has already been used for identification of TC J-aggregates and for studying their dynamics on the surface NP clusters in solutions [29–36].

In view of the significance of the dye-to-NP adsorption mechanism, here the mechanism of TC dye adsorption on the surface of AgNP clusters with citrate anion stabilization is investigated. In order to probe the presence of TC dye molecules on the nanoscale (i.e. on individual AgNP clusters), Ag colloids are mixed with TC dye solutions, and subsequently drop-cast onto freshly cleaved mica or SiO_2 substrates and, after drying, investigated using colocalized Raman microspectroscopy and atomic force microscopy (AFM). The key mechanism used for the identification of a small amount of TC dye molecules adsorbed on AgNP clusters is SERS [32]. The measurements are complemented by rigorous numerical simulations of plane wave scattering on AgNP clusters, showing that the electromagnetic enhancement of the Raman signal originates dominantly from the nanogaps between adjacent AgNPs within the clusters. The analysis of the SERS spectra acquired at the AgNP clusters on mica substrate and the fact that the majority of the SERS signal comes from the nanogaps indicate that the citrate anions impede the efficient dye adsorption.

2. Materials and methods

2.1. Chemicals

Silver nitrate ($AgNO_3$), potassium chloride (KCl), and sodium borohydride ($NaBH_4$) trisodium citrate ($Na_3C_6H_5O_7 \times 3H_2O$) of the highest purity were purchased from Sigma Aldrich and used as received.

Thiacyanine dye (3,3-disulfopropyl-5,5-dichlorothiacyanine sodium salt, TC) was purchased from Hayashibara Biochemical Laboratories, Okayama, Japan.

2.2. Samples

Aqueous solutions of borate- and citrate-capped AgNPs were synthesized by $NaBH_4$ reduction of $AgNO_3$, as described in Refs. [12,14]. For the synthesis of citrate-capped AgNPs, $Na_3C_6H_5O_7 \times 3H_2O$ was used as a stabilizing agent. The solution of borate-capped AgNPs was prepared immediately before use as the colloid is stable only up to a few hours. Oppositely, the solution of citrate-capped AgNPs is stable for a longer period of time, measured in months, due to the protective citrate anion mantle. The average diameter of both borate- and citrate-capped AgNPs is around 10 nm (see Section S1 of the Supplementary information). The nominal concentration of citrate-capped AgNPs in water solution is c_{Ag} = 16 nM (see Fig. S1 for the related absorption spectra).

Aqueous TC dye solution with nominal concentration c_{TC} = 50 μM of TC and 1 mM of KCl was prepared by dissolving the solid TC in water and by adding KCl afterwards. Water purified with a Millipore Milli-Q water system was used in all cases. The absorption spectra of the TC dye is given in Fig. S1 in the Supplementary information.

The Ag colloid and the TC dye solution are mixed, and the resulting mixture (see Fig. S1 in the Supplementary information for the related absorption spectra) is drop-cast on a substrate. The adsorption of TC molecules on the surface of borate-capped AgNPs happens almost instantaneously [13,12], and the mixture was therefore drop-cast on the substrate a few minutes after mix-

ing the two solutions. On the other hand, the adsorption of TC dye on the surface of citrate-capped AgNPs is a much slower process [26,14] and for that reason the mixture was left overnight and afterwards drop-cast on a substrate.

For the investigation of TC/citrate-capped AgNP clusters, as well as for initial characterization of pristine citrate-capped AgNP clusters, mica was used as a substrate. Mica has an atomically flat, hydrophilic surface on which the AgNPs are easily deposited, while its contribution to the total Raman signal is small (see Section S2 of the Supplementary information). In addition to mica, highly oriented pyrolytic graphite (HOPG) and SiO_2 substrates were used as their surfaces are hydrophobic and, therefore, facilitate the formation of large, closely spaced AgNP clusters as well as more efficient aggregation of the TC dye on their surface. In particular, HOPG is used for Raman characterization of concentrated TC dye, since the dye efficiently aggregates on its surface. The SiO_2 is used for the control study of AgNPs having dye/borate anions conformed to their surface, since the large closely spaced AgNP clusters are required for fast Raman/SERS characterization of the initially unstable borate-capped AgNPs. Raman spectra of the TC dye, Mica, Si and HOPG are shown in Fig. S2 in the Supplementary information.

2.3. Methods

The AgNP clusters on a substrate are investigated using colocalized Raman microspectroscopy and AFM. The two techniques are used simultaneously thus providing spatially resolved chemical information of the sample along with its surface topography at the same place. In this way one is able to identify and assert the size of the SERS active AgNP clusters while obtaining the chemical identity of the analyte adsorbed on the surface of AgNPs. The AFM is operated in tapping mode in order to minimize the lateral force between the tip and the sample induced by lateral movements of the tip across the sample. The cantilever-tip system is oscillated at the characteristic first order resonance which is usually in the 90–230 kHz range. For Raman spectroscopy and SERS measurements a linearly polarized semiconductor laser operating at a wavelength of 532 nm is used. The laser power was varied from 2 to 0.2 mW within the $\sim$0.3 $\times$ 0.3 μm sized focus. The experiments are performed using commercial NTegra Spectra system from NT-MDT.

To numerically solve the classical Maxwell equations we have used the finite element method implemented within the Comsol Multiphysics software package [37]. We consider clusters of AgNPs having a diameter of 10 nm on a substrate under plane wave illumination. The Ag dielectric constant is taken from Rakic et al. [38]. The substrate is assumed to be semi-infinite and isotropic with a dielectric constant of 2.25, which roughly corresponds to the dielectric constants of both mica and SiO_2 at visible frequencies. The surrounding medium is vacuum and its dielectric constant is 1. For purposes of efficient meshing, AgNPs are assumed to lie 1 nm above the substrate. The clusters are formed in the plane which is parallel to the substrate by allowing AgNPs to have random position but enforcing the following conditions: (i) there is a certain minimal allowed distance d between two AgNPs; two AgNPs separated by the minimal distance are said to be adjacent; (ii) each AgNP must be adjacent to at least one other AgNP, thus ensuring that each randomly generated cluster is connected. By imposing these two conditions, we were able to randomly generate various cluster geometries and mimic the lack of control over the clusters morphology in the experiment.

The absorption $\sigma_a(\lambda)$, scattering $\sigma_s(\lambda)$ and extinction $\sigma_{ext}(\lambda)$ cross sections are calculated as a function of wavelength λ, according to their well-known definition [39]. The electric-field enhancement $f(\mathbf{r}, \lambda)$ is defined as the squared ratio of magnitudes of the local electric field $\mathbf{E}_L(\mathbf{r}, \lambda)$ and the incoming electric field $\mathbf{E}_0(\lambda)$, with $\mathbf{r}$ denoting the coordinate at which the former is evaluated.

Following Kerker et al. [40], the SERS enhancement factor is defined as $F(\mathbf{r}, \lambda_{inc}, \lambda) = f(\mathbf{r}, \lambda_{inc})f(\mathbf{r}, \lambda)$ with λ_{inc} and λ denoting the laser and Stokes wavelength, respectively. Since the measured PL/Raman signal being reported in this paper originates from large (relative to a cluster), diffraction limited, spots of 300 nm approximate diameter, it cannot be directly related to the spatially-resolved field and SERS enhancement factors. Instead, we consider their integrals over the cluster surface S and the corresponding cluster-averaged SERS factor $\langle F(\lambda_{inc}, \lambda) \rangle$ defined as

$$\langle F(\lambda_{inc}, \lambda) \rangle = \frac{1}{S} \int_S F(\mathbf{r}, \lambda_{inc}, \lambda) dS. \qquad (1)$$

3. Results and discussion

3.1. Surface-enhanced Raman spectroscopy of pristine citrate-capped AgNPs

Fig. 1(a) shows an AFM topograph of pristine AgNP clusters on mica surface. The corresponding PL/Raman map is shown in Fig. 1(b). The intensity of every pixel in the PL/Raman map is obtained by dividing the sum of PL/Raman intensities across the entire spectral range (100–2000 cm^{-1}) with the number of spectral points. The color bar in panel (b) thus enumerates the average photon count. Bright areas in Fig. 1(b) represent the regions of enhanced signal, henceforth referred to as hotspots. These regions coincide with AgNP clusters consisting of a large number of AgNPs (with diameters in the 10–50 nm range), as seen by comparing the PL/Raman map with the AFM topography image. In fact, we find that the hotspots are dominantly formed within larger AgNP clusters, such as those in Fig. 1(a), regardless of the substrate which is used (mica, SiO$_2$ or HOPG).

Fig. 1(d) and (e) shows two sets of consecutively acquired spectra with a 40 s time step taken at two hotspots from Fig. 1(b) using 532 nm laser with intensity of $\approx 200\,\mu W/\mu m^2$. The spectra in panels (c) and (d) are similar, but cannot be quantitatively compared. Both sets feature a wide background which spreads over the entire spectral range, and a pronounced band blinking in the 1000–1800 cm^{-1} range (shaded region) which hinders a quantitative analysis. Considering that citrate anions are used for stabilizing the AgNPs, our hypothesis is that the blinking spectra is the SERS signal from the citrate anion mantle, sensitive to local heating in hotspots due to the small size of citrate anions, while the wide background is PL coming from the AgNP clusters.

3.2. Numerical simulations of light scattering on random AgNP clusters

In order gain an insight into hotspot formation and assess the Raman enhancement factors, we employ a numerical model to calculate the electromagnetic fields scattered on randomly generated AgNP clusters. The motivation for considering random AgNP clusters is to get an idea on the variability of the electric field enhancement upon changing the cluster geometry and to identify any invariants which could be used to interpret SERS measurements on clusters whose exact geometry is unknown. A typical cluster consisting of 20 AgNPs is shown in Fig. 2(a). In this example we set the minimal AgNP distance at $d = 0.8$ nm while the adjacent AgNPs are indicated by solid (red) lines Fig. 2(a). The extinction cross-section of the AgNP cluster in panel (a) is plotted in Fig. 2(b),
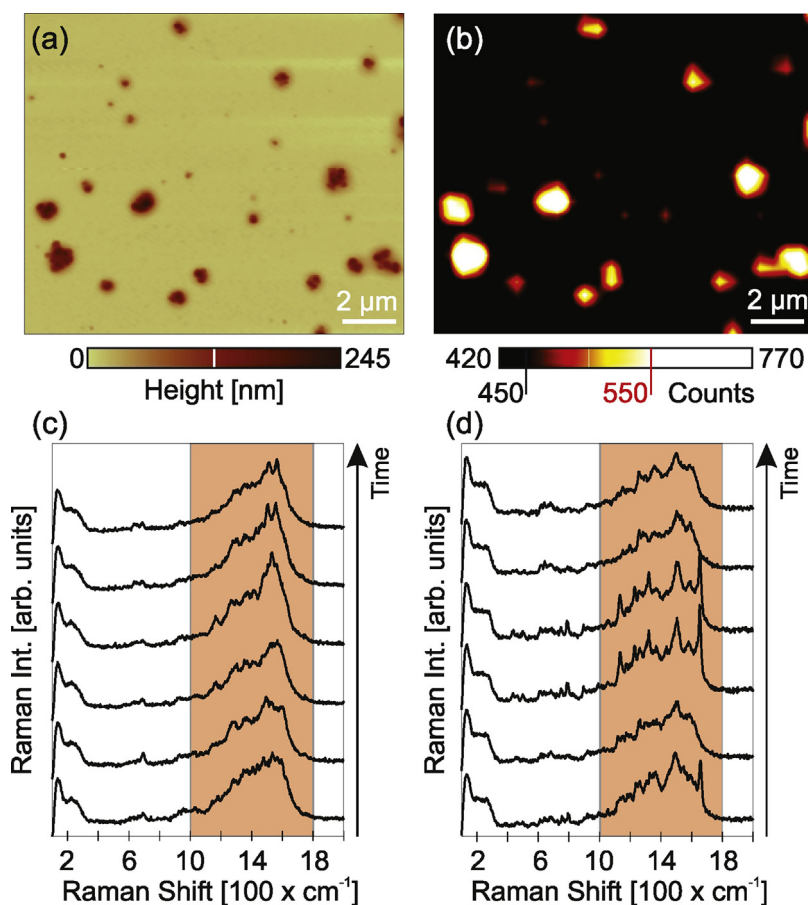

Fig. 1. (a) AFM topograph of pristine AgNP clusters drop-cast onto a freshly-cleaved mica substrate. (b) Corresponding PL/Raman map. (c), (d) Typical SERS spectra acquired within two hot spots in panel (b). The spectra were measured consecutively with a 40 s time step. The excitation laser wavelength is 532 nm.
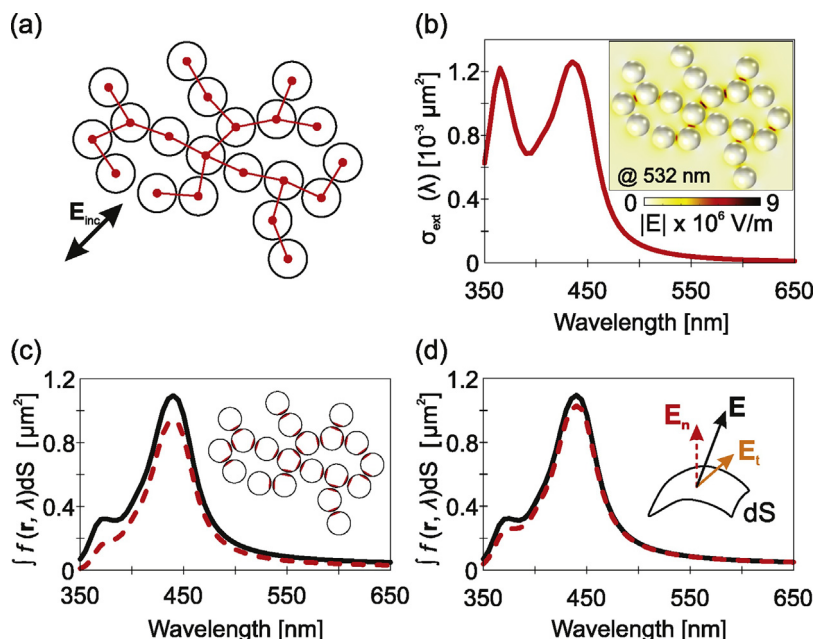
Fig. 2. (a) Sketch of a typical cluster geometry used in the numerical model. Normal incidence is assumed for the incoming wave while its electric field is polarized parallel to the plane of the cluster and oriented as indicated by the arrow. The incident field intensity is set to 200 μW/μm². (b) Extinction spectra of the cluster in panel (a). The inset shows the electric field magnitude distribution at 532 nm. (c) Surface integrals of the intensity enhancement over the entire cluster surface (solid black line) and over the entire gap area (dashed red line) plotted as the function of the wavelength. (d) Surface integrals of the total field enhancement (solid, black) and the ratio of the field component perpendicular to the AgNP surface (dashed, red) both taken over the entire cluster surface. (For interpretation of the references to color in this legend, the reader is referred to the web version of the article.)

as a function of the incident wavelength. For the considered cluster, the scattering cross-section is negligible with respect to the absorption cross-section and therefore $\sigma_{ext} \approx \sigma_a$. The two peaks observed at 365 and 435 nm, represent the single particle and cluster surface plasmon, respectively. Below we find that the wavelength of the former is virtually independent on the presence of other AgNPs, while the cluster plasmon wavelength redshifts with increasing cluster size. Upon the excitation of a cluster plasmon, the electric field is resonantly enhanced over the entire cluster. Although the distribution of resonant fields is highly dependent on the details of AgNP arrangement [41], the highest enhancement is known [42,43] to be invariably reached within the gaps between adjacent AgNPs, which is corroborated by our numerical simulations of many random AgNP arrangements.

The inset of Fig. 2(b) shows the spatial distribution of the electric field magnitude in the plane containing the NP centers, excited at 532 nm which is far from the cluster plasmon at 435 nm. This hints that the highest field enhancements are reached in NP gaps for any wavelength and not just for resonances. Fig. 2(c) shows the surface integral of the field enhancement evaluated over: (i) the entire cluster surface, consisting of the surfaces of all AgNPs and (ii) over the entire gap area, consisting of the sum of gap areas of individual AgNPs, defined as parts of the NP surface located very close to the adjacent AgNP, as indicated by the (red) shading in Fig. 2(c) inset. According to this definition, the surface over which the (ii) integral is evaluated is a small fraction of the (i) integral. However, the spectra in Fig. 2(c) show that these integrals have virtually the same value away from surface plasmon resonances. The difference around the cluster plasmon wavelength is also not significant, being of the order of 10%. This shows that regardless of the cluster geometry, the majority of the SERS signal of any species adsorbed uniformly on AgNPs is likely to come from the gap region (see also Fig. S3 in the Supplementary information).

Another important question regarding the fields on AgNP clusters is their orientation with respect to the AgNP surface, as

it determines the SERS cross section of vibrational modes of molecules adsorbed on the AgNP surface. To evaluate the extent to which the electric field is perpendicular to the local surface, in Fig. 2(d) we evaluate the surface integrals (taken over the entire cluster) of (i) the square of the normalized total electric field magnitude, which equals $f(\mathbf{r}, \lambda)$ by definition (solid, black), and (ii) the square of the normalized magnitude of the electric field component perpendicular to the AgNP surface (dashed, red). The comparison of the two spectra in Fig. 2(d) shows that the contribution of the tangential component of the local electric field is negligible, indicating that in such clusters the perpendicular component of the electric field is the principal source of the SERS signal.

Having established that for an arbitrarily chosen AgNP cluster the large majority of the SERS signal comes from gaps between AgNPs and is associated with the perpendicular electric field component, we now focus on the cluster-averaged SERS enhancement factor $\langle F(\lambda_{inc}, \lambda) \rangle$ and investigate how is it affected by the cluster size and geometry. The typical case is illustrated in Fig. 3(a) in which we consider a hierarchy of 3 NP clusters shown in the inset, each having twice as many AgNPs as the previous one. The first one represents a randomly chosen connected arrangement of 5 AgNPs with $d = 0.8$ nm. The second is obtained by adding 5 more AgNPs so that each new AgNP is adjacent to one of the existing AgNPs. Finally, the third and largest cluster is obtained by adding 10 more AgNPs to the second one. The corresponding $\langle F(\lambda_{inc}, \lambda) \rangle$ spectra in Fig. 3(a) shows two main effects of the cluster size increase. First, the enhancement peaks associated with the cluster plasmon undergoes a gradual redshift. Second, the surface-average enhancement $\langle F(\lambda_{inc}, \lambda) \rangle$ increases, meaning that the actual SERS signal enhancement given by $S \times \langle F(\lambda_{inc}, \lambda) \rangle$ will increase even more rapidly with adding new particles to the cluster. For example, a cluster having 5 AgNPs exhibits an average Raman enhancements of the order of 10 in the 532–600 nm range, whereas a cluster having 20 AgNPs yields 10 times higher values in the same range. In previous studies on AuNP chains [44], the increase of particle number has been found
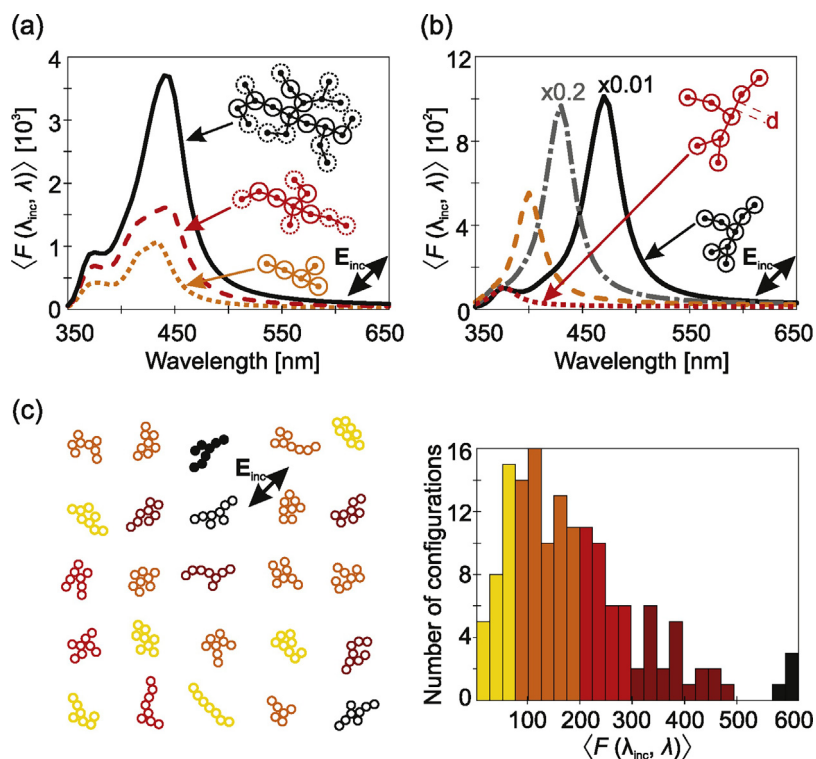
Fig. 3. (a) The average Raman enhancement calculated as a function of the emission wavelength for clusters having 5 particles (dotted orange line), 10 particles (dashed red line) and 20 particles (solid black line). (b) The average Raman enhancement calculated as a function of the emission wavelength for a cluster with 8 particles when the minimal distance between the particles is varied. Particles connected by lines, in the inset, are at the minimal distance d from each other. Solid (black) line corresponds to $d = 0.5$ nm, whereas dash-dotted (gray) line, dashed (orange) line and dotted (red) line correspond to $d = 1$ nm, $d = 2$ nm and $d = 5$ nm, respectively. (c) The left panel shows some of the 150 considered cluster variants and the electric field polarization direction. All the clusters have 8 particles, with the minimal distance $d = 0.8$ nm. The right panel shows a histogram of the average Raman enhancement calculated at the emission wavelength 550 nm for all 150 cluster variants. In all calculations normal incidence at a wavelength 532 nm and the incident field intensity of 200 μW/μm² are assumed. (For interpretation of the references to color in this legend, the reader is referred to the web version of the article.)

to either increase or decrease the average Raman enhancement, depending on the relative position of the incident wavelength and the cluster (chain) plasmon.

In Fig. 3(b) we consider the role of the spacing d between adjacent AgNPs. For a cluster comprising 8 AgNPs decreasing d from 5 nm down to 0.5 nm is seen to result in drastic changes of $\langle F(\lambda_{inc}, \lambda) \rangle$. The cluster plasmon is rapidly blueshifted and approaches the single-particle plasmon as the AgNPs are moved further apart (see also panel (c) of Fig. S3 in the Supplementary information). Similar conclusions have been previously reported for the AuNP linear chains embedded in a dielectric medium [42,45]. Meanwhile, the peak values of $\langle F(\lambda_{inc}, \lambda) \rangle$ are seen to decrease very rapidly since the gap field enhancement becomes less effective with increasing d. For example, the lowest considered minimal distance of 0.5 nm yields SERS enhancements as high as 10^4 in the 532–600 nm range.

Lastly, by evaluating the average Raman enhancement at the excitation and Stokes wavelengths of 532 nm and 550 nm, respectively, for a 150 randomly generated 8 AgNP clusters, we evaluate how the cluster morphology affects the non-resonant SERS enhancement value. The variety of clusters that have been considered in the 150 member ensemble, is represented by 25 typical members sketched in the left panel of Fig. 3(c). The histogram of $\langle F(\lambda_{inc}, \lambda) \rangle$ values is shown in the right panel, where the column colors are selected so that they correspond to the color of the associated cluster in the left panel. The distribution is quite wide, spanning the range from 50 to 600. By comparing the two panels of Fig. 3(c), we see that the highest enhancements are reached in chain shaped clusters having the chain axis aligned with the incident electric field, such as the one illustrated in Fig. 3(c) by filled circles. The effect of disorder of the linear AuNP chain on the Raman

enhancement was studied in Ref. [43], where increasing disorder was found to diminish the Raman enhancement. In this case, the highest Raman enhancements were found for AuNP chains, when the incident electric field is oriented along the chain axis.

The brief numerical analysis of light scattering on random AgNP clusters made in this section shows that the overall SERS enhancement is highly dependent the cluster geometry and its orientation relative to the electric field polarization. The sensitivity of $\langle F(\lambda_{inc}, \lambda) \rangle$ to fine details, such as the gap spacing, makes its exact evaluation very difficult even when electron microscopy is used for determining the AgNP arrangement with nanometer spatial resolution [46]. In the present case, the possibility of resonant enhancement cannot be excluded, since the cluster plasmon resonances are seen to redshift in elongated clusters with a larger number of particles than the ones considered here [42,43]. However, beside the well elaborated enormous Raman enhancements having a resonant origin [42], we have shown that in the non-resonant case enhancement factors in the range of 10^2–10^3 are to be expected.

3.3. Surface-enhanced Raman spectroscopy of TC coated AgNPs I: influence of citrate capping anions on the TC dye adsorption

In the TC/AgNP mixture, the AgNPs may have the J-aggregates or dye monomers or dimers adsorbed on their surface, or even remain pristine. Therefore, it is expected that AgNP clusters drop-cast from the mixture would have a variety of SERS spectra corresponding to those of different dye conformations, citrate anions and even their combinations. To make a clear distinction between the non-aggregated and aggregated molecules one must have an
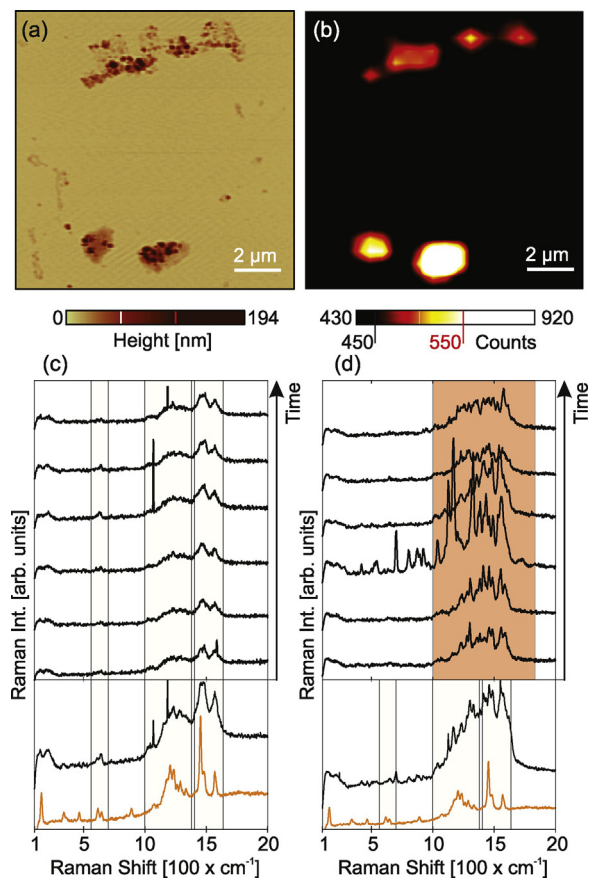
Fig. 4. (a) AFM topograph of TC dye coated Ag NP clusters which are drop-cast on mica. (b) Corresponding PL/Raman map. (c) and (d) Typical SERS spectra acquired within the hot spots, by consecutive measurements with 40 s time step. The excitation laser wavelength is 532 nm. In the lower parts of panels (c) and (d) shown are the SERS spectra obtained by summation of the corresponding consecutively acquired spectra, and the Raman spectra of the drop-cast TC dye. (For interpretation of the references to color in this legend, the reader is referred to the web version of the article.)

excitation resonant with the absorption of either aggregated or non-aggregated dye molecules [32,47]. Here we use a non-resonant laser line at 532 nm which does not allow identification of different dye conformations. However, AgNP clusters are very efficient enhancers at this wavelength, as it is shown in Section 3.1 and thus through the SERS effect alone we are able to determine if the TC dye molecules are adsorbed on AgNPs or not.

Comparison of the AFM topograph and the corresponding Raman map in Fig. 4(a) and (b) reveals that the hot spots are located within the larger AgNP clusters, as in the case of pristine AgNPs in Section 3.1. The SERS spectra acquired at these hot spots can be unambiguously categorized in two groups: one featuring stable Raman bands during successive measurements and the other having blinking Raman bands. The wide background from the AgNP clusters exists in this case as well. Fig. 4(c) and (d) shows the two distinct spectra types. The recording time step is 40 s and the laser intensity is $\approx 200\,\mu W/\mu m^2$.

The consecutively measured SERS spectra having stable Raman bands are reminiscent of the drop-cast TC dye Raman spectrum. The similarity between the two becomes even more convincing after summation of ten consecutively measured spectra, six of which are displayed in Fig. 4(c). By applying markers to the three wave-number regions, I (300–1000 cm^{-1}), II (1050–1250 cm^{-1}), III (1400–1600 cm^{-1}), where the TC dye has its characteristic Raman bands (see Fig. S2 in the Supplementary information), we find that in region I around 600 cm^{-1} the summed SERS spectrum has

two bands matching those of a drop-cast TC dye, which is plotted again, for clarity, below the summed spectrum. The modes around 400 cm^{-1} and 900 cm^{-1} are, however, absent in the related TC dye SERS. In the remaining regions II and III the two spectra have, more or less, the same Raman bands and even similar backgrounds. Hence, our experiments corroborate the fact that the dye molecules are adsorbed on the surface of the AgNPs, and point out another interesting possibility – the dye molecules drop-cast on the surface of HOPG may be similarly organized as the dye molecules on the surface of the AgNPs.

Panel (d) in Fig. 4 displays SERS spectra characterized by a pronounced band blinking in the 1000–1800 cm^{-1} range, as indicated by gray (orange) region. The resemblance of the spectra in Fig. 4(d) and those of pristine AgNPs in Fig. 1(c) and (d) suggests that the TC dye molecules are not adsorbed on the surface of the AgNPs. However, the sum of the consecutive recordings, shown in the lower part of Fig. 4(d), reveals certain SERS bands in region II and III which are overlapping the drop-cast TC dye bands. Occasional emergence of Raman bands which could belong to the TC dye bands in regions I, II and III, however, is a common event even for the SERS spectra of pristine AgNPs. Having in mind that practically the entire enhanced Raman signal originates form the analyte located in the nanogaps, the blinking SERS signal can be interpreted as a consequence of mixing of the pristine AgNPs blinking SERS and the TC dye SERS which are collected at different nanogaps where the former has the dominant contribution. Consequently, we are unable to conclude whether the AgNP clusters exhibiting blinking SERS bands have the dye molecules adsorbed on their surface or not. However, the existence of the two distinct SERS spectra clearly points out that the AgNPs are partially covered by the TC dye molecules. This further indicates that during the adsorption process, the TC dye molecules are either competing with citrate anions in order to replace them on the surface of AgNPs or that the TC dye molecules have a difficulty conforming over the citrate anion mantle. Hence, we proceed further by changing the concentration of TC dye in the mixture while maintaining the concentration of AgNPs constant at $c_{Ag} = 16\,nM$.

The blinking and TC dye SERS spectra observed for $0.01c_{TC} = 0.5\,\mu M$, $0.1c_{TC} = 5\,\mu M$, and $0.5c_{TC} = 25\,\mu M$ of TC, are shown in Fig. 5(a)–(c), respectively. By analyzing spectra at the hotspots within various Raman maps, we find that the AgNP clusters deposited from the solution with the lowest dye concentration yield no clear dye SERS spectra, whereas the AgNP clusters deposited from the solution with the two higher dye concentration provide a number of distinct TC dye SERS spectra at the hotspots, shown in Fig. 5. Comparison of the summed SERS spectra, in the lower parts of panels (a), (b) and (c) in Fig. 5, and the concentrated TC dye Raman spectra corroborates that the SERS spectra in panels (b) and (c) correspond to the one of the TC dye. As expected, using TC dye concentrations of $0.01c_{TC} = 0.5\,\mu M$, $0.1c_{TC} = 5\,\mu M$ in the final solution yields either pristine or partially covered AgNP clusters, a fact that concurs with the results in Ref. [14]. However, observation of the blinking type SERS within the AgNP clusters derived from the mixture with the highest TC dye concentration of $0.5c_{TC} = 25\,\mu M$, for which all of the AgNPs in the solution should be covered by the dye molecules [14], further indicates that the citrate anion mantle impedes the adsorption of the TC dye molecules.

3.4. Surface-enhanced Raman spectroscopy of TC coated AgNPs II: influence of borate and citrate capping anions on the TC dye adsorption

In order to examine if the citrate anions impede the TC dye adsorption, we have performed an additional set of measurements on a control sample – borate–capped AgNPs mixed with the TC dye and deposited on the surface of 300 nm thick SiO_2, which is thermally grown on the Si wafer. Meanwhile, the borate-capped AgNPs
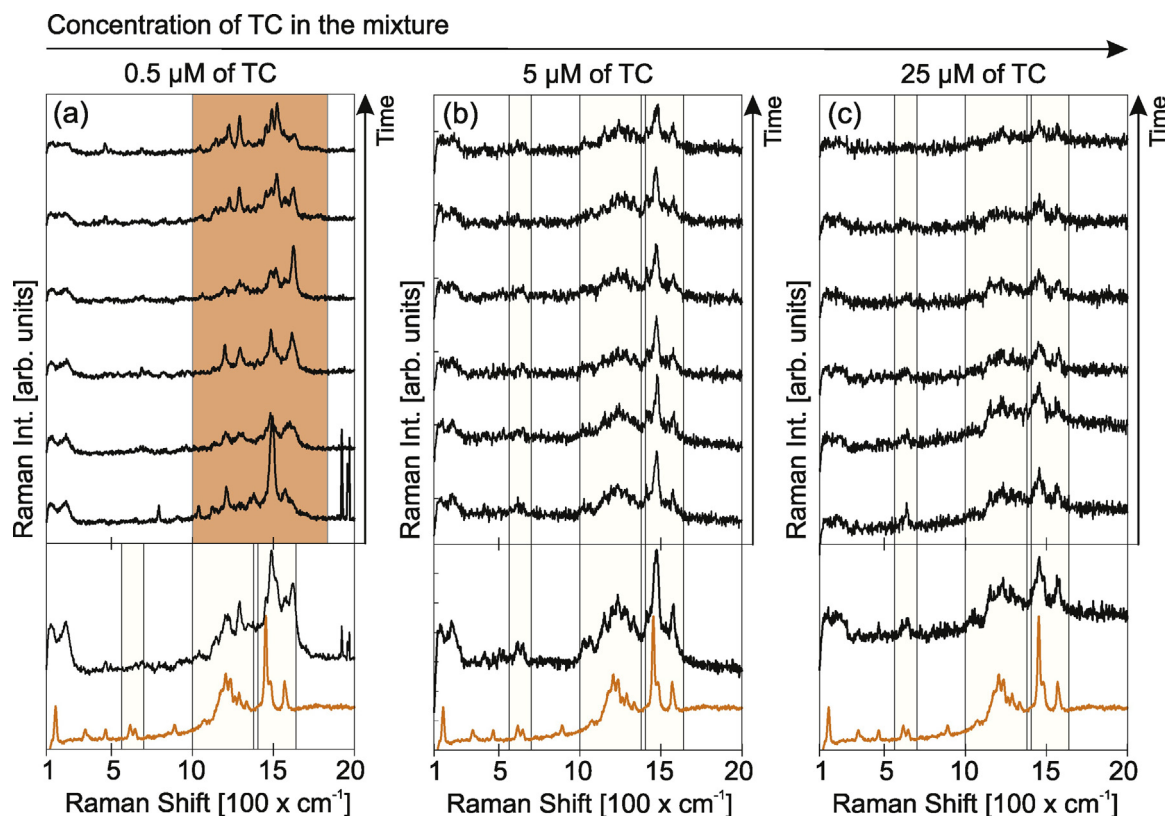
Concentration of TC in the mixture

Fig. 5. Blinking and TC dye SERS spectra (acquired by consecutive measurements with 40 s time step) at hotspots on the samples made by varying the TC concentration in TC-Ag NP mixture: (a) 0.5 μM, (b) 5 μM and (c) 25 μM. All shown spectra were taken under the same conditions using 532 nm laser with intensity of 200 μW/μm².

are unstable with the average lifetimes of the order of couple of hours in the colloid dispersion and are usually stabilized by sodium citrate (or rather by the citrate anions which replace the borate anions while conforming to the surface of the AgNPs), as explained in Ref. [14]. The related lifetimes are much shorter upon deposition of these AgNPs on a substrate. The SiO₂ surface is hydrophobic, and, therefore, promotes formation of closely spaced clusters larger than those observed on mica, since the droplet drop-cast of the former dries over a certain area rather than spreading all over the surface. Such an arrangement, along with the enhanced contrast between the SiO₂ surface and the clusters, is absolutely necessary for fast acquisition of the SERS signal from the unstable, dye/borate-capped AgNP clusters.

Fig. 6(a)–(c) shows the three Raman maps corresponding to: (i) AgNP clusters deposited on mica from a solution having a (citrate-capped) AgNP to the TC dye concentration ratio of 22 nM/17 μM≈1.3 × 10⁻³, (ii) AgNP clusters deposited on mica from a solution having a (citrate capped) AgNP to the TC dye concentration ratio of 16 nM/25 μM ≈ 0.64 × 10⁻³, (iii) AgNP clusters deposited on SiO₂/Si from a solution having a (borate-capped) AgNP to the TC dye concentration ratio of 10 nM/16 μM≈0.63 × 10⁻³, respectively. The (red) diamonds mark the spatial positions within the hotspots where the blinking type of Raman spectra is observed, whereas the (green) squares mark the pixels having the TC dye type of Raman spectra. These maps share the color bar which is located below them. Panels (d), (e) and (f) of Fig. 6 display examples of the spectra collected at the hotspots within the corresponding maps in panels (a), (b) and (c), respectively. For comparison, the concentrated TC dye Raman spectra is plotted in each panel, below all the other spectra.

The dye/borate-capped AgNPs deposited on the SiO₂/Si, form a higher number of larger clusters than the dye/citrate-capped AgNPs on mica, as seen by comparing the Raman maps in panels (a), (b)

and (c), as expected. The SERS spectra acquired at these clusters is exclusively of the TC dye type, as seen in panel (c). In fact, we find this to be the case for every recorded Raman map. In contrast, the dye/citrate-capped AgNP clusters exhibit both the blinking and the TC dye SERS, even when the ratio of the citrate-capped AgNPs and the TC dye concentrations in solution is approximately the same as the one of the borate-capped AgNPs and the TC dye (compare panels (b) and (c) in Fig. 6). The adsorption of the TC dye seems to be more efficient if the AgNPs have borate anions initially conformed to their surface and, therefore, we conjecture that the citrate anions indeed interfere with the adsorption process of the TC dye molecules.

Our findings are in agreement with the previous spectrophotometric study of J-aggregation of TC dye on the surface of AgNPs [26,13,14,12], where is found that the capping anions (borate or citrate), as well as added KCl, have an important role in the adsorption and J-aggregation of the dye molecules. In case of borate-capped AgNPs, the J-aggregation is found to be a fast process (k_{app} = 4.97 s⁻¹) whose kinetics can be explained in terms of autocatalysis. Differently, kinetics measurements of J-aggregation on the surface of citrate-capped AgNPs has shown that the J-aggregation occurs via a two-step slower process (adsorption and aggregation, k_{app1} = 0.008 s⁻¹ and k_{app2} = 0.11 s⁻¹). Also, in the case of citrate-capped AgNPs was found that the quantity of added KCl has an important role in the adsorption of TC dye molecules.

This conclusion is further supported by the analysis of the DFT calculated adsorption energies of the TC dye, borate and citrate anions on the surface of Ag, reported in our previous work [26] (see also Section S4 of the Supplementary information).

4. Summary

In summary, the analysis of SERS enhancement based on rigorous simulations of Maxwell equations for the case of plane wave
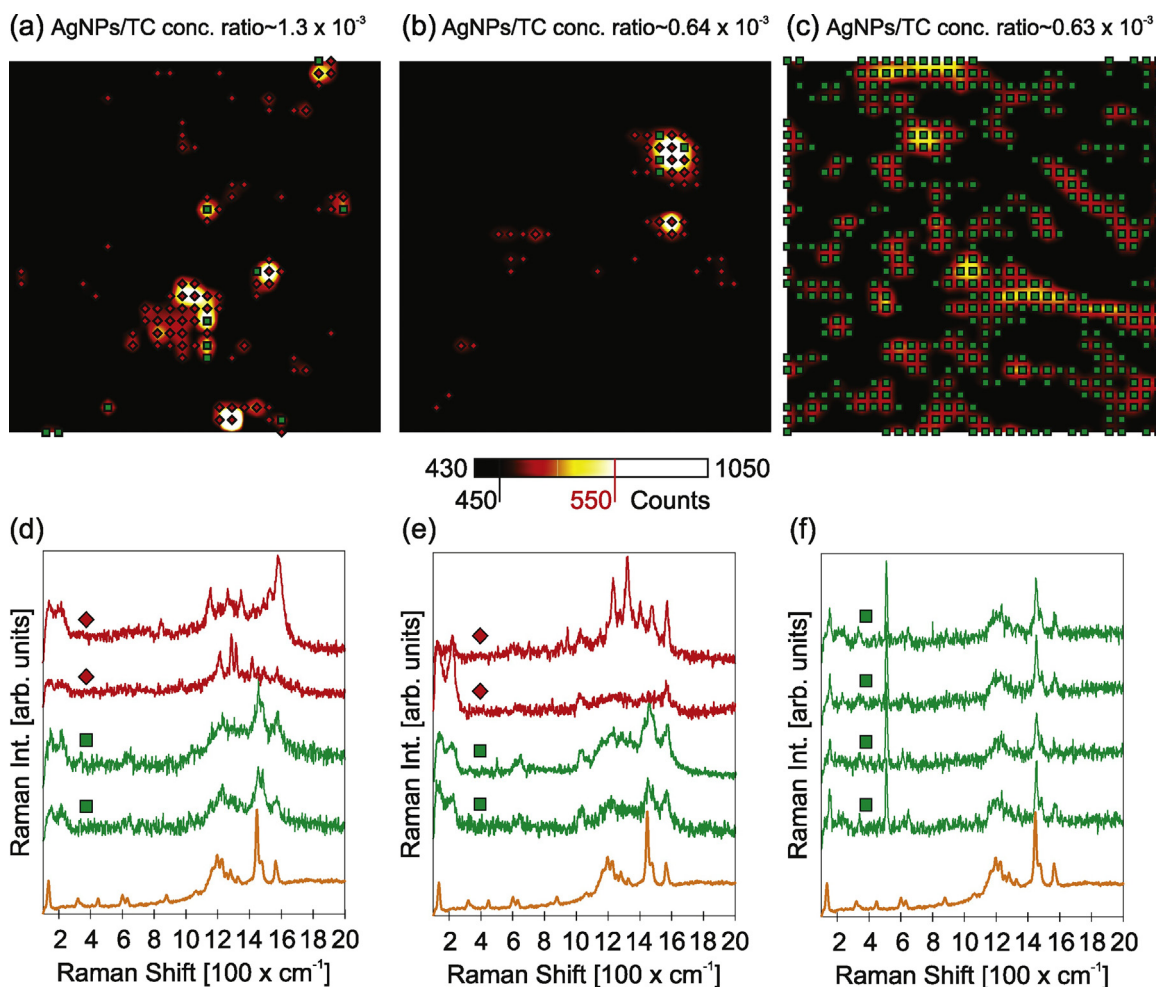
Fig. 6. Raman maps of (a) clusters deposited on mica from a solution having a (citrate capped) NP to the TC dye concentration ratio of 22 nM/17 μM ≈ 1.3 × 10⁻³, (b) clusters deposited on mica from a solution having a (citrate capped) NP to the TC dye concentration ratio of 16 nM/25 μM ≈ 0.64 × 10⁻³ (c) clusters deposited on SiO₂/Si from a solution having a (borate capped) NP to the TC dye concentration ratio of 10 nM/16 μM ≈ 0.64 × 10⁻³. (d)–(f) Examples of the blinking and dye SERS spectra observed in the Raman maps, displayed below the corresponding Raman maps.

scattering on random silver nanoparticle clusters on various substrates has shown that, for the investigated nanoparticles and the 532 nm excitation laser, typical enhancement factors in the range of 10^2–10^3 can be expected. The highest field enhancement factors are reached at collective nanoparticle plasmon resonances, which lie in the 400–500 nm range for medium sized clusters (around 20 nanoparticles), and become redshifted in elongated clusters with an increasing number of particles. From an inspection of electromagnetic field distribution on nanoparticle surfaces, a conclusion is reached that at least 90% of the SERS total enhancement originates from nanogaps between adjacent nanoparticles, implying that the experiments are sensitive only to adsorbates located in these gaps.

Combined AFM and PL mapping of citrate-capped AgNP clusters with dye molecules adsorbed from solutions of variable TC concentration have shown that, even at highest TC concentrations, not all hotspots exhibit Raman signatures characteristic of TC dye molecules, indicating that the clusters are only partially covered by dye molecules. In contrast, the control experiment carried out with borate-capped AgNP clusters, with similar nanoparticle and dye concentrations, has shown a complete dye-coverage of AgNP clusters.

These results are a direct demonstration that the citrate anions, while useful for stabilizing the colloid, impede the efficient TC dye adsorption.

Acknowledgements

Appendix A. Supplementary data

Supplementary data associated with this article can be found, in the online version, at https://doi.org/10.1016/j.apsusc.2017.10.148.

References

[1] A. Manjavacas, F.J.G.d. Abajo, P. Nordlander, Quantum plexcitonics: strongly interacting plasmons and excitons, Nano Lett. 11 (6) (2011) 2318–2323.
[2] N.T. Fofang, T.-H. Park, O. Neumann, N.A. Mirin, P. Nordlander, N.J. Halas, Plexcitonic nanoparticles: plasmon exciton coupling in nanoshell-J-aggregate complexes, Nano Lett. 8 (10) (2008) 3481–3487.
[3] E. Dulkeith, A.C. Morteani, T. Niedereichholz, T.A. Klar, J. Feldmann, S.A. Levi, F.C.J.M. van Veggel, D.N. Reinhoudt, M. Möller, D.I. Gittins, Fluorescence quenching of dye molecules near gold nanoparticles: radiative and nonradiative effects, Phys. Rev. Lett. 89 (2002) 203002–203006.
[4] J. Zhao, X. Zhang, Y.C. Ranjit, A.J. Haes, R.P. Van Duyne, Localized surface plasmon resonance biosensors, Nanomedicine 1 (2006) 219–228.

[5] M.A. Noginov, G. Zhu, A.M. Belgrave, R. Bakker, V.M. Shalaev, E.E. Narimanov, S. Stout, E. Herz, T. Suteewong, U. Wiesner, Demonstration of a spaser-based nanolaser, Nature 460 (2009) 1110–1112.

[6] N. Kometani, M. Tsubonishi, T. Fujita, K. Asami, Y. Yonezawa, Preparation and optical absorption spectra of dye-coated Au, Ag, and Au/Ag colloidal nanoparticles in aqueous solutions and in alternate assemblies, Langmuir 17 (3) (2001) 578–580.

[7] A. Yoshida, N. Kometani, Effect of the interaction between molecular exciton and localized surface plasmon on the spectroscopic properties of silver nanoparticles coated with cyanine dye J-aggregates, J. Phys. Chem. C 114 (7) (2010) 2867–2872.

[8] V.S. Lebedev, A.S. Medvedev, D.N. Vasil'ev, D.A. Chubich, A.G. Vitukhnovsky, Optical properties of noble-metal nanoparticles coated with a dye J-aggregate monolayer, Quantum Electron. 40 (3) (2010) 246.

[9] Y. Kitahama, M. Kashihara, T. Itoh, Y. Ozaki, Surface-enhanced phosphorescence measurement by an optically trapped colloidal Ag nanoaggregate on anionic thiacarbocyanine H-aggregate, J. Phys. Chem. C 117 (6) (2013) 2460–2466.

[10] A. Vujačić, V. Vasić, M. Dramićanin, S.P. Sovilj, N. Bibić, J. Hranisavljević, G.P. Wiederrecht, Kinetics of J-aggregate formation on the surface of Au nanoparticle colloids, J. Phys. Chem. C 116 (7) (2012) 4655–4661.

[11] A. Vujačić, V. Vasić, M. Dramićanin, S.P. Sovilj, N. Bibić, S. Milonjić, V. Vodnik, Fluorescence quenching of 5,5-disulfopropyl-3,3-dichlorothiacyanine dye adsorbed on gold nanoparticles, J. Phys. Chem. C 117 (13) (2013) 6567–6577.

[12] B.B. Laban, V. Vodnik, A. Vujačić, S.P. Sovilj, A.B. Jokić, V. Vasić, Spectroscopic and fluorescence properties of silver-dye composite nanoparticles, Russ. J. Phys. Chem. A 87 (13) (2013) 2219–2224.

[13] B. Laban, V. Vodnik, M. Dramićanin, M. Novaković, N. Bibić, S.P. Sovilj, V.M. Vasić, Mechanism and kinetics of J-aggregation of thiacyanine dye in the presence of silver nanoparticles, J. Phys. Chem. C 118 (40) (2014) 23393–23401.

[14] B. Laban, V. Vodnik, V. Vasić, Spectrophotometric observations of thiacyanine dye J-aggregation on citrate capped silver nanoparticles, Nanospectroscopy 1 (2015) 54–60.

[15] F. Würthner, T.E. Kaiser, C.R. Saha-Möller, J-aggregates: from serendipitous discovery to supramolecular engineering of functional dye materials, Angew. Chem. Int. Ed. 50 (15) (2011) 3376–3410.

[16] M. Kawasaki, T. Sato, T. Yoshimoto, Controlled layering of two-dimensional J-aggregate of anionic cyanine dye on self-assembled cysteamine monolayer on Au(111), Langmuir 16 (12) (2000) 5409–5417.

[17] R.W. Owens, D.A. Smith, Stm imaging of cyanine dye J-aggregates formed on carboxyl-terminated self-assembled monolayers, Langmuir 16 (2) (2000) 562–567.

[18] H. Yao, S. Kitamura, K. Kimura, Morphology transformation of mesoscopic supramolecular J aggregates in solution, Phys. Chem. Chem. Phys. 3 (2001) 4560–4565.

[19] N. Vranken, P. Foubert, F. Khn, R. Gronheid, I. Scheblykin, M. Van der Auweraer, F.C. De Schryver, Influence of the deposition method on the topography and spectroscopy of J-aggregates of a thiacarbocyanine dye adsorbed to a Langmuir film, Langmuir 18 (22) (2002) 8407–8417.

[20] H. Yao, Y. Kagoshima, S. Kitamura, T. Isohashi, Y. Ozawa, K. Kimura, Superstructures of mesoscopic monomolecular sheets of thiacyanine J aggregates in solution, Langmuir 19 (21) (2003) 8882–8887.

[21] H. Yao, T. Isohashi, K. Kimura, Large birefringence of single J-aggregate nanosheets of thiacyanine dye in solution, Chem. Phys. Lett. 396 (4–6) (2004) 316–322.

[22] S. Özcelik, M.M. Demir, B. Birkan, Probing nanoscale domains of J-aggregates deposited on a mica surface, J. Phys. Chem. B 108 (15) (2004) 4679–4683.

[23] H. Yao, K. Domoto, T. Isohashi, K. Kimura, In situ detection of birefringent mesoscopic H and J aggregates of thiacarbocyanine dye in solution, Langmuir 21 (3) (2005) 1067–1073.

[24] V.V. Prokhorov, O.M. Perelygina, S.I. Pozin, E.I. Mal'tsev, A.V. Vannikov, A.Y. Tsivadze, Tubular structure of J-aggregates of cyanine dye, Dokl. Chem. 460 (1) (2015) 1–4.

[25] T.H. James, The Theory of the Photographic Process, 4th ed., Macmillan, New York, 1977.

[26] B. Laban, I. Zeković, D. Vasić Aníćijević, M. Marković, V. Vodnik, M. Luce, A. Cricenti, M. Dramićanin, V. Vasić, Mechanism of

3,3-disulfopropyl-5,5-dichlorothiacyanine anion interaction with citrate-capped silver nanoparticles: adsorption and J-aggregation, J. Phys. Chem. C 120 (32) (2016) 18066–18074.

[27] M. Kerker, O. Siiman, L.A. Bumm, D.-S. Wang, Surface enhanced Raman scattering (SERS) of citrate ion adsorbed on colloidal silver, Appl. Opt. 19 (19) (1980) 3253–3255.

[28] O. Siiman, L.A. Bumm, R. Callaghan, C.G. Blatchford, M. Kerker, Surface-enhanced Raman scattering by citrate on colloidal silver, J. Phys. Chem. 87 (6) (1983) 1014–1023.

[29] D.L. Akins, S. Zelik, H.-R. Zhu, C. Guo, Aggregation-enhanced Raman scattering of a cyanine dye in homogeneous solution, J. Phys. Chem. A 101 (18) (1997) 3251–3259.

[30] Y. Kitahama, Y. Tanaka, T. Itoh, Y. Ozaki, Wavelength-dependent surface-enhanced resonance Raman scattering by excitation of a transverse localized surface plasmon, J. Phys. Chem. C 113 (27) (2009) 11877–11883.

[31] Y. Kitahama, Y. Tanaka, T. Itoh, Y. Ozaki, Time-resolved surface-enhanced resonance Raman scattering spectra of thiacyanine molecules in water, Chem. Lett. 38 (1) (2009) 54–55.

[32] Y. Kitahama, Y. Tanaka, T. Itoh, M. Ishikawa, Y. Ozaki, Identification of thiacyanine J-aggregates adsorbed on single silver nanoaggregates by surface-enhanced Raman scattering and emission spectroscopy, Bull. Chem. Soc. Jpn. 82 (9) (2009) 1126–1132.

[33] Y. Kitahama, A. Ogawa, Y. Tanaka, S. Obeidat, T. Itoh, M. Ishikawa, Y. Ozaki, Difference in time dependence of surface-enhanced Raman scattering spectra of thiacarbocyanine J- and H-aggregates adsorbed on single silver nanoaggregates, Chem. Phys. Lett. 493 (4–6) (2010) 309–313.

[34] Y. Kitahama, Y. Tanaka, T. Itoh, Y. Ozaki, Power-law analysis of surface-plasmon-enhanced electromagnetic field dependence of blinking SERS of thiacyanine or thiacarbocyanine adsorbed on single silver nanoaggregates, Phys. Chem. Chem. Phys. 13 (2011) 7439–7448.

[35] C.R. Zamecnik, A. Ahmed, C.M. Walters, R. Gordon, G.C. Walker, Surface-enhanced Raman spectroscopy using lipid encapsulated plasmonic nanoparticles and J-aggregates to create locally enhanced electric fields, J. Phys. Chem. C 117 (4) (2013) 1879–1886.

[36] Y. Kitahama, D. Araki, Y.S. Yamamoto, T. Itoh, Y. Ozaki, Different behaviour of molecules in dark SERS state on colloidal Ag nanoparticles estimated by truncated power law analysis of blinking SERS, Phys. Chem. Chem. Phys. 17 (2015) 21204–21210.

[37] COMSOL MULTIPHYSICS v5.2, COMSOL, Inc.

[38] A.D. Rakić, A.B. Djurišić, J.M. Elazar, M.L. Majewski, Optical properties of metallic films for vertical-cavity optoelectronic devices, Appl. Opt. 37 (22) (1998) 5271–5283.

[39] C.F. Frontiers, D.R. Huffman, Absorption and Scattering by an Arbitrary Particle, Wiley-VCH Verlag GmbH, 2007, pp. 57–81.

[40] M. Kerker, D.-S. Wang, H. Chew, Surface enhanced Raman scattering (SERS) by molecules adsorbed at spherical particles, Appl. Opt. 19 (19) (1980) 3373–3388.

[41] L.O. Herrmann, V.K. Valev, J. Aizpurua, J.J. Baumberg, Self-sifting of chain plasmons: the complex optics of au nanoparticle clusters, Opt. Express 21 (26) (2013) 32377–32385.

[42] C. Tserkezis, R.W. Taylor, J. Beitner, R. Esteban, J.J. Baumberg, J. Aizpurua, Optical response of metallic nanoparticle heteroaggregates with subnanometric gaps, Part. Part. Syst. Char. 31 (1) (2014) 152–160.

[43] R. Esteban, R.W. Taylor, J.J. Baumberg, J. Aizpurua, How chain plasmons govern the optical response in strongly interacting self-assembled metallic clusters of nanoparticles, Langmuir 28 (24) (2012) 8881–8890.

[44] R.W. Taylor, R. Esteban, S. Mahajan, J. Aizpurua, J.J. Baumberg, Optimizing SERS from gold nanoparticle clusters: addressing the near field by an embedded chain plasmon model, J. Phys. Chem. C 120 (19) (2016) 10512–10522.

[45] N. Harris, M.D. Arnold, M.G. Blaber, M.J. Ford, Plasmonic resonances of closely coupled gold nanosphere chains, J. Phys. Chem. C 113 (7) (2009) 2784–2791.

[46] Y. Ozaki, K. Kneipp, R. Aroca, Frontiers of Surface-Enhanced Raman Scattering, John Wiley & Sons Ltd, 2014.

[47] D.L. Akins, Theory of Raman scattering by aggregated molecules, J. Phys. Chem. 90 (8) (1986) 1530–1534.

PAPER

Refractive index sensing with hollow metal–insulator–metal metasurfaces

View the article online for updates and enhancements.

Refractive index sensing with hollow metal–insulator–metal metasurfaces

Borislav Vasić[1,*] and **Goran Isić**[1,2]

[1] Institute of Physics Belgrade, University of Belgrade, Pregrevica 118, 11080 Belgrade, Serbia
[2] Texas A&M University at Qatar, PO Box 23874, Education City, 23874 Doha, Qatar

E-mail: bvasic@ipb.ac.rs

CrossMark

Abstract
Refractive index sensing with metal–insulator–metal (MIM) metasurfaces featuring a
continuous dielectric film between two metallic layers suffers from a low spatial overlap
between high field enhancement regions and the analyte placed above. Recent studies have thus
turned toward hollow MIM metasurfaces, particularly suited for fluid analytes which can
infiltrate the hollow cavities. Here we describe a general procedure for reaching the optimal
design in three most relevant configurations: mushroom-type structures with narrow dielectric
pedestals carrying the top metallic ribbon array, hollow structures with the metallic ribbon array
resting on a distant lateral support, and hollow structures in which the metallic ribbons are
carried by an encapsulating layer from top. We contend that since a majority of the resonant
eigenmode energy is contained within the analyte, very high refractive index sensitivities are
possible for three different measurement methods: spectral, reflectance and phase interrogation.
This is confirmed by numerical simulations demonstrating terahertz spectral sensitivities of
above 700 GHz RIU^{-1} with a normalized sensitivity of around 0.6 RIU^{-1} (RIU stands for
refractive index unit). Detection limits and dynamic ranges are estimated for both bulk
refractive index sensing and thin film detection. Refractive index sensitivities and corresponding
figure-of-merit factors are shown to reach maxima in the critical coupling regime characterized
by equal radiative and non-radiative decay rates of the resonant mode which is controlled by
cavity height. Since this regime is associated with a zero reflectance which prevents
measurements of any signal, metasurfaces should operate close to the critical coupling point
where reflected beam is still measurable. The final optimization is done by decay rate
engineering in order to achieve narrower resonances and improve sensing performance.

Supplementary material for this article is available online

Keywords: metasurfaces, metal–insulator–metal structures, refractive index sensing,
critical coupling

(Some figures may appear in colour only in the online journal)

1. Introduction

Metasurfaces comprising planar resonators with narrow spectral features and strong electric field enhancement are good candidates for efficient and label-free refractive index sensors. The flat outline is important because it simplifies fabrication and results in a compact structure while sharp spectral features can be accurately measured using well-established modern detection techniques. High sensitivity is ensured by designing the metasurface so that the analyte ends up at electric field hotspots, while the ensuing refractive-index dependent modification of the spectral response allows for label-free sensing and eliminates the need for a delicate labeling process. As the resonant frequency is swept across the entire electromagnetic spectrum simply by geometrical scaling, metasurfaces have

* Author to whom any correspondence should be addressed.

been found particularly interesting for applications at mid-infrared, terahertz and microwave frequencies where due to a long wavelength, a strong electric field enhancement is required for detecting refractive index changes of deeply sub-wavelength structures such as thin fluid and molecular films [1–4].

Initial work on metasurfaces for terahertz thin film sensing relied on standard split-ring resonators [5, 6]. Subsequently, it was established that increasing the Q-factor, e.g. by means of employing resonators with Fano lineshapes, improves the sensitivity [7–9]. Further progress was made upon realizing [1] that a large fraction of resonant eigenmode energy contained in the thick and typically high refractive index substrate harms sensitivity. Various approaches to increase the spatial overlap between the resonantly enhanced electric fields and analyte have been attempted, including the utilization of thin [10, 11] or low refractive index substrates [12], lifting of metasurfaces above substrates by dielectric pillars [13] or partially etching the substrates thus making pedestals which hold metasurfaces [14–17].

More recently, attention moved toward metasurfaces which, in addition to the layer of metallic elements on top, include a solid metal film underneath separated by an insulating layer [18], collectively referred to as metal–insulator–metal (MIM) metasurfaces. A distinct feature of such structures are leaky eigenmodes confined between the top metal patch and the underlying metal film [19], offering the possibility of highly enhanced field coupling with an analyte [20]. As a result, MIM metasurfaces have been recognized as promising platforms for sensing based on frequency shift measurements (spectral interrogation) [20–25]. The reflectance (intensity) interrogation based on the measurement of the reflected field intensity is also very efficient when MIM metasurfaces operate as electromagnetic absorbers. Then, a high electric field generated inside MIM cavities leads to a nearly complete absorption of an incident electromagnetic field and a near-zero reflection. Any change of the refractive index of a surrounding medium results in a huge relative change of the reflected field intensity [26, 27] which can be detected even by the naked eye [28]. Finally, the phase of reflected field is associated with a very steep slope in the case of a near-complete absorption. This feature provides a large phase variation upon refractive index changes and very efficient phase sensing [29, 30]. Generally, MIM metasurfaces operating as electromagnetic absorbers are very suitable for sensing since the wave injected into the MIM cavities remains trapped which results in an extreme sensitivity of reflected field to even small perturbations inside the MIM cavities [31]. However, in the original setting whereby the analyte layer is located on top of MIM cavities, the spatial overlap with resonant fields is still relatively low.

Further improvement is reached employing a structured dielectric layer [32–34], especially if parts of the dielectric under the metal patch are etched away forming narrow dielectric pedestals which carry the metal patches in so called mushroom-type MIM metasurfaces [35–37]. The highest analyte-resonant field overlap is achieved in hollow MIM metasurfaces [38–41] suitable especially for fluid analytes which can infiltrate the hollow cavities. In view of the

many diverse approaches and geometries considered for MIM metasurface sensing, a lack of well-defined design procedures and operating regimes which would yield optimal sensitivity is apparent. It should also be noted that so far only spectral interrogation has been considered, while questions on efficiency of sensing based on reflectance and phase measurements remain open.

Here, we present a general analysis of hollow MIM metasurfaces and describe a procedure by which the optimal design (an optimal metasurface is defined as the one with maximized refractive index sensitivity) can be attained for three most relevant configurations (two versions of hollow cavity arrays and the mushroom structure) operating with three different interrogation methods based on frequency, reflectance and phase measurements. The paper is organized in the following way. The modeling of metasurfaces and their operating regimes are described in section 2. The design procedure is discussed in section 3. The spatial overlap between an analyte and MIM cavity modes is analysed in section 4. Bulk refractive index sensitivities are evaluated and discussed in section 5. It is demonstrated that the refractive index sensitivity is maximized in the critically coupled regime where the radiative and non-radiative decay rates of the resonant mode are equal, while in practice, an optimal working point should be close to the critical coupling point. The dynamic range for the sensing and thin film sensitivities are considered in section 6. The final optimization is done by decay rate engineering in order to achieve narrower resonances, which is examined in section 7. At the end, in section 8, we discuss the operation at oblique incidence and issues relevant for practical realization.

2. Sensing structures, modeling and operating regimes

The schematics of four metasurfaces considered in this paper are shown in figure 1. For simplicity, we discuss metasurfaces which are periodic along x- and invariant along the y-direction, while the analysis of structures periodic along both directions would follow along the same lines. In each of cases depicted in figure 1, there is an array of parallel metallic ribbons on top. The dielectric-loaded MIM structure (metasurface 1) from figure 1(a) is transformed into a mushroom-type structure (metasurface 2) from figure 1(b) by etching away parts of the dielectric spacer in order to make isolated dielectric pedestals carrying the metallic ribbons. Two hollow geometries are investigated. The first one (metasurface 3) in figure 1(c) has a top metallic slit array which would, in practice, stand on very distant spacers such as dielectric beads. A fluid analyte, e.g. coming from environment above, can infiltrate the space between two metallic layers through slits. In the second hollow structure (metasurface 4), depicted in figure 1(d), the metallic ribbons are deposited on a transparent encapsulating layer which acts as their mechanical support. In this case, a fluid analyte can flow laterally through the hollow channel.

All configurations can be accounted for by varying the dielectric spacer width w_s in the following way: in dielectric-loaded metasurfaces it is equal to the unit cell width ($w_s = P$),
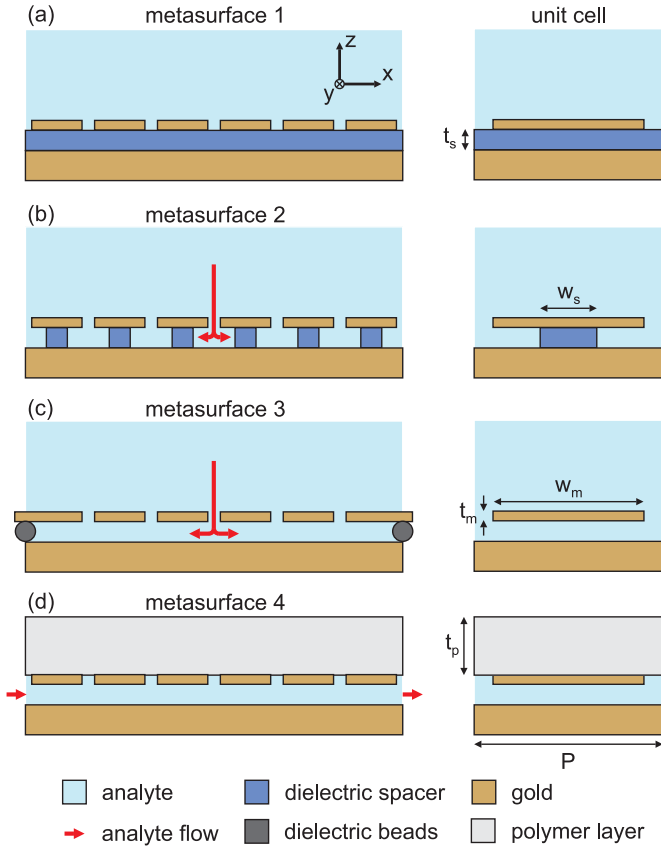
Figure 1. Cross sections (xz-plane) of MIM metasurfaces considered in this paper (left) and corresponding unit cells (right): (a) dielectric-loaded metasurface with a continuous dielectric spacer (metasurface 1), (b) mushroom-type metasurface with a dielectric pedestal in the center (metasurface 2), (c) hollow metasurface with the metallic ribbon array standing on a lateral support (metasurface 3), and (d) hollow metasurface encapsulated by a polymer layer (metasurface 4). All metasurfaces are periodic along x- and invariant along the y-direction.

Figure 2. (a) Reflectance and (b) phase spectra for two values of the analyte refractive index n_a and $n_a + \Delta n_a$. Corresponding changes of (c) reflectance (the absolute and relative changes, $\Delta R = R(n_a + \Delta n_a) - R(n_a)$ and $\rho R = \Delta R / R(n_a)$, respectively) and (d) phase ($\Delta \Phi = \Phi(n_a + \Delta n_a) - \Phi(n_a)$).

figure 1(a), in mushroom-type structures it is narrower than the metallic ribbon width ($w_s < w_m$), figure 1(b), while in hollow metasurfaces it is completely removed ($w_s = 0$), figures 1(c) and (d). Numerical calculations were done using rigorous coupled wave analysis implemented in the Reticolo code [42]. The unit cells of metasurfaces employed in simulations are presented on the right hand side of figure 1. The period P, metallic ribbon width w_m and spacer thickness (i.e. cavity height) t_s are selected according to the design procedure described below. The thickness of top metallic ribbons is $t_m = 300$ nm, whereas the metasurface from figure 1(d) is encapsulated by a polymer layer with the thickness $t_p = 40\ \mu$m.

The refractive index $n_a = 1.5$ of the reference analyte was chosen as representative for typical low-loss liquids at terahertz frequencies, such as hexane ($n_a = 1.37$), octane ($n_a = 1.391$), decane ($n_a = 1.405$), and ethanol ($n_a = 1.6$) [39, 43]. The refractive index sensitivity was calculated by increasing n_a to $n_a + \Delta n_a$, where $\Delta n_a = 0.1$ in the case of frequency interrogation, $\Delta n_a = 0.01$ in the case of reflectance interrogation, and $\Delta n_a = 0.001$ in the case of phase interrogation. Metallic parts were assumed to be
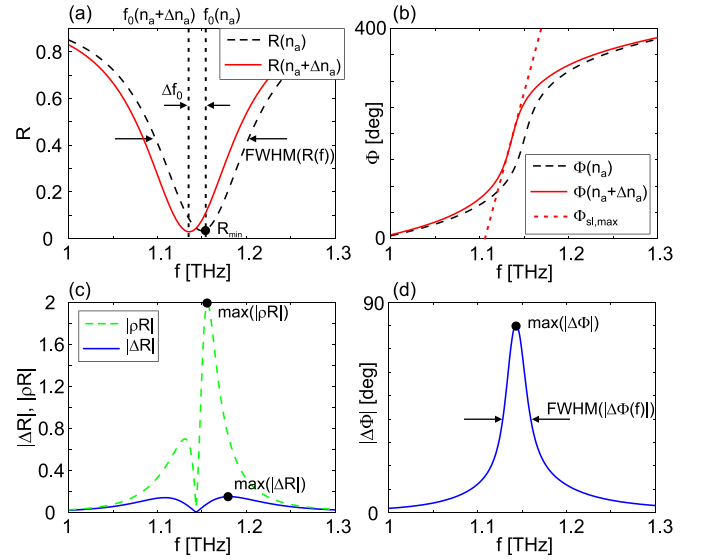
made of gold and modeled by Drude permittivity (plasma frequency $\omega_p = 1.37 \times 10^{16}$ rad s^{-1}, collision frequency $\gamma_c = 4.05 \times 10^{13}$ rad s^{-1}) [44] whereas polyimide with a refractive index of $n_s = 1.8 + j0.06$ [45, 46] was assumed for dielectric spacers in metasurfaces 1 and 2. The encapsulating layer for metasurface 4 in figure 1(d) was modeled by a low-loss polymer Zeonor with a refractive index of $n_p = 1.518 + j0.0009$ [47].

The sensing mechanism is based on shifting of a metasurface resonance due to small changes of n_a. As a result, the resonant frequency f_0 as well as the reflectance R and phase Φ at the operating frequency (not necessary equal to the resonant one) are changed as illustrated in figures 2(a) and (b). Three refractive index sensitivities (frequency, reflectance and phase), corresponding to three distinct interrogation methods, are calculated, as defined by the formula $S_I(f) = |\Delta I(f)|/\Delta n_a$, where f in parentheses denotes the operation frequency (relevant only for reflectance and phase interrogation). Depending on the chosen interrogation method, $I(f)$ stands for resonant frequency f_0, reflectance $R(f)$, or phase $\Phi(f)$. $\Delta I(f)$ denotes the change of $I(f)$ resulting from a given change Δn_a of n_a, as illustrated in figure 2. According to this definition, for reflectance and phase $S_I(f)$ is operation frequency dependent, while it is not the case for frequency interrogation.

Figure-of-merit (FOM) factors are introduced in order to evaluate the sensing efficiency from the viewpoint of listed interrogation methods. Each FOM factor is defined as the ratio between sensitivity $S_I(f)$ and a conveniently selected nonideality metric $N_I(f)$: $\text{FOM}_I(f) = S_I(f)/N_I(f)$. In spectral interrogation, narrower resonances are easier and more precisely detected. Therefore, N_f is usually taken as the resonance linewidth $\text{FWHM}\{R(f)\}$, defined as the full-width at half maximum (FWHM) of the reflectance spectra $R(f)$, figure 2(a). For intensity interrogation, $N_R(f)$ can be taken to
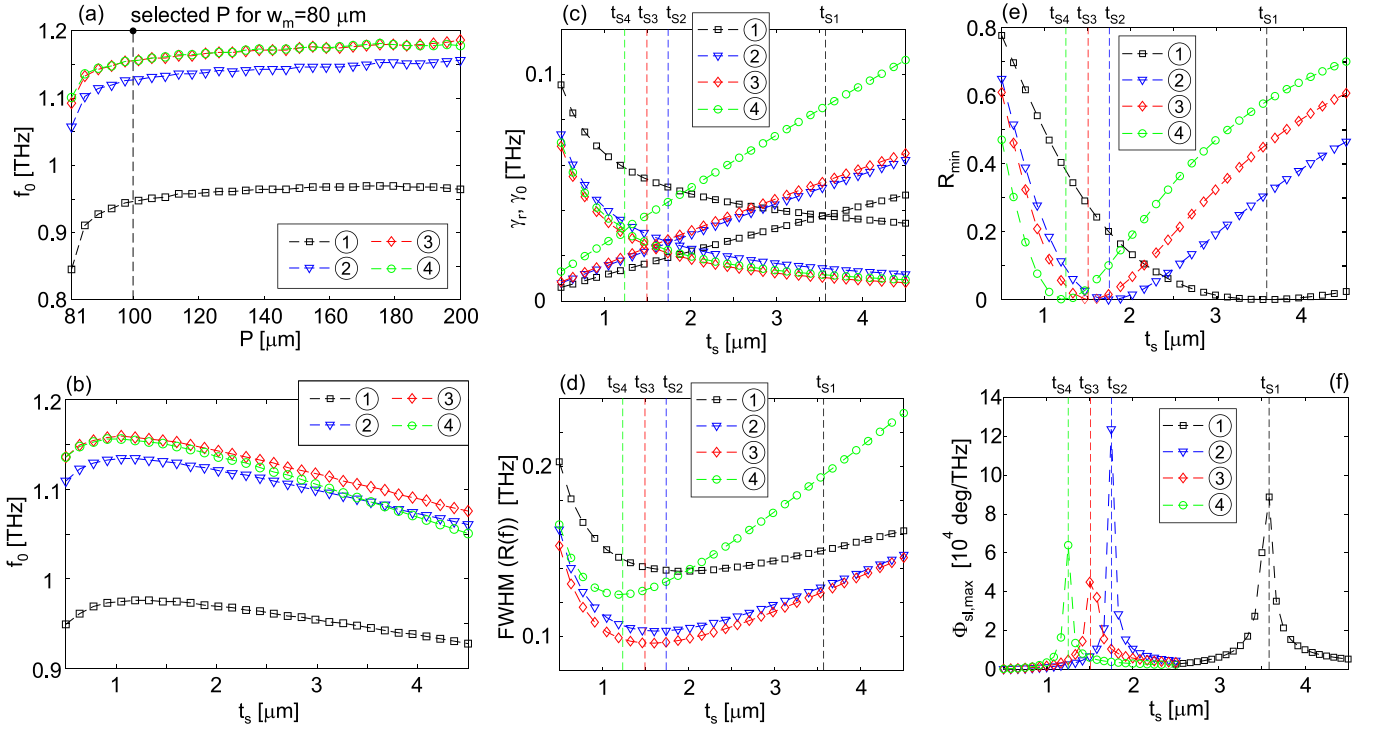
Figure 3. Resonant frequency as a function of (a) period P and (b) spacer thickness t_s. The vertical dashed line in (a) denotes the selected period of 100 μm. (c) Radiative and non-radiative decay rates, γ_r, γ_0, and (d) spectral width (FWHM) of resonant modes, (e) the minimal reflectance $R_{\min}$ and (f) the maximal phase slope $\Phi_{\mathrm{sl,max}}$ (illustrated in figure 2(b)) for all considered metasurfaces as a function of t_s. The critical coupling for the considered metasurfaces 1–4 is approximately achieved for $t_{s1} = 3.5$ μm, $t_{s2} = 1.75$ μm, $t_{s3} = 1.5$ μm, and $t_{s4} = 1.25$ μm, respectively, which are denoted by the vertical dashed lines.

be equal to the reflectance [26] $R(f)$ at operation frequency. This is justified by the fact that the accuracy of measurements is maximized for structures operating near the point of darkness with a near zero reflection [26]. Then any variation of surrounding refractive index would result in a huge relative change of the reflectance (theoretically infinite for the zero reflectance in the working point) as shown in figure 2(c). In order to avoid extremely low and experimentally non-achievable values, the minimal reflectance in numerical calculations was set to 0.01. Finally, for phase interrogation, $N_\Phi(f)$ is set equal to the spectral width FWHM$\{\Delta\Phi(f)\}$, figure 2(d), because steeper phase change is easier to detect [48].

The spectral response of MIM metasurfaces is known to be determined through the interplay of radiative and non-radiative decay processes of the resonant mode [49], as quantified by their respective rates γ_r and γ_0. In this sense, there are three possible operating regimes [49, 50]: undercoupled ($\gamma_r < \gamma_0$), overcoupled ($\gamma_r > \gamma_0$), and critically coupled ($\gamma_r = \gamma_0$). Radiative and non-radiative decay rates are most directly obtained by fitting the actual reflection coefficient (measured or numerically simulated) to the so-called temporal coupled-mode theory model [51]. For the single channel case considered here, it amounts to fitting $R(f)$ to $R_{\mathrm{TCMT}} = 1 - 4\gamma_0\gamma_r/((f-f_0)^2 + (\gamma_0 + \gamma_r)^2)$, with γ_r and γ_0 as fitting parameters [49, 52]. The calculations below were done for reflectance spectra with variable spacer thickness t_s (typical spectra for metasurface 4 are given in figure S1 of supplementary materials (available online at stacks.iop.org/JPD/54/285106/mmedia)). Since $R(f)$ has an inverted Lorentzian shape, its FWHM is qual to $2(\gamma_r + \gamma_0)$.

3. Design procedure

The geometry of MIM metasurfaces is determined by three parameters, metallic ribbon width w_m, period P, and spacer thickness t_s. The cavity mode is a standing wave with the wavelength determined by the metallic ribbon width. According to the cavity or standing-wave resonance model [49, 53], the resonant frequency of MIM cavities can be approximated with $f_0 = c/(2w_m n_c)$, where c is the velocity of light in vacuum and n_c is the cavity refractive index. The considered metasurfaces are designed for operation around 1 THz due to a straightforward fabrication of terahertz structures, whereas applications at higher frequencies are discussed below. For the chosen resonant frequency, the cavity model gives w_m around 83 and 100 μm for the spacer refractive index of 1.8 (polyimide spacer for metasurface 1) and 1.5 (spacer with completely infiltrated analyte for metasurfaces 3 and 4). Finally, we adopted $w_m = 80$ μm.

We start by considering a unit cell width that seems reasonable, $P = 100$ μm. In particular, it is chosen with the aim of achieving a large ratio w_m/P since it implies that the resonant eigenmode will span the majority of the unit cell (meaning that a high field enhancement over a large fraction of the unit cell is obtained). The resonant frequency is practically independent of P for periods larger than 100 μm as depicted in figure 3(a). On the other hand, for smaller periods the cavity modes are not localized anymore, and due to their hybridization [19], f_0 decreases. Later, in section 7, we will consider how changing P affects sensitivity, reaching a somewhat unexpected
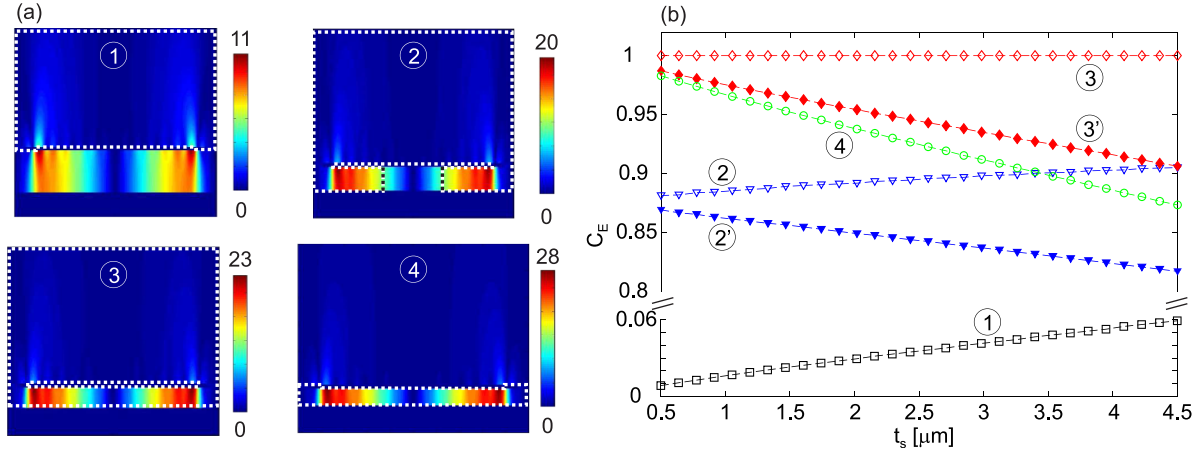
Figure 4. (a) Spatial distribution of the electric field enhancement $|E_z/E_0|$ of the resonant modes within unit cells for all four metasurfaces. The calculations were done for $t_{s1} = 3.5\ \mu\text{m}$, $t_{s2} = 1.75\ \mu\text{m}$, $t_{s3} = 1.5\ \mu\text{m}$, and $t_{s4} = 1.25\ \mu\text{m}$, respectively, and at resonant frequencies. The areas containing an analyte are encircled by dotted lines. (b) C_E factor as a function of spacer thickness. In structures 1–3, the height of the areas with the analyte was limited to 10 μm for the sake of numerical calculations. Metasurfaces marked with 2′ and 3′ are modified versions of metasurfaces 2 and 3, respectively, where the fraction of electric field energy in the analyte above the metasurfaces is omitted.

conclusion. In the dielectric pedestal case, metasurface 2 in figure 1(b), we fix $w_s = P/3$.

The resonant frequency weakly depends on the spacer thickness as shown in figure 3(b). On the other hand, t_s dominantly controls radiative and non-radiative decay rates, presented in figure 3(c), and thus determines the operating regime of MIM metasurfaces [49, 50]. Typically for MIM metasurfaces, γ_r grows approximately linearly with t_s while γ_0 decays as $1/t_s$ [49]). The critical coupling is determined by the point of intersection of these two curves when $\gamma_r = \gamma_0$. The intersection points from figure 3(c) approximately give the following spacer thicknesses (denoted by vertical lines in figure 3): $t_{s1} = 3.5\ \mu\text{m}$ for metasurface 1, $t_{s2} = 1.75\ \mu\text{m}$ for metasurface 2, $t_{s3} = 1.5\ \mu\text{m}$ for metasurface 3, and $t_{s4} = 1.25\ \mu\text{m}$ for metasurface 4. The resonance width is minimized for t_s values which are usually close to the critical coupling point, figure 3(d). A slight deviation is observed only for metasurface 1 due to higher non-radiative decay rates as a result of losses in the polyimide spacer. At the same time, the minimal reflectance R_{min}, figure 3(e), and maximal phase slope $\Phi_{\text{sl,max}}$, figure 3(f), reach extrema exactly at the critical coupling point. These results indicate that the operation of metasurfaces around the critical coupling point could be beneficial for sensing since reduced resonance width and low reflectance provide enhanced FOMs with the spectral and reflectance interrogation, respectively, while a large phase slope facilitates sensing with phase interrogation.

4. Fraction of electric field energy in analyte

Regardless of interrogation method, the sensing is based on the spectral shift of a metasurface resonance due a small change of analyte refractive index. Therefore, a larger spectral shift is expected to give a larger refractive index sensitivity in all three interrogation methods. According to the perturbation theory, the relative frequency change $\Delta f_0/f$ of an electromagnetic

cavity with refractive index n and dielectric permittivity ε due to a small change of refractive index Δn is given by the following approximate equation [54, 55]

$$\frac{\Delta f_0}{f} = -\frac{\Delta n}{n}\frac{\int_{\text{analyte}} \varepsilon |E|^2 \mathrm{d}V}{\int_{\text{all space}} \varepsilon |E|^2 \mathrm{d}V} = -\frac{\Delta n}{n}C_E, \qquad (1)$$

where E is the electric field while C_E is the fraction of electric field energy confined within the volume of an analyte to be sensed. Therefore, the relative frequency shift for a given refractive index change $\Delta n/n$ depends only on factor C_E. The maximal relative frequency shift of $(\Delta f_0/f)_{\text{max}} = \Delta n/n$ is then achieved for $C_E = 1$ when the entire electric field energy of an electromagnetic resonator is stored within the analyte.

Spatial distributions of the electric field enhancement $|E_z/E_0|$ (E_0 is the magnitude of the incident electric field) are displayed in figure 4(a) for all four metasurfaces. The cavity modes with a high field enhancement are excited between two metallic layers and their overlap with an analyte (encircled for a better visibility) is drastically increased in metasurfaces 2–4. Using such spatial distributions, factor C_E was calculated as a function of spacer thickness and depicted in figure 4(b). C_E is maximal and equal to 1 for metasurface 3 since the analyte is infiltrated both in MIM cavities as well as above them. For metasurfaces 2 and 4, a fraction of the electric energy is stored inside the dielectric pedestal (metasurface 2) and the encapsulating layer (metasurface 4) and therefore does not overlap with analyte. As a result, the nominator in equation (1) is decreased leading to a lower C_E. For t_s around 1.5 μm, C_E is reduced by only $\sim 10\%$ and $\sim 5\%$, respectively. On the other hand, in the dielectric-loaded metasurface 1, the analyte is out of the region with a high field enhancement leading to a very low C_E less than 0.1.

In calculations of C_E factors for modified metasurfaces 2 and 3, marked with 2′ and 3′, only the electric field energy inside MIM cavities was taken into account, while
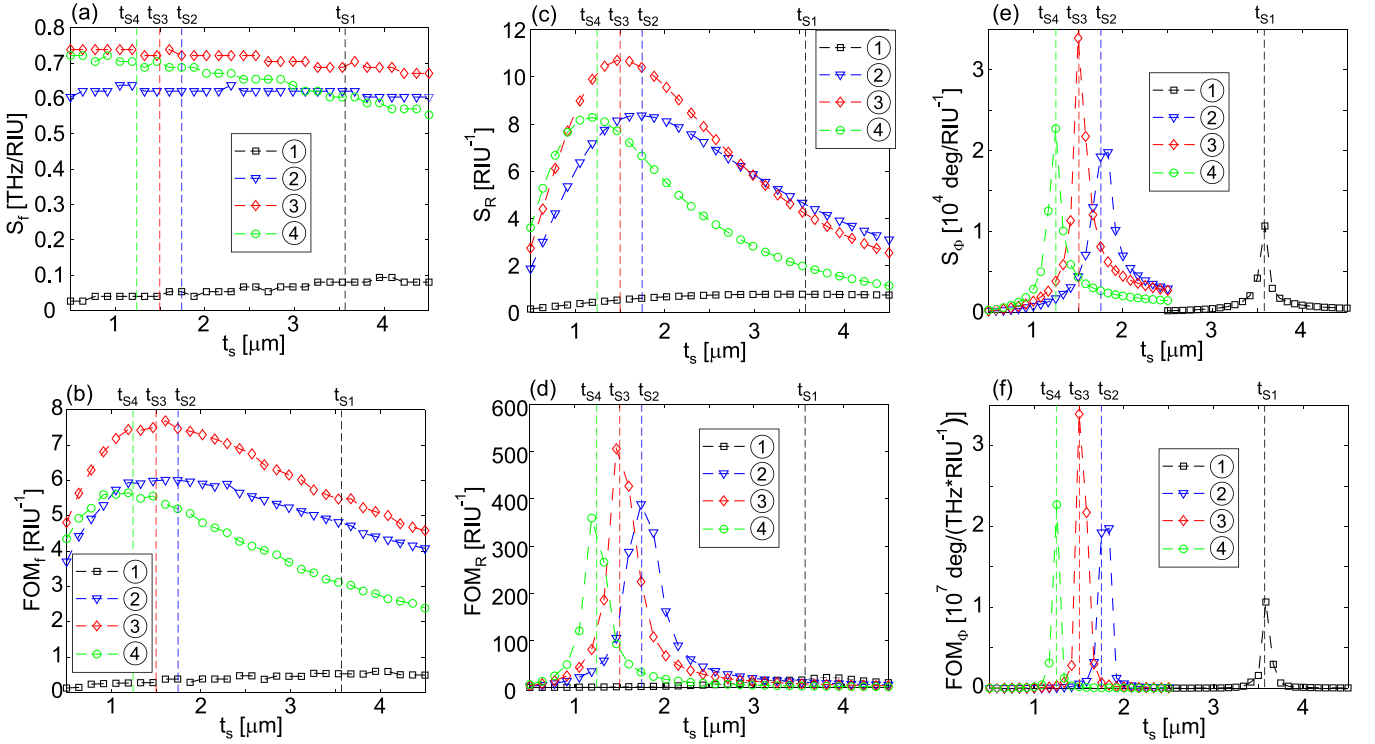
Figure 5. Bulk refractive index sensitivities and corresponding FOM factors: (a) S_f and (b) FOM$_f$, (c) S_R and (d) FOM$_R$, (e) S_Φ and (f) FOM$_\Phi$.

the fraction above the metasurfaces was omitted. An analogous case for metasurface 4 was not considered since the analyte is already confined between two metallic layers. Since the electric field enhancement is dominantly distributed inside the MIM cavities, C_E for the modified metasurfaces is only slightly decreased by around 5%. This indicates that metasurfaces 2 and 3 can operate with high refractive index sensitivities even for analytes confined just inside them as will be discussed later in section 6.

5. Bulk refractive index sensitivity

The numerically calculated refractive index sensitivities S_f, S_R, S_Φ, and corresponding FOM factors, FOM$_f$, FOM$_R$, FOM$_\Phi$ are given in figure 5. For reflectance and phase interrogation in which these quantities are operation frequency dependent, the operation frequency is set to the value at which sensitivity reaches its maximum over a conveniently chosen spectral interval enclosing the resonance (thus the operation frequency is slightly different at each t_s). Due to a large C_E factor of metasurfaces 2–4, the spectral and reflectance sensitivities are enhanced by around order of magnitude compared to the dielectric-loaded configuration of metasurface 1. The phase sensitivity of metasurfaces 2–4 is increased 2–3 times. The lower enhancement of the phase sensitivity is achieved because S_Φ dominantly depends on the phase slope which is very high in the case of the dielectric-loaded structure as well, figure 3(f). Except S_f which is independent on the operating regime, all sensitivities and FOM factors are maximized around the critical coupling point. In mushroom-type

metasurfaces, the pedestal width w_s of around 40% of the metallic ribbon width w_m is already sufficiently narrow to provide sensitivities comparable to hollow metasurfaces.

The spectral sensitivity S_f, figure 5(a), around the critical coupling point is above 0.6 THz RIU^{-1} for metasurface 2 and above 0.7 THz RIU^{-1} for metasurfaces 3 and 4 (RIU stands for refractive index unit). According to the perturbation theory and equation (1), $|S_f| = (f_0/n_a)C_E$ while the maximal sensitivity $|S_f|_{max} = f_0/n_a$ is achieved for $C_E = 1$, when the fraction of the electric field energy in an analyte is maximized. As a result, the maximal theoretical sensitivities for the critically coupled metasurfaces are the following: 0.63 THz RIU^{-1} for metasurface 1 ($f_0 = 0.95$ THz), 0.75 THz RIU^{-1} for metasurfaces 2 ($f_0 = 1.12$ THz), and 0.77 THz RIU^{-1} for metasurfaces 3 and 4 ($f_0 = 1.15$ THz). The numerical results show that metasurfaces 2, 3, and 4 reach 83%, 95%, and 90% of the theoretically predicted spectral sensitivity, as a result of large C_E factors, $C_E \approx 0.89$, $C_E = 1$, and $C_E \approx 0.96$, respectively. On the other hand, metasurface 1 with a very low C_E factor less than 0.05 achieves only 13% of S_f predicted by the perturbation theory. While the spectral sensitivity does not depend on spacer thickness, FOM factor FOM$_f$, figure 5(b), is inversely proportional to resonance width FWHM($R(f)$) and reaches the maximum around the critical coupling point where FWHM is minimized, figure 3(d).

The reflectance sensitivity S_R, figure 5(c), has a maximum around the critical coupling point. Here the resonance width is minimized, figure 3(d), which provides maximal ΔR (illustrated in figure S2 of supplementary material). The maximal sensitivity is achieved with metasurface 3. Due to the largest

C_E factor, it is associated with largest spectral shifts reflectance changes for the same refractive index variation. FOM factor FOM_R, figure 5(d), inversely proportional to reflectance, has a sharp peak at the critical coupling point where the reflectance reaches the minimal value close to zero, figure 2(e).

The phase sensitivity S_Φ, figure 5(e), and corresponding FOM_Φ, figure 5(f), are also maximized at the critical coupling point. Phase difference due to refractive index change grows with the slope of the phase curve $\Phi(f)$ (illustrated in figure S3 of supplementary material), which is maximized at the critical coupling point as depicted in figure 3(f). FOM factor FOM_Φ is also maximized at the critical coupling point since it is inversely proportional to the spectral width of $\Phi(f)$ which is minimized at this point (given in figure S3 of supplementary material).

Although the refractive index sensitivities and FOM factors are maximized at the critical coupling point, this operating regime is associated with zero reflectance which prevents measurements of any signal. Therefore, practical devices should be designed to operate close to the critical coupling point where reflected beam is still measurable. Such small detuning from the critical coupling point can be also expected in realistic devices due to unintentional deviations of t_s introduced during fabrication. According to experimental data [56], it is safe to adopt that the minimal reflectance for reliable terahertz reflection and phase measurements is $R_{th} = 0.01$. According to figure 3(e), the minimal reflectance R_{min} is below the established threshold of 0.01 for $\Delta t_s \approx 150$ nm around t_{si} ($i = 1$–4). Therefore, realistic and experimentally measurable sensitivities are obtained for the spacer thicknesses $t_{si} \pm \Delta t_s$.

The spectral interrogation is independent on spacer thickness and obviously not influenced by fluctuations of t_s. The reflectance sensitivity is also robust, S_R for metasurface 3 decreases by only $\sim 3\%$ for $\Delta t_s = 150$ nm as can be seen from figure 5(c). On the other hand, the phase sensitivity, figure 5(e), is severely affected by deviations of t_s and it decreases by more than 50% for $\Delta t_s = 150$ nm. Therefore, realistic values for S_Φ are around 1×10^4 deg RIU^{-1}.

Bulk refractive index sensitivities S_f for metasurfaces 3 and 4 are above 700 GHz RIU^{-1}, while the normalized sensitivity S_f/f_0 is around 0.6 RIU^{-1} (for f_0 around 1.15 THz). These values are slightly larger than the best experimental results achieved so far with hollow metasurfaces and for similar n_a around 1.5 ($S_f \approx 500$ GHz RIU^{-1} [38], normalized sensitivity 0.31–0.55 RIU^{-1} [39]). The obtained sensitivities also exceeds the results previously obtained with other sensing platforms at terahertz frequencies, such as waveguides [57] ($S_f = 91.25$ GHz RIU^{-1}) and Fabry–Pérot cavities (normalized sensitivity of around 0.52 RIU^{-1}) [58]. At the same time, the cavity height of hollow metasurfaces ($\approx 1.5\ \mu$m) is much smaller than the thickness of waveguide (≈ 1 mm) and Fabry–Pérot cavities ≈ 50–70 μm which indicates that hollow metasurfaces are good candidates for more compact and lower limit of detection sensing.

The comparison of refractive index sensitivities with intensity (reflectance) interrogation is more difficult since it has been much less employed. The sensitivity of holey MIM metasurface operating in transmission mode [59] of around 0.67 RIU^{-1} is order of magnitude lower than the sensitivity of hollow metasurfaces. The main benefit of the reflectance interrogation is large FOM factor and relative reflectance change for structures operating with a near-zero reflection. The phase interrogation is still practically unexplored at terahertz frequencies. The obtained phase sensitivity of around 1×10^4 deg RIU^{-1} is comparable to maximal phase sensitivities of up to 10^5 deg RIU^{-1} obtained at optical frequencies [60]. Since metasurfaces 2–4 are associated with high spectral, reflectance, and phase sensitivities at the same time, the same MIM geometry can be employed for efficient sensing with multiple interrogation methods.

According to the calculated refractive index sensitivities for metasurface 3 of $S_f \approx 700$ GHz RIU^{-1}, $S_R \approx 10$ RIU^{-1}, and $S_\Phi \approx 10^4$ deg RIU^{-1} and the corresponding resolutions [61] for spectral, reflectance and phase measurements of $\delta f = 2$–5 GHz, $\delta R = 0.01$, and $\delta \Phi = 1°$, respectively, the limit of detection for refractive index sensing is estimated at 0.003–0.007 ($<10^{-2}$) for the spectral interrogation, 10^{-3} for the reflectance interrogation, and finally, only 10^{-4} for the phase interrogation.

6. Dynamic range and thin film sensitivity

In previous sections, refractive index sensitivities have been calculated by increasing an analyte refractive index $n_a = 1.5$ for a fixed and small Δn_a. On the other hand, dynamic range defines the range of Δn_a for which the specified sensitivity can be reached. Figures 6(a)–(c) depict changes of a measured signal (Δf_0, ΔR, $\Delta \Phi$) for Δn_a varied up to 0.5 ($n_a + \Delta n_a$ in the range 1.5–2) for the spectral and reflectance interrogation, and up to 0.01 ($n_a + \Delta n_a$ in the range 1.5–1.51) for the phase interrogation. The insets of figures 6(a)–(c) display corresponding refractive index sensitivities. The sensing with spectral interrogation provides a wide dynamic range since $|\Delta f_0|$ almost linearly grows with Δn_a (figure 6(a)) in the whole range. At the same time, the resulting sensitivity S_f decreases by only 30% for $\Delta n_a = 0.5$. On the other hand, $|\Delta R|$ is approximately linear only for $n_a + \Delta n_a$ in the range from 1.5 to 1.6 (figure 6(b)). For $\Delta n_a \gtrsim 0.1$, the slope of $|\Delta R|$ curve progressively falls down while $|\Delta R|$ approaches the maximal value of 1. As a result, the reflectance sensitivity decreases by almost order of magnitude for $\Delta n_a = 0.5$. The phase interrogation is characterized with a very narrow dynamic range since $\Delta \Phi$ is linear up to only $\Delta n_a = 0.002$ while S_Φ falls down by four times for $\Delta n_a = 0.01$ (figure 6(c)). Therefore, from the point of view of the limit of detection, the phase interrogation provides the best sensing performance, but such high sensitivity is achievable in a very narrow range of Δn_a in the order of 10^{-3}.

So far we have considered bulk refractive index sensitivities, but they stay on the same level if an analyte is confined just within MIM cavity, in the channel between bottom metallic plate and top metallic resonators. This is illustrated in figure S4 of supplementary material for metasurfaces 2 and 3, while the analyte is already confined in metasurface 4. The reason for such behavior is high C_E factor even in the case when the fraction of electric field energy above metasurfaces is omitted,
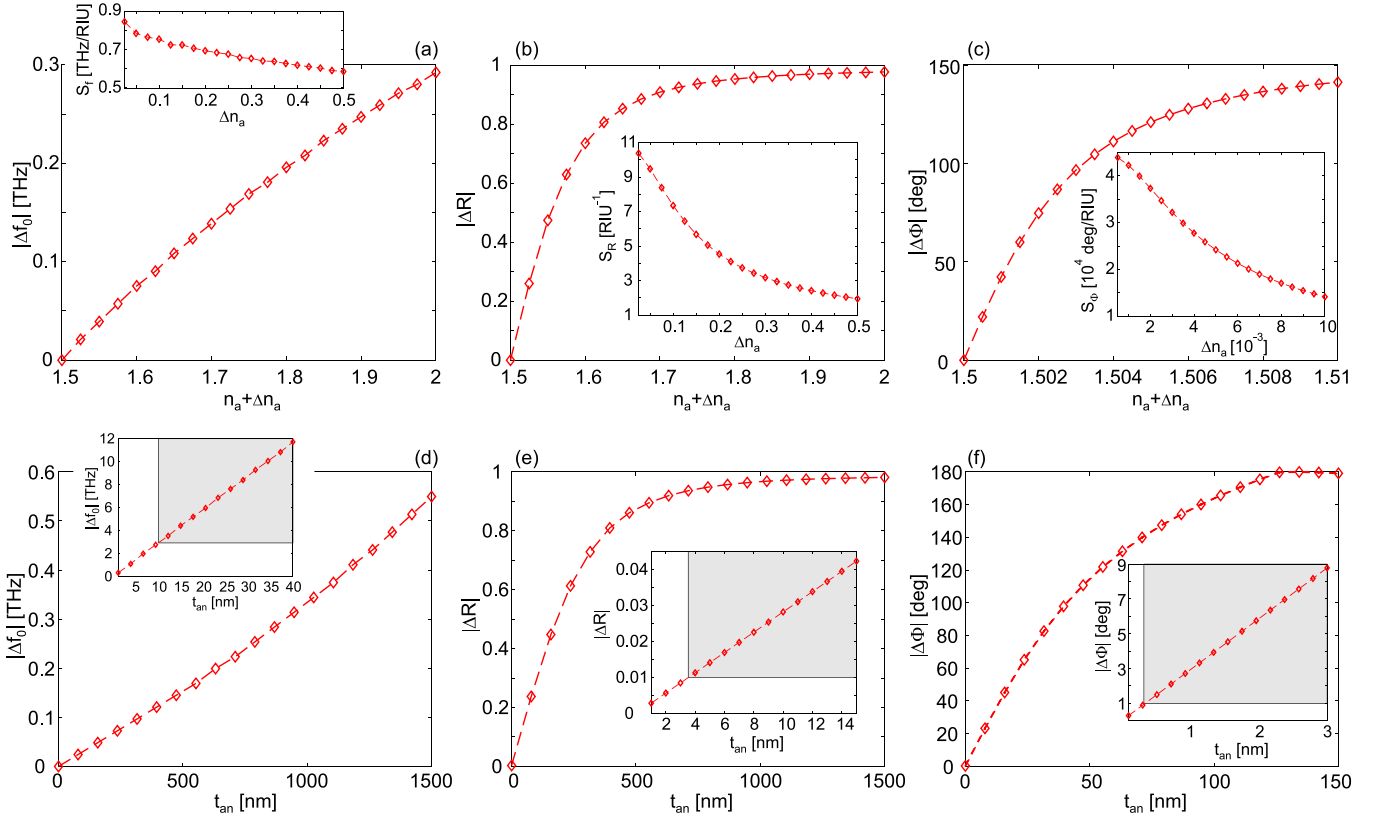
Figure 6. Dynamic range for metasurface 3: (a) $|\Delta f_0|$, (b) $|\Delta R|$, and (c) $\Delta \Phi$ for increasing Δn_a. The inset depicts changes of the corresponding sensitivities. Thin film refractive index sensitivities for metasurface 3: (d) $|\Delta f_0|$, (e) $|\Delta R|$, and (f) $\Delta \Phi$ as a function of analyte thickness t_a. The inset depicts changes of the measured signal for ultra-thin films in order to determine limits of detection. Shaded areas denote measurable film thicknesses.

as illustrated for metasurfaces 2′ and 3′ in figure 4(b). Therefore, obtained bulk refractive index sensitivities can be easily transformed into thin film sensitivities by dividing them with spacer thickness (t_{s2}, t_{s3}, t_{s4}). For metasurfaces 3 and 4, thin film sensitivities in the spectral interrogation are around 4.7×10^5 GHz (RIU^{-1} mm^{-1}), and around 4×10^5 GHz (RIU^{-1} mm^{-1}) for metasurface 2. These values are very high considering the highest spectral sensitivities (in the range 10^3–2.1×10^5 GHz (RIU^{-1} mm^{-1})) reported so far with terahertz metasurfaces [4].

Metasurfaces 2–4 provide the sensing of analytes confined within MIM cavities and therefore with a deep subwavelength thickness, where the ratio of the free-space wavelength λ_0 and the analyte (spacer) thickness is around 150–200. As a result, such metasurfaces are suitable for sensing of thin films. Limits of detection were estimated for metasurface 3. In numerical calculations, a thin film with refractive index $n_a = 1.5$ and a variable thickness t_a up to the spacer thickness $t_s = 1.5$ μm was placed inside MIM cavities, on the top of the bottom metallic plate. The rest of the cavities remained hollow. The results for changes of resonant frequency, reflectance, and phase with increasing film thickness t_a are given in figures 6(d)–(f).

Similar to the previous analysis of dynamic range, $|\Delta f_0|$ approximately linearly grows with t_a up to the maximal thickness of 1.5 μm. On the other hand, the dynamic ranges for the reflectance and phase measurements are narrower, since

ΔR and $\Delta \Phi$ are linear up to $t_a \approx 250$ nm and $t_a \approx 40$ nm, respectively. At the same time, ΔR and $\Delta \Phi$ go into the saturation (characterized with maximal $\Delta R = 1$ and $\Delta \Phi = 180°$) for $t_a \approx 1$ μm and $t_a \approx 130$ nm, respectively. Limits of detection of thin film thickness are determined from the insets of figures 6(d)–(f). If assumed resolution is $\delta f = 2$–5 GHz for the spectral interrogation and $\delta R = 0.01$ for the reflectance interrogation [61], the limits of detection are around 10 and 4 nm, respectively (the insets of figures 6(d) and (e)). Therefore, the spectral and reflectance interrogation allow detection of very thin films with a large λ_0/t_a ratio of around 5×10^4. The ultimate sensitivity for thin film detection is achieved with the phase interrogation since the accuracy of phase measurements of $\delta \Phi = 1°$ enables the detection of films with angstrom thickness as shown in the inset of figure 6(f). According to these results, hollow metasurfaces provide very high sensitivities for detection of thin film thickness as well, which are comparable to the best sensitivities achieved so far [62, 63].

7. Optimization by decay rate engineering

The main focus of the previous analysis was on the reaching of the maximal C_E factor by maximizing the overlap of an analyte and regions with a high electric field enhancement in order to minimize the influence of underlying substrate. Another direction to improve sensing performance is to design
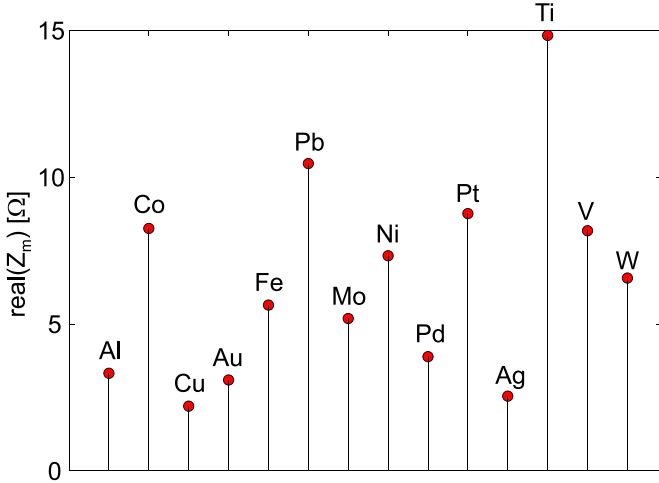
Figure 7. Real part of metal wave impedance Z_m for 14 metals [44] at 1 THz.
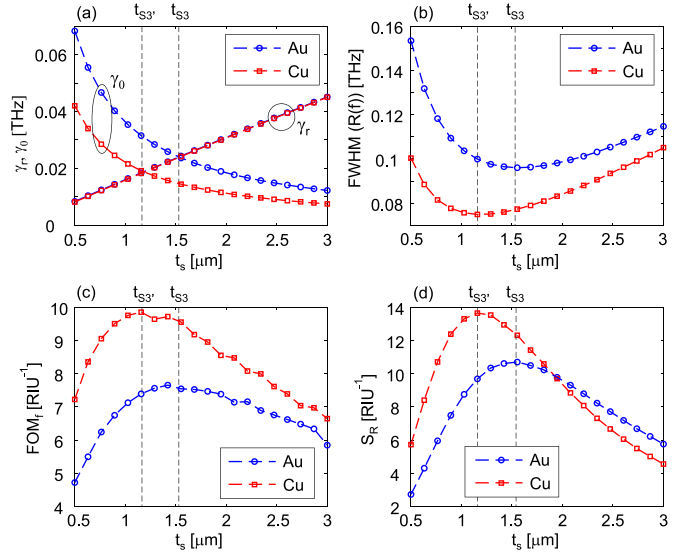

Figure 8. Metasurface 3 made with gold and copper: (a) decay rates, (b) resonance width, (c) FOM factor in the spectral interrogation, and (d) reflectance sensitivity.
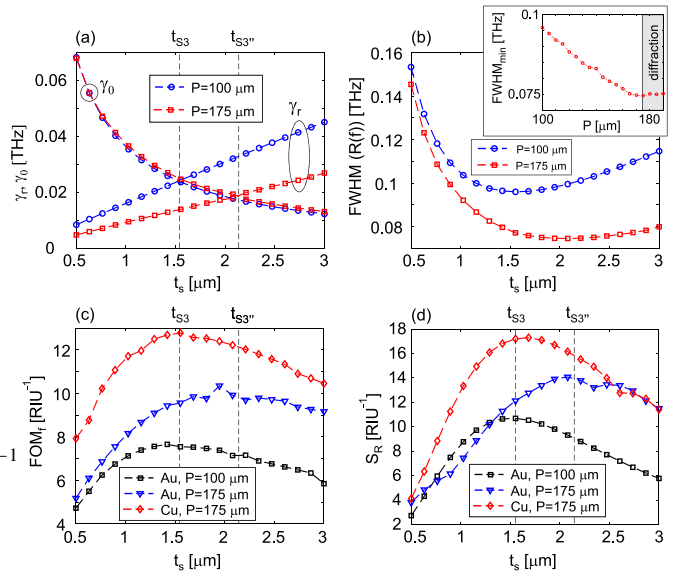

Figure 9. Metasurface 3 with larger period: (a) decay rates, (b) resonance width, (c) FOM factor in the spectral interrogation, and (d) reflectance sensitivity. The inset of (b) displays the resonance width as a function of a metasurface period.

metasurfaces with narrow resonances. Here we consider two possibilities: the utilization of a metal with lower losses and increasing of period P. Gold has been traditionally employed for making metallic parts of metasurfaces. Still, metal with lower losses would provide lower non-radiative decay rates, more narrow resonances and larger refractive index sensitivities. Metal losses are determined by the integral of Poynting vector flux through the surface enclosing metallic domains, and it can be shown that the metallic losses are proportional to the real part of the metal wave impedance ($Z_m = \sqrt{\mu_0/\varepsilon_0\varepsilon_m}$, where μ_0 is vacuum permeability, ε_0 is vacuum permittivity, and ε_m is metal permittivity) [52]. The real part of the metal wave impedance for 14 metals [44] at 1 THz (close to the operating frequency of considered metasurfaces) is presented in figure 7. As can be seen, copper has the lowest impedance and therefore, below it is considered as a candidate to replace gold.

In the numerical calculations, copper is modeled with Drude parameters, the plasma frequency $\omega_p = 1.12 \times 10^{16}$ rad s^{-1} and collision frequency $\gamma_c = 1.38 \times 10^{13}$ rad s^{-1} [44] which is four times lower than the collision frequency of gold. Decay rates for metasurface 3 made from gold and copper are depicted in figure 8(a). Radiative decay rates stay the same, but non-radiative decay rates are decreased in the case of copper resonators due to a lower absorption. As a result, the critical coupling is achieved for thinner spacer thickness $t_{s3'} \approx 1.2\ \mu$m (compared to $t_{s3} \approx 1.5\ \mu$m in the case of gold). The lower non-radiative decay rates result in narrower resonances with lower FWHM as shown in figure 8(b). Finally, copper based metasurface has a larger FOM$_f$ factor (by around 30%) and larger S_R (by around 25%) as displayed in figures 8(c) and (d), respectively. Influence of lower γ_0 on S_f and S_Φ is weak and they stay practically the same.

Increasing unit cell size and metasurface period P is another way to decrease resonance width. In this case, radiative decay rates are decreased since they scale as $\sim P^{-1}$ [64]. This is illustrated in figure 9(a) for metasurface 3 and periods $P = 100\ \mu$m (taken so far in the previous calculations) and $P = 175\ \mu$m. Non-radiative decay rates stay practically the same since they stem from losses in metallic parts which are fixed, whereas

the critical coupling is now shifted to thicker spacers with $t_{s3''} \approx 2.15\ \mu$m. The resonance width depicted in figure 9(b) is decreased for the larger period, while the minimal FWHM is reached for P around 175 μm as shown in the inset of figure 9(b). For larger periods, in addition to the zeroth order, the first diffraction order becomes propagative as well, which limits the minimal FWHM. As in the previous case, decreased resonance width leads to larger FOM$_f$ (by around 45%) and S_R (by around 30%) as presented in figures 9(c) and (d), respectively. Still, this improvement is achieved for the spacer thickness increased by around 40% which preserves thin film sensitivities at the same level. Finally, an optimal structure

would comprise of copper resonators with a larger period of $P = 175$ μm. Due to decreased both radiative and non-radiative decay rates in such structure, FOM_f and S_R are increased by around 85% and 60%, respectively (figures 9(c) and (d)), compared to the initial metasurface 3 made of gold and with the period $P = 100$ μm. The optimal structure is achieved for the same spacer thickness as the initial metasurface 3 ($t_{s3} \approx$ 1.5 μm) since the increase and decrease of t_s due to larger period and the utilization of copper, respectively, are compensated by each other. As a result, the observed improvement is reflected in thin film sensitivities as well.

8. Discussion

All presented results were obtained for the normal incidence. Still, the operation at oblique incidence could be more favorable for practical measurements in order to spatially separate the incoming and reflected beam. The cavity modes of MIM metasurfaces (field distributions plotted in figure 4(a)) are localized and their resonant frequencies weakly depend on angle of incidence (AOI) (depicted in figures S5(a) and (b) of supplementary material). The minimal reflectance increases (figure S5(c) of supplementary material) and the maximal phase slope decreases (figure S5(d) of supplementary material) with AOI which results in lower reflectance and phase sensitivity. For the operation at a larger AOI, metasurfaces can be always redesigned by tuning spacer thickness in order to reestablish the operation near to the critical coupling point. For example, the spacer thickness in metasurface 3 operating at AOI= 30° should be just increased from $t_{s3} = 1.5$ to 2 μm as shown in figure S6 of supplementary material. On the other hand, tunable AOI can be used in order to adjust the optimal operating conditions when spacer thickness deviates from the optimal one mainly due to fabrication imperfections [29]. Taking metasurface 3 again as an example, deviation of the spacer thickness by $\Delta t_s = 250$ nm from the optimal value $t_s = 1.5$ μm is compensated by the operation at AOI around 20° when the structure is returned back near to the point of critical coupling as illustrated in figure S7 of supplementary material. At the same time, tunable AOI can be used in order to increase reflection and get sufficiently high signal (figure S5(c) of supplementary material).

Operation at oblique incidence provides an additional benefit since measurements can be performed by spectroscopic ellipsometry. This technique is very attractive for sensing devices [29] since it simultaneously gives both amplitude and phase signals while relative measurements provide an ultimate sensitivity for detection of thin films. Although the ellipsometry is dominantly employed at optical and infrared frequencies, recent developments make the technique applicable at terahertz frequencies as well [65, 66]. The operation of proposed sensing structures in transmission mode is possible with similar metasurfaces consisting of a double layer of spatially separated metallic patches and an analyte under investigation between them [67].

Hollow cavities of MIM metasurfaces can be easily infiltrated by a fluid analyte, bringing it into the region with a high field enhancement. However, more sophisticated fabrication methods are required to produce such metasurfaces. In the case of mushroom-type structures [68], a partial etching of the dielectric spacer underneath top metallic stripes is needed to narrow the spacer and make a dielectric pedestal out of it. Such structures were successfully fabricated and employed for surface enhanced Raman spectroscopy [69, 70] as well as for refractive index sensing at mid-infrared [36] and even optical frequencies [35, 37].

Hollow structures were dominantly realized at microwaves [71] and terahertz frequencies [38–41, 72]. Similar planar MIM structures with a nanofluidic channel between two metallic layers were implemented at mid-infrared frequencies and applied for enhanced infrared spectroscopy of molecules and liquids [73–75], while vertical MIM cavities were used for gas sensing [76]. Finally, hollow MIM metasurfaces have been recently fabricated even at near-infrared frequencies [77]. In practical applications, hollow metasurfaces are convenient for the combination with a microfluidic channel placed between bottom metallic plate and array of top metallic resonators [39, 41].

The operation close to the critical coupling point can be adjusted by choosing an appropriate thickness of the dielectric pedestal in mushroom-type structures or lateral spacer height. In the static case when there is no possibility for a post-fabrication tuning of the spacer thickness, metasurfaces are designed with an analyte filled inside MIM cavities. On the other hand, the spacer thickness can be mechanically tunable in some hollow structures, by vertically moving the layer with top metallic resonators [71, 72]. With this option included, the critical coupling can be adjusted for a broader range of analyte refractive index. However, because of technological challenges, so far this option has been implemented only at microwaves [71] and terahertz frequencies [72]. In order to make metasurfaces more robust to fabrication inaccuracies and provide dynamically tunable critical coupling, an additional approach could be to employ the concept of disordered structures with just a few tunable unit cells [78].

An additional option to improve the sensitivity of the dielectric-loaded MIM metasurface from figure 1(a) is to use dielectric spacer as a label [79]. Although in this configuration an analyte is above the metasurface, due to its interaction with the label, the spacer properties (such as refractive index) are modified. In this way, changes in the analyte are transformed into changes of the spacer which is in a region with a high field enhancement. Still, such kind of sensing requires appropriate labeling for every analyte.

9. Conclusions

Hollow MIM metasurfaces enable an excellent spatial overlap between analyte and regions with high electric field enhancement, so that the fraction of resonant eigenmode energy stored in the analyte tends to unity. This is the dominant factor responsible for a large refractive index sensitivity (normalized sensitivity of above 0.6 RIU^{-1}). We have estimated the attainable detection limit for the refractive index sensing at

$< 10^{-2}$ RIU for spectral interrogation, 10^{-3} RIU for reflect-ance interrogation, and 10^{-4} RIU for phase interrogation. Such high resolutions are achievable in a dynamic range of around 0.5 and 0.1 RIU for the spectral and reflectance inter-rogation, respectively, whereas the price for the ultrahigh detection limit provided by the phase interrogation is a nar-row dynamic range of only 10^{-3} RIU. Since the ratio of free-space wavelength and effective analyte thickness defined by cavity height is very large (around 150), hollow metasurfaces are promising for sensing low amounts of analyte with a deeply subwavelength thickness. The attainable detection limit for the film thickness sensing is in the order of nanometers for the spectral and reflectance interrogation, and in the order of ang-stroms in the case of the phase interrogation. At the critical coupling point with equal radiative and non-radiative decay rates of the resonant mode, the resonance width is minimized, reflectance tends to zero providing a huge relative change, while the phase slope is maximized. These properties enable maximal sensitivities and FOM factors simultaneously in all three interrogation methods (spectral, reflectance, and phase). Simple semi-analytical model of reflective metasurfaces based on temporal coupled-mode theory confirms that the critical coupling point is the optimal working regime for such sens-ing structures [80]. In order to provide high enough output reflectance, realistic structures should be slightly detuned from the critical coupling point by choosing a proper spacer thick-ness of MIM cavities prior to fabrication or by slightly adjust-ing AOI for a post-fabrication tuning. Improved FOM factor in the spectral interrogation and reflectance sensitivity were achieved by decreasing the resonant mode width, by using copper instead of gold due to lower losses, and by increasing metasurface period in order to decrease non-radiative losses. Following this approach, future study should focus on a design of MIM metasurfaces with asymmetric top metallic struc-tures in order to achieve narrow resonances [81]. In order to employ hollow metasurfaces for the sensing of chiral analytes, future works should consider structures with chiral top metal-lic resonators [82]. In comparison with the standard dielectric-loaded MIM metasurfaces, the fabrication of hollow metasur-faces is more challenging. However, their implementation has already been demonstrated from microwave to near-infrared frequencies, where their full potential will be achieved by their integration with microfluidic structures.

Data availability statement

All data that support the findings of this study are included within the article (and any supplementary files).

Acknowledgments

ORCID iDs

Borislav Vasić ⓘ https://orcid.org/0000-0002-1575-8004
Goran Isić ⓘ https://orcid.org/0000-0002-6841-9356

References

[1] O'Hara J F, Singh R, Brener I, Smirnova E, Han J, Taylor A J and Zhang W 2008 Thin-film sensing with planar terahertz metamaterials: sensitivity and limitations *Opt. Express* **16** 1786–95

[2] Wu C, Khanikaev A B, Adato R, Arju N, Yanik A A, Altug H and Shvets G 2012 Fano-resonant asymmetric metamaterials for ultrasensitive spectroscopy and identification of molecular monolayers *Nat. Mater.* **11** 69–75

[3] O'Hara J F, Withayachumnankul W and Al-Naib I 2012 A review on thin-film sensing with terahertz waves *J. Infrared Millim. Terahertz Waves* **33** 245–91

[4] Beruete M and Jáuregui-López I 2020 Terahertz sensing based on metasurfaces *Adv. Opt. Mater.* **8** 1900721

[5] Driscoll T, Andreev G O, Basov D N, Palit S, Cho S Y, Jokerst N M and Smith D R 2007 Tuned permeability in terahertz split-ring resonators for devices and sensors *Appl. Phys. Lett.* **91** 062511

[6] Sun Y, Xia X, Feng H, Yang H, Gu C and Wang L 2008 Modulated terahertz responses of split ring resonators by nanometer thick liquid layers *Appl. Phys. Lett.* **92** 221101

[7] Debus C and Bolivar P H 2007 Frequency selective surfaces for high sensitivity terahertz sensing *Appl. Phys. Lett.* **91** 184102

[8] Reinhard B, Schmitt K M, Wollrab V, Neu J, Beigang R and Rahm M 2012 Metamaterial near-field sensor for deep-subwavelength thickness measurements and sensitive refractometry in the terahertz frequency range *Appl. Phys. Lett.* **100** 221101

[9] Singh R, Cao W, Al-Naib I, Cong L, Withayachumnankul W and Zhang W 2014 Ultrasensitive terahertz sensing with high-Q Fano resonances in metasurfaces *Appl. Phys. Lett.* **105** 171101

[10] Tao H *et al* 2010 Performance enhancement of terahertz metamaterials on ultrathin substrates for sensing applications *Appl. Phys. Lett.* **97** 261909

[11] Srivastava Y K, Cong L and Singh R 2017 Dual-surface flexible THz Fano metasensor *Appl. Phys. Lett.* **111** 201101

[12] Brian B, Sepúlveda B, Alaverdyan Y, Lechuga L M and Käll M 2009 Sensitivity enhancement of nanoplasmonic sensors in low refractive index substrates *Opt. Express* **17** 2015–23

[13] Dmitriev A, Hägglund C, Chen S, Fredriksson H, Pakizeh T, Käll M and Sutherland D S 2008 Enhanced nanoplasmonic optical sensors with reduced substrate effect *Nano Lett.* **8** 3893–8

[14] Otte M A, Estévez M-C, Carrascosa L G, González-Guerrero A B, Lechuga L M and Sepúlveda B 2011 Improved biosensing capability with novel suspended nanodisks *J. Phys. Chem. C* **115** 5344–51

[15] Aćimović S S, Šípová H, Emilsson G, Dahlin A B, Antosiewicz T J and Käll M 2017 Superior LSPR substrates based on electromagnetic decoupling for on-a-chip high-throughput label-free biosensing *Light Sci. Appl.* **6** 17042

J. Phys. D: Appl. Phys. **54** (2021) 285106

B Vasić and G Isić

[16] Moritake Y and Tanaka T 2018 Impact of substrate etching on plasmonic elements and metamaterials: preventing red shift and improving refractive index sensitivity *Opt. Express* **26** 3674–83

[17] Meng K *et al* 2019 Increasing the sensitivity of terahertz split ring resonator metamaterials for dielectric sensing by localized substrate etching *Opt. Express* **27** 23164–72

[18] Hibbins A P, Sambles J R, Lawrence C R and Brown J R 2004 Squeezing millimeter waves into microns *Phys. Rev. Lett.* **92** 143904

[19] Todorov Y, Tosetto L, Teissier J, Andrews A M, Klang P, Colombelli R, Sagnes I, Strasser G and Sirtori C 2010 Optical properties of metal-dielectric-metal microcavities in the THz frequency range *Opt. Express* **18** 13886–907

[20] Cong L, Tan S, Yahiaoui R, Yan F, Zhang W and Singh R 2015 Experimental demonstration of ultrasensitive sensing with terahertz metamaterial absorbers: a comparison with the metasurfaces *Appl. Phys. Lett.* **106** 031107

[21] Ye J and Van Dorpe P 2011 Improvement of figure of merit for gold nanobar array plasmonic sensors *Plasmonics* **6** 665

[22] Lu X, Zhang L and Zhang T 2015 Nanoslit-microcavity-based narrow band absorber for sensing applications *Opt. Express* **23** 20715–20

[23] Wang B-X, Zhai X, Wang G-Z, Huang W-Q and Wang L-L 2015 A novel dual-band terahertz metamaterial absorber for a sensor application *J. Appl. Phys.* **117** 014504

[24] Lu X, Wan R and Zhang T 2015 Metal-dielectric-metal based narrow band absorber for sensing applications *Opt. Express* **23** 29842–7

[25] Luo S, Zhao J, Zuo D and Wang X 2016 Perfect narrow band absorber for sensing applications *Opt. Express* **24** 9288–94

[26] Liu N, Mesch M, Weiss T, Hentschel M and Giessen H 2010 Infrared perfect absorber and its application as plasmonic sensor *Nano Lett.* **10** 2342–8

[27] Cheng F, Yang X and Gao J 2014 Enhancing intensity and refractive index sensing capability with infrared plasmonic perfect absorbers *Opt. Lett.* **39** 3185

[28] Wang X, Luo C, Hong G and Zhao X 2013 Metamaterial optical refractive index sensor detected by the naked eye *Appl. Phys. Lett.* **102** 091902

[29] Kravets V G *et al* 2013 Singular phase nano-optics in plasmonic metamaterials for label-free single-molecule detection *Nat. Mater.* **12** 304–9

[30] Vasić B and Gajić R 2014 Enhanced phase sensitivity of metamaterial absorbers near the point of darkness *J. Appl. Phys.* **116** 023102

[31] del Hougne P, Brahima Yeo K, Besnier P and Davy M 2019 On-demand coherent perfect absorption in complex scattering systems: time delay divergence and enhanced sensitivity to perturbations (arXiv: 2010.06438)

[32] Zhou H, Yang C, Hu D, Li D, Hui X, Zhang F, Chen M and Mu X 2019 Terahertz biosensing based on bi-layer metamaterial absorbers toward ultra-high sensitivity and simple fabrication *Appl. Phys. Lett.* **115** 143507

[33] Wang W *et al* 2020 Enhancing sensing capacity of terahertz metamaterial absorbers with a surface-relief design *Photon. Res.* **8** 519–27

[34] Li Y, McLamb M, Park S, Childers D, Boreman G D and Hofmann T 2020 Reciprocal plasmonic metasurfaces: theory and applications (arXiv: 2005.00685)

[35] Shen Y *et al* 2013 Plasmonic gold mushroom arrays with refractive index sensing figures of merit approaching the theoretical limit *Nat. Commun.* **4** 2381

[36] Bhattarai K, Ku Z, Silva S, Jeon J, Kim J O, Lee S J, Urbas A and Zhou J 2015 A large-area, mushroom-capped plasmonic perfect absorber: refractive index sensing and Fabry-Perot cavity mechanism *Adv. Optical Mater.* **3** 1779–86

[37] Zhu J, Lin G, Huang Y, Zhang K, Wu M, Wu W and Lu P 2020 Three-dimensional cavity-coupled metamaterials for plasmonic color and real-time colorimetric biosensors *Nanoscale* **12** 4418–25

[38] Soltani A, Neshasteh H, Mataji-Kojouri A, Born N, Castro-Camus E, Shahabadi M and Koch M 2016 Highly sensitive terahertz dielectric sensor for small-volume liquid samples *Appl. Phys. Lett.* **108** 191105

[39] Hu X, Xu G, Wen L, Wang H, Zhao Y, Zhang Y, Cumming D R S and Chen Q 2016 Metamaterial absorber integrated microfluidic terahertz sensors *Laser Photonics Rev.* **10** 962–9

[40] Duan G, Schalch J, Zhao X, Zhang J, Averitt R D and Zhang X 2018 An air-spaced terahertz metamaterial perfect absorber *Sens. Actuators* A **280** 303–8

[41] Lan F *et al* 2019 Dual-band refractometric terahertz biosensing with intense wave-matter-overlap microfluidic channel *Biomed. Opt. Express* **10** 3789–99

[42] Hugonin J P and Lalanne P 2005 *Reticolo Code for Grating Analysis* (Palaiseau: Institute d'Optique)

[43] Laib J P and Mittleman D M 2010 Temperature-dependent terahertz spectroscopy of liquid n-alkanes *J. Infrared Millim. Terahertz Waves* **31** 1015–21

[44] Ordal M A, Bell R J, Alexander J R W, Long L L and Querry M R 1985 Optical properties of fourteen metals in the infrared and far infrared: Al, Co, Cu, Au, Fe, Pb, Mo, Ni, Pd, Pt, Ag, Ti, V and W *Appl. Opt.* **24** 4493–9

[45] Tao H, Strikwerda A C, Fan K, Bingham C M, Padilla W J, Zhang X and Averitt R D 2008 Terahertz metamaterials on free-standing highly-flexible polyimide substrates *J. Phys. D: Appl. Phys.* **41** 232004

[46] Ma Y, Chen Q, Grant J, Saha S C, Khalid A and Cumming D R S 2011 A terahertz polarization insensitive dual band metamaterial absorber *Opt. Lett.* **36** 945–7

[47] George P A, Hui W, Rana F, Hawkins B G, Smith A E and Kirby B J 2008 Microfluidic devices for terahertz spectroscopy of biomolecules *Opt. Express* **16** 1577–82

[48] Lodewijks K, Van Roy W, Borghs G, Lagae L and Van Dorpe P 2012 Boosting the figure-of-merit of LSPR-based refractive index sensing by phase-sensitive measurements *Nano Lett.* **12** 1655–9

[49] Isić G, Vasić B, Zografopoulos D C, Beccherelli R and Gajić R 2015 Electrically tunable critically coupled terahertz metamaterial absorber based on nematic liquid crystals *Phys. Rev. Appl.* **3** 064007

[50] Qu C *et al* 2015 Tailor the functionalities of metasurfaces based on a complete phase diagram *Phys. Rev. Lett.* **115** 235503

[51] Fan S, Suh W and Joannopoulos J D 2003 Temporal coupled-mode theory for the Fano resonance in optical resonators *J. Opt. Soc. Am.* A **20** 569–72

[52] Isić G and Gajić R 2014 Geometrical scaling and modal decay rates in periodic arrays of deeply subwavelength terahertz resonators *J. Appl. Phys.* **116** 233103

[53] Balanis C A 2005 *Antenna Theory* (New York: Wiley)

[54] Joannopoulos J D, Johnson S G, Winn J N and Meade R D 2008 *Photonic Crystals: Molding the Flow of Light* (Princeton, NJ: Princeton University Press)

[55] Unger A and Kreiter M 2009 Analyzing the performance of plasmonic resonators for dielectric sensing *J. Phys. Chem.* C **113** 12243–51

[56] Miao Z, Wu Q, Li X, He Q, Ding K, An Z, Zhang Y and Zhou L 2015 Widely tunable terahertz phase modulation with gate-controlled graphene metasurfaces *Phys. Rev. X* **5** 041027

[57] Mendis R, Astley V, Liu J and Mittleman D M 2009 Terahertz microfluidic sensor based on a parallel-plate waveguide resonant cavity *Appl. Phys. Lett.* **95** 171113

[58] Liu Z *et al* 2020 High-Q metamaterials based on cavity mode resonance for THz sensing applications *AIP Adv.* **10** 075014

[59] Yahiaoui R, Strikwerda A C and Jepsen P U 2016 Terahertz plasmonic structure with enhanced sensing capabilities *IEEE Sens. J.* **16** 2484–8

[60] Huang Y H, Ho H P, Kong S K and Kabashin A V 2012 Phase-sensitive surface plasmon resonance biosensors: methodology, instrumentation and applications *Ann. Phys.* **524** 637–62

[61] Jepsen P U and Fischer B M 2005 Dynamic range in terahertz time-domain transmission and reflection spectroscopy *Opt. Lett.* **30** 29–31

[62] Park H-R, Chen X, Nguyen N-C, Peraire J and Oh S-H 2015 Nanogap-enhanced terahertz sensing of 1 nm thick ($\lambda/10^6$) dielectric films *ACS Photonics* **2** 417–24

[63] Srivastava Y K, Ako R T, Gupta M, Bhaskaran M, Sriram S and Singh R 2019 Terahertz sensing of 7 nm dielectric film with bound states in the continuum metasurfaces *Appl. Phys. Lett.* **115** 151105

[64] Isić G, Sinatkas G, Zografopoulos D C, Vasić B, Ferraro A, Beccherelli R, Kriezis E E and Belić M 2019 Electrically tunable metal semiconductor metal terahertz metasurface modulators *IEEE J. Sel. Top. Quantum Electron.* **25** 1–8

[65] Neshat M and Armitage N P 2013 Developments in THz range ellipsometry *J. Infrared Millim. Terahertz Waves* **34** 682–708

[66] Chen X, Parrott E P J, Huang Z, Chan H-P and Pickwell-MacPherson E 2018 Robust and accurate terahertz time-domain spectroscopic ellipsometry *Photon. Res.* **6** 768–75

[67] Karmakar S, Kumar D, Varshney R K and Chowdhury D R 2020 Strong terahertz matter interaction induced ultrasensitive sensing in Fano cavity based stacked metamaterials *J. Phys. D: Appl. Phys.* **53** 415101

[68] Ogawa S, Fujisawa D, Hata H, Uetsuki M, Misaki K and Kimata M 2015 Mushroom plasmonic metamaterial infrared absorbers *Appl. Phys. Lett.* **106** 041105

[69] Cetin A E, Yilmaz C, Galarreta B C, Yilmaz G, Altug H and Busnaina A 2020 Fabrication of sub-10-nm plasmonic gaps for ultra-sensitive Raman spectroscopy *Plasmonics* **15** 1165–71

[70] Dai F, Horrer A, Adam P-M and Fleischer M 2020 Accessing the hotspots of cavity plasmon modes in vertical metal-insulator-metal structures for surface enhanced Raman scattering *Adv. Optical Mater.* **8** 1901734

[71] Kim J, Jeong H and Lim S 2019 Mechanically actuated frequency reconfigurable metamaterial absorber *Sens. Actuators* A **299** 111619

[72] Schalch J, Duan G, Zhao X, Zhang X and Averitt R D 2018 Terahertz metamaterial perfect absorber with continuously tunable air spacer layer *Appl. Phys. Lett.* **113** 061113

[73] Le T H H and Tanaka T 2017 Plasmonics-nanofluidics hybrid metamaterial: an ultrasensitive platform for infrared absorption spectroscopy and quantitative measurement of molecules *ACS Nano* **11** 9780–8

[74] Le T H H, Morita A, Mawatari K, Kitamori T and Tanaka T 2018 Metamaterials-enhanced infrared spectroscopic study of nanoconfined molecules by plasmonics-nanofluidics hybrid device *ACS Photonics* **5** 3179–88

[75] Shih K, Ren Z, Wang C and Lee C 2019 MIR plasmonic liquid sensing in nano-metric space driven by capillary force *J. Phys. D Appl. Phys.* **52** 394001

[76] Su D-S, Tsai D P, Yen T-J and Tanaka T 2019 Ultrasensitive and selective gas sensor based on a channel plasmonic structure with an enormous hot spot region *ACS Sens.* **4** 2900–7

[77] Okatani T, Sekiguchi S, Hane K and Kanamori Y 2020 Surface-plasmon-coupled optical force sensors based on metal insulator metal metamaterials with movable air gap *Sci. Rep.* **10** 14807

[78] Imani M F, Smith D R and del Hougne P 2020 Perfect absorption in a disordered medium with programmable meta-atom inclusions *Adv. Funct. Mater.* **30** 2005310

[79] Lee M, Jeon H and Kim S 2015 A highly tunable and fully biocompatible silk nanoplasmonic optical sensor *Nano Lett.* **15** 3358–63

[80] Vasić B 2021 A semi-analytical approach for refractive index sensors based on reflective metasurfaces accepted for publication in *J. Opt. Soc. Am.* B **38** 1676–83

[81] Liu L, Li Z, Cai C, Zhu W, Zheng X, Zhang W, Xu J and Liu Z 2020 High-Q hybridized resonance in a plasmonic metasurface of asymmetric aligned magnetic dipoles *Appl. Phys. Lett.* **117** 081108

[82] Wang J, Li G, Ou K, Yu F, Chen J, Li Z, Chen X and Lu W 2021 Controllable chiral emissions from free-electron driven plasmonic metasurfaces *J. Phys. D: Appl. Phys.* **54** 105105

Beam Steering Efficiency in Resonant Reflective Metasurfaces

Goran Isić [ID], Dimitrios C. Zografopoulos [ID], Danka B. Stojanović [ID], Borislav Vasić [ID], and Milivoj R. Belić [ID]

Abstract—Beam steering is one of the prevailing functions performed by electromagnetic metasurfaces. Its efficiency depends on a large number of physical parameters associated with resonant elements comprising the metasurface and is thus notoriously difficult to optimize. Here we formulate a theoretical model for evaluating the diffraction efficiency of an array of lossy resonant elements whose spectral response is dominated by the coupling between a leaky eigenmode and a single incoming/outgoing channel. We use it to deduce a formula for the maximum attainable diffraction efficiency and the gradient parameter profile for which it is achieved. The optimization procedure is demonstrated on the example of an electrically tunable liquid-crystal terahertz beam steering metasurface. Finally, the proposed model is benchmarked against rigorous metasurface simulations.

Index Terms—Gradient metasurfaces, beam steering, temporal coupled-mode theory, tunable metamaterials.

I. INTRODUCTION

IN THE early days of optics, light has been directed using reflection and refraction exclusively. In contrast, radio waves have always been generated, guided and detected by components whose size is comparable to their free-space wavelength. Technological progress over the past decades, allowing the preparation of thin layers and fabrication of submicron structures,

has gradually lead to the development of optical components that, similarly to their radio counterparts, have wavelength or subwavelength sized elements. These diffractive optical components have since been attracting a growing research attention for their potential to provide improved characteristics or entirely new functionality. Binary optics technology [1], involving surface relief gratings with step-like profiles for light guiding, is a prominent early example.

Electromagnetic metasurfaces [2] embody one of the more recent research topics in optics aimed at using subwavelength, often resonant, optically thin structures for purposes of controlling light. The subwavelength elements, organized into unit cells, can nowadays be fabricated with nanoscopic precision, a wide range of materials and physical parameters exhibiting a desired in-plane gradient, giving virtually an arbitrary number of degrees of freedom for designers of novel optical components [3], [4].

Beam steering, also called anomalous reflection in the literature [2], [5], [6], whereby the incoming beam is reflected into a desired direction, is amongst the simplest functions these structures can provide. Beam steering metasurfaces are graded structures [4], [7] in many ways analogous to reflectarray antenna used at microwave frequencies since the 1960s [8]. In fact, many resonant metasurface element designs have either been inspired by, or rediscovered independently from, the vast knowledge accumulated over the years on microwave reflectarrays [9]–[11]. The novel terminology is, however, usually warranted by specific traits associated with operation at terahertz or higher frequencies. A number of demonstrations has so far been reported, including operation at optical [5], [12] and terahertz [13], [14] frequencies. In terms of possible applications, tunable beam steering metasurfaces are particularly interesting, especially if tuning is performed by electrical means. Various ideas have been proposed, e.g. exploiting the electric field effect in conducting oxides [15], graphene [16], semiconductor heterojunctions [17] or by switching nematic liquid crystals [18], but only few have so far been actually demonstrated [19], [20].

A major problem in developing a novel beam steering metasurface implementation, especially if it involves tunable or reconfigurable operation, is making a realistic estimate of the attainable diffraction efficiency (DE). In all but the trivial case when resonant absorption is negligible and the available phase range equals 2π, increasing DE involves some kind of trade off between amplitude and phase characteristics achievable often only through blind fine-tuning a large number of parameters. In such circumstances it is virtually impossible to identify the
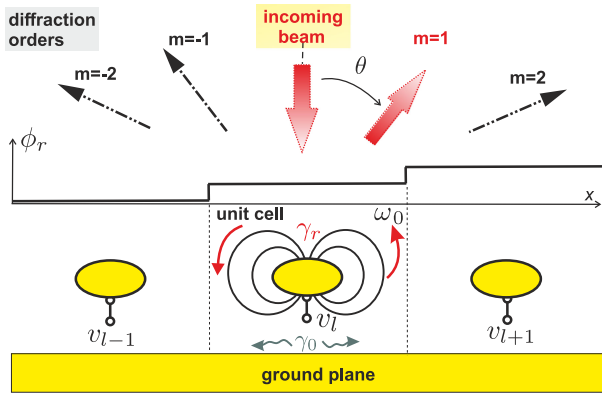
Fig. 1.   The generic beam steering metasurface considered in this article.

optimal gradient parameter profile, let alone understand the role of all resonant element physical parameters.

Here we formulate a theoretical model for beam steering efficiency, relying on scalar diffraction [21] and temporal coupled-mode theory [22]. We use it to derive analytical expressions for the optimal gradient profiles and the highest achievable DE for a wide class of reflective metasurfaces. As a proof of concept demonstration, our method is applied for the analysis of beam steering in electrically tunable liquid crystal (LC) terahertz metasurfaces [18], allowing the assessment of its accuracy and range of validity.

II. PROBLEM STATEMENT

A generic beam steering metasurface is depicted in Fig. 1. It comprises an array of resonant elements above an opaque, usually metallic, surface. While mutually similar, the resonant elements exhibit a gradual variation in one (or more) of their physical parameters, generating a step-like variation of phase shift ϕ_r the wave experiences upon reflection. This parameter will henceforth be referred to as the control parameter and denoted by v_l, as in Fig. 1. For clarity, we refer to v in singular number, but it makes no difference if it involves two or more actual physical parameters. For example, v may represent one (or more) of linear dimensions of the resonant element [5], [9], [12], [13], a voltage if the unit cell is electrically tunable [16]–[19] or anything else that can be used to modulate ϕ_r along the unit cell array.

We assume that the metasurface is a periodic array of supercells comprising N unit cells. Each unit cell is characterized by a set Π of parameters that are identical across the metasurface and the control parameter v which varies from cell to cell. Since the metasurface is periodic, the pattern of control parameters $\{v_n\}$ is also periodic, i.e. $v_{l+N} = v_l$ for any l. As N is arbitrarily selected, our analysis is applicable to a wide range of metasurfaces. Fig. 1 depicts a perpendicularly incident plane wave being diffracted into a number of diffraction orders $m = \pm 1, \pm 2, \ldots,$ because the super cell width L is at least several times larger than the free-space wavelength λ. The device operates by ensuring that the phase shift ϕ_r provided by each unit cell is such that the diffraction efficiency η_m of all but one diffraction orders is close

to zero, so that the reflected field is dominated by one diffraction order whose propagation direction is $\theta_m = \operatorname{asin}(m\lambda/L)$.

The problem of designing an efficient metasurface can be broken down into two stages. The first has a character of local optimization. In it the optimal control profile $\{v_n\}$, defined as the one which maximizes η_m for a given supercell size N and with given unit cell parameters Π, needs to be determined. The brute-force search for $\{v_n\}$, whereby all possible profiles are evaluated, has exponential complexity $\mathcal{O}(c^N)$ and is thus unfeasible even with modern computational resources for any meaningful N, e.g. $N \geq 5$. Considering that one needs to solve Maxwell's equations rigorously for the entire supercell to evaluate η_m for any given $\{v_n\}$, which is often challenging to run once, let alone through a loop, the optimal $\{v_n\}$ can never be rigorously determined for all practical purposes. In the second stage, one needs to understand how Π affects the optimal η_m and possibly sweep the Π-space searching for the global optimum. It, of course, implies repeating the first stage as the optimal control profile changes with Π.

Under these circumstances, the best one can hope for is a simplified model providing guidelines on optimal control and selection of unit cell parameters that yield an acceptable efficiency. To this end, here we start by invoking the scalar diffraction theory and the Fraunhofer approximation [21], [23], according to which the diffraction efficiency into the m-th diffraction order can be written as

$$\eta_m = \operatorname{sinc}^2\left(\frac{m}{N}\right)|S_N|^2, \tag{1}$$

with the diffraction sum S_N given by

$$S_N = \frac{1}{N}\sum_{n=0}^{N-1} r_n e^{-imn\alpha}, \quad \alpha = \frac{2\pi}{N}. \tag{2}$$

In the above equation, r_n represents the reflection coefficient for an array of unit cells equal to the n-th cell in the considered metasurface, i.e. r_n corresponds to a metasurface in which the supercell comprises only one unit cell with control parameter equal to v_n. Equation (1) has been widely used in designing multilevel surface relief gratings [24] with many studies devoted to assessing its accuracy [25]. The extent to which Eq. (1) is applicable to resonant arrays is, on the other hand, currently unclear since it has so far not been investigated in context of metasurfaces. On general grounds, it may be expected to be exact in the limit of $\theta \to 0$, while for any finite deflection angle θ, the accuracy depends on the specific characteristics of the near fields at resonance. For purposes of illustration, in Section IV we demonstrate the validity of Eq. (1) by comparing its predictions with a rigorous numerical solution of Maxwell equations for the case of an array of metal-insulator-metal (MIM) resonators infiltrated by a nematic LC.

Our analysis is focused on the simplest type of resonant elements for which we demand that their spectral characteristic close to resonant frequencies is dominated by the interaction of a quasi-normal mode (i.e. leaky eigenmode) [26] with a single incoming/outgoing channel. More formally, we assume that the reflection coefficient $r(\omega)$ of a uniform array of such
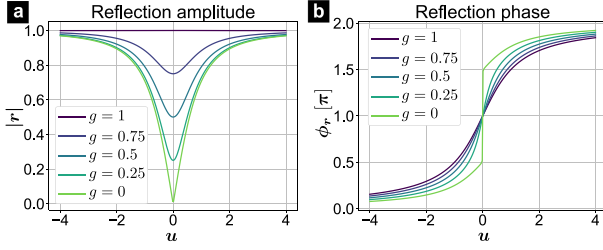
Fig. 2. Single-channel TCMT model: (a) Reflection amplitude and (b) phase drawn for various overcoupling parameter g values. The plots in this article have been prepared with the help of Matplotlib [30].

resonators can be accurately described by the temporal coupled-mode theory (TCMT) model for a single-channel resonant system [22], [27]

$$r(\omega) = \frac{u - \mathrm{i}g}{u + \mathrm{i}}, \quad u = \frac{\omega - \omega_0}{\gamma_\mathrm{r} + \gamma_0}, \quad g = \frac{\gamma_\mathrm{r} - \gamma_0}{\gamma_\mathrm{r} + \gamma_0}. \quad (3)$$

Here the resonant angular frequency ω_0, radiative decay rate γ_r and non-radiative decay rate γ_0 are the standard TCMT parameters, while ω denotes the operation frequency. For purposes of the analysis below, a representation of r in terms of two new parameters is more helpful. The parameter u, introduced as the normalized deviation from the resonant frequency in Eq. (3), can be seen as the resonators' state variable. Meanwhile, the overcoupling parameter g, defined as the normalized difference between the radiative and non-radiative decay rate and also related to the reflection coefficient at resonance frequency by $g = -r(\omega_0)$, quantifies the ability of the resonator array to generate phase shift without losing energy. Equation (3) provides an accurate description of resonator arrays with quality factors [28] high enough so that the direct (background) reflection defined as in Ref. [22] is spectrally flat in the resonance region. The formalism can readily be generalized [29] both in terms of multiple incoming/outgoing channels and quasi-normal modes. Fig. 2 shows $r(u)$ plotted according to Eq. (3).

III. OPTIMAL CONTROL

We will consider the optimization of $|S_N|$ only for the 1-st diffraction order, since for any $|m| > 1$ case there exists an equivalent $m = 1$ case (possibly with a smaller supercell). This is because the set of elements $\{\mathrm{e}^{-\mathrm{i}mn\alpha}\}$ for $n = 0, 1, \ldots, N - 1$, which appear as summation terms in Eq. (2) for $|m| > 1$ is a subset of elements $\{\mathrm{e}^{-\mathrm{i}n\alpha}\}$ for $n = 0, 1, \ldots, N - 1$ in the summation for $m = 1$.

Let $[u_{(1)}, u_{(2)}]$ denote the interval onto which v-space is mapped by $u(v)$ and let $v_{(i)}$, $i = 1, 2$, be defined by $u_{(i)} = u(v_{(i)})$. The procedure for identifying the optimal control profile $\{v_n\}$ may be classified based on how g depends on v. In order of how they are addressed below, we distinguish the (a) lossless case, (b) flat tuning, (c) general case and (d) skewed tuning.

The lossless case is characterized by $g(v) = 1$ and for it analytic expressions exist. We refer by flat tuning to the case $g(v) = g_0$ with g_0 being a constant and show that it can be reduced to the lossless case. For the general case, with $g(v)$

being arbitrary, we describe a simple numerical solution. Finally, by skewed tuning we denote the general case which fulfills the condition that $g(v) = g_0 + au(v)$ and we show that it can also be reduced to the lossless case in a similar manner as flat tuning. We show below that skewed tuning is an excellent approximation for realistic situations making it the model of choice in practice.

A. Lossless Resonators

In lossless (i.e. ideal) resonators $g_0 = 1$, so that, according to Fig. 2, changing u only affects ϕ_r, while $|r| = 1$. The optimal control then involves identifying the phase profile $\{\phi_n\}$ which maximizes $|S_N|$ as given by Eq. (2). If the tuning phase range $\Delta\phi$, defined as

$$\Delta\phi = \phi_{(2)} - \phi_{(1)}, \quad \phi_{(i)} = \phi_r(v_{(i)}), \quad i = 1, 2, \quad (4)$$

is greater or equal to $(N - 1)\alpha$, then it is obvious that there exists an equidistant phase profile $\{\phi_n\}$, with phase step equal to α, such that $|S_N| = 1$, which is the largest value $|S_N|$ can reach under any conditions.

For $\Delta\phi < (N - 1)\alpha$, which is likely to be the case almost always in practice, it is straightforward but a bit tedious (and hence omitted here) to show that the phase profiles $\{\phi_n^{\mathrm{id}}\}$ listed below maximize $|S_N|$ allowing it to reach the value denoted by S_N^{id} (the superscript 'id' here stands for ideal, i.e. lossless).

For odd $N = 2l + 1$ and s defined as $s = \Delta\phi/2\alpha$, $\{\phi_n^{\mathrm{id}}\}$ and S_N^{id} are given by

$$\phi_{l+1\pm k}^{\mathrm{id}} = \begin{cases} \phi_{\mathrm{mid}}, & k = 0, \\ \phi_{\mathrm{mid}} \pm k\alpha, & 0 < k \leq \lfloor s \rfloor, \\ \phi_{\mathrm{mid}} \pm \frac{\Delta\phi}{2}, & \lfloor s \rfloor < k \leq l \end{cases} \quad (5)$$

$$S_N^{\mathrm{id}} = 1 + 2\lfloor s \rfloor + 2\mathrm{Re}\left\{\frac{1 - \mathrm{e}^{\mathrm{i}(l-\lfloor s \rfloor)\alpha}}{1 - \mathrm{e}^{\mathrm{i}\alpha}}\mathrm{e}^{\mathrm{i}(\lceil s \rceil - s)\alpha}\right\}. \quad (6)$$

Here $\lfloor x \rfloor$ denotes the largest integer less than or equal to x, $\lceil x \rceil$ is the smallest integer greater than or equal to x and $\phi_{\mathrm{mid}} = (\phi_{(1)} + \phi_{(2)})/2$ is the phase value at the middle of the available phase interval $[\phi_{(1)}, \phi_{(2)}]$.

For even $N = 2\tilde{l}$ and s defined as $s = \Delta\phi/2\alpha - 1/2$, we have

$$\phi_{l+1/2\pm(k+1/2)}^{\mathrm{id}} = \begin{cases} \phi_{\mathrm{mid}} \pm \left(k + \frac{1}{2}\right)\alpha, & 0 \leq k \leq \lfloor s \rfloor, \\ \phi_{\mathrm{mid}} \pm \frac{\Delta\phi}{2}, & \lfloor s \rfloor < k < l. \end{cases} \quad (7)$$

$$S_N^{\mathrm{id}} = 2 + 2\lfloor s \rfloor + 2\mathrm{Re}\left\{\frac{1 - \mathrm{e}^{\mathrm{i}(l-1-\lfloor s \rfloor)\alpha}}{1 - \mathrm{e}^{\mathrm{i}\alpha}}\mathrm{e}^{\mathrm{i}(\lceil s \rceil - s)\alpha}\right\}. \quad (8)$$

To be accurate, we note that the expressions listed above provide the maximum attainable value of $|S_N|$ in all but some practically irrelevant cases that occur at $\Delta\phi < \pi/3$. The phase profiles as a function of $\Delta\phi$ given by Eqs. (5) and (7) might appear cumbersome, but their meaning is simple, as plotted in Fig. 3(a) and (b), by the $g_0 = 1$ curves. They merely show that the optimal profile in the lossless case involves equidistant spacing, with a step equal to α, distributed symmetrically around ϕ_{mid} until the phase range is exhausted, with setting all the remaining phase elements to $\phi_{(1)}$ and $\phi_{(2)}$.
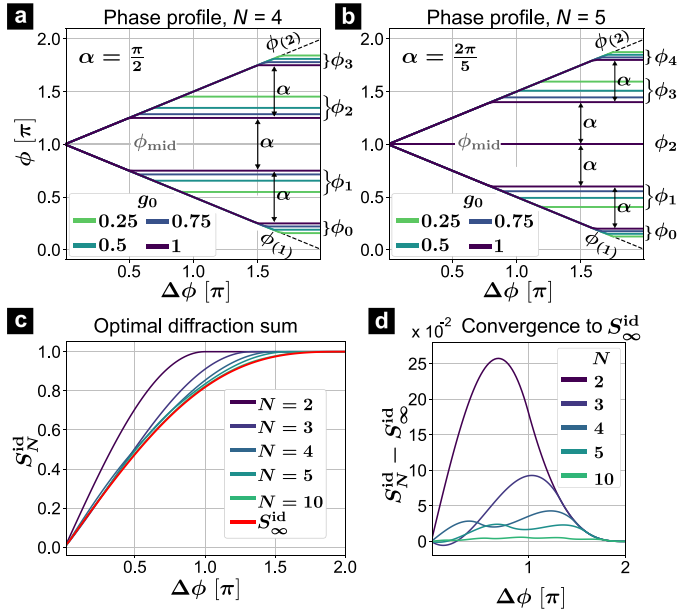
Fig. 3.   Phase profiles under optimal control for the flat tuning problem, drawn assuming $\phi_{\mathrm{mid}} = \pi$ for (a) even $N = 4$ and (b) odd $N = 5$. The lossless case profiles ϕ_n^{id} correspond to ϕ_n for $g_0 = 1$. (c) Diffraction sum maxima as a function of available phase range for various N and (d) their convergence towards S_∞^{id}.

The resonator state profile $\{u_n^{\mathrm{oc}}\}$ under optimal control is found from $\{\phi_n^{\mathrm{id}}\}$ using

$$u_n^{\mathrm{oc}} = \tan \frac{\phi_n^{\mathrm{id}} - \pi}{2}, \qquad (9)$$

which follows from Eq. (3) when $g = 1$. Finally, one obtains the optimal control profile $\{v_n^{\mathrm{oc}}\}$ from $v_n^{\mathrm{oc}} = u^{-1}(u_n^{\mathrm{oc}})$, where $u^{-1}(u)$ is the inverse of $u(v)$.

The plots of S_N^{id}, evaluated as a function of $\Delta\phi$ according to Eqs. (6) and (8) are shown in Fig. 3(c) for several values of N. As expected, S_N^{id} reaches unity for any $\Delta\phi \geq (N-1)\alpha$ (note that α also changes with N). Although there is a variation of S_N^{id} with N, Fig. 3(c) shows that the S_N^{id} curves quickly converge towards their $N \to \infty$ asymptote S_∞^{id}. This is more evident in Fig. 3(d) where the differential $S_N^{\mathrm{id}} - S_\infty^{\mathrm{id}}$ is shown to be less than 0.03 for $N = 5$ and less than 0.01 for $N = 10$, for any $\Delta\phi$. Therefore, already for $N \geq 5$ one may safely use S_∞^{id} as an estimate for the maximum $|S_N|$ value achievable under optimal control.

B. Flat Tuning

Now, let us consider the more interesting case of $g_0 < 1$ and denote the maximum of $|S_N|$ (obtained under optimal control) by $S_N(g_0)$. As in the lossless case, tuning v leads to sweeping one of the constant-g curves in Fig. 2 within the $[u_{(1)}, u_{(2)}]$ interval, except that here $|r|$ also changes with v, so that ϕ_r values close to π (i.e. $u \approx 0$) are penalized by smaller values of $|r|$. The optimal control problem in this case can be reduced to the ideal $g_0 = 1$ case, by noting that for any profile $\{u_n\}$ the

following identity holds

$$\sum_{n=0}^{N-1} \frac{u_n - \mathrm{i}g_0}{u_n + \mathrm{i}} \mathrm{e}^{-\mathrm{i}n\alpha} = \frac{1+g_0}{2} \sum_{n=0}^{N-1} \frac{u_n - \mathrm{i}}{u_n + \mathrm{i}} \mathrm{e}^{-\mathrm{i}n\alpha}, \qquad (10)$$

which can be seen by adding a factor proportional to $\sum_{n=0}^{N-1} \exp(-\mathrm{i}n\alpha) = 0$ to the left-hand side. This means that the S_N value of an array of g_0 resonators with state profile $\{u_n\}$ is equal $(1+g_0)/2$ times the S_N value of lossless resonators ($g_0 = 1$) having the same state profile. It then implies that the considered array of g_0-resonators with the set of available states $[u_{(1)}, u_{(2)}]$ has the same state profile $\{u_n^{\mathrm{oc}}\}$ under optimal control as the array of lossless resonators with the same set of available states, while the maximal diffraction sum is

$$S_N(g_0) = \frac{1+g_0}{2} S_N^{\mathrm{id}}. \qquad (11)$$

Now let us assume that we are given an array of g_0 resonators with specified values of $u_{(1)}$ and $u_{(2)}$ and asked to determine the corresponding optimal control profile $\{u_n^{\mathrm{oc}}\}$. The way we would do it is to first determine $\phi_{(1)}$ and $\phi_{(2)}$ which define the set of available phases corresponding to lossless resonators with the same $u_{(i)}$ values

$$\phi_{(i)} = 2 \arctan u_{(i)} + \pi, \quad i = 1, 2. \qquad (12)$$

Then, we proceed as in Section III-A to determine the corresponding $\{\phi_n^{\mathrm{id}}\}$ while $S_N(g_0)$ is obtained from Eq. (11) using the value S_N^{id} evaluated for $\Delta\phi = \phi_{(2)} - \phi_{(1)}$. Finaly, the desired $\{u_n^{\mathrm{oc}}\}$ is retrieved from $\{\phi_n^{\mathrm{id}}\}$ with the help of Eq. (9) and from it the control profile $\{v_n^{\mathrm{oc}}\}$ by inverting the corresponding $u(v)$ mapping. The phases $\{\phi_n\}$ under optimal control of the g_0-resonator array can be obtained as the arguments of the reflection coefficients $\{r_n\}$ evaluated by plugging $\{u_n^{\mathrm{oc}}\}$ into Eq. (3). These phase profiles are shown for several exemplary cases in Fig. 3(a) and (b) (the $g_0 < 1$ curves). As expected, the optimal phases are seen to be slightly deflected away from the $\phi \approx \pi$ region as it is associated with smaller $|r|$ values, with the deflection being larger for smaller g_0 values.

The outlined procedure for optimal control in case of flat tuning is straightforward, but non-trivial and thus understanding in which circumstances is it warranted would be helpful. Upon inspecting Fig. 3(a)–(d), one finds that for $g_0 > 0.75$, the optimal $\{\phi_n\}$ differs only very slightly from the $\{\phi_n^{\mathrm{id}}\}$ set, which means that the diffraction sum obtained by using simply $\{\phi_n^{\mathrm{id}}\}$ instead of the optimal $\{\phi_n\}$ will be only marginally smaller than the value given by Eq. (11). Meanwhile, from Fig. 3(c), one finds that $S_N^{\mathrm{id}} > 0.95$ if $\Delta\phi > 1.5\pi$, implying that not much is to be gained by fine optimization when the available phase range is above 1.5π. An analogous conclusion holds for the general and skewed tuning cases discussed below. Therefore, the analysis presented in this article makes most sense for lossy resonant metasurfaces - there is no point in applying it to systems with $g_0 \approx 1$ and $\Delta\phi \approx 2\pi$ as the accuracy of the underlying scalar diffraction theory is lower than the prescribed gain. In those cases one is likely to be well off using the lossless profile with phase steps equal to α, as given by Eqs. (5) and (7).
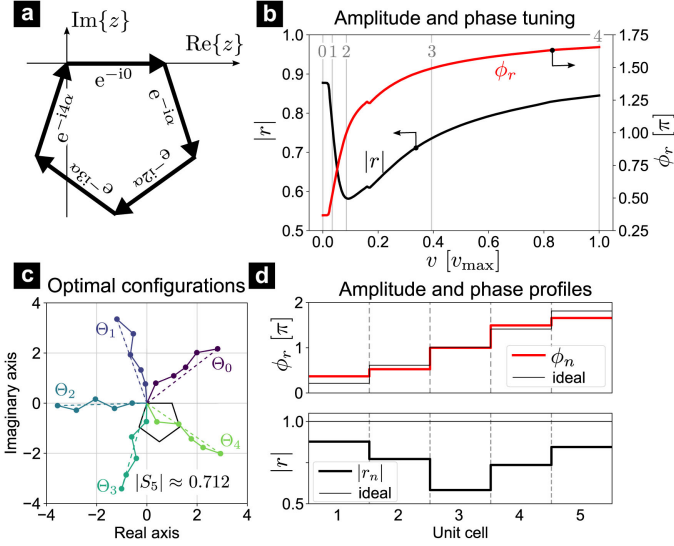
Fig. 4. (a) Graphical interpretation of the optimal control problem. (b) $r(v)$ example for the metasurface described in Section IV. (c) Maximal values of $|S_5|$ for $r(v)$ given under (b). (d) Optimal phase and amplitude profiles.

C. General Case

Let us, for the purposes of this section, leave aside all the previous considerations involving the TCMT model and the u and g parameters. Consider instead a more general problem of maximizing $|S_N|$ given by Eq. (2) by a control profile $\{v_n\}$ defining the r_n terms in Eq. (2) through $r_n = r(v_n)$, where $r(v)$ is an arbitrary complex-valued function such that $|r| \leq 1$.

This problem has a simple graphical interpretation if we look at how the different $\exp(-in\alpha)$ terms are added together in the complex plane. If $r_n = 1$ for all n, the $\exp(-in\alpha)$ terms form a regular convex N-sided poligon, as depicted in Fig. 4(a) for the $N = 5$ case. As pointed out before, any $m > 1$ case will involve the same terms but perhaps permuted, so that they form some other regular, convex or star, N'-sided polygon for N' being a divisor of N. Since the polygon is closed, the sum amounts to zero. The effect of multiplying by r_n amounts to rotating the corresponding $\exp(-in\alpha)$ term clockwise by ϕ_n and reducing its amplitude by a factor $|r_n|$. Therefore, maximizing $|S_N|$ is equivalent to maximizing the length of the broken line obtained by rectifying the mentioned polygons through multiplication by r_n.

This problem has a simple solution which we illustrate considering a particular example of $r(v)$, shown in Fig. 4(b). The shown curves represent the reflection coefficient on an array of MIM resonators infiltrated by a nematic LC, while v represents the gate voltage which tunes the nematic molecule orientation. Further details of this example will be given below and, in particular, in Section IV.

Finding the optimal $\{v_n\}$ can be broken down into two steps. In the first, we select an angle Θ and search for the $\{v_n\}$ that maximizes the projection of the broken line representing S_N onto that direction. Since the projection of S_N is equal to the sum of the projections of the $r_n \exp(-in\alpha)$ terms on Θ, this search involves N independent optimizations of each of the

$r_n \exp(-in\alpha)$ terms, which is easily done even by the brute-force sweep of the entire v space (i.e. available v values). The second step involves repeating the first step for all Θ between 0 and 2π, to find the direction $\Theta_{\max}$ onto which the S_N projection is maximal for $\{v_n^{\max}\}$. It is easy to see that the set $\{v_n^{\max}\}$ represents the optimal control profile for the initial problem.

Applying the above procedure onto the $N = 5$ example, with $r(v)$ given in Fig. 4(b), we obtain $N = 5$ values of $\Theta_{\max}$ which all yield the maximum of $|S_5| \approx 0.712$. These angles are denoted by Θ_i, $i = 0, 1, \ldots, 4$ and drawn in Fig. 4(c), together with the optimal broken lines. The multiplicity of equivalent optima is a consequence of the N-fold rotational symmetry of the geometrical problem, with each solution corresponding to one of the N cyclic permutations of $\{r_n\}$ in the supercell. This, of course, means that when searching for $\Theta_{\max}$, it is sufficient to sweep only the $[0, \alpha]$ range. The optimal $|r_n|$ and ϕ_n profiles corresponding to the Θ_0 case are shown in Fig. 4(d). The optimal voltage values $\{v_n^{\max}\}$ are indicated by the vertical gray lines in Fig. 4(b) and enumerated by the corresponding index $n = 0, 1, \ldots, 4$.

Although general and simple, easily reproducing the results from Sections III-A and III-B, the numerical procedure described in this section only provides the correct solution, with no insight on how it is conditioned by the unit cell characteristics.

D. Skewed Tuning

While capturing its nature, the flat tuning model of Section III-B does not give an accurate quantitative assessment in the tuning problem used as the example in Fig. 4 because the g value changes noticeably over the v space. To explain this, we will consider in more detail the characteristics of the LC cell whose reflection function was shown in Fig. 4(b). Again, for the purposes of this section, the LC cell is to be seen as a representative example of a terahertz metasurface while its specific details are given in Section IV. The reflection spectra for several typical v values are given in Fig. 5(a) and (b) (dots), together with best TCMT fits drawn by solid lines. In fact, the $v_n, n = 0, 1, \ldots, 4$ values for which these curves are drawn are equal to $\{v_n^{\max}\}$ from the previous section.

First, we notice that the TCMT fits reproduce the actual LC cell spectra rather well, thus justifying the use of the TCMT model. The $r(v)$ curves in Fig. 4(b) have, in fact, been drawn for the operation frequency $f = 1\,\text{THz}$, meaning that their values correspond to the intersection of the reflection spectra and the $f = 1\,\text{THz}$ vertical line in Fig. 5(a) and (b). The extracted TCMT parameters as a function of v are drawn in Fig. 5(c), while the functions $u(v)$ and $g(v)$ can be inferred from Eq. (3). In particular, with increasing v, u increases because $f_0 = \omega_0/2\pi$ decreases, as seen in Fig. 5(c). Meanwhile, g decreases from around 0.65 at v_0 to around 0.52 at v_4, which can be seen by observing that the $|r(\omega_0)|$ value (reflection amplitude at resonance) decreases for increasing v_n.

To account for the variation of g, let us assume that $u(v)$ and $g(v)$ are arbitrary but so that the linear relationship
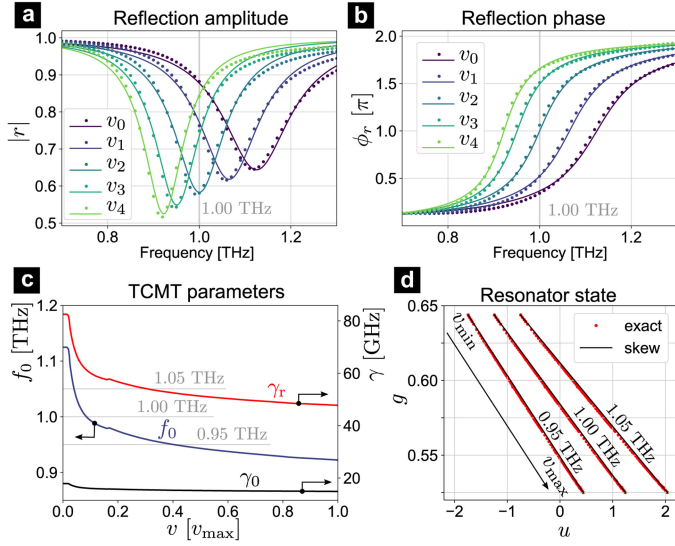
$$g(v) = g_0 + au(v), \tag{13}$$

Fig. 5.   (a) Reflection amplitude and (b) phase spectra for the metasurface described in Section IV, drawn for 5 values of v - the same ones that maximize $|S_5|$ in Fig. 4. Dots are the actual data points while solid lines represent the TCMT fit. (c) Extracted TCMT parameters as a function of v. (d) Plots of (u, g) pairs through which the resonator is swept by tuning v.
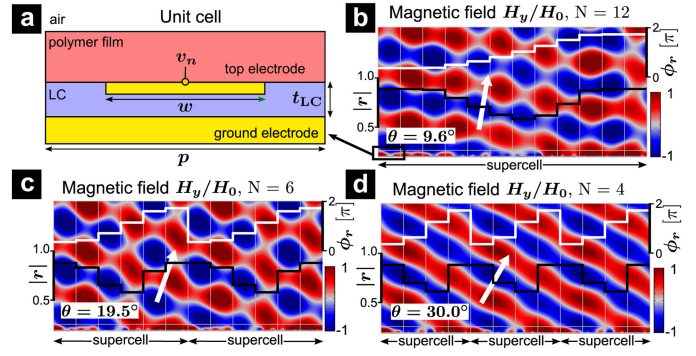

Fig. 6.   (a) The $x - z$ plane cross section of the LC MIM unit cell. (b)–(d) Scattered magnetic field colormaps with overlayed reflection amplitude and phase profiles, drawn over $x - z$ range $1800\,\mu\mathrm{m} \times 900\,\mu\mathrm{m}$ involving 12 unit cells. The supercell size is (b) $N = 12$, (c) $N = 6$ and (d) $N = 4$ while the unit cell parameters are given in Eq. (17).

is fulfilled, which we refer to as skewed tuning because of the skewed appearance of successive reflection spectra with decreasing g as in Fig. 5(a). Introducing $g_{(i)} = g(v_{(i)})$, the coefficients g_0 and a can be expressed as

$$g_0 = \frac{u_{(2)} g_{(1)} - u_{(1)} g_{(2)}}{u_{(2)} - u_{(1)}}, \quad a = \frac{g_{(2)} - g_{(1)}}{u_{(2)} - u_{(1)}}. \quad (14)$$

It turns out that Eq. (13) is an excellent approximation as long as the relative variation of g over the v space is small. To show this for the LC cell example, in Fig. 5(d) we plot the exact $(u(v), g(v))$ data points along with the lines generated by Eq. (13), for three different operation frequencies. The extent to which the skewed tuning model matches the exact u and g data, means that it is virtually exact in this case, which has been verified by comparing its prediction with the numerical model from the previous section. Taking this into account, it is reasonable to expect this to be an accurate model for other metasurface types.

As in the flat tuning case, one can easily show that the identity

$$\sum_{n=0}^{N-1} \frac{u_n - \mathrm{i}(g_0 + a u_n)}{u_n + \mathrm{i}} e^{-\mathrm{i}n\alpha} =$$

$$\frac{1 + g_0 - \mathrm{i}a}{2} \sum_{n=0}^{N-1} \frac{u_n - \mathrm{i}}{u_n + \mathrm{i}} e^{-\mathrm{i}n\alpha}, \quad (15)$$

holds for any profile $\{u_n\}$. This then implies that the maximal value of $|S_N|$ under optimal control in skewed tuning, denoted by $S_N(g_0, a)$, is given by

$$S_N(g_0, a) = \frac{|1 + g_0 - \mathrm{i}a|}{2} S_N^{\mathrm{id}} \approx \frac{1 + g_0}{2} S_N^{\mathrm{id}}, \quad (16)$$

and that the optimal control profile $\{v_n\}$ can be determined in a manner analogous to the flat tuning case.

Neglecting a in the right hand side of Eq. (16) is justified as follows: Firstly, a is at least several times smaller than $\Delta g = g_{(2)} - g_{(1)}$ in any practically relevant case because for reasonable tuning efficiency $\Delta u = u_{(2)} - u_{(1)}$ has to be at least 2, meaning that a is typically an order of magnitude smaller than $1 + g_0$. Secondly, because of the absolute value in the middle term in Eq. (16), a contributes to the factor that multiplies S_N^{id} via a term proportional to $a/(1 + g_0)$, meaning that the overall contribution of a is typically two orders of magnitude smaller than $1 + g_0$ and thus negligible. Therefore, the maximum attainable $|S_N|$ value under skewed tuning is given by an equation identical to the one for flat tuning, Eq. (11), the only difference being that now g_0 is determined by Eq. (14).

IV. EXAMPLE: TERAHERTZ BEAM STEERING WITH LC METASURFACES

To validate our model and illustrate the design method on a realistic example, we consider a metasurface consisting of an array of MIM cavities infiltrated by a nematic LC depicted in Fig. 6(a). Here the control parameter v, exhibiting a gradual variation over the array of unit cells along the horizontal direction (x axis), is the voltage applied to the top electrode while the bottom metal layer serves as the ground. The structure is assumed invariant along the out-of-plane direction (y-axis), so that applying a distinct voltage to each cell is straightforward, similarly as in [19].

When $v = 0$, the nematic LC molecules are all oriented along the y-axis because of a thin polymer alignment layer covering the electrodes. Then the z-component of the LC permittivity tensor is equal to n_{o}^2, with n_{o} being the ordinary LC refractive index. Upon increasing v, the nematic molecules realign themselves along the vertical direction (z-axis). This process saturates at a voltage value $v_{\max}$ when virtually all LC molecules are vertically oriented with the z-component of the permittivity tensor becoming close to n_{e}^2 and n_{e} being the extraordinary

index. The physics of the devices considered herein is modelled by a rigorous multiphysics model involving Maxwell equations for electromagnetic waves and the **Q**-tensor model for LC switching. The LC parameters of the nematic mixture 1825 [31] with $n_o = 1.554 + 0.018i$ ind $n_e = 1.941 + 0.022i$ have been assumed, while Zeonor is assumed for the encapsulating polymer layer carying the electrodes [32] with a refractive index of $n_{poly} = 1.518 + 0.001i$ [33] in the terahertz range. The electrodes are assumed to be made of copper, instead of the commonly used gold, because it is known to have a lower absorption rate at terahertz frequencies [34]. The copper permittivity $\varepsilon_m(\omega)$ was assumed to have the Drude form with the copper plasma $\omega_p = 1.12 \times 10^{16}$ rad/s and collision frequency $\gamma_{c,Cu} = 1.38 \times 10^{13}$ rad/s taken from [35]. For further details on modelling LC MIM cavities in the terahertz, the reader is referred to our previous work [18], [36], [37].

The data shown in Figs. 4 and 5, and used as example in previous sections, corresponds to a unit cell having the following dimensions

$$w = 75\,\mu m, \quad p = 150\,\mu m \quad \text{and} \quad t_{LC} = 5\,\mu m. \quad (17)$$

The operation of an electrically tunable beam steering metasurface utilizing such a unit cell is demonstrated in Fig. 6(b)–(d). The colormaps represent the $x - z$ plane cross section of the scattered field generated by a p-polarized (**H** field pointing out of plane) perpendicularly incident $f = 1$ THz electromagnetic field with magnetic field amplitude H_0 illuminating the metasurface. Following the procedure described in previous sections, here the optimal control voltage profiles have been determined for three exemplary supercell sizes: $N = 12, 6$ and 4. Applying these voltages to LC MIM cells, results in the phase and amplitude profiles shown as overlays on Fig. 6(b)–(d) and leads to the scattered field being predominantly steered along the stated angle θ corresponding to the $m = 1$ diffraction order.

We now address the accuracy of the presented model. First we wish to assert the claim made earlier stating that the model becomes exact as the deflection angle $\theta \to 0$, which is a general feature of scalar diffraction theory. To this end, we again consider the metasurface with unit cell with parameters from Eq. (17) and determine the optimal control profiles for $N = 3, 4, \ldots, 40$. To obtain the exact η_1 values, we solve Maxwell's equations exactly for the supercell at $f = 1$ THz and determine η_1 as the squared modulus of the 1-st term of the scattered field Fourier series. In Fig. 7(a) we plot this against the η_1 values obtained from our model

$$\eta_1 = \left| \text{sinc}\left(\frac{1}{N}\right) \frac{1 + g_0}{2} S_N^{id} \right|^2, \quad (18)$$

with g_0 given by Eq. (14). Values of η_1 obtained through numerical optimization following Section III-C overlap the plotted curve, demonstrating the accuracy of the skewed tuning model. For reference, the diffraction angles θ corresponding to the 1-st diffraction order are given in the inset of Fig. 7(a). Therefore, the model is rather accurate, especially for $N > 10$. A similar trend is to be expected for other unit cell parameters or different metasurface types, except that the particular N values may vary.
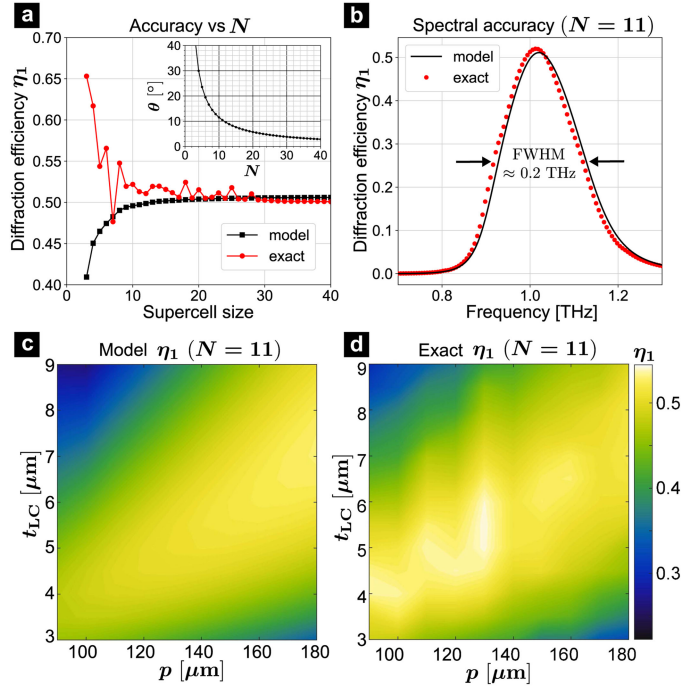

Fig. 7. Comparison of rigorously calculated η_1 with values obtained from the proposed model as a function of (a) supercell size, (b) operation frequency and (c), (d) unit cell width p and LC cell height t_{LC}. In each case, the applied voltage profile corresponds to optimal control at $f = 1.02$ THz. Colormaps have been prepared following [38].

Next, we test the spectral accuracy. For a particular supercell size ($N = 11$), we determine the spectral behavior of η_1 for the metasurface optimized at $f = 1$ THz and compare it with values obtained by using Eqs. (1) and (3) but with changing f while keeping the TCMT parameter profiles optimized for 1 THz. The results in Fig. 7(b) also show a remarkable accuracy, indicating that for $N > 10$ the presented model can be used for accurately determining the device operation bandwidth.

As pointed out before, the significance of the model presented in this article is that it establishes a direct connection between η_1 and the unit cell parameters Π, helping the global optimization. For example, the physically intuitive relationship between TCMT parameters of terahertz MIM resonators and their various parameters has been addressed in our previous work, see [27], [36], [39]. To demonstrate how the presented model fares in terms of predicting the η_1 variation with unit cell geometrical parameters, we fix the supercell size to $N = 11$ and sweep both the unit cell width p and the LC cell height t_{LC}. For each geometry, we determine the optimal control voltage profile and assess η_1 both using Eq. (18) and the rigorous supercell simulations. The results are shown by the colormaps in Fig. 7(c) and (d). The model is again found to be rather accurate over the entire parameter plane, with deviations occuring for some p values, likely due to the onset of additional diffraction orders. Therefore, we conclude that the model described in this article can be used for understanding the variation of DE over the unit cell parameter space and thus provide help in designing novel beam steering metasurfaces.

V. SUMMARY

We have formulated a theoretical model for assessing the diffraction efficiency of beam steering metasurfaces in terms of resonant eigenmode parameters. The model has been used to identify the control parameter profile yielding the highest diffraction efficiency and to express this efficiency by a simple formula. To illustrate the model and efficiency optimization procedure, a detailed example involving electrically tunable LC terahertz metasurfaces has been analyzed. The theoretical predictions of the model have been compared with rigorous numerical simulations involving large supercells and shown to exhibit remarkable accuracy for sufficiently small deflection angles. The results presented in this work will help the design of novel beam steering metasurfaces by providing optimization guidelines and a way to quickly assess the best possible performance achievable by a particular resonant element.

REFERENCES

[1] G. Swanson, *Binary Optics Technology: The Theory and Design of Multilevel Diffractive Optical Elements*. MIT, Cambridge, MA, USA, Tech. Rep. 854, 1989.

[2] N. Yu *et al.*, "Light propagation with phase discontinuities: Generalized laws of reflection and refraction," *Science.*, vol. 334, pp. 333–337, 2011.

[3] P. Genevet, F. Capasso, F. Aieta, M. Khorasaninejad, and R. Devlin, "Recent advances in planar optics: From plasmonic to dielectric metasurfaces," *Optica*, vol. 4, no. 1, pp. 139–152, Jan. 2017.

[4] F. Ding, A. Pors, and S. I. Bozhevolnyi, "Gradient metasurfaces: A review of fundamentals and applications," *Rep. Prog. Phys.*, vol. 81, 2018, Art. no. 026401.

[5] S. Sun *et al.*, "High-efficiency broadband anomalous reflection by gradient meta-surfaces," *Nano Lett.*, vol. 12, pp. 6223–6229, 2012.

[6] O. Tsilipakos *et al.*, "Pairing toroidal and magnetic dipole resonances in elliptic dielectric rod metasurfaces for reconfigurable wavefront manipulation in reflection," *Adv. Opt. Mater.*, vol. 6, no. 22, 2018, Art. no. 1800633.

[7] D. Headland, Y. Monnai, D. Abbott, C. Fumeaux, and W. Withayachumnankul, "Tutorial: Terahertz beamforming, from concepts to realizations," *APL Photon.*, vol. 3, no. 5, 2018, Art. no. 051101.

[8] D. Berry, R. Malech, and W. Kennedy, "The reflectarray antenna," *IEEE Trans. Antennas Propag.*, vol. AP-11, no. 6, pp. 645–651, Nov. 1963.

[9] D. Pozar and T. Metzler, "Analysis of a reflectarray antenna using microstrip patches of variable size," *Electron. Lett.*, vol. 29, pp. 657–658, Apr. 1993.

[10] J. Huang and J. Encinar, *Reflectarray Antenna*. Hoboken, NJ, USA: Wiley, 2008.

[11] F. Liu *et al.*, "Intelligent metasurfaces with continuously tunable local surface impedance for multiple reconfigurable functions," *Phys. Rev. Appl.*, vol. 11, 2019, Art. no. 044024.

[12] A. Pors, O. Albrektsen, I. Radko, and S. I. Bozhevolnyi, "Gap plasmon-based metasurfaces for total control of reflected light," *Sci. Rep.*, vol. 3, 2013, Art. no. 2155.

[13] T. Niu *et al.*, "Experimental demonstration of reflectarray antennas at terahertz frequencies," *Opt. Express*, vol. 21, no. 3, pp. 2875–2889, Feb. 2013.

[14] X. You *et al.*, "Terahertz reflectarray with enhanced bandwidth," *Adv. Opt. Mater.*, vol. 7, no. 20, 2019, Art. no. 1900791.

[15] A. Forouzmand and H. Mosallaei, "Tunable two dimensional optical beam steering with reconfigurable indium tin oxide plasmonic reflectarray metasurface," *J. Opt.*, vol. 18, 2016, Art. no. 125003.

[16] T. Yatooshi, A. Ishikawa, and K. Tsuruta, "Terahertz wavefront control by tunable metasurface made of graphene ribbons," *Appl. Phys. Lett.*, vol. 107, 2015, Art. no. 053105.

[17] P. P. Iyer, M. Pendharkar, and J. A. Schuller, "Electrically reconfigurable metasurfaces using heterojunction resonators," *Adv. Opt. Mater.*, vol. 4, pp. 1582–1588, 2016.

[18] B. Vasić, G. Isić, R. Beccherelli, and D. C. Zografopoulos, "Tunable beam steering at terahertz frequencies using reconfigurable metasurfaces coupled with liquid crystals," *IEEE J. Sel. Top. Quantum Electron.*, vol. 26, no. 5, Sep./Oct. 2020, Art. no. 7701609.

[19] Y.-W. Huang *et al.*, "Gate-tunable conducting oxide metasurfaces," *Nano Lett.*, vol. 16, pp. 5319–5325, 2016.

[20] J. Wu *et al.*, "Liquid crystal programmable metasurface for terahertz beam steering," *Appl. Phys. Lett.*, vol. 116, no. 13, 2020, Art. no. 131104.

[21] J. W. Goodman, *Introduction to Fourier Opt. Englewood*, CO, USA: Roberts & Company, 2005.

[22] S. Fan, W. Suh, and J. D. Joannopoulos, "Temporal coupled-mode theory for the fano resonance in optical resonators," *J. Opt. Soc. Am. A*, vol. 20, no. 3, pp. 569–572, Mar. 2003.

[23] M. Born and E. Wolf, *Principles of Optics*. Cambridge, U.K.: Cambridge Univ. Press, 2005.

[24] G. Swanson, *Binary Opt. Technol.: Theor. Limits on the Diffraction Efficiency of Multilevel Diffractive Opt. Elements*. Cambridge, MA, USA, MIT Tech. Rep. 914, 1991.

[25] D. A. Pommet, M. G. Moharam, and E. B. Grann, "Limits of scalar diffraction theory for diffractive phase elements," *J. Opt. Soc. Amer. A*, vol. 11, no. 6, pp. 1827–1834, Jun. 1994.

[26] P. Lalanne, W. Yan, K. Vynck, C. Sauvan, and J.-P. Hugonin, "Light interaction with photonic and plasmonic resonances," *Laser Photon. Rev.*, vol. 12, no. 5, Art. no. 1700113.

[27] G. Isić and R. Gajić, "Geometrical scaling and modal decay rates in periodic arrays of deeply subwavelength terahertz resonators," *J. Appl. Phys.*, vol. 116, no. 23, 2014, Art. no. 233103.

[28] T. Lepetit, E. Akmansoy, J.-P. Ganne, and J.-M. Lourtioz, "Resonance continuum coupling in high-permittivity dielectric metamaterials," *Phys. Rev. B*, vol. 82, 2010, Art. no. 195307.

[29] W. Suh, Z. Wang, and S. Fan, "Temporal coupled-mode theory and the presence of non-orthogonal modes in lossless multimode cavities," *IEEE J. Quantum Electron.*, vol. 40, no. 10, pp. 1511–1518, Oct. 2004.

[30] J. D. Hunter, "Matplotlib: A 2 d graphics environment," *Comput. Sci. Eng.*, vol. 9, no. 3, pp. 90–95, 2007.

[31] M. Reuter *et al.*, "Highly birefringent, low-loss liquid crystals for terahertz applications," *APL Mater.*, vol. 1, 2013, Art. no. 012107.

[32] A. Ferraro, D. C. Zografopoulos, R. Caputo, and R. Beccherelli, "Guided-mode resonant narrowband terahertz filtering by periodic metallic stripe and patch arrays on cyclo-olefin substrates," *Sci. Rep.*, vol. 8, 2018, Art. no. 17272.

[33] P. A. George *et al.*, "Microfluidic devices for terahertz spectroscopy of biomolecules," *Opt. Express*, vol. 16, pp. 1577–1582, 2008.

[34] M. A. Belkin *et al.*, "Terahertz quantum cascade lasers with copper metal-metal waveguides operating up to 178 k," *Opt. Express*, vol. 16, no. 5, pp. 3242–3248, Mar. 2008.

[35] M. A. Ordal, R. J. Bell, R. W. Alexander, L. L. Long, and M. R. Querry, "Optical properties of fourteen metals in the infrared and far infrared: Al, Co, Cu, Au, Fe, Pb, Mo, Ni, Pd, Pt, Ag, Ti, V, and W," *Appl. Opt.*, vol. 24, no. 24, pp. 4493–4499, Dec. 1985.

[36] G. Isić, B. Vasić, D. C. Zografopoulos, R. Beccherelli, and R. Gajić, "Electrically tunable critically coupled terahertz metamaterial absorber based on nematic liquid crystals," *Phys. Rev. Appl.*, vol. 3, Jun. 2015, Art. no. 064007.

[37] B. Vasić, D. C. Zografopoulos, G. Isić, R. Beccherelli, and R. Gajić, "Electrically tunable terahertz polarization converter based on overcoupled metal-isolator-metal metamaterials infiltrated with liquid crystals," *Nanotechnology.*, vol. 28, 2017, Art. no. 124002.

[38] P. Kovesi, "Good colour maps: How to design them," 2015, *arXiv/1509.03700*.

[39] G. Isić *et al.*, "Electrically tunable metal-semiconductor-metal terahertz metasurface modulators," *IEEE J. Sel. Top. Quantum Electron.*, vol. 25, no. 3, May/Jun. 2019, Art. no. 8500108.

PAPER

Pseudo-refractive index and excitonic features of single layer CdSe/CdS core–shell nanoplatelet films

View the article online for updates and enhancements.

Pseudo-refractive index and excitonic features of single layer CdSe/CdS core–shell nanoplatelet films

Milka M Jakovljević[1,4] , **Sonja Aškrabić**[1] , **Goran Isić**[1,2] , **Borislav Vasić**[1] , **Radoš Gajić**[1] **and Mikhail Artemyev**[3]

[1] Institute of Physics Belgrade, University of Belgrade, Pregrevica 118, 11080 Belgrade, Serbia
[2] Texas A & M University at Qatar, PO Box 23874 Education City, 23874 Doha, Qatar
[3] Research Institute for Physical Chemical Problems of the Belarusian State University, Leningradskaya str. 14, 220030 Minsk, Belarus

E-mail: milka@ipb.ac.rs

CrossMark

Abstract
Semiconductor CdSe/CdS core–shell nanoplatelets exhibit narrow and intense absorption and photoluminescence spectra in the visible range, which makes them suitable for numerous applications in optoelectronics. Of particular interest is the preparation and optical characterization of thin films with an accurately controlled amount of nanoplatelets. Here we report on the use of spectroscopic ellipsometry for investigating the optical properties of ultrathin films composed of a single layer of negatively charged CdSe/CdS core–shell nanoplatelets prepared by the electrostatic layer-by-layer deposition on SiO_2/Si substrates. Combining the ellipsometric spectra with atomic force microscopy measurements, we were able to infer the nanoplatelet film extinction spectra which was found to exhibit the two characteristic exciton peaks albeit blueshifted relative to the colloidal nanoplatelets.

Keywords: semiconductor core–shell nanoplatelets, single-layer electrostatic deposition, spectroscopic ellipsometry, refractive index

(Some figures may appear in colour only in the online journal)

1. Introduction

Nanoplatelets (NPLs) or colloidal quantum wells have an atomically flat surface [1]. Their thickness is quantized to an integer number of monolayers, which enables thickness tunable emission. NPLs made of $A^{II}B^{VI}$ semiconductors such as CdS, CdSe, and CdTe are especially interesting because their absorption and photoluminescence (PL) bands lie in the visible range and because of very high absorption and PL excitation efficiency [1–3]. The optical properties of core only NPLs such as quantum yield [4], photostability [5], and reduced fluorescence emission blinking [6, 7] are greatly improved by epitaxial growth of semiconductor shells [8]. All these properties make NPLs good candidates for applications

in optoelectronics. Compared to quantum dots or nanorods, NPLs exhibit extremely narrow intense bands on both absorption and PL spectra, which is essential for color purity of light-emitting diodes [9–11]. They have directed emission and polarization, fast radiative lifetimes related to the giant oscillator strength effect allowing high quantum yields, and promising lasing properties [12, 13].

An important part of nanodevice design is the formation of high quality nanostructured films. Numerous techniques are used for nanoparticle deposition on various substrates, including spin-coating, drop-casting, doctor-blading, self-assembling, etc Although these techniques lead to formation of relatively thick films, their precise composition is hard to control [14]. One of the bottom-up methods for creating well-organized, layer-by-layer assemblies of nanoparticles is based on electrostatic interactions [15–17]. It

---

[4] Author to whom any correspondence should be addressed.

allows the assembly of ultrathin nanoparticle films by exposing a charged substrate to alternating solutions of polymer molecules and nanoparticles charged with opposite signs, with a single polymer molecule-nanoparticle stack representing the smallest building block in the deposition procedure.

UV–vis absorption spectroscopy exhibiting a linear relationship between the absorption coefficient in the region of the first absorption maximum and the number of nanoparticle monolayers is the standard technique for monitoring the growth of layered structures, and for their optical characterization [18]. It is, however, inadequate when the layers are extremely thin or if the substrate is opaque. One way to overcome this issue is to use spectroscopic ellipsometry (SE) in reflection mode. Owing to its high surface sensitivity, SE has an important role in optical characterization of ultrathin nanostructured films, and various relevant characteristics such as optical functions, film thickness, surface roughness etc can be determined [19]. The key aspect of SE is an appropriate model, capable of accounting for all relevant structural elements of multilayer samples, especially close to material interfaces.

SE was used to measure the dielectric function of thin semiconductor nanocomposite films formed by spin-coating [20–22], but the thicknesses of these films were of the order of tens of nanometers. SE of somewhat thinner HgTe nanocrystal film, self-assembled by a tenfold repetition of layer-by-layer electrostatic deposition showed that the dispersion relation of nanocrystals can be modeled by critical points [23]. However, the investigation of optical properties of a single layer composed of charged layer and oppositely charged nanocrystals on the top is very challenging, due to the strong correlation between the thickness of the film and its refractive index [24, 25].

In this work, we performed the extraction of pseudo refractive index of a NPL monolayer, whose thickness is around 5 nm and which consists of a single layer of negatively charged CdSe/CdS core–shell NPLs deposited on the top of the positively charged molecular layer on a SiO$_2$(85 nm)/Si(bulk) substrate. Real and imaginary parts of refractive index of the composite film and the substrate were extracted using point-by-point inversion from the SE experimental data [26]. In this procedure, all the parameters of the model including refactive indicies (Si, SiO$_2$, and positively charged molecular layer) and thicknesses (SiO$_2$, positively charged molecular layer and NPLs film) must be fixed except for *n* and *k* of the NPLs film. Then *n* and *k* values are allowed to vary independently at each wavelength, and are results of this analysis. This is quite effective procedure for determining the complex refractive index of a sample, particulary when dielectric function modeling is difficult in some specific regions. Atomic force microscopy (AFM) analysis of morphology and measured thickness of the NPL film are used to interpret the data obtained by SE measurements.

2. Material and methods

2.1. Sample preparation

Hydrophobic CdSe/CdS core–shell NPLs with 4.5 ML CdSe core were synthesized according to a published procedure
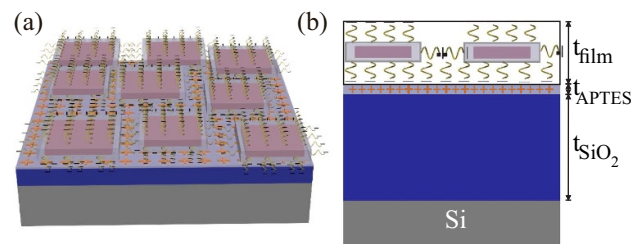

Figure 1. Film formed by close packed CdS/CdSe NPLs on the substrate schematics: (a) 3D view and (b) vertical cross section.

[27]. In order to make NPLs solubilized and negatively charged, hence suitable for electrostatic self-assembly, the hydrophobic NPLs were functionalized with mercaptoacetic acid (MAA). The surface of a commercial highly n-doped Si wafer covered with SiO$_2$ film (of nominal thickness $\sim$ 85 nm), was treated in aqueous solution of aminopropyl trietoxy silane (APTES) dissolved in toluene in order to charge SiO$_2$ positively. After being left in solution for 20 min, the substrate was rinsed with toluene. Finally, the wafer with a monolayer of APTES was treated in a colloidal solution of negatively charged CdSe/CdS NPLs to form a 2D layer of close-packed NPLs on SiO$_2$ film surface. The schematics of the structure is shown in figure 1.

2.2. Characterization

2.2.1. Spectroscopic ellipsometry.
Spectroscopic ellipsometry measures the change in the state of polarization of the incident light upon reflection from the sample. It gives the ratio of the two complex Fresnel reflection coefficients, $\widetilde{r}_p$ and $\widetilde{r}_s$, for light polarized parallel and perpendicular to the plane of incidence, respectively, $\rho = \widetilde{r}_p/\widetilde{r}_p = \tan \Psi e^{i\Delta}$.

SE measurements were performed using rotating-polarizer spectroscopic ellipsometer (SOPRA GES5E-IRSE VASE). The measured quantities were the two ellipsometric parameters, tan Ψ and cos Δ, and the spectral range was 200–700 nm (with step size 2 nm). During the measurements 'previous tracking mode' is used. This means that the angle of nonrotating exit polarizer in the setup, often called analyzer, at one point (energy or wavelength) is set to the value of Ψ attained at the previous point. This is done in order to keep the reflected beam close to being circularly polarized and measurements at optimal sensitivity [28]. We measured the SE spectra of both the bare SiO$_2$(85 nm)/Si substrate and the substrate with the NPL monolayer on top. The dielectric function of highly doped Si substrate does not necessarily coincide with spectra found in the literature, therefore bare substrate characterization is important to minimize potential errors in the extraction procedure. The final SE spectra of the film were obtained by averaging over 10 consecutive measurements of 10 s duration for each point in spectra, in order to minimize random errors and to improve signal to noise ratio. All the calculations were performed using home-developed code in MATLAB.

2.2.2. AFM characterization.
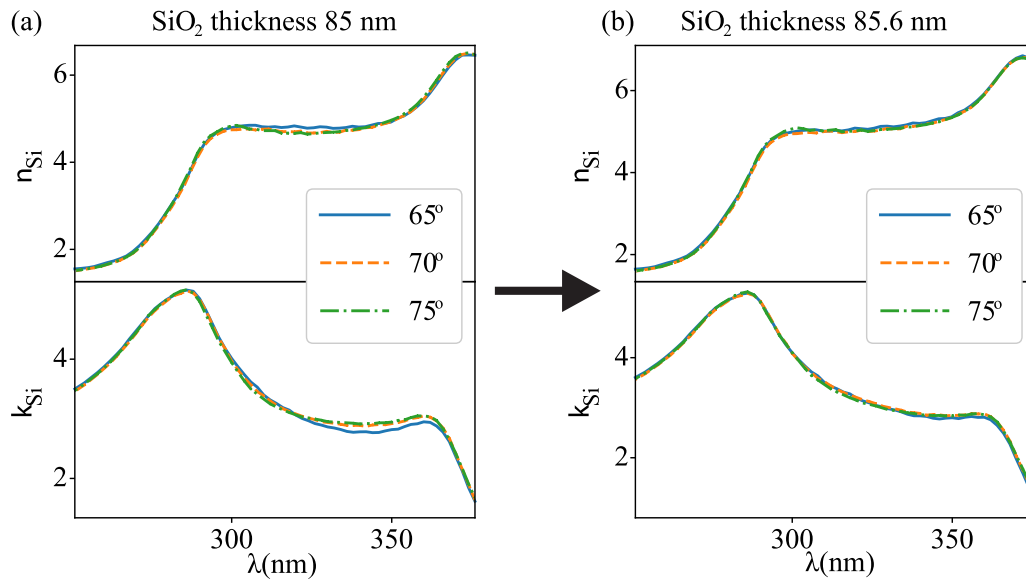The morphological characterization of CdSe/CdS core–shell NPL films was performed

Figure 2. Real (top) and imaginary (bottom) part of the Si refractive index retrieved assuming the SiO$_2$ layer thickness is (a) 85 nm and (b) 85.6 nm.

by AFM, using the NTEGRA Prima system in ambient conditions. Topographic imaging was carried out in tapping AFM mode using NSG01 probes from NT-MDT. The main aim of the morphological characterization was to measure the thickness of the CdSe/CdS core–shell film, the value which was further included in the fitting procedure of ellipsometric spectra. The film thickness was determined by the following procedure. Topography was measured on five $2 \times 2 \, \mu m^2$ areas. For every scan area, an average height and surface roughness were calculated. Both values were further averaged across all considered areas. The final film thickness was calculated as a sum of the averaged height and averaged roughness.

2.3. Ellipsometry data analysis

The initial step in the NPL film refractive index (point-by-point) extraction is to properly characterize the substrate. Commercially made Si wafer was used with nominally 85 nm thick SiO$_2$ obtained using thermal oxidation. The Si wafer has < 001 > orientation, and is n-type semiconductor highly doped with P (concentration $\sim 10^{15}$ cm^{-3}, resistivity 3–5 Ω cm), therefore it differs from the intrinsic Si, and has slightly different optical properties [29].

The SE spectra of the substrate were measured at three different angles of incidence (AOI) 65°, 70°, and 75°. Typically, there is a strong correlation between the data at different AOI, especially when the overlayer is thin [30]. However, when the SE spectra are measured over the energy range where the substrate has a sharp optical structure (like critical points) the spectra of extracted data at different AOI do not coincide if the thickness of SiO$_2$ is not properly determined [31]. This property was used to extract the optical function of Si in the wafer and oxide thickness with assumption that the dielectric function of SiO$_2$ is known and equivalent to the one from SOPRA refractive index base [32]. Once the substrate optical properties are known, direct extraction (or point-by-point inversion)
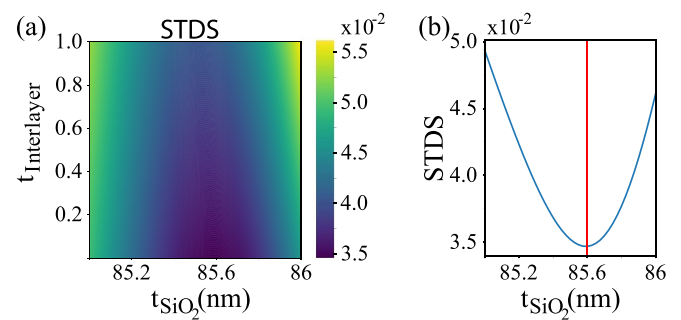

Figure 3. (a) Mapped error function for thicknesses of the SiO$_2$ layer in range 85–86 nm and interlayer thickness in range 0–1 nm. (b) Selected error function for different SiO$_2$ thickness without interlayer.

of index of refraction of the composite (mixture) consisting of the CdSe/CdS core–shell NPLs with ligands and air was performed. Here we refer to refractive index of composite as pseudo refractive index of the NPL film, assuming that the film is effectively uniform in its volume. Refractive index of APTES was taken from the literature [33], and its monolayer thickness is estimated to be 0.6 nm based on the length of the molecule. The SE measurements of the sample with film were analyzed at single angle, 75°, since the measurements at different angles did not provide any additional information.

3. Results and discussion

3.1. Substrate characterization

Ellipsometric measurements of the substrate were performed at three different AOI 65°, 70° and 75°. Assuming that the optical model used here is SiO$_2$(85 nm)/Si, the extracted refractive indices of Si from three different AOI ellipsometric measurements coincide almost perfectly, except
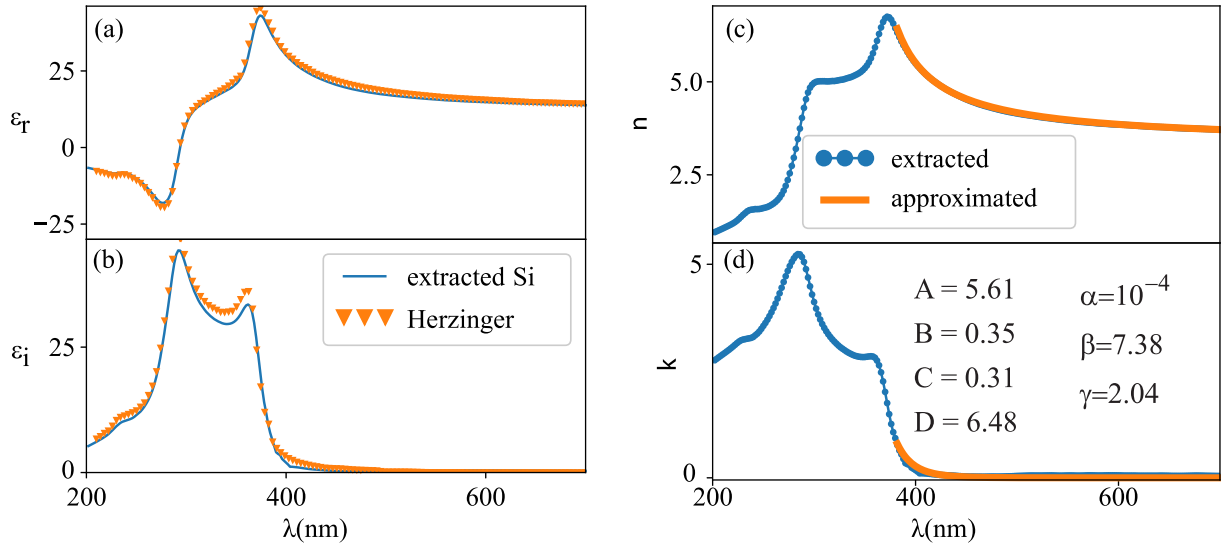
Figure 4. (a) Real and (b) imaginary part of extracted dielectric function of highly doped Si and lightly doped Si (taken from Herzinger *et al* [34]). (c) Real and (d) imaginary part of refractive index of highly doped Si substrate extracted from the measurements (dotted line) and approximated with analytical function to minimize the noise.

at wavelengths that are close to the critical points of Si 2(a). Arwin and Aspnes showed that owing to the sharp features in the dielectric function of Si near the critical points, it is possible to unambiguously determine the thickness and dielectric function of thin films on Si substrate [31]. Here, a part of spectra close to critical points is used for calculation of oxide thickness and dielectric function of Si. We quantify the spectral overlap by the standard deviation of the three spectra (STDS):

$$STDS = \sqrt{\frac{\sum_{i=1}^{N_\lambda} \sum_{j=1}^{N_{AOI}} \left[(n_{ij} - \bar{n}_i)^2 + (k_{ij} - \bar{k}_i)^2 \right]}{2N_\lambda N_{AOI} - 1}}, \quad (1)$$

where n_{ij} and k_{ij} are real and imaginary parts of refractive index at λ_i and angle j, $\bar{n}_i$ and $\bar{k}_i$ are the mean values for the three AOI at λ_i, N_λ is the number of wavelengths, and N_{AOI} is the number of angles of incidence (AOI = 65°, 70°, 75°). The initial model with only substrate and SiO$_2$ film was extended by adding an interlayer between SiO$_2$ and Si, to test how its presence influences the STDS. A commonly used model to describe this layer assumes that its dielectric permittivity is a 50% mixture of both materials, and is approximated with Bruggeman effective medium formula. The STDS was calculated in range 252–376 nm at 63 points, for thickness of SiO$_2$ layer in range 85–86 nm, while the interface layer thickness was in range 0–1 nm. The map of the error function is shown in figure 3(a). The minimum value of STDS is at 85.6 nm, with no interface layer figure 3(b). The extracted refractive indices at three different AOI for the thickness of 85 and 85.6 nm are shown in figure 2, and at thickness of SiO$_2$ 85.6 nm when STDS is minimal, three spectra are almost identical, figure 2(b).

The real and imaginary parts of dielectric function of calculated mean spectra, for the three spectra obtained by direct inversion at 65°, 70°, and 75° of highly doped Si in range 200–700 nm are shown in figures 4(a) and (b). They are plotted together with results from Herzinger [34]. The differences in the spectra originate from the fact that there is a difference between the doping levels and type of dopants (here highly P-doped, in the Herzinger paper slightly B-doped), and potentially from the method of Si crystal growth.

In point-by-point extraction, calculated refractive indices at different wavelengths do not directly depend on each other and the measurement noise is directly transferred to the extracted optical data [30]. Eventually, all the measurement noise, including that from the substrate optical constants, is propagated into the extracted data of the film. To avoid this effect, in the 380–700 nm range the real part of silicon refractive index, obtained by direct extraction, is fitted to the Sellmeier empirical formula [34], while the imaginary part is approximated by an exponential tail [30]:

$$n^2 = D + A \frac{\lambda^2}{\lambda^2 - B^2} - C\lambda^2, \quad (2)$$

$$k = \alpha e^{\beta(hc/\lambda - \gamma)}. \quad (3)$$

The seven model parameters are: *D*, *A*, *B*, *C* for approximation of *n*, and the extinction amplitude α, the exponent factor β, and the band edge γ for approximation of *k*. The fitted refractive index of Si, and thickness of SiO$_2$ layer in range 380–700 nm, figures 4(c) and (d), were further used in extraction of optical properties of NPL film.

3.2. Surface morphology and thickness of the NPL film

The typical topography of a $2 \times 2\ \mu m^2$ area of the CdSe/CdS core–shell NPL film is depicted in figures 5(a) and (b). NPLs are represented by bright grains with an effective diameter of around several tens of nanometers. NPLs are well deposited onto SiO$_2$ substrate, they are separated from each other and
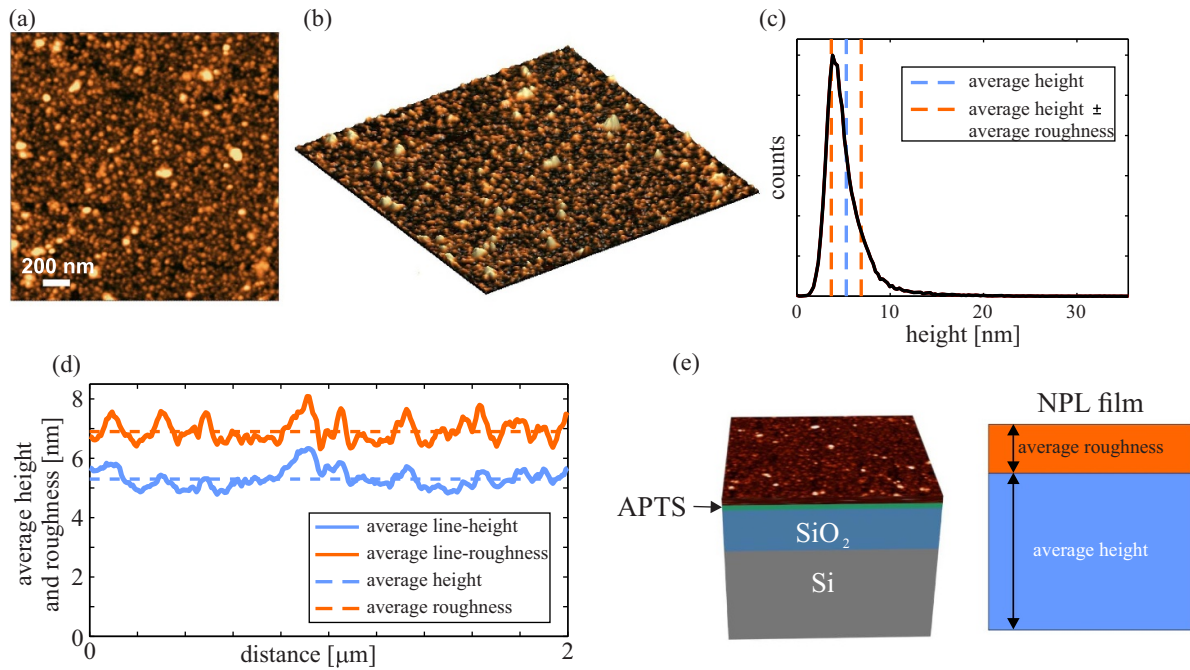
Figure 5. (a) CdSe/CdS core–shell NPL film topography colormap and (b) its three-dimensional rendering. The scan area is $2 \times 2\ \mu m^2$, whereas the height scale is 12 nm and brightness is linearly proportional to height. (c) Height distribution of the topographic image in part (a). (d) Average line-height and line-roughness for the topographic image in part (a). (e) Model of the considered film: it is a two-component structure with the bottom layer having the thickness of the average height and the top layer with the thickness equal to the average roughness.

form a monolayer. A small number of clusters represented by wider and higher grains and depicted by brighter grains can also be observed. Histogram of the height distribution is given in figure 5(c). The average height of 5.3 nm and the average roughness of 1.6 nm are indicated by dashed lines. In the calculation of the film thickness, the zero-thickness which corresponds to the substrate was taken from narrow air gaps (represented with a dark colour) between neighboring NPLs. The histogram is characterized by a single and narrow peak indicating a good uniformity of the film thickness. According to AFM images, the film roughness mainly originates from narrow air gaps between neighboring NPLs, from their not-flat orientation and formation of small local clusters.

In order to better represent the film morphology, the average height and roughness profiles (called average line-height and line-roughness respectively) of the topographic image in figure 5(a) are shown in figure 5(d). Here the averaging was done along the vertical lines. Dashed lines in figure 5(d) represent the height and roughness averaged over the entire topographic image and they correspond to the dashed lines in figure 5(c). The average height profile represents the layer comprised of NPLs, whereas the roughness profile represents a mixture of NPLs and air. According to these results, the film can be represented by a combination of two layers having the thickness equal to the average height (the bottom layer) and roughness (the top layer). This model is schematically represented in figure 5(e). Finally, the whole film can be approximated as a single layer with the effective thickness equal to the sum of the average height and roughness. After the averaging over five different areas, the calculated film thickness was 5.3 ± 1.6 nm.
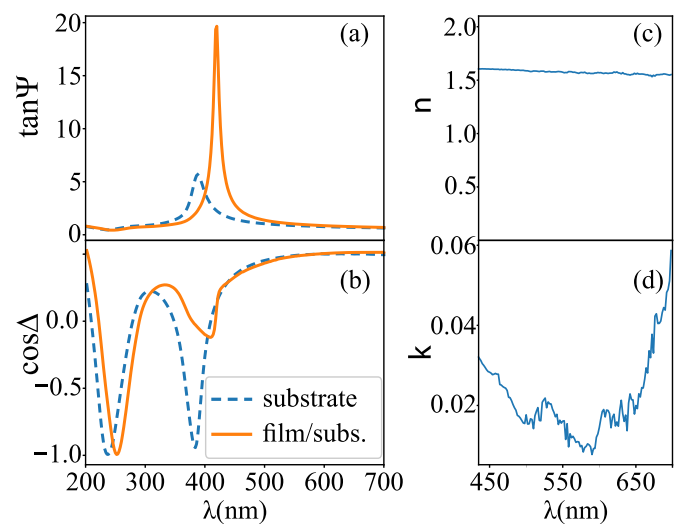

Figure 6. (a) $\tan\Psi$ and (b) $\cos\Delta$ at 75° for bare substrate (dashed line) and substrate with NPLs on it (full line) at range from 200 to 700 nm. (c) n and (d) k of extracted refractive index of the film at shortened range 430–700 nm.

3.3. Extraction of NPL film's refractive index

SE spectra of bare substrate and substrate with APTES and NPLs on the top are shown in figures 6(a) and (b). The shifts in the SE spectra of the film compared to the SE spectra of the bare substrate confirm the presence of an overlayer. When the film thickness is in the nanometer range, the thickness, constituent volume ratios and the mixture's refractive index are correlated, so the modeling procedure with all these
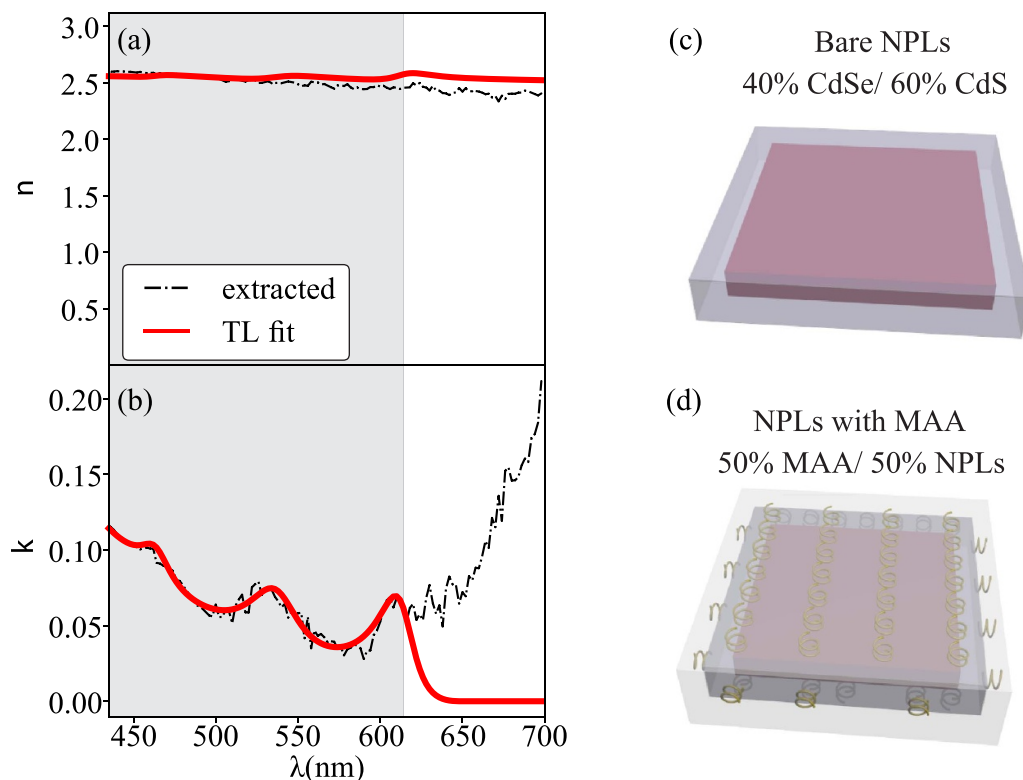
Figure 7. (a) Real and (b) imaginary part of extracted refractive index of NPLs. Dash-dot lines represent values obtained by direct extraction, while full lines represent TL fits. The greyed area denotes part of extracted spectra used in TL fitting, while the rest of the spectra is extrapolation by the model. (c) Schematic of bare NPLs, where estimated volume ratio of bulk CdSe and CdS is 40%/60%. (d) Schematic of MAA covered NPLs, where estimated volume ratios of MAA and NPLs is 50%/50%.

parameters included and fitting directly to the SE curve is very delicate. Therefore, we are extracting the refractive index of the film (mixture) by direct inversion according to the model shown in figure 5(e). AFM-deduced values for thickness of closely packed NPL film (5.3 nm) and roughness (1.6 nm) were used in the ellipsometric model. Since the NPL film is not a bulk material, its roughness can be incorporated as the less dense NPL film (50% air and 50% film). It originates from the fact that surface of NPLs is not completely flat, NPLs do not form closely packed monolayer, as well as from deposition of NPL clusters that appear as bright spots in AFM topographic images, figures 5(a) and (b).

The detailed description of the film includes NPLs covered with MAA and mixed with air at some ratios. The lateral size of the NPLs, deduced from high resolution AFM measurements [35] is around 30 nm, so 10–30 times smaller than the wavelengths of the incident light, and effective medium approximation would be a natural choice for calculation of their optical properties [19]. Estimated thickness of the MAA on the NPLs is approximately 1 nm. This means that the volume fraction of the bare NPLs in MAA covered NPLs is around 50% ($28 \times 28 \times 3.1/30 \times 30 \times 5.1$), figure 7(d). Assuming that the refractive index of the NPLs is close to the one of the mixture of bulk CdSe [32] 40% and CdS [36] 60%, figure 7(c), covered with MAA, the estimated fraction of the air is around 40%.

Going backward, assuming the same coverage of MAA, and fraction of air in the film whose optical properties were

extracted, figures 6(c) and (d), the real and imaginary parts of extracted refractive index of NPLs are shown in figures 7(a) and (b). The SE measurement noise is directly transferred to the spectra of *n* and *k*, and an unexpected increase in *k* and decrease in *n* at wavelengths greater than 610 nm are a consequence of approaching the end of the measuring range of the ellipsometer used in the experiment. The extracted dielectric function (refractive index) is further parametrized using Tauc–Lorentz (TL) oscillator model given by:

$$\varepsilon_{i,TL}(E) = \begin{cases} \sum_{i=1}^{N} \frac{1}{E} \frac{A_i \cdot E_i \cdot C_i \cdot (E-E_g)^2}{(E^2-E_i^2)^2+C_i^2 \cdot E^2}, & E \geq E_g \\ 0, & E < E_g \end{cases} \quad (4)$$

where A_i is the strength, C_i is the broadening, and E_i is the peak central energy of the *i*th oscillator, while E_g is the gap energy. The real part of the dielectric function is derived from the expression of ε_i using Kramers–Kronig integration. This model accounts for the band gap of the NPLs, and prevents absorption contributions below the band gap that appear due to the decreased measurement sensitivity. The TL model is fitted in range 430–610 nm, while the upturn in the extracted *k* above 610 nm is attributed to the experimental artefact, and extrapolated by the TL model [30].

The absorbance of the NPLs in chloroform solution shows two characteristic excitonic resonances at 560 and 620 nm (figure 8). The extinction coefficient of the NPLs in the film is evaluated from the absorption coefficient *k* through $\alpha = 4\pi k/\lambda$. The total absorption in the free-standing NPL film (mixture) is
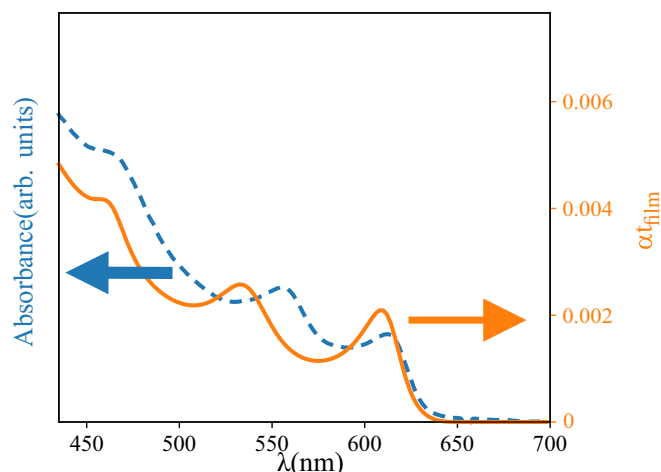
Figure 8. Absorbance (arbitrary units) spectra of CdSe/CdS core–shell NPLs in a chloroform solution (dashed line), and estimated absorption in the 5.3 nm NPLs film (full line).

then approximately αt_{film}, where t_{film} is the film thickness. The exciton peaks of the NPLs in the film are slightly blueshifted compared to the ones in the solution. This shift could be caused by a strain induced by the ligand exchange of oleic acid, used in the solution, by MAA during the electrostatic deposition [37], decrease of the refractive index of surrounding media, or by the interaction of the NPLs with substrate and/or APTES film.

Another important aspect of figure 8 is the very low magnitude (below 0.5%) of the estimated NPL film absorption even if it was free-standing or deposited on a weakly reflecting substrate. It proves that the standard optical characterization involving transmission spectrophotometry would be very difficult to realize for the investigated monolayer NPL films and thus stands in favor of the appropriateness of the method used in this article.

4. Conclusion

CdSe/CdS core–shell nanoplatelet films prepared on SiO_2/Si substrates by electrostatic single-layer deposition have been investigated. We have found that the presence of a monolayer NPL film on optically opaque SiO_2/Si substrates can be established using SE in combination with AFM measurements. While AFM provides the film thickness and demonstrates its surface morphology, the appearance of excitonic signatures in the NPL film extinction spectrum inferred from ellipsometry confirms the presence of CdSe/CdS core–shell NPLs. The two exciton peaks are found to be slightly blueshifted compared to the excitonic peaks in the absorption spectra of colloidal NPLs, which can be explained by the ligand exchange, interaction of NPLs with the SiO_2 substrate and the APTES film and/or by the decrease of the refractive index of the surrounding. These results assert SE as a promising tool for probing the optical properties of monolayer NPL films on arbitrary substrates, which is hardly possible using standard optical absorption measurements.

Direct extraction or point-by-point inversion is highly reliant on the exact knowledge of the refractive indices and thicknesses in the underlying structure, so it is important to characterize the substrate before measuring NPL films and extracting their optical parameters. Here we determined the refractive index of highly doped Si while the thickness of the SiO_2 layer was determined by exploiting the fact that the regions of the spectra close to the sharp optical structure (at critical points of Si) are more sensitive to change of the angle of incidence.

ORCID iDs

Milka M Jakovljević https://orcid.org/0000-0002-8536-3796
Sonja Aškrabić https://orcid.org/0000-0003-1945-040X
Goran Isić https://orcid.org/0000-0002-6841-9356
Borislav Vasić https://orcid.org/0000-0002-1575-8004
Mikhail Artemyev https://orcid.org/0000-0002-6608-0002

References

[1] Ithurria S, Tessier M D, Mahler B, Lobo R P S M, Dubertret B and Efros A L 2011 *Nat. Mater.* **10** 936–41
[2] Achtstein A W, Antanovich A, Prudnikau A, Scott R, Woggon U and Artemyev M 2015 *J. Phys. Chem. C* **119** 20156–61
[3] Pedetti S, Nadal B, Lhuillier E, Mahler B, Bouet C, Abécassis B, Xu X and Dubertret B 2013 *Chem. Mater.* **25** 2455–62
[4] Tessier M D, Mahler B, Nadal B, Heuclin H, Pedetti S and Dubertret B 2013 *Nano Lett.* **13** 3321–8
[5] Talapin D V, Mekis I, Götzinger S, Kornowski A, Benson O and Weller H 2004 *J. Phys. Chem. B* **108** 18826–31
[6] Chen Y, Vela J, Htoon H, Casson J L, Werder D J, Bussian D A, Klimov V I and Hollingsworth J A 2008 *J. Am. Chem. Soc.* **130** 5026–7
[7] Mahler B, Spinicelli P, Buil S, Quelin X, Hermier J and Dubertret B 2008 *Nat. Mater.* **7** 659–64
[8] Mahler B, Nadal B, Bouet C, Patriarche G and Dubertret B 2012 *J. Am. Chem. Soc.* **134** 18591–8
[9] Chen Z, Nadal B, Mahler B, Aubin H and Dubertret B 2014 *Adv. Funct. Mater.* **24** 295–302
[10] Vitukhnovsky A G, Lebedev V S, Selyukovm A S, Vashchenko A A, Vasiliev R B and Sokolikova M S 2015 *Chem. Phys. Lett.* **619** 185–8
[11] Zhang F *et al* 2016 *Nanoscale* **8** 12182–8
[12] Grim J Q, Christodoulou S, Stasio F, Krahne R, Cingolani R, Manna L and Moreels I 2014 *Nat. Nanotechnol.* **9** 891–5
[13] She C, Fedin I, Dolzhnikov D S, Dahlberg P D, Engel G S, Schaller R D and Talapin D V 2015 *ACS Nano* **9** 9475–85

[14] Talapin D V, Lee J S, Kovalenko M V and Shevchenko E V 2010 *Chem. Rev.* **110** 389–458

[15] Zucolotto V, Gattas-Asfura K, Tumolo T, Perinotto A, Antunes P, Constantino C, Baptista M, Leblanc R and Oliveira J O 2005 *Appl. Surf. Sci.* **246** 397–402

[16] Gao M, Zhang X, Yang B, Li F and Shen J 1996 *Thin Solid Films* **284-285** 242–5

[17] Franzl T, Shavel A, Rogach A L, Gaponik N, Klar T A, Eychmüller A and Feldmann J 2005 *Small* **1** 392–5

[18] Peng W, Rupich S M, Shafiq N, Gartstein Y N, Malko A V and Chabal Y J 2015 *Chem. Rev.* **115** 12764–96

[19] Losurdo M and Hingerl K 2013 *Ellipsometry at Nanoscale* (Berlin: Springer)

[20] Dement D B, Puri M and Ferry E 2018 *J. Phys. Chem.* C **122** 21557–68

[21] Diroll B T, Gaulding E A, Kagan C R and Murray C B 2015 *Chem. Mater.* **27** 6463–9

[22] Malak S T, Lafalce E, Jung J, Lin C H, Smith M J, Yoon Y J, Lin Z, Vardeny Z V and Tsukruk V V 2016 *J. Mater. Chem.* C. **4** 10069–81

[23] Rinnerbauer V, Hingerl K, Kovalenko M and Heiss W 2007 *Appl. Surf. Sci.* **254** 291–4

[24] Isić G *et al* 2011 *J. Nanophotonics* **5** 051809

[25] Matković A, Ralević U, Chhikara M, Jakovljević M M, Jovanović D, Bratina G and Gajić R 2013 *J. Appl. Phys.* **114** 093505

[26] Tompkins H G and Irene E A 2005 *Handbook of Ellipsometry* (New York: William Andrew, Inc.)

[27] Antanovich A, Prudnikau A and Artemyev M 2016 *Optical Properties of Semiconductor Colloidal Quantum Wells*, in: A, S A (eds.) *Fundamental and Applied Nano-Electromagnetics* (Netherlands: Springer) p 220

[28] Aspnes D A 1974 *J. Opt. Soc. Am.* **64** 639–46

[29] Aspens D E, Studna A A and Kinsbron E 1984 *Phys. Rev.* B **29** 768–79

[30] Herzinger C M, Snyder P G, Johs B and Woollam J A 1995 *J. Appl. Phys.* **77** 1715–24

[31] Arwin H and Aspnes D E 1984 *Thin Solid Films* **113** 101–13

[32] Palik E D 1985 *Handbook of Optical Constants of Solids* (New York: Academic)

[33] Goyal D K, Pribil G K, Woollam J A and Subramanian A 2008 *Mat. Sci. Eng.* B **149** 26–33

[34] Herzinger C M, Johs B, McGahan W A and Woollam J A 1998 *J. Appl. Phys.* **83** 3323–36

[35] Vasić B, Askrabić S, Jakovljević M M and Artemyev M 2020 *Appl. Surf. Sci.* **513** 145822

[36] Ninomiya S and Adachi S 1995 *J. Appl. Phys.* **78** 1183–90

[37] Atanovich A, Achtstein A W, Matsukovich A, Prudnikau A, Bhaskar P, Gurin V, Molinari M and Artemyev M 2017 *Nanoscale* **9** 18042–53

Tunable Beam Steering at Terahertz Frequencies Using Reconfigurable Metasurfaces Coupled With Liquid Crystals

Borislav Vasić , Goran Isić , Romeo Beccherelli , *Member, IEEE*, and Dimitrios C. Zografopoulos

Abstract—**Metasurfaces with a spatially varying phase profile enable the design of planar and compact devices for manipulating the radiation pattern of electromagnetic fields. Aiming to achieve tunable beam steering at terahertz frequencies, we numerically investigate metasurfaces consisting of one dimensional arrays of metal-insulator-metal (MIM) cavities infiltrated with liquid crystals (LCs). The spatial phase profile is defined by a periodic voltage pattern applied on properly selected supercells of the MIM-cavity array. By means of the electro-optic effect, the voltage controls the orientation of LC molecules and, thus, the resulting effective LC refractive index. Using this approach, the spatial phase profiles can be dynamically switched among a flat, binary, and gradient profile, where the corresponding metasurfaces function as mirrors, beam splitters or blazed gratings, respectively. Tunable beam steering is achieved by changing the diffraction angle of the first diffraction order, through the reconfiguration of the metasurface period via the proper adjustment of the applied voltage pattern.**

Index Terms—**Beam steering, tunable metasurfaces, liquid crystals, terahertz frequencies.**

I. INTRODUCTION

TUNABLE beam-splitting and steering devices are integral components of terahertz (THz) systems that are required for wireless communications, measurements, imaging and sensing [1]–[3]. In addition to common electromechanical scanning and phased-array systems [4], there are several proposals for

dynamically tunable THz beam steering utilizing wedge-shaped devices [5] and leaky-wave antennas [6] with liquid crystals (LCs), gratings with semiconductors [7], [8] and specially designed THz systems [9]. Still, further developments are needed in order to engineer more compact and faster devices with increased efficiency and advanced functionalities.

One promising approach in this direction is the application of metasurfaces, namely planar and periodic arrays of subwavelength electromagnetic resonators which strongly enhance light-matter interaction [10], [11] and have been demonstrated to facilitate the design of efficient THz modulators [12]–[17]. Gradient metasurfaces [18]–[22] are a natural choice for beam-steering applications since they introduce a spatially varying phase shift at the interface between two media thus providing additional opportunities for wavefront shaping [23]–[26]. In the case of gradient metasurfaces with linear phase shift profile, the beam-steering angle is dictated by the gradient of the linear phase profile [23]–[25]. Therefore, tunable beam steering with such metasurfaces can be realized by dynamically varying the phase gradient [27]–[32], which is a known concept applied in tunable microwave reflectarrays [33]–[35] and optical phased arrays [36]. However, the rigorous approach requires changing the period of the metasurface with simultaneous readjustment of the phase in order to keep the linear phase shift from $0°$ to $360°$ within each period [37]–[40], which is challenging for practical realizations. The $360°$ phase-shift requirement is relaxed in binary metasurfaces, periodic structures with just two spatial zones introducing phase shifts of either $0°$ or $180°$. They operate as beam splitters like classical binary optical gratings [41]. Tunable beam splitting with adjustable diffraction angles can be then realized by less demanding phase modulation between $0°$ and $180°$ [27], [42], [43].

The phase modulation is the underlying physical foundation for tunable beam steering with both gradient and binary metasurfaces. The modulation efficiency strongly depends on the selection of the tunable elements and their applicability for a specified frequency range. So far, semiconductors [7], [8], [31] and graphene [37], [44] have been mostly employed at THz frequencies. However, they are Drude materials with tunable absorption which makes them more suitable not for phase, but amplitude THz modulators [45], [46]. On the other hand, recently it has been demonstrated that the large inherent birefringence of LCs combined with the possibility for electrical
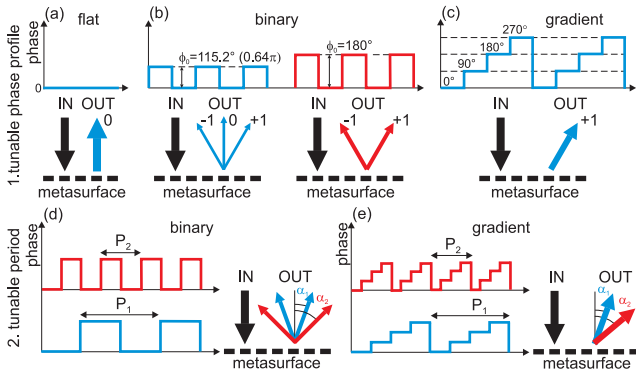
Fig. 1. Principles of tunable beam steering: 1. control of DE for zero and first order is achieved by modulation of the phase profile from (a) flat to (b) binary, or to (c) gradient, 2. tunable angle α of the first diffraction order is obtained by changing the period of either (d) binary or (e) gradient metasurfaces.

modulation of their refractive index render them promising for frequency tunable THz metamaterials, which can provide both amplitude [14], [47], [48] and phase [49] modulation. Still, the interplay between amplitude and phase modulation needs careful design.

In this paper, we investigate one-dimensional arrays of metal-insulator-metal (MIM) cavities infiltrated with LCs targeting the design of tunable binary and gradient metasurfaces at THz frequencies working in reflection mode. Compared to conventional LC cells, such MIM resonant cavities have been previously [14], [49] found particularly promising for LC-based technology as the enhanced light-matter interaction allows an orders of magnitude speedup in LC switching. The phase tuning is achieved by the electro-optic modulation of the spatial profile of the LC refractive index. The same metallic stripes that form the MIM resonant cavities are also employed for the application of the low-frequency LC control voltage. In binary metasurfaces, the LC refractive index is periodically varied in order to achieve periodic phase gratings with either $0°$ or ϕ_0 phase zones, where $\phi_0 \in [0°, 180°]$. Beam splitters with tunable diffraction efficiency (DE) are implemented by modulating the LC refractive index in the zones with non-zero phase ϕ_0 thus controlling the interplay of the DEs for the $0°$ and ± 1 orders. Next, we design gradient metasurfaces with a four-level discretized linear phase profile ($0°$, $90°$, $180°$, $270°$) that behave like blazed gratings thus allowing for switchable beam steering of the impinging THz beam between the $0°$ and $+1$ diffraction order. A routine for the maximization of DE in real lossy systems is also presented, leading to significant improvement in the grating's performance. In the case of both binary and gradient metasurfaces, the beam splitting/steering angle can be dynamically adjusted by reconfiguring the grating period, thanks to the subwavelength dimensions of the employed MIM resonant cavities.

II. MODULATION PRINCIPLES AND MODELING

The physical principles for tunable beam steering of the proposed devices are illustrated in Fig. 1. The metasurface acts as a phase grating with tunable phase profile. DEs for a
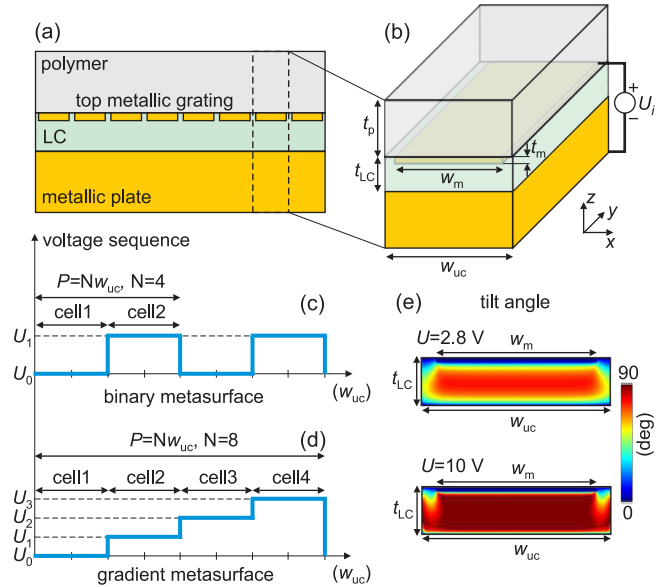

Fig. 2. (a) Cross-section of considered metasurfaces and (b) unit cell. Voltage patterns for (c) binary and (d) gradient metasurfaces. (e) Tilt angle of LC molecules within in a single unit cell for two chracteristic bias voltages.

grating with symmetrical rectangular phase profile are given by: $\cos^2(\phi_0/2)$ for zero order, $(2/\pi m)^2 \sin^2(\phi_0/2)$ for odd orders ($m = \pm 1, \pm 3, \ldots$), and zero for even orders ($m = \pm 2, \pm 4, \ldots$), where ϕ_0 is the phase difference between two levels as depicted in Fig. 1(b) [50]. A metasurface with flat phase ($\phi_0 = 0°$) operates as a mirror which just reflects an incoming wave (zero order) as depicted in Fig. 1(a). On the other hand, metasurfaces with the binary phase profiles presented in Fig. 1(b) act as beam splitters. If $\phi_0 = 115.2°$ (0.64π), the outgoing wave is split into three diffraction orders, 0 and ± 1, with same DE (higher orders are neglected due to low DE). Furthermore, the zero-order beam can be suppressed when the phase difference is exactly $\phi_0 = 180°$, leaving just the ± 1 diffraction orders.

Blazed gratings are realized by gradient metasurfaces with the sawtooth phase profile depicted in Fig. 1(c). They provide an additional option to single out just $+1$ (-1) diffraction order (for the positive (negative) phase slope with respect to the x-axis). For the sake of simplicity and practical realization, here the sawtooth profile is discretized into four phase levels $0°$, $90°$, $180°$, $270°$.

By changing the phase profile from flat to binary or gradient as presented in Figs. 1(a-c), it is possible to control the DE of zero and first order. In order to achieve beam steering with the same amplitude, but at a tunable angle, it is necessary to control the diffraction angle as shown in Figs. 1(d) and 1(e). The diffraction angle of the first order is $\alpha = \arcsin(\lambda/P)$, where λ is the wavelength and P is the grating period. Therefore, a tunable diffraction angle can be achieved by changing the metasurface period with simultaneous readjustment of the phase in order to keep either the binary or gradient profile.

The cross section of the considered metasurface is presented in Fig. 2(a), whereas its three-dimensional unit cell with indicated geometrical parameters is depicted in Fig. 2(b). The metasurfaces consist of a bottom gold plate, a layer of the nematic liquid

crystal with thickness t_{LC}, a top metallic grating made of parallel gold ribbons with width w_m, and a polymer layer with thickness t_p which serves as a substrate for the grating and simultaneously encapsulates the LC. The unit cell size is w_{uc}.

The phase profile of the metasurfaces is controlled by the pattern of voltage control signals U_i applied between the back-reflector ground plane and each one of the unit cells. The applied voltage controls the orientation of LC molecules and the spatial variation of the effective LC refractive index. The pattern of the LC bias voltages produces the desired phase profile along the x-axis of the metasurface. In the case of binary metasurfaces, this pattern consists of two voltage levels U_0 and U_1, with the low level U_0 fixed to zero, as schematically depicted in Fig. 2(c). The number of voltage levels in the pattern for gradient metasurfaces in Fig. 2(d) is defined by the number of discrete phase levels chosen for the approximation of the sawtooth phase profile, which is four in this study. We define a phase cell as series of k adjacent unit cells that have the same bias voltage and hence same phase value. The metasurface period/supercell in binary structures consists of 2 phase cells (2 k unit cells) corresponding to phase levels 0° and ϕ_0, whereas in gradient metasurfaces, it consists of 4 phase cells (4 k unit cells) implementing the phase levels 0°, 90°, 180°, 270°. Therefore, the metasurface period is defined as $P = Nw_{uc}$, where N is the number of unit cells per period, 2k and 4k in the case of binary and gradient metasurfaces, respectively. Two examples for a binary metasurface with N = 4 and gradient metasurface with N = 8 are schematically shown in Figs. 2(c) and 2(d), respectively.

Numerical calculations of both the LC studies and full-wave propagation of the THz waves were done by means of the finite-element method using COMSOL Multiphysics. The voltage-dependent LC orientation and switching dynamics were solved by the Q-tensor implementation of the Landau-de Gennes theory for uniaxial nematics, a powerful tool capable of resolving biaxial solutions, nematic order variations and defects in complex LC systems [51]. The spatial profile of the local molecular orientation, which coincides with the optical axis of the unixial anisotropic LC, was calculated by minimizing the total energy in the LC bulk, composed by thermotropic, elastic, and electrostatic energy contributions. Once the LC orientation is known, the complex permittivity tensor which describes the LC dielectric properties in the THz spectrum was calculated and fed into an electromagnetic full-wave solver, using the same finely-resolved mesh employed in the LC studies. This way, the spatial variation of the LC anisotropic permittivity was rigorously taken into account in our analysis [14], [49]. The Drude model [52] was employed for gold permittivity. For both the equations governing LC orientation and electromagnetic wave propagation, periodic boundary conditions were imposed on lateral boundaries of the supercell. Our numerical model thus cannot account for the effects of the finite device surface area. However, all devices considered in this work are designed for steering well collimated incoming THz beams with millimeter-scale waists, meaning that the device active area will in practice extend laterally at least a couple of millimeters or circa 50 - 100 unit cells, so the edge effects will always be negligible.

The profile of the tilt angle, defined as the angle between the x-y plane and the LC local optical axis, for the nematic mixture 1825 [53] is given for two characteristic voltage levels in Fig. 2(e) ($t_{LC} = 3.35\,\mu m$). For zero voltage, the in-plane orientation of the molecules (xy-plane) is provided by well-established LC alignment layers, e.g. rubbed polymer such as Nylon-6 with negligible thickness as far as the electromagnetic problem is concerned. Strong anchoring along the y-axis with a pretilt angle of 1° was considered for the top and bottom aligning surfaces of the LC cell. The dielectric permittivity of the LC layer in the z-direction (which determines the spectral position of MIM cavity resonances) is then equal to the ordinary permittivity ε_o. Due to the electro-optic effect, the applied bias voltage (the example for $U = 2.8\,V$ is given) and resulting electric field lead to the reorientation of the LC molecules. Finally, for 10 V, practically all LC molecules in the volume of the LC cell beneath the top metallic ribbon are oriented vertically (the tilt angle is 90°) thus giving the extraordinary permittivity ε_e in z-direction. According to measurement results, the refractive indices of the highly birefringent nematic mixture 1825 around the working frequency of 2.5 THz are $n_o = 1.54 + j0.013$ and $n_e = 1.911 + j0.018$ [53] which gives a large change of the LC refractive index of around 0.37 for a low voltage sweep of 10 V only.

The metasurface shown in Fig. 2 operates as a tunable phase shifter when the MIM resonators are in the overcoupled regime [49], defined by the requirement that the resonant mode radiative decay rate γ_{rad} is larger than absorption decay rate γ_{abs} [14]. When $\gamma_{rad} \gg \gamma_{abs}$, the metasurface simultaneously provides both a large phase change and high reflection in the vicinity of resonance. By tuning the LC refractive index from n_o to n_e, the resonance is spectrally shifted producing a phase shift $\Delta\Phi$ at the fixed operating frequency f_{op}. The LC thickness t_{LC} is the main geometrical parameter which determines the relative magnitude of γ_{rad} and γ_{abs} and, consequently, the achievable phase shift. Therefore, in order to find the optimal structure, the reflectance and phase are calculated as a function of t_{LC} while other geometrical parameters are fixed. The unit cell size and metallic ribbon width in all binary and gradient metasurfaces considered here, are $w_{uc} = 32\,\mu m$ and $w_m = 28\,\mu m$, respectively. Such values provide the resonant frequency around the targeted $f_{op} \approx 2.5$ THz. The top substrate is Zeonor, a cyclo-olefin polymer with very low losses at THz, with layer thickness of $40\,\mu m$ and refractive index $1.518 + j0.0009$, respectively [54]. Metallic ribbon arrays similar to those considered here have been experimentally patterned on Zeonor substrates by standard photolithography [55].

The power reflectance for zero voltage applied to all unit cells is given in Fig. 3(a). The resonance can be identified by the dip in the reflectance map which is red-shifted for a thicker LC layer while simultaneously the reflectance becomes higher. For 10 V of applied voltage, the resonance is significantly red-shifted compared to the previous case owing to the higher LC refractive index that interacts with the z-polarized resonant mode, while the overall reflectance is a bit lower as depicted in Fig. 3(b). The phase difference $\Delta\Phi$ between these two states is displayed in Fig. 3(c) indicating a large phase change across the resonance.
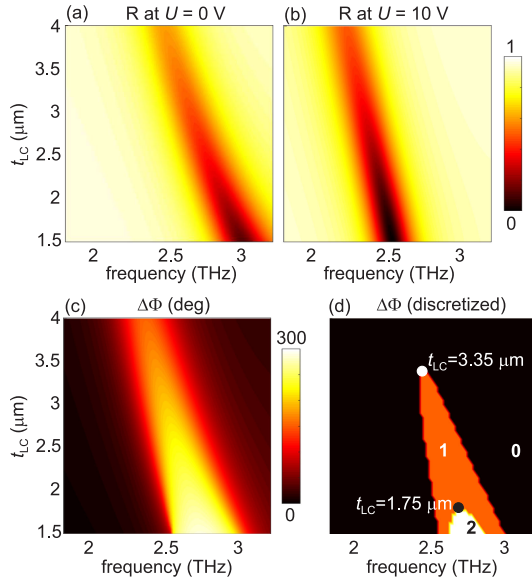
Fig. 3. The reflectance as a function of frequency and LC thickness t_{LC} for two voltages (the same voltage applied to all unit cells): (a) $U = 0$ V and (b) $U = 10$ V. (c) Phase difference $\Delta\Phi$ between the cases for 0 V and 10 V, and (d) its discretized representation (for sake of better visibility), where the area with $\Delta\Phi \geq 180°$ ($\Delta\Phi \geq 270°$) is represented by 1 (2).

Fig. 4. The reflectance as a function of frequency and polymer layer thickness t_p for two voltages (the same voltage applied to all unit cells): (a) $U = 0$ V and (b) $U = 10$ V. (c) Phase difference $\Delta\Phi$ between the cases for 0 V and 10 V.

Fig. 5. (a) Diffraction efficiency for 0th, 1st, and 2nd order as a function of frequency and voltage U_1 of the investigated binary metasurface for N = 8. (b) Diffraction efficiencies as a function of the voltage for the fixed operating frequency 2.42 THz.

Larger values of $\Delta\Phi$ are obtained with thinner LC cells because the decrease of t_{LC} in overcoupled MIM cavities reduces the total resonance linewidth $\gamma_{rad} + \gamma_{abs}$. However, this comes at the expense of bringing the resonant mode closer to critical coupling which implies a lower reflectance [14].

Areas with desired $\Delta\Phi$ are represented in the discretized phase map in Fig. 3(d) with three levels: "1" if $\Delta\Phi \geq 180°$ needed for binary metasurfaces, "2" if $\Delta\Phi \geq 270°$ needed for four-level gradient metasurfaces (this area is a subset of domain 1), whereas the rest of the phase map is not of interest and it is represented with "0" level. In order to design efficient metasurfaces, reflectance should be as high as possible. Therefore, the maximum LC thickness is selected to provide the maximum phase difference required for binary 180° and gradient metasurfaces 270°. These are found along the boundaries of domain 0 and 1 and a the boundaries between domain 1 and 2, respectively. It is worth noting that the choices for t_{LC} are in general, not unique for a single frequency. However we choose for the highest possible values of t_{LC}, such that the device does not suffer from additional losses. These values are $t_{LC} = 3.35\,\mu m$ for binary and $t_{LC} = 1.75\,\mu m$ for gradient metasurfaces, for an operating frequency $f_{op} = 2.42$ THz and 2.7 THz, respectively. The reflectance of the unit cell at $U = 0$ V and 10 V for the binary (gradient) grating is 0.71 and 0.62 (0.7 and 0.73), respectively.

Although the role of the top polymer layer is to act as a mechanical support for the proposed LC-based beam steering devices, it also influences both reflectance and phase difference because of Fabry-Pérot resonances. The power reflectance for two voltages $U = 0$ V and $U = 10$ V (the same voltage applied to all unit cells) and the phase difference between these two states are presented in Figs. 4(a-c), respectively, as a function of frequency and polymer layer thickness. As can be seen, both the
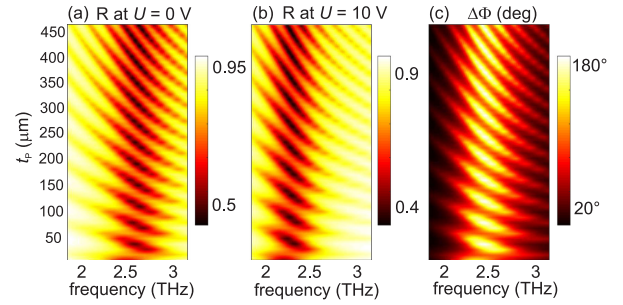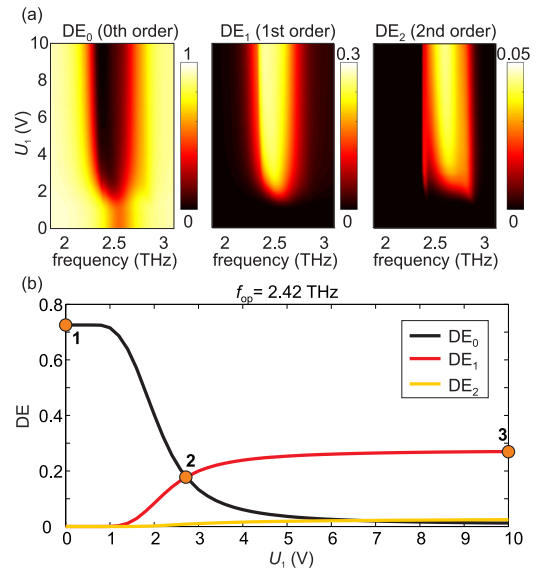
reflectance and phase difference are characterized with fringes due to Fabry-Perot resonances in the polymer layer. Therefore, the polymer thickness influences the device performance and it has to be taken into account. The chosen polymer is commercialized in foils with a set of thickness values. In the the current design, we have have selected $t_p = 40\,\mu m$, a value that does not deteriorate the operation of the device and that we already found suitable for the microfabrication of metallic structures [55].

III. TUNABLE BEAM SPLITTERS WITH BINARY METASURFACES

Having selected the LC thickness, all geometrical parameters of the investigated metasurfaces are defined. The analysis starts with a reference case of the binary metasurface with N = 8 unit cells per period, which acts as a beam splitter with tunable diffraction efficiency. The level U_1 in the voltage pattern shown in Fig. 2(c) is varied in the range 0–10 V. The maps for the voltage dependence of DEs for three lowest orders are depicted in Fig. 5(a), whereas the cross-sections of these maps for the

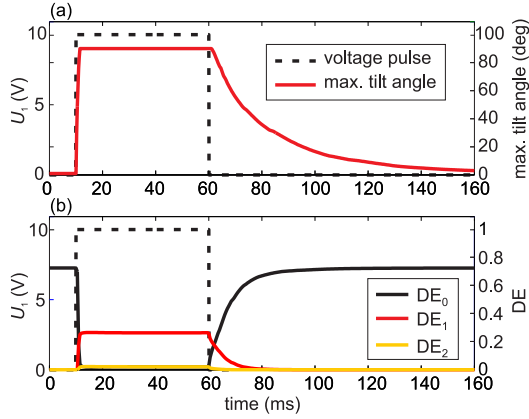Fig. 6. The transient response of the binary metasurface for a 50 ms and 10 V rectangular pulse: (a) the maximum tilt angle, and (b) DEs for three lowest diffraction orders.

Fig. 7. DE_1 as a function of frequency for the binary metasurface at $U_1 = 10$ V. The bandwidth is defined as FWHM of DE_1.

operating frequency $f_{op} = 2.42$ THz are shown in Fig. 5(b). As can be seen, for zero voltage (working point 1), just zero order is reflected and the binary metasurface operates as a mirror, with a reflectance of 0.71, namely that of the unit cell in the case of $U = 0$ V, as calculated in Fig. 3(a). For $U_1 = 2.8$ V (working point 2), the metasurface divides an incoming wave into three beams, corresponding to $-1, 0, +1$ orders with the same DE of around 0.18. For sufficiently high voltage (working point 3 at $U_1 = 10$ V), the zeroth order is practically suppressed (DE is just 0.01). The metasurface then splits an incoming beam into -1 and $+1$ diffraction orders with the same DE of around 0.27. DE for the second order mode is low in the whole frequency range under investigation.

The transient response of the binary metasurface was investigated by applying a rectangular voltage pulse (with a duration of 50 ms and amplitude of 10 V). Results for the maximum tilt angle of LC molecules and DEs for the three lowest orders are illustrated in Figs. 6(a) and 6(b), respectively. The voltage is turned-on at $t = 10$ ms. As a result of the biasing electric field, LC molecules are vertically reoriented in a few ms and the tilt angle reaches $90°$. DE_0 simultaneously falls down while DE_1 rises. Inverse processes take place at $t = 60$ ms when the voltage is turned-off. As can be seen, the response speed is limited by the fall time starting at $t = 60$ ms during which LC molecules undergo elastic relaxation back into the initial state dictated by the orientation of the planar alignment. The resulting switch-off time for the LC molecules is around 50 ms. Please note, that DE_1, which is the key property of interest, switches notably faster, in less than 20 ms. The switching times of LC-based devices scale with the inverse square of the LC thickness. In this work, the LC-infiltrated resonant MIM cavities feature a deeply subwavelength thickness ($\lambda/36$), which results in two orders of magnitude faster switching compared with non-resonant LC-THz modulators that employ LC cells with a thickness comparable to the wavelength.

The modulation speed is compatible with several applications such as THz time-domain imaging and spectroscopy [61]. A few times improvement could be expected by exploiting the expertise
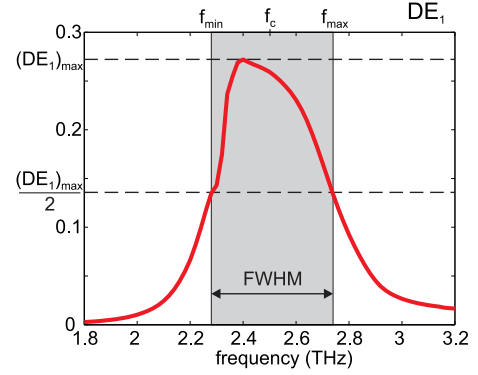
accrued in LC display technology on the synthesis of novel LC molecules with low-viscosity and high-$\Delta\varepsilon$ at THz frequencies. Another technique to increase the switching speed of nematic LC cells is by using a polymer network to stabilize the LC molecules [62], [63]. Finally, one of the most promising ways to increase the device speed is by employing dual-frequency nematic mixtures [64], thus equalizing the switch on and off times and pushing the overall response time of the beam steerer towards 1 ms, which is practically a fundamental limit of nematic LC-based devices.

The proposed beam-steering devices belong to the class of diffractive optics elements which inherently have a narrow bandwidth. Here it is defined as the full width at half maximum (FWHM) or 3-dB attenuation in DE_1 which is presented in Fig. 7 as a function of frequency for $U_1 = 10$ V. The absolute value of the bandwidth is 0.46 THz, while the relative bandwidth, namely the FWHM over its central frequency f_c, is 18%.

IV. TUNABLE BLAZED GRATINGS WITH GRADIENT METASURFACES

The geometry of the gradient metasurface is essentially the same as for the binary structure, except the LC thickness is reduced to 1.75 μm. The period of the considered metasurface consists of N = 4 unit cells. The metasurface with zero voltage applied to all cells behaves as a flat mirror just reflecting an normally-incident beam with $DE_0 = 0.73$ at the operating frequency 2.7 THz. The four-level gradient phase profile $0°$, $90°$, $180°$, $270°$ given in Fig. 1(c) is provided by the corresponding voltage pattern from Fig. 2(c) with $U_0 = 0$ V, $U_1 = 1.8$ V, $U_2 = 2.2$ V, $U_3 = 10$ V. The reflectance and phase for four cells with the specified voltages are given in Figs. 8(a) and 8(b), respectively. As can be seen, the phase is linearly changing across the cells from $0°$ to $270°$. The reflectance is high, above 0.7 for cells 1 and 4, since they implement the phase levels $0°$ and $270°$, respectively, which are away from the MIM cavity resonance. On the other hand, the inner cells 2 and 3 implement the phase levels $90°$ and $180°$, which are located in close vicinity to the cavity resonance, so the resulting reflectance for these cells is very low, around 0.1. DEs for the gradient metasurface are shown in Fig. 8(c). DE_{+1} is just slightly above 0.3. This low
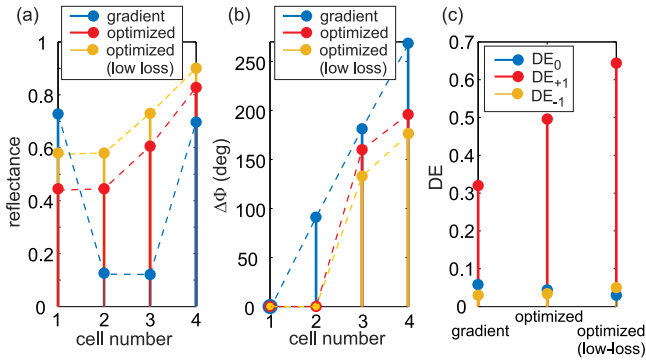
Fig. 8. (a) Reflectance and (b) phase for cells 1–4 in the gradient, optimized gradient, and optimized gradient metasurface with lower loss LC. (c) DEs (−1, 0, +1 orders) for the gradient, optimized gradient, and optimized gradient metasurface with low losses.
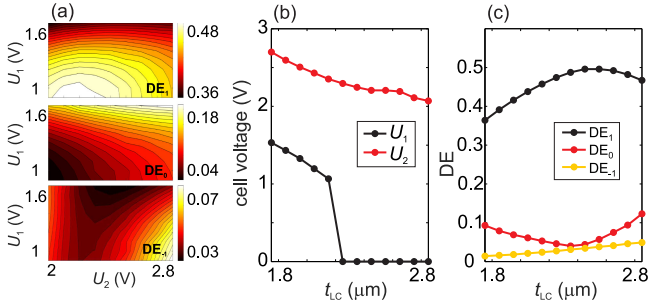

Fig. 9. The optimization procedure performed in order to maximize DE_{+1}: (a) DEs for varying voltages U_1 and U_2 with fixed $U_0 = 0$ V and $U_3 = 10$ V, (b) the evolution of U_1 and U_2 which give maximum DE_{+1} as a function of LC thickness, and (c) DEs as a function of t_{LC}.

efficiency is the result of high absorption in cells 2 and 3. At the same time, 0 and −1 orders are suppressed with DEs less than 0.05.

Such large variations of the reflectance among the four cells can lead to sub-optimal performance, even if the implemented discretized phase profile is linear. This is a general issue of beam steering gratings that involve lossy resonators [40]. In order to maximize DE_{+1}, a simple optimization procedure was performed. Bias voltages for cells 1 and 4 were kept constant at $U_0 = 0$ V and $U_3 = 10$ V, respectively, while the voltages applied on cells 2 and 3 were swept from 0 to 10 V. The same procedure was repeated for the LC thickness in the range from the initial value $1.75\,\mu m$ to $2.85\,\mu m$. Thicker LC layers were considered in order to enhance overall reflection and DE_{+1} by reducing the absorption losses in the overcoupled MIM cavities. The results of the optimization procedure are presented in Fig. 9. DE maps for $t_{LC} = 2.45\,\mu m$ are given in Fig. 9(a). The evolution of the bias voltages for cells 2 and 3 which give maximum DE_{+1} is depicted in Fig. 9(b). DEs as a function of LC thickness are presented in Fig. 9(c). As can be seen, the maximum DE_{+1} is achieved for $U_1 = 0$ V, $U_2 = 2.2$ V, and $t_{LC} = 2.45\,\mu m$. The results for the optimized gradient structure are presented in Fig. 8. The reflectance is increased for all cells except for cell 1, the phase is not linear anymore, whereas DE_{+1} is increased

to around 0.5, which is a significant improvement compared to 0.3 for the non-optimized structure.

The main source of losses in the considered metasurfaces is the field absorption within the LC layer. Therefore, further improvement in DE can be achieved by considering LCs with lower losses. The results for the optimized gradient metasurface (with $t_{LC} = 2.55\,\mu m$) infiltrated with a speculated LC with the same real part of the refractive index, but with one order of magnitude lower losses (imaginary part of the refractive index) are given in Fig. 8 as well, to compare with previous structures. Such low-loss LCs have been recently realized and characterized at millimeter waves [56], and it can be expected that they could retain such low amounts of absorption losses also in the THz spectrum, given the material dispersion behaviour of most nematic LCs [57]. As can be seen, the reflectance is increased in all cells 1-4 compared to the optimized structure while the phase profile stays almost the same. DE_{+1} increases to around 0.65 which is quite close to the theoretical maximum of around 0.8 for a 4-level reflective grating. It can be remarked in Fig. 8(b) that the phase profiles of the optimized structures deviate significantly from the predefined $0° - 90° - 180° - 270°$ values. Therefore, in order to maximize the DE_{+1} of the investigated beam steering metasurface, it is crucial to increase and equalize the reflectance of each unit cell within a metasurface period.

V. TUNABLE BEAM STEERING

Beam steering with a tunable diffraction angle is achieved by varying the metasurface period as schematically represented in Figs. 1(d) and 1(e). Results for the beam steering with a binary metasurface are depicted in Fig. 10(a). The number of unit cells per period is varied from N = 4 to N = 20, which corresponds to P varying in the range $128 - 640\,\mu m$. Simultaneously, the voltage pattern from Fig. 2(b) is modified accordingly with voltage levels $U_0 = 0$ V and $U_1 = 10$ V, such that each grating is composed of two phase cells of total width $Nw_{uc}/2$ with values 0 and $180°$. As can be seen in Fig. 10(a), the diffraction angle of the first order changes from $75.6°$ to $11.2°$ in accordance with the well-known formula $\alpha = \arcsin(\lambda/P)$. Diffraction angle for −1 order changes in the same way for the negative angles. The highest $DE_{\pm1}$ of 0.31 is achieved for the smallest period (N = 4), whereas $DE_{\pm1}$ slightly falls down with increasing P down to around 0.25 for N = 20. The binary metasurface was designed with the phase difference $\Delta\Phi_0 = 180°$. Therefore, it acts as a beam splitter with just ±1 diffraction orders, while other orders can be neglected since their DEs are below 0.05.

The results for the beam steering with gradient metasurfaces are depicted in Fig. 10(b). Here N changes from 4 to 12, while P is in the range $128 - 384\,\mu m$. The optimized phase profile for N = 4 was applied in other two cases as well. In all cases, the voltage pattern was the same: $U_0 = 0$ V, $U_1 = 0$ V, $U_2 = 2.2$ V, $U_3 = 10$ V. Diffraction angle for the first order changes from $60.2°$ (N = 4) to $25.7°$ (N = 8) and $16.8°$ (N = 12). DE_{+1} is high, around 0.5 for N = 4, but it falls down for larger periods, so it is around 0.4 for N = 8, and around 0.35 for N = 12. Other diffraction orders are quite well suppressed for N = 4, however they become more pronounced for larger
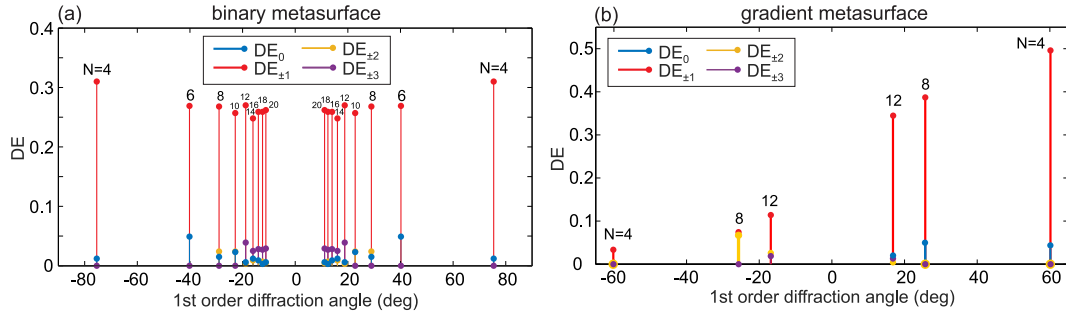
Fig. 10. DEs with a variable period as a function of the first order diffraction angle: (a) binary (the phase difference is $\Delta\Phi_0 = 180°$,) and (b) gradient metasurface. The period is represented by the number N of unit cells per period and it varies (a) from $128\,\mu\mathrm{m}$ (for N = 4) to $640\,\mu\mathrm{m}$ (for N=20) and (b) from $128\,\mu\mathrm{m}$ (for N = 4) to $384\,\mu\mathrm{m}$ (for N=12). Geometrical parameters are the following: the unit cell size $w_{\mathrm{uc}} = 32\,\mu\mathrm{m}$, the metallic ribbon width $w_{\mathrm{m}} = 28\,\mu\mathrm{m}$, and the LC thickness (a) $t_{\mathrm{LC}} = 3.35\,\mu\mathrm{m}$) and (b) $t_{\mathrm{LC}} = 2.45\,\mu\mathrm{m}$.

periods. Better performance, i.e. higher DE of the dominant beam and higher suppression of undesired orders, are expected by following an optimization procedure as described for the case N = 4.

The accuracy of the reported beam-steering angles depends only on the metasurface period for a given wavelength of operation. The considered metal stripe array can be readily fabricated by standard photolithography with resolution better than $1\,\mu\mathrm{m}$ and accuracy of the pitch value better than 100 nm [55]. Therefore, without resorting to more sophisticated nanofabrication processes, the tolerance of the period value in the considered metasurfaces would be less than 0.5%, which translates in a maximum deviation of approximately 1 degree for the steering angle for N = 4, and vanishing for larges pitch values.

VI. DISCUSSION

Standard tunable elements for beam-steering devices, such as diodes employed for microwave coding metasurfaces [27] and reflectarrays [33], [34], and ITO commonly used at near-infrared frequencies [38], [42], are not applicable for THz devices. Phase-change materials [58] require the temperature tuning which limits achievable modulation speed. Electromechanical metasurfaces [32] could be utilized for efficient beam steering, but they require more sophisticated fabrication and control, and they are prone to faster degradation of their moving parts, especially at THz frequencies.

On the other hand, LCs as low-loss dielectrics with a continuous tuning of dielectric permittivity are simple and efficient tunable elements. For the LC mixture 1825, the achieved DE is 0.5–0.6. Further improvement of DEs can be achieved by using LCs with lower losses, as demonstrated in the case of the optimized gradient structure (Fig. 8(c)) whose DE reaches around 0.65 when infiltrated with a novel LC mixture having an order of magnitude lower losses [56]. Such high DE is quite close to the theoretical limit of around 0.8.

The achieved DEs are higher than those obtained in THz beam-steering devices with semiconductors as tunable elements [7], [8], [31]. These were made from thin semiconductor films [8] or from metasurfaces coupled with thin semiconductor layers [31]. In both cases, the modulation principle is based

on the control of free charge carries in semiconductors. Although this provides efficient modulation of the real part of semiconductors' permittivity, a significant imaginary part leads to a pronounced absorption and limits achievable efficiency to around 0.2–0.3 [31].

Graphene-based metasurfaces are also appealing for beam steering at THz frequencies [37], [44]. They are also made of MIM-cavity based resonators. Still, very high voltages of around 1 kV are needed because of thick insulating layers of MIM cavities at THz frequencies. Such high voltages are not suitable for practical applications because of huge power consumption and safety issues. At the same time, THz devices require large-area graphene, dominantly fabricated by chemical vapour deposition. Losses in such graphene at THz frequencies are several times higher [59] than the ones theoretically predicted and used for numerical calculations [37]. At the same time, the conductivity of chemical vapour deposition graphene is spatially inhomogeneous [60], which also induces significant constraints for making THz modulators.

MIM metasurfaces enhance the efficiency of THz beam-steering devices compared to LC based wedge-shaped devices [5] and Fabry-Perot cavities with LC layers [6]. MIM cavities provide very compact devices since the thickness of the active LC layer is decreased by orders of magnitude, from millimiters [5] and hundreds of microns [6], to just several microns in the case considered here. Since the speed scales with the square of the LC thickness [14], the modulation speed in LC devices with MIM cavities is greatly improved to a few tens of milliseconds. Moreover, such thickness values for the LC cell are fully compatible with the mature technology used in the fabrication of LC displays.

DEs for considered metasurfaces are around 0.6 for binary, and 0.5 for gradient metasurfaces. As already mentioned, absorption within the LC layer is the main source of losses. The LC layer is thinner in gradient metasurfaces because a larger phase difference is required, which implies a higher absorption and a slightly lower DE compared to binary metasurfaces. In order to increase DE, low-loss LCs are one possible solution. Another approach can be the utilization of metasurfaces with simultaneous control of both amplitude and phase [65]. This could be implemented by two-dimensional arrays of MIM

cavities and by angular reorientation of top metallic elements of different shapes. In this way, it could be possible to achieve required phase difference and retain high reflection amplitude.

VII. CONCLUSION

In a summary, we demonstrated that the functionality of beam-steering metasurfaces based on one dimensional arrays of MIM cavities infiltrated with LCs can be adjusted by dynamically controlling the spatial voltage pattern. As a result, the metasurfaces can be switched from a mirror, to beam splitter and blazed grating, while the angle of the diffracted beam can be adjusted by reconfiguring the metasurface period. DE in the range 0.5–0.6 can be further increased by using novel LC mixtures with low losses. The proposed components can find direct application in THz systems, as they feature i) flat profile and compact dimensions with a subwavelength thickness, ii) fast switching speed of around 20 ms, iii) continuous control of the LC effective index with a low power consumption and driving voltages not higher than 10 V, and iv) technological scalability of their design and working frequency up to several THz. The last point is particularly relevant as the performance of other standard approaches for tunable THz devices using e.g. electronics (PIN diodes, varactors) or MEMS rapidly degrades or becomes impractical above 1 THz. Together with previously demonstrated LC based tunable metasurfaces for the amplitude [14] and polarization modulation [49], they provide a multifunctional platform for tunable THz devices.

REFERENCES

[1] M. Tonouchi, "Cutting-edge terahertz technology," *Nature Photon.*, vol. 1, pp. 97–105, 2007.

[2] T. Kleine-Ostmann and T. Nagatsuma, "A review on Terahertz communications research," *J. Infrared Millimeter THz Waves*, vol. 32, pp. 143–171, 2011.

[3] P. U. Jepsen, D. G. Cooke, and M. Koch, "Terahertz spectroscopy and imaging—Modern techniques and applications," *Laser Photon. Rev.*, vol. 5, pp. 124–166, 2011.

[4] X. Fu, F. Yang, C. Liu, X. Wu, and T. J. Cui, "Terahertz beam steering technologies: From phased arrays to field-programmable metasurfaces," *Adv. Opt. Mater.*, 2019, Art. no. 1900628.

[5] B. Scherger *et al.*, "Discrete terahertz beam steering with an electrically controlled liquid crystal device," *J. Infrared Millimeter THz Waves*, vol. 33, pp. 1117–1122, 2012.

[6] W. Fuscaldo *et al.*, "Tunable Fabry-Perot cavity THz antenna based on leaky-wave propagation in nematic liquid crystals," *IEEE Antennas Wireless Propag. Lett.*, vol. 16, pp. 2046–2049, 2017.

[7] S. Busch, B. Scherger, M. Scheller, and M. Koch, "Optically controlled terahertz beam steering and imaging," *Opt. Lett.*, vol. 37, pp. 1391–1393, 2012.

[8] T. P. Steinbusch, H. K. Tyagi, M. C. Schaafsma, G. Georgiou, and J. Gómez Rivas, "Active terahertz beam steering by photo-generated graded index gratings in thin semiconductor films," *Opt. Exp.*, vol. 22, pp. 26 559–26 571, 2014.

[9] K.-i. Maki and C. Otani, "Terahertz beam steering and frequency tuning by using the spatial dispersion of ultrafast laser pulses," *Opt. Exp.*, vol. 16, pp. 10 158–10 169, 2008.

[10] A. P. Hibbins, J. R. Sambles, C. R. Lawrence, and J. R. Brown, "Squeezing millimeter waves into microns," *Phys. Rev. Lett.*, vol. 92, 2004, Art. no. 143904.

[11] Y. Todorov *et al.*, "Strong light-matter coupling in subwavelength metal-dielectric microcavities at terahertz frequencies," *Phys. Rev. Lett.*, vol. 102, 2009, Art. no. 186402.

[12] H.-T. Chen *et al.*, "Active terahertz metamaterial devices," *Nature*, vol. 444, pp. 597–600, 2006.

[13] H.-T. Chen *et al.*, "A metamaterial solid-state terahertz phase modulator," *Nature Photon.*, vol. 3, pp. 148–151, 2009.

[14] G. Isić, B. Vasić, D. C. Zografopoulos, R. Beccherelli, and R. Gajić, "Electrically tunable critically coupled terahertz metamaterial absorber based on nematic liquid crystals," *Phys. Rev. Appl.*, vol. 3, 2015, Art. no. 064007.

[15] M. Rahm, J.-S. Li, and W. J. Padilla, "THz wave modulators: A brief review on different modulation techniques," *J. Infrared Millimeter THz Waves*, vol. 34, pp. 1–27, 2013.

[16] M. R. Hashemi, S. Cakmakyapan, and M. Jarrahi, "Reconfigurable metamaterials for terahertz wave manipulation," *Rep. Prog. Phys.*, vol. 80, 2017, Art. no. 094501.

[17] W. J. Padilla and R. D. Averitt, "Properties of dynamical electromagnetic metamaterials," *J. Opt.*, vol. 19, 2017, Art. no. 084003.

[18] N. Yu *et al.*, "Light propagation with phase discontinuities: Generalized laws of reflection and refraction," *Science*, vol. 334, pp. 333–337, 2011.

[19] C. Pfeiffer *et al.*, "Efficient light bending with isotropic metamaterial huygens' surfaces," *Nano Lett.*, vol. 14, pp. 2491–2497, 2014.

[20] H.-T. Chen, A. J. Taylor, and N. Yu, "A review of metasurfaces: Physics and applications," *Rep. Prog. Phys.*, vol. 79, 2016, Art. no. 076401.

[21] N. M. Estakhri and A. Alù, "Recent progress in gradient metasurfaces," *J. Opt. Soc. Amer. B*, vol. 33, pp. A21–A30, 2016.

[22] F. Ding, A. Pors, and S. I. Bozhevolnyi, "Gradient metasurfaces: A review of fundamentals and applications," *Rep. Prog. Phys.*, vol. 81, 2017, Art. no. 026401.

[23] S. Sun *et al.*, "High-efficiency broadband anomalous reflection by gradient meta-surfaces," *Nano Lett.*, vol. 12, pp. 6223–6229, 2012.

[24] T. Niu *et al.*, "Experimental demonstration of reflectarray antennas at terahertz frequencies," *Opt. Exp.*, vol. 21, pp. 2875–2889, 2013.

[25] Z. Wei, Y. Cao, X. Su, Z. Gong, Y. Long, and H. Li, "Highly efficient beam steering with a transparent metasurface," *Opt. Exp.*, vol. 21, pp. 10 739–10 745, 2013.

[26] M. Farmahini-Farahani, J. Cheng, and H. Mosallaei, "Metasurfaces nanoantennas for light processing," *J. Opt. Soc. Amer. B*, vol. 30, pp. 2365–2370, 2013.

[27] T. J. Cui, M. Q. Qi, X. Wan, J. Zhao, and Q. Cheng, "Coding metamaterials, digital metamaterials and programmable metamaterials," *Light Sci. Appl.*, vol. 3, 2014, Art. no. e218.

[28] M. Maasch, M. Roig, C. Damm, and R. Jakoby, "Voltage-tunable artificial gradient-index lens based on a liquid crystal loaded fishnet metamaterial," *IEEE Antenn. Wireless Propag. Lett.*, vol. 13, pp. 1581–1584, 2014.

[29] L. Zou, M. Cryan, and M. Klemm, "Phase change material based tunable reflectarray for free-space optical inter/intra chip interconnects," *Opt. Exp.*, vol. 22, pp. 24 142–24 148, 2014.

[30] G. Kaplan, K. Aydin, and J. Scheuer, "Dynamically controlled plasmonic nano-antenna phased array utilizing vanadium dioxide," *Opt. Mater. Exp.*, vol. 5, pp. 2513–2524, 2015.

[31] X. Su *et al.*, "Active metasurface terahertz deflector with phase discontinuities," *Opt. Exp.*, vol. 23, pp. 27 152–27 158, 2015.

[32] L. Cong *et al.*, "Active multifunctional microelectromechanical system metadevices: Applications in polarization control, wavefront deflection, and holograms," *Adv. Opt. Mater.*, vol. 5, 2017, Art. no. 1600716.

[33] D. Sievenpiper and J. Schaffner, "Beam steering microwave reflector based on electrically tunable impedance surface," *Electron. Lett.*, vol. 38, pp. 1237–1238, 2002.

[34] T. H. Hand and S. A. Cummer, "Reconfigurable reflectarray using addressable metamaterials," *IEEE Antennas Wireless Propag. Lett.*, vol. 9, pp. 70–74, 2010.

[35] S. Bildik, S. Dieter, C. Fritzsch, W. Menzel, and R. Jakoby, "Reconfigurable folded reflectarray antenna based upon liquid crystal technology," *IEEE Trans. Antennas. Propag.*, vol. 63, no. 1, pp. 122–132, Jun. 2015.

[36] P. F. McManamon *et al.*, "Optical phased array technology," *Proc. IEEE*, vol. 84, no. 2, pp. 268–298, Feb. 1996.

[37] T. Yatooshi, A. Ishikawa, and K. Tsuruta, "Terahertz wavefront control by tunable metasurface made of graphene ribbons," *Appl. Phys. Lett.*, vol. 107, 2015, Art. no. 053105.

[38] A. Forouzmand and H. Mosallaei, "Tunable two dimensional optical beam steering with reconfigurable indium tin oxide plasmonic reflectarray metasurface," *J. Opt.*, vol. 18, 2016, Art. no. 125003.

[39] P. P. Iyer, M. Pendharkar, and J. A. Schuller, "Electrically reconfigurable metasurfaces using heterojunction resonators," *Adv. Opt. Mater.*, vol. 4, pp. 1582–1588, 2016.

[40] F. Liu *et al.*, "Intelligent metasurfaces with continuously tunable local surface impedance for multiple reconfigurable functions," *Phys. Rev. Appl.*, vol. 11, 2019, Art. no. 044024.

[41] D. C. O'Shea, T. J. Suleski, and D. W. Kathman, A. D. Prather, *Diffractive Optics: Design, Fabrication, and Test*. Bellingham, WA, USA: SPIE, 2004.

[42] Y.-W. Huang *et al.*, "Gate-tunable conducting oxide metasurfaces," *Nano Lett.*, vol. 16, pp. 5319–5325, 2016.

[43] M. Kim, J. Jeong, J. K. S. Poon, and G. V. Eleftheriades, "Vanadium-dioxide-assisted digital optical metasurfaces for dynamic wavefront engineering," *J. Opt. Soc. Amer. B*, vol. 33, pp. 980–988, 2016.

[44] E. Carrasco, M. Tamagnone, and J. Perruisseau-Carrier, "Tunable graphene reflective cells for THz reflectarrays and generalized law of reflection," *Appl. Phys. Lett.*, vol. 102, 2013, Art. no. 104103.

[45] G. Isić *et al.*, "Electrically tunable metal-semiconductor-metal terahertz metasurface modulators," *IEEE J. Sel. Topics Quantum Electron.*, vol. 25, no. 3, May/Jun. 2019, Art. no. 8500108.

[46] B. Vasić, M. M. Jakovljević, G. Isić, and R. Gajić, "Tunable metamaterials based on split ring resonators and doped graphene," *Appl. Phys. Lett.*, vol. 103, 2013, Art. no. 011102.

[47] D. Shrekenhamer, W.-C. Chen, and W. J. Padilla, "Liquid crystal tunable metamaterial absorber," *Phys. Rev. Lett.*, vol. 110, 2013, Art. no. 177403.

[48] R. Kowerdziej, M. Olifierczuk, J. Parka, and J. Wróbel, "Terahertz characterization of tunable metamaterial based on electrically controlled nematic liquid crystal," *Appl. Phys. Lett.*, vol. 105, 2014, Art. no. 022908.

[49] B. Vasić, D. C. Zografopoulos, G. Isić, R. Beccherelli, and R. Gajić, "Electrically tunable terahertz polarization converter based on overcoupled metal-isolator-metal metamaterials infiltrated with liquid crystals," *Nanotechnology*, vol. 28, 2017, Art. no. 124002.

[50] M. A. Golub, "Laser beam splitting by diffractive optics," *Opt. Photon. News*, vol. 15, no. 2, pp. 36–41, 2004.

[51] D. C. Zografopoulos, R. Beccherelli, and E. E. Kriezis, "Beam-splitter switches based on zenithal bistable liquid-crystal gratings," *Phys. Rev. E*, vol. 90, 2014, Art. no. 042503.

[52] M. A. Ordal, R. J. Bell, J. R. W. Alexander, L. L. Long, and M. R. Querry, "Optical properties of fourteen metals in the infrared and far infrared: Al, Co, Cu, Au, Fe, Pb, Mo, Ni, Pd, Pt, Ag, Ti, V, and W," *Appl. Opt.*, vol. 24, pp. 4493–4499, 1985.

[53] M. Reuter *et al.*, "Highly birefringent, low-loss liquid crystals for terahertz applications," *APL Mater.*, vol. 1, 2013, Art. no. 012107.

[54] P. A. George, W. Hui, F. Rana, B. G. Hawkins, A. E. Smith, and B. J. Kirby, "Microfluidic devices for terahertz spectroscopy of biomolecules," *Opt. Exp.*, vol. 16, pp. 1577–1582, 2008.

[55] A. Ferraro, D. C. Zografopoulos, R. Caputo, and R. Beccherelli, "Guided-mode resonant narrowband terahertz filtering by periodic metallic stripe and patch arrays on cyclo-olefin substrates," *Sci. Rep.*, vol. 8, 2018, Art. no. 17272.

[56] V. Lapanik, G. Sasnouski, S. Timofeev, E. Shepeleva, G. Evtyushkin, and W. Haase, "New highly anisotropic liquid crystal materials for high-frequency applications," *Liquid Crystals*, vol. 45, pp. 1242–1249, 2018.

[57] D. C. Zografopoulos, A. Ferraro, and R. Beccherelli, "Liquid-crystal high-frequency microwave technology: Materials and characterization," *Adv. Mater. Technol.*, vol. 4, 2019, Art. no. 1800447.

[58] M. R. M. Hashemi, S.-H. Yang, T. Wang, N. Sepúlveda, and M. Jarrahi, "Electronically-controlled beam-steering through vanadium dioxide metasurfaces," *Sci. Rep.*, vol. 6, 2016, Art. no. 35439.

[59] C. Lee, J. Y. Kim, S. Bae, K. S. Kim, B. H. Hong, and E. J. Choi, "Optical response of large scale single layer graphene," *Appl. Phys. Lett.*, vol. 98, 2011, Art. no. 071905.

[60] J. L. Tomaino *et al.*, "Terahertz imaging and spectroscopy of large-area single-layer graphene," *Opt. Exp.*, vol. 19, pp. 141–146, 2011.

[61] H. Guerboukha, K. Nallappan, and M. Skorobogatiy, "Toward real-time terahertz imaging," *Adv. Opt. Photon.*, vol. 10, pp. 843–938, 2018.

[62] Y. Utsumi, T. Kamei, K. Saito, and H. Moritake, "Increasing the speed of microstrip-line-type polymer-dispersed liquid-crystal loaded variable phase shifter," *IEEE Trans. Microw. Theory Tech.*, vol. 53, no. 11, pp. 3345–3353, Nov. 2005.

[63] K. Altmann, M. Reuter, K. Garbat, M. Koch, R. Dabrowski, and I. Dierking, "Polymer stabilized liquid crystal phase shifter for terahertz waves," *Opt. Exp.*, vol. 21, pp. 12 395–12 400, 2013.

[64] T. Kuki, H. Fujikake, and T. Nomoto, "Microwave variable delay line using dual-frequency switching-mode liquid crystal," *IEEE Trans. Microw. Theory Tech.*, vol. 50, no. 11, pp. 2604–2609, Nov. 2002.

[65] L. Liu *et al.*, "Broadband Metasurfaces with Simultaneous Control of Phase and Amplitude," *Adv. Mater.*, vol. 26, pp. 5031–5036, 2014.

Borislav Vasić was born in Vinkovci, Croatia, in 1982. He received the Diploma in microcomputer electronics from the Faculty of Technical Sciences, University of Novi Sad, Novi Sad, Serbia, in 2005, and the Ph.D. degree in nanoelectronics and photonics from the Faculty of Electrical Engineering, University of Belgrade, Beograd, Serbia, 2012. His research interests include design of tunable photonics devices based on metamaterials and plasmonic structures.

Goran Isić was born in Subotica, Yugoslavia, in 1982. He received the Diploma in physical electronics from the School of Electrical Engineering, University of Belgrade, Beograd, Serbia, in 2006 and the Ph.D. degree in quantum electronics from the School of Electronic and Electrical Engineering, University of Leeds, Leeds, U.K., in 2011. His research interest include nano-optics, nanospectroscopy, plasmonics, metamaterials and resonant optical systems in general.

Romeo Beccherelli (M'12) was born in Plovdiv, Bulgaria, in 1969. He received the Laurea (*cum laude*) and Ph.D. degrees in electronic engineering from the Sapienza University of Rome, Rome, Italy, in 1994 and 1998, respectively. In 1997, he joined as a Postdoctoral Research Assistant with the Department of Engineering Science, University of Oxford, Oxford, U.K. In 2001, he was appointed Researcher and a Senior Researcher with the National Research Council of Italy, Institute for Microelectronics and Microsystems, Rome, in 2006. He has invented two patents and authored more than 90 scientific papers in international journals, more than 110 conference proceedings papers, and 4 book chapters. His current research interests include sensor arrays, photonics and plasmonics based on liquid crystals, and metamaterial and metasurface devices and systems for processing microwaves and terahertz waves. His doctoral thesis was awarded the International Otto Lehman Prize 1999 in liquid crystal technology by the University of Karlsruhe (Germany) and the Otto Lehmann Foundation.

Dimitrios C. Zografopoulos was born in Thessaloniki, Greece, in 1980. He received the Diploma in electrical and computer engineering and the Ph.D. degree from the Aristotle University of Thessaloniki, Thessaloniki, Greece, in 2003 and 2009, respectively. In 2011, he was a Postdoctoral Research Fellow with the Greek States Scholarship Foundation and a Visiting Research Fellow with the Department of Electronics Technology, Carlos III University of Madrid, Madrid, Spain. He subsequently moved under a two-year Intra-European Marie-Curie Fellowship to the Institute for Microelectronics and Microsystems, Italian National Research Council of Italy, Rome, where he is currently a Researcher. He has authored or coauthored more than 70 scientific papers in international journals and two book chapters. His current research interests include the investigation of photonic/plasmonic waveguides, tunable metamaterials and metasurfaces, and the interaction between electromagnetic waves and liquid crystals.

Electrically Tunable Metal–Semiconductor–Metal Terahertz Metasurface Modulators

Goran Isić 🄳, Georgios Sinatkas 🄳, *Student Member, IEEE*, Dimitrios C. Zografopoulos 🄳, Borislav Vasić,
Antonio Ferraro 🄳, *Member, IEEE*, Romeo Beccherelli 🄳, *Member, IEEE*,
Emmanouil E. Kriezis 🄳, *Senior Member, IEEE*, and Milivoj Belić 🄳

Abstract—We propose metal–semiconductor–metal cavity arrays as active elements of electrically tunable metasurfaces operating in the terahertz spectrum. Their function is based on reverse biasing the Schottky junction formed between top metal strips and the n-type semiconductor buried beneath. A gate bias between the strips and a back metal reflector controls the electron depletion layer thickness thus tuning the Drude permittivity of the cavity array. Using a rigorous multiphysics framework which combines Maxwell equations for terahertz waves and the drift-diffusion model for describing the carrier behavior in the semiconductor, we find a theoretically infinite extinction ratio, insertion loss of around 10%, and picosecond intrinsic switching times at 1 THz, for a structure designed to enter the critical coupling regime once the depletion layer reaches the bottom metal contact. We also show that the proposed modulation concept can be used for devices operating at the higher end of the terahertz spectrum, discussing the limitations on their performance.

Index Terms—Terahertz metasurfaces, tunable metamaterials.

G. Isić is with the Graphene Laboratory of Center for Solid State Physics and New Materials, Institute of Physics Belgrade, University of Belgrade, Belgrade 11080, Serbia, and also with the Texas A&M University at Qatar, Doha 23874, Qatar (e-mail: isicg@ipb.ac.rs).

G. Sinatkas and E. E. Kriezis are with the School of Electrical and Computer Engineering, Aristotle University of Thessaloniki, Thessaloniki 54124, Greece (e-mail: gsinatka@auth.gr; mkriezis@auth.gr).

D. C. Zografopoulos, A. Ferraro, and R. Beccherelli are with the Consiglio Nazionale delle Ricerche, Istituto per la Microelettronica e Microsistemi, Rome 00133, Italy (e-mail: dimitrios.zografopoulos@artov.imm.cnr.it; antonio.ferraro@artov.imm.cnr.it; romeo.beccherelli@artov.imm.cnr.it).

B. Vasić is with the Graphene Laboratory of Center for Solid State Physics and New Materials, Institute of Physics Belgrade, University of Belgrade, Belgrade 11080, Serbia (e-mail: bvasic@ipb.ac.rs).

M. Belić is with the Texas A&M University at Qatar, Doha 23874, Qatar (e-mail: milivoj.belic@qatar.tamu.edu).

Color versions of one or more of the figures in this paper are available online at http://ieeexplore.ieee.org.

Digital Object Identifier 10.1109/JSTQE.2019.2893762

I. INTRODUCTION

T ERAHERTZ science has been steadily attracting a growing interest over the past decades. Lying above the upper limit of frequencies attainable in electronic devices and yet below frequencies at which light can be efficiently generated and detected, the current terahertz technology is faced with many challenges [1]. Among them, the development of fast electro-optic modulators for free-space terahertz signals, exhibiting low insertion loss and high modulation depth, has been gaining in importance over the past years considering the rapidly growing demands of wireless communications [2].

Following initial successful demonstrations of electro-optic modulation in terahertz [3], [4], the culprit of the very low modulation efficiency has been identified as the incompatibility of submillimeter wavelengths with much smaller features of the underlying electronic system [5]. A substantial increase in modulation efficiency has since been provided by various metallic structures [6], [7] whose resonant response translates into a stronger light-matter interaction helping bridge the two scales. Devices combining semiconductors (mainly gallium arsenide, GaAs) with metasurfaces have been of particular interest [8] as they offer high-speed modulation, a perspective of on-chip integration using established semiconductor technologies [9] and are fully compatible with quantum cascade lasers [1], the most promising source of terahertz radiation. Other material systems, such as liquid crystals [10]–[12] and graphene [13]–[15] more recently, have also been considered in depth, each presenting its own set of comparative advantages.

After the first prototype was introduced [6], a number of semiconductor-based terahertz metasurface modulators have been considered [7], [16]–[20] with widely ranging performance parameters. Perhaps the most convincing demonstration so far has been the double-channel heterostructure modulator [18] achieving modulation speed above 1 GHz and a modulation depth of 85%. Leaving important technical details aside, the above devices all derive their operation principle from the original work [6]. It involves a cut metal wire taking various shapes (e.g. a split-ring resonator or a dipole antenna) placed on top of a semiconductor, in which modulation occurs as a result of tuning the semiconductor conductivity beneath the gap, since a high conductivity effectively short-circuits the two parts.

Here we consider an alternative device concept whose main characteristic is that the tunable resonant element is buried
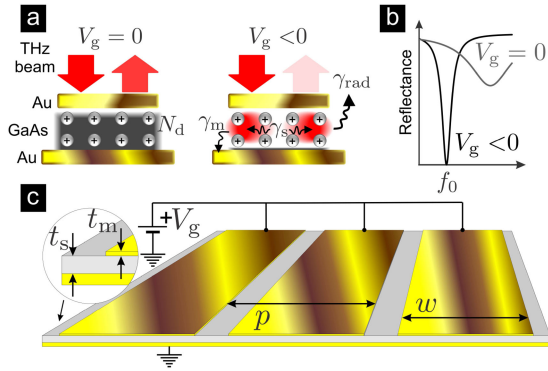
Fig. 1.   (a) Operation principle, (b) Typical bias-dependent reflectance spectra, (c) A section of the device shown in real scale (in the actual device, the strips are repeated periodically). The epitaxial GaAs layer is selectively n-doped beneath the strips.

into the semiconductor akin to the one recently used in electrically tunable infrared polaritonic metasurfaces [21]. It comprises a metal-semiconductor-metal cavity of deeply subwavelength thickness known for providing a substantial light-matter interaction enhancement [22]. Such cavities have recently been employed in electrical control of intersubband polaritons [23], terahertz [24], [25] and infrared quantum detectors [26] and vertical-external-cavity surface-emitting quantum cascade lasers [27], [28]. In contrast to the listed examples which all rely on AlGaAs quantum heterostructures, the active region in our case is simply a single n-doped epitaxial layer of GaAs forming a Schottky contact at the interface with the top metal layer, allowing for tuning the n-GaAs permittivity by applying a gate voltage.

II. OPERATION PRINCIPLE AND DEVICE GEOMETRY

The basic element of the device is a metal-semiconductor-metal cavity array depicted in Fig. 1(a). A Schottky junction is formed between the top electrode (gate) and the epitaxial semiconductor layer while the contact to the bottom electrode (ground) is ohmic. The gold and GaAs combination of materials is considered because its optical properties in metal-semiconductor-metal cavities [29] as well as the relevant Schottky [30], [31] and ohmic contact [32] characteristics are well documented, however a range of other materials may suffice as well. At zero bias, the electron concentration n_e in each cavity (gray shading) is considered equal to the fully ionized donor concentration N_d (small spheres). If the doping is very high, so that the plasma oscillation frequency ω_p is above the incoming field frequency, the Drude response will be fast enough to screen the external fields out of the cavities and the device will act as a mirror. Upon applying a sufficiently large reverse voltage, the depletion layer of the Schottky junction extends over the entire cavity which now supports a photonic mode with eigenfrequency $\omega_0 = 2\pi f_0$ and is characterized by a radiative decay rate γ_{rad} and a non-radiative decay rate γ_0, the latter being the sum of the rate of photon absorption in the metal γ_m and semiconductor γ_s. If the geometrical parameters of the cavity

are chosen appropriately [11], the critical coupling condition

$$\gamma_{rad} = \gamma_0, \tag{1}$$

may be reached, ensuring the total absorption of an externally incident terahertz beam. Therefore, by switching V_g, a large reflectance modulation may be achieved in a band of frequencies around f_0, as depicted in Fig. 1(b).

In fact, the analysis below shows that efficient modulation does not strictly require a sub-plasma frequency operation ($\omega_p/\omega_0 > 1$), as long as the free carriers are able to blueshift ω_0 enough. Formally, one may analyze the eigenfrequency $\omega_0(V_g)$ and decay rates $\gamma_m(V_g)$, $\gamma_s(V_g)$, $\gamma_{rad}(V_g)$ as functions of V_g. However, since the quantitative connection between such a dependence and the modulation efficiency is not straightforward, here a direct approach is adopted whereby the decay rates are analyzed only for fully depleted cavities after which the modulation efficiency is evaluated without further reference to them.

For convenience, here the simplest implementation of the described concept is considered, as depicted in realistic scale in Fig. 1(c). The device represents a periodic array of long rectangular strips of width w and pitch p, connected to a common potential V_g at the far end. It is operative for one polarization (across the strips) only, but polarization-insensitive variants [11] can be straightforwardly devised by replacing the strips with symmetrical patches (e.g. circular or square-shaped). Invoking the temporal coupled-mode theory (TCMT) formalism [33], [34], the complex reflection coefficient of metal-semiconductor-metal cavity arrays with fundamental optical modes in the terahertz range [22] can, to an excellent approximation, be written as [35]

$$r(\omega) = \frac{\omega - \omega_0 + i(\gamma_0 - \gamma_{rad})}{\omega - \omega_0 + i(\gamma_0 + \gamma_{rad})}. \tag{2}$$

We use the TCMT formalism in conjunction with rigorous numerical simulations (see Appendix IV), whereby the three parameters ω_0, γ_0 and γ_{rad} are extracted by fitting Eq. (2) to the numerically calculated $r(\omega)$. While useful in providing a simple way of parametrizing the optical response of the device, the real advantage of the TCMT formalism stems from the fact that γ_0 and γ_{rad} are physically meaningful quantities which can be related to the cavity geometry and eigenmode field distribution, thus facilitating the design of cavities with desired $r(\omega)$.

The process of identifying a geometry which yields a critically coupled optical mode at a desired frequency f_0 can be illustrated on the example of $f_0 = 1$ THz. According to Fig. 1(c), it involves deciding on values of three geometrical parameters, w, p and t_s. Here the gold strip thickness t_m is set to 0.3 μm instead of being considered as a free parameter because its exact value is insignificant, as long as it is much smaller than the wavelength but large enough to ensure optical opacity. The cavity width w is determined from the target f_0 because the fundamental optical mode is a transverse-magnetic standing wave [22] whose eigenfrequency is only weakly affected by changing t_s and p (see Figs. 2(a,b) below). A slight lateral spill of the standing wave fields beyond the strip edges implies that the half-wavelength in the semiconductor $\lambda_{0,GaAs}/2$ is slightly larger than w.
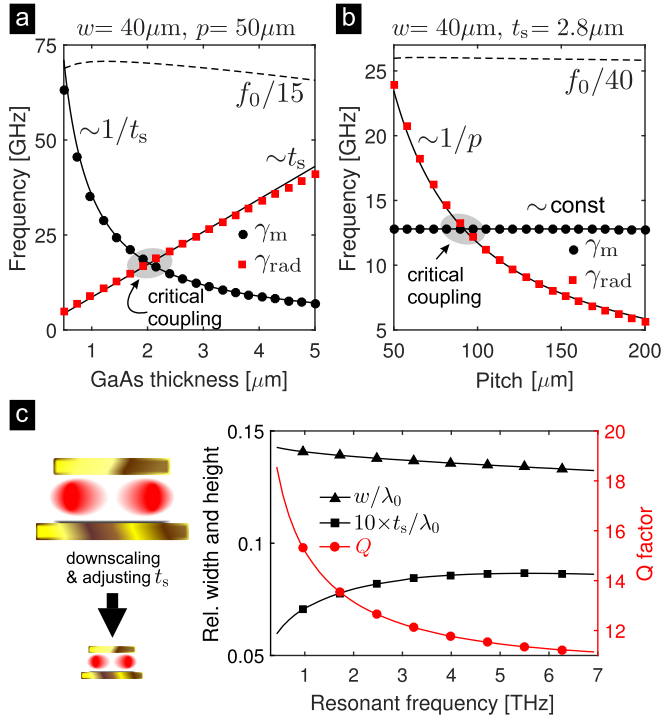
Fig. 2. TCMT parameters as a function of (a) semiconductor layer thickness, (b) pitch. (c) Geometrical parameters yielding critical coupling at full depletion (p is fixed at $1.25\,w$).

Assuming $n_{\mathrm{GaAs}} = 3.3$ at 1 THz, yields $\lambda_{0,\mathrm{GaAs}}/2 \approx 45.45\,\mu\mathrm{m}$, starting from which we easily find $w = 40\,\mu\mathrm{m}$ to yield $f_0 \approx 1$ THz.

To establish the role of GaAs thickness, in Fig. 2(a) we fix $p = 50\,\mu\mathrm{m}$ and plot the TCMT parameters as a function of t_s. Since the cavity is assumed to be fully depleted, the absorption rate in the semiconductor layer γ_s will be negligible while γ_0 becomes equal to the metal absorption rate γ_m plotted in Fig. 2(a). The numerically calculated values of γ_m and γ_rad, represented by circles and squares respectively, are seen to fit very well to a t_s^{-1} and t_s curve (solid lines). The origin of the observed scaling of γ_m and γ_rad has been examined in Appendix C of [11] for the mathematically analogous case of circular patch cavities filled with a liquid crystal. This scaling follows from a straightforward consideration of how the modal fields are redistributed when the cavity height is changed, with the only subtlety being the eigenmode field normalization. Here we limit the discussion to noting that the observed trend is what one would expect: compressing the eigenmode into a thinner cavity causes the fields to penetrate more into the cladding on top and bottom, implying higher absorption in the metal and, therefore, the increase of γ_m with decreasing t_s. On the other hand, the radiation loss of a cavity must be proportional to the fraction of its surface not covered by metal and since the latter is proportional to t_s, we infer that γ_rad should decrease as t_s is decreased. In Fig. 2(a), adjusting t_s alone is found to be sufficient for achieving critical coupling, seen as the crossing of γ_m and γ_rad curves in Fig. 2(a). In fact, since two curves proportional to $\sim t_\mathrm{s}^{-1}$ and $\sim t_\mathrm{s}$ always have an intersection, we infer that adjusting t_s alone will be sufficient to fulfill Eq. (1) for any reasonable cavity. Meanwhile, the dashed

line depicting $f_0/15$ shows that f_0 undergoes only a small relative variation over the considered t_s interval, meaning that once t_s is fixed, w may be readjusted to set f_0 exactly to the desired value.

The effect of changing the pitch is considered in Fig. 2(b) where t_s is set to a representative value of $2.8\,\mu\mathrm{m}$. For p below $50\,\mu\mathrm{m}$, the strips spacing becomes too small, leading to the hybridization of adjacent cavity modes and their delocalization [29]. At the higher end, p is limited by the requirement that only the zeroth diffraction order is propagative. The calculated γ_m datapoints (circles) fit very well to the constant line. This follows from the fact that once adjacent cavities become sufficiently separated, the field of their eigenmodes becomes identical to the field of an isolated cavity. Since γ_m is determined by field penetration into the metal, it cannot depend on p. On the other hand, γ_rad is seen to decrease rapidly with p, which might appear surprising because it implies that the power emitted by each cavity is affected by p. This, however, is a natural consequence of the fact that the cavities represent an array of mutually coherent emitters. In Appendix IV we give a short proof that $\gamma_\mathrm{rad} \sim p^{-1}$ approximately. This is confirmed in Fig. 2(b), with the $\sim p^{-1}$ fit (full line) matching the numerical data very well over the entire considered range of p. In this case, the dashed line representing $f_0/40$ shows that f_0 is virtually independent of p. Since γ_m remains invariant, there will be cases in which changing p alone will not be sufficient to reach critical coupling. For example, cavities with higher aspect ratios (t_s/w) will be highly overcoupled $\gamma_\mathrm{m} \ll \gamma_\mathrm{rad}$, so even at $p \approx \lambda_0$, γ_rad might still be substantially larger than γ_m. The reverse problem occurs with very small aspect ratios (highly undercoupled cavities), as in that case even for $p \approx w$, γ_rad might still be well below γ_m.

Now, consider a cavity with eigenfrequency ω_0 in which Eq. (1) is fulfilled for given t_s and p. If we decrease p, in order to retain critical coupling, we also have to decrease t_s. Since p does not affect it, γ_m is modified only because t_s was decreased, meaning that we end up with a cavity having both γ_m and γ_rad larger than in the initial cavity. Therefore, decreasing p increases the bandwidth $\Delta f = (\gamma_\mathrm{m} + \gamma_\mathrm{rad})/\pi$ of the device. A shorter p is also important as it allows smaller values for t_s, translating into lower operation voltage and higher speed. For these reasons, in what follows we set the pitch to $p = 1.25\,w$, (a value close to the onset of cavity mode hybridization) and adjust t_s until critical coupling is reached.

The above procedure may be repeated for an arbitrary frequency f_0. However, in order to find w and t_s that ensure critical coupling over the entire terahertz spectrum, it is more straightforward to employ geometrical scaling. Downscaling all geometrical parameters of a cavity array by a factor, upscales the TCMT parameters approximately by the same factor. However, small deviations from linear scaling due to material dispersion result in a cavity that does not meet the critical coupling condition exactly [35], meaning that t_s will have to be slightly adjusted to restore it. Figure 2(c) shows the values of w and t_s that yield critically coupled cavities, for resonant frequencies ranging from 0.3 THz up to 7 THz, beyond which GaAs cannot be used for this purpose, due to its optical phonons and onset of the reststrahlen band [29]. The plotted quantities are actually
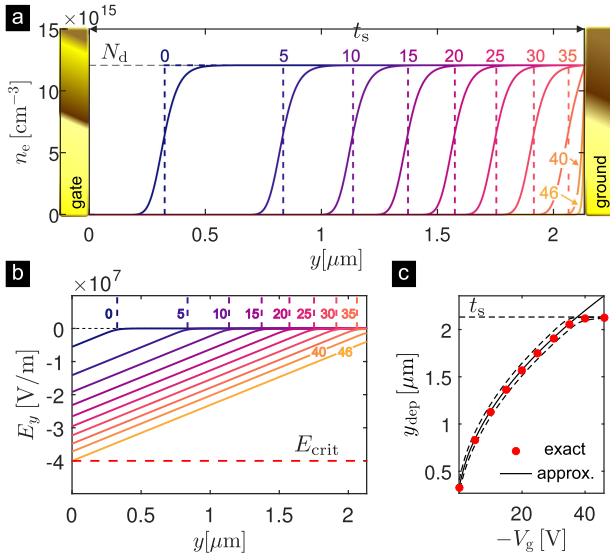
Fig. 3. Schottky junction under reverse bias showing the depletion layer reach-through effect. The profiles are drawn along the symmetry axis of a cavity with $p = 52.72\,\mu\text{m}$, $w = 42.18\,\mu\text{m}$, $t_\text{s} = 2.13\,\mu\text{m}$, $t_\text{m} = 0.3\,\mu\text{m}$ and $N_\text{d} = 1.2 \times 10^{16}\,\text{cm}^{-3}$, designed to operate at 1 THz. (a) Electron concentration (solid line - rigorous model, dashed - FDA) parametrized by $-V_\text{g}$, (b) Corresponding electric field profiles, (c) Depletion layer width with dashed lines indicating the transition width, defined as location where n_e reaches the $0.1\,N_\text{d}$ and $0.9\,N_\text{d}$ marks.

normalized to the free-space wavelength λ_0, demonstrating the mentioned deviation from the linear scaling law. For the same reason, the Q factor $Q = \omega_0/2(\gamma_\text{m} + \gamma_\text{rad}) = \omega_0/4\gamma_\text{rad}$ is seen to decrease slowly going towards higher frequencies.

III. DOPING CONCENTRATION AND PERFORMANCE ANALYSIS

A nonzero concentration $n_\text{e}(\mathbf{r})$ of free electrons in the cavity introduces a Drude term to the optical permittivity ε_opt of GaAs. The total permittivity becomes inhomogeneous and is given by [36], [37]

$$\varepsilon_\text{s}(\mathbf{r}, \omega) = \varepsilon_\text{opt}\left(1 - \frac{\omega_\text{p}^2(\mathbf{r})}{\omega(\omega + \text{i}\gamma_\text{c})}\right), \qquad (3)$$

where the plasma frequency ω_p and intraband electron collision rate γ_c read

$$\omega_\text{p}(\mathbf{r}) = \sqrt{\frac{n_\text{e}(\mathbf{r})q^2}{\varepsilon_\text{opt}\varepsilon_0 m_c^*}}, \qquad \gamma_\text{c} = \frac{q}{\mu_n m_c^*}, \qquad (4)$$

while the realistic doping-dependent conduction band electron mobility μ_n is evaluated following [38]. At zero gate bias, $n_\text{e} \approx N_\text{d}$ in the entire cavity, except in a thin depletion layer beneath the gate. It is thus clear that the higher N_d is, the greater the voltage-induced change of permittivity will be, resulting in more effective modulation. The upper limit on N_d is set by the requirement that the cavity can be fully depleted before the avalanche breakdown of the Schottky junction.

To estimate the highest possible value of N_d, we consider the characteristic Schottky junction behavior under reverse bias illustrated in Fig. 3(a), where $n_\text{e}(\mathbf{r})$ is plotted along the vertical

axis going through the center of the cavity, with $-V_\text{g}$ as a parameter. The profiles drawn by solid lines are obtained using a rigorous solid-state physics framework based on a majority-carrier solution scheme (for details see Appendix B). For comparison, the step-like n_e profiles of the full depletion approximation (FDA) [39] are indicated by dashed lines. Apart from being abrupt, the FDA curves are a rather good match to the rigorous ones. This is demonstrated in Fig. 3(c) where the depletion layer width y_dep, defined as the distance from the junction at which n_e reaches $0.5\,N_\text{d}$, is drawn against $-V_\text{g}$ for both the rigorous (circular datapoints) and FDA model (solid line), the latter being given by

$$y_\text{dep} = \sqrt{\frac{2\varepsilon_\text{stat}\varepsilon_0(\psi_\text{bi} - V_\text{g})}{qN_\text{d}}}, \qquad (5)$$

where $\psi_\text{bi} = 0.9\,\text{V}$ is the Schottky barrier height of the n-GaAs/Au interface, q the elementary charge and $\varepsilon_\text{stat} = 12.9$ the electrostatic dielectric permittivity of GaAs. With increasing reverse voltage, the depletion layer expands until it reaches the ground gold layer. In itself, the reach-through phenomenon is not associated with critical behavior [40], as a further increase of $-V_\text{g}$ merely causes a charge buildup on the gold side of the contact. To simplify the evaluation of the breakdown voltage, we employ the commonly-used critical field approximation [40], whereby the avalanche breakdown is assumed to occur once the electric field passes a critical value E_crit. The latter is dependent on the doping concentration, but for simplicity we take $E_\text{crit} = 4 \times 10^7\,\text{V/m}$ as a representative value [30] for the range of N_d considered in this work.

Neglecting the effect of strip edges, the only nonzero component of the static electric field is E_y and it reaches its highest value at the Schottky junction. According to FDA, $-E_\text{max} = qN_\text{d}y_\text{dep}/\varepsilon_\text{stat}\varepsilon_0$, from which we find the highest doping for $E_\text{max} = E_\text{crit}$ when $y_\text{dep} = t_\text{s}$

$$N_\text{d,max} = \frac{\varepsilon_\text{stat}\varepsilon_0 E_\text{crit}}{qt_\text{s}}. \qquad (6)$$

This value, however, is arrived at neglecting the tail of the actual n_e profile. To see this, note that in the Fig. 3 example, FDA predicts $-V_\text{g} = 37.48\,\text{V}$ as the reach-through voltage, while the actual n_e profiles in Fig. 3 show that even at $-V_\text{g} = 40\,\text{V}$, there is still a non-negligible concentration of electrons in the cavity. To reduce the remanent n_e at the ground contact, the cavity should be biased slightly above the reach-through voltage and to achieve this without avalanche breakdown, a slightly lower doping concentration is used, $N_\text{d} = 0.9 \times N_\text{d,max}$. The cavity shown in Fig. 3 has $t_\text{s} = 2.13\,\mu\text{m}$, giving $N_\text{d,max} = 1.34 \times 10^{16}\,\text{cm}^{-3}$, so the actual value used is $N_\text{d} = 1.2 \times 10^{16}\,\text{cm}^{-3}$. The numerically calculated electric field profiles $E_y(y)$ are shown in Fig. 3(b). On this scale, the latter virtually overlap with the field profiles predicted by FDA. From these, we find that the breakdown occurs around $-V_\text{g} \approx 46\,\text{V}$.

As a proof of concept, in Fig. 4 we analyze the switching of a device designed to operate at 1 THz. The first four panels, (a)–(d), depict $n_\text{e}(\mathbf{r})$, the normalized terahertz field magnitude $|\mathbf{E}(\mathbf{r})|/E_0$ excited by an incoming linearly polarized plane wave
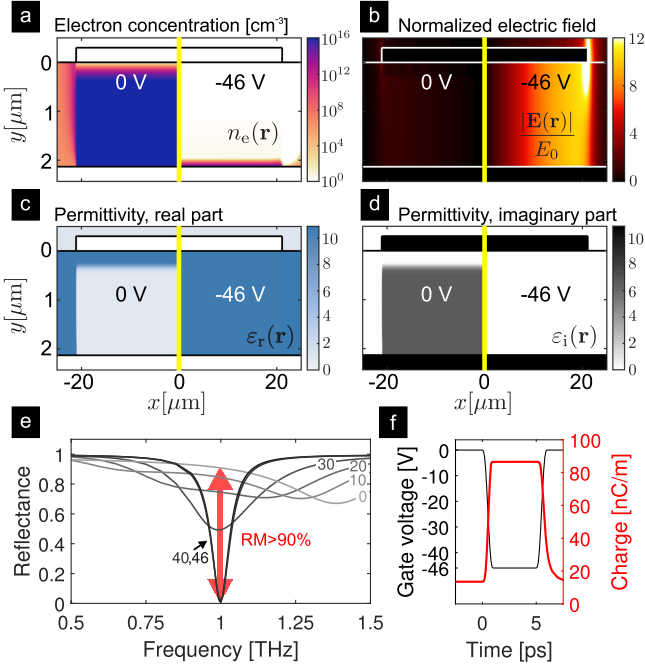
Fig. 4. Proof of concept simulation for the 1 THz device (for details, see Appendix IV and B). (a) Electron concentration, (b) High-frequency electric field distribution resulting from illumination at 1 THz, (c) Real and (d) imaginary part of permittivity at 1 THz. For better contrast, the range used in colormaps of panels (b)–(d) is saturated by cutting out the high electric field values at strip corners in (b), and gold permittivity values in (c) and (d). (e) Reflectance spectra parametrized by $-V_\mathrm{g}$, (f) Transient response of the total charge in cavity to a 5 ps reverse bias pulse. (All the colormaps used in this article have been produced by a source code kindly provided by Peter Kovesi, see [41].)

with field amplitude E_0 falling perpendicularly onto the strip array, as well as the real $\varepsilon_\mathrm{r}(\mathbf{r})$ and imaginary $\varepsilon_\mathrm{i}(\mathbf{r})$ parts of $\varepsilon_\mathrm{s}(\mathbf{r})$ given by Eq. (3). For conciseness in illustrating the switching effect of the gate voltage, we exploit the mirror symmetry of the problem. Noting that the calculated distributions exhibit this symmetry, in Figs. 4(a)–(d) we use the left half of the unit cell to plot the quantities calculated at $V_\mathrm{g} = 0\,\mathrm{V}$ while those corresponding to $V_\mathrm{g} = -46\,\mathrm{V}$ are shown in the right half.

The depleted cavity ($V_\mathrm{g} = -46\,\mathrm{V}$) is seen to be virtually free of electrons, except at the bottom contact (note the logarithmic scale of the colormap). Consequently, ε_s is very close to ε_opt practically everywhere, thus justifying the assumptions made in designing the cavities in previous section. At the microscopic scale, the efficiency of the device is demonstrated by the huge difference in the electromagnetic field intensity evident from Fig. 4(b), where the field is seen to hardly penetrate the cavity at $V_\mathrm{g} = 0\,\mathrm{V}$, while at $V_\mathrm{g} = -46\,\mathrm{V}$ the field enhancement in the cavity is around 10.

Figure 4(e) shows the calculated reflectance spectra $R(\omega) = |r(\omega)|^2$ parametrized by $-V_\mathrm{g}$. At f_0 we have $R(\omega_0; 0\,\mathrm{V}) \approx 90\%$ and $R(\omega_0; -46\,\mathrm{V}) \approx 0\%$. Introducing the reflectance modulation (RM), and insertion loss (IL) as

$$\mathrm{RM} = R(\omega_0; 0\,\mathrm{V}) - R(\omega_0; V_\mathrm{g,min}),$$
$$\mathrm{IL} = 1 - R(\omega_0; 0\,\mathrm{V}), \qquad (7)$$

with $V_\mathrm{g,min}$ denoting the avalanche breakdown voltage, we find RM and IL to be approximately 90% and 10%, respectively, which is excellent for solid-state terahertz modulators [5]. Since $R(\omega_0; V_\mathrm{g,min}) \approx 0\%$ by design, the proposed modulator will have a very high (theoretically infinite) extinction ratio which will in practice be limited by device fabrication tolerance. Previously considered Schottky junction based modulators [6], [7] used similar doping concentrations and, consequently, similar gate-induced permittivity changes. The origin of the increased modulation efficiency of the proposed device is the almost complete overlap of the resonant terahertz fields with the region in which ε_s is modified, which is known to be proportional to the change in resonant frequency and decay rates [42]. Finally, we note that the fact that the 40 V and 46 V reflectance curves almost overlap, indicates that the critical coupling effect is rather robust to the presence of the remanent electron concentration at the bottom electrode. It further implies that meeting the $\gamma_0 \approx \gamma_\mathrm{rad}$ condition reasonably well should not be particularly difficult in practice, especially considering that various post-processing steps might also help [34].

Switching times in the subnanosecond range are among the key advantages of solid-state terahertz modulators over those based on liquid crystals, phase change or thermal tuning [8] where the switching time is in the millisecond range at best [11]. In recently demonstrated semiconductor-based terahertz modulators [16], [21] with $\sim 10\,\mathrm{MHz}$ operating frequencies, the speed has been found to be limited not by the inherent response time of the device but by the driving circuit. More recently, however, modulation above 1 GHz has been demonstrated [18]. Therefore, with driving circuits being perfected, the inherent switching time of terahertz modulators might become the limiting factor.

An important aspect of the proposed device is its very high intrinsic speed, as a consequence of the ultrathin active region. This is demonstrated by numerical simulations of the cavity charge $Q(t)$ (per unit length along the strip axis) transient upon applying a rectangular pulse of reverse bias shown in Fig. 4(f). The $-V_\mathrm{g}(t)$ pulse duration is set to 5 ps, with 0.5 ps 10%–90% rise and fall times. The corresponding rise time of $Q(t)$ is well below 1 ps, while the fall time is somewhat longer and calculated to be around 1 ps.

Such a short intrinsic response time originates from the very small distance t_s between the contacts, which is well below $\lambda_0/100$ as shown in Fig. 2(c). Here, as well as in [21], it is achieved by using a deeply-subwavelength cavity, while in [16], [18] the small distance between the electrodes is achieved at the expense of device complexity. Devices with laterally arranged contacts are likely to have a much longer intrinsic response time, increasing with the distance between the electrodes, as demonstrated in [43].

Having seen that the proposed device performs very well at $f_0 = 1\,\mathrm{THz}$, we now examine how changing f_0 affects the modulator performance. The above procedure for determining the appropriate donor concentration in conjuction with cavity parameters shown in Fig. 2(c) can be repeated to obtain the N_d values shown in Fig. 5(a). The corresponding inverse gate voltages required for full depletion are shown in panel (b), while
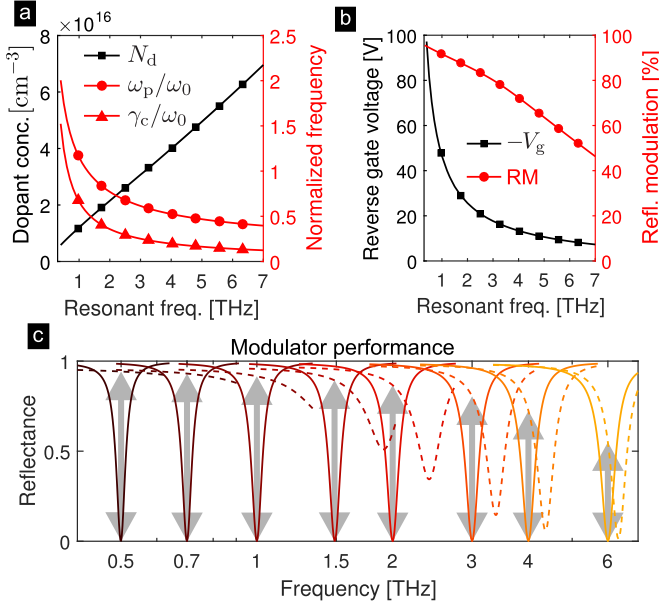
Fig. 5.　Device parameters for operation across the terahertz spectrum, to be combined with geometrical parameters in Fig. 2(c). (a) Doping and normalized Drude parameters, (b) Gate voltage required for full cavity depletion and reflectance modulation. (c) Characteristic reflectance spectra for devices operating across the terahertz spectrum (solid line - biased, dashed line - no bias). The vertical gray arrows indicate the reflectance modulation.

the reflectance spectra for eight modulators with f_0 ranging over the terahertz spectrum are depicted in (c). In the latter, solid lines depict $R(\omega)$ in fully depleted state and the dashed lines the zero bias state. Note that the horizontal axis in Fig. 5(c) is shown in logarithmic scale, in order to better resolve all the depicted spectra. The thick vertical gray arrows indicate RM for each of the depicted modulators.

Extracting RM for spectra at various f_0, we obtain the curve in Fig. 5(b) showing the gradual decline of RM from more than 95% at 0.3 THz to around 46% at 7 THz. The reason for such behavior can be understood by noting that, because the electrostatic field at the junction must be less than E_{crit}, the surface density σ of the total charge in the cavity remains invariant with respect to f_0 and equals $N_d t_s$. This implies that as t_s is decreased, N_d and ω_p increase, but so that ω_p scales (roughly) as $\sim f_0^{1/2}$. Meanwhile, the modulation efficiency is determined by the change of permittivity in the cavity which can be effected by bias, which is equal to the Drude term contribution and proportional to ω_p/ω_0. The latter is drawn in Fig. 5(a) and, as expected, found to scale (roughly) as $\sim f_0^{-1/2}$.

Another feature arising at high f_0 is the change of the character of the cavity tuning. At 1 THz, the Drude contribution to ε_s has comparable real and imaginary parts, which is apparent in Fig. 4(c) and (d) and a consequence of the ratio γ_c/ω_0 being close to unity. Plotting this ratio in Fig. 5(a), we find that it also decreases at higher f_0, meaning that the voltage-induced change of permittivity becomes mainly real. The imaginary part of ε_s implies absorption in the semiconductor, introducing the semiconductor absorption term γ_s to the nonradiative decay rate. In terms of the reflectance spectra, this means that the cavity designed to be critically coupled at full depletion, is driven further

away from this condition at zero bias and has a significant amount of reflection at resonance (slightly shifted though). Such a behavior is nicely seen in the Fig. 4(e) plot. As f_0 approaches 7 THz, this changes significantly, as γ_s at zero bias remains rather small so the reflectance at cavity resonance remains close to zero, as seen in the $f_0 = 6$ THz modulator example in Fig. 5(c).

IV. SUMMARY

This article proposes a terahertz electro-optic modulator comprising an array of metal-semiconductor-metal cavities of deeply subwavelength thickness. The modulator operates by depleting the carriers from the doped semiconductor layer buried beneath a Schottky junction. Combining the extremely high terahertz field confinement with a reversely-biased Schottky junction in the reach-through regime, allows for a modulation performance that is predicted to match or even surpass existing devices. The proof of concept analysis presented for the modulator operating at 1 THz, based on a rigorous multiphysics framework incorporating Maxwell equations for terahertz waves and the drift-diffusion model describing carriers in the cavity, predicts an insertion loss around 10%, reflectance modulation of 90% and a theoretically infinite extinction ratio associated with cavities designed to work in the critically coupled regime. The performance is found to decrease in modulators designed to operate in the higher end of the terahertz spectrum, reaching insertion loss of 54% and reflectance modulation falling to 46% at 7 THz. This decline has been shown to be an inherent characteristic of the Drude response in which the plasma frequency scales as the square root of carrier concentration. In addition to forging strong light-matter interaction, the ultrathin cavity has been shown to allow for ultrafast intrinsic response times, which have been shown to be in the picosecond range.

APPENDIX A
LIGHT SCATTERING ANALYSIS

To obtain $r(\omega)$, the Maxwell equations are solved in frequency domain using the scattered field formulation with the background field $\mathbf{E}_b(\mathbf{r})$ being the sum of the incoming and the plane wave reflected from the opaque back metal electrode (normal incidence is assumed), and the scattered field $\mathbf{E}_s(\mathbf{r})$ being induced by the presence of the inhomogeneously doped semiconductor and the array of metal strips. The problem is represented by a two-dimensional model with a rectangular simulation domain, where the side boundaries are related with periodic conditions on $\mathbf{E}_s(\mathbf{r})$, while the air superstrate above the structure is represented by a few-wavelength-thick domain terminated by a perfectly matched layer. The solution at both the top and bottom boundaries is set by the zero-field (Dirichlet) boundary condition. $r(\omega)$ is obtained from $\mathbf{E}_s(\mathbf{r})$ as the complex coefficient of the zeroth diffraction order (the only propagating one in all considered cases).

The gold permittivity $\varepsilon_m(\omega)$ was assumed to have the Drude form

$$\varepsilon_m(\omega) = 1 - \frac{\omega_{p,\mathrm{Au}}^2}{\omega(\omega + i\gamma_{c,\mathrm{Au}})}, \qquad (8)$$

with the gold plasma $\omega_\mathrm{p} = 1.37 \times 10^{16}$ rad/s and collision frequency $\gamma_{\mathrm{c,Au}} = 4.05 \times 10^{13}$ rad/s taken from [44].

The reasoning in the article relies on the concept of a leaky eigenmode whose interaction with the environment is quantified by its radiative γ_rad and non-radiative γ_0 decay rates. These may be introduced in an intuitive manner by assuming that both the dissipative effects (absorption in metal and semiconductor) and the coupling between the eigenmode and environment are weak enough to be treated perturbatively. In that case, the eigenmode energy U exhibits an exponential temporal decay with a decay rate equal to $\gamma_\mathrm{rad} + \gamma_0$, whereby the total loss power $P_\mathrm{loss} = P_\mathrm{rad} + P_0$ is broken down into the radiation P_rad and absorption P_0 terms so that $\gamma_\mathrm{rad} = P_\mathrm{rad}/2U$ and $\gamma_0 = P_0/2U$. A deeper analysis employing TCMT [45] reveals a general connection between the decay rates of a weakly coupled resonant system and its scattering matrix [46] which, in case of a single-port system with one eigenmode, implies Eq. (2). For sufficiently high quality factors, the TCMT parameters are directly related to the complex eigenfrequency $\tilde{\omega} = \omega_0 + i\omega_\mathrm{I}$ of the associated cavity quasi-normal mode [47], with $\omega_\mathrm{I} = \gamma_0 + \gamma_\mathrm{rad}$. As TCMT itself is not the focus of this work, the reader is referred to [35] and [11] for further details on the formalism in the current context.

To explain the dependence of γ_rad on p, let us assume that the cavity array eigenmode is excited and allowed to decay both radiatively and via absorption, and let $H(x) = H(x, y_0)$ denote the magnetic field phasor (only the z-component is nonzero) along a horizontal line $y = y_0$ chosen at an arbitrary height above the cavity array. Assuming the spacing between adjacent cavities is large enough, the total field $H(x)$ may be represented as a sum of fields emitted by individual cavities, $H(x) = \sum_{n=-\infty}^{\infty} H_\mathrm{uc}(x - np)$, where $H_\mathrm{uc}(x) = H_\mathrm{uc}(x, y_0)$ is the magnetic field profile of an eigenmode of a single cavity centered at $x = 0$. Since $H(x)$ is periodic in x, it can be expanded into a Fourier series $H(x) = \sum_{m=-\infty}^{\infty} H^{(m)} \exp(im\Delta k)$ where $\Delta k = 2\pi/p$ and m is the diffraction order. The dependence of $H^{(m)}$ on p is seen after introducing the Fourier transform of the single-cavity field by $h_\mathrm{uc}(k) = \int_{-\infty}^{\infty} H_\mathrm{uc}(x) \exp(-ikx)\mathrm{d}x$ and noting that $H^{(m)} = h_\mathrm{uc}(m\Delta k)/p$, while $h_\mathrm{uc}(m\Delta k)$ is obviously independent on p. In the considered spectral range, only the zeroth diffraction order is propagative so the radiated power flux through a unit cell equals $P_\mathrm{uc,rad} = z_0 p |H^{(0)}|^2/2 = z_0 |h_\mathrm{uc}(0)|^2/2p$, with z_0 denoting the free-space impedance. Finally, denoting by U_uc the energy contained in one cavity, and by N the total number of cavities in the array (formally $N \to \infty$) we have

$$\gamma_\mathrm{rad} = \frac{P_\mathrm{rad}}{2U} = \frac{N P_\mathrm{uc,rad}}{2N U_\mathrm{uc}} = \frac{z_0 |h_\mathrm{uc}(0)|^2}{4 U_\mathrm{uc}} p^{-1}, \qquad (9)$$

thus proving the $\sim p^{-1}$ scaling stated in the article.

APPENDIX B
SOLID-STATE ANALYSIS

The gate bias effect on the carrier distribution is described using a rigorous solid-state physics framework based on a majority-carrier solution scheme, consisting in the conservation

Parameter	GaAs
Static permittivity, $\varepsilon_\mathrm{stat}$	12.90
High-frequency permittivity, ε_opt	10.89
Effective electron mass, m_c^*/m_0	0.067
Energy band gap, E_g (eV)	1.424
Electron affinity, χ_0 (eV)	4.07
Conduction band density of states, N_c (cm^{-3})	4.7×10^{17}
Valence band density of states, N_v (cm^{-3})	9.0×10^{18}

law for charge (Poisson equation) and the time-dependent current continuity equations [48], [49]. The current density is expressed by the drift-diffusion expressions, while the simplified Maxwell-Boltzmann energy distribution is used for the carrier concentration, allowed by the moderate doping level of the n-GaAs cavity. The Schottky contact is described as a source/sink for carriers, treated as a surface recombination mechanism [50]. The Schottky barrier height of the n-GaAs/Au interface is considered 0.9 V, while the effective Richardson's constant for the n-doped GaAs is set equal to 4.4 Acm^{-2}K^{-2} [39]. The lateral intrinsic GaAs sections are interfaced to the central n-GaAs (under the strips) using quasi-Fermi level continuity boundary conditions. The resulting system of partial differential equations is set to additionally satisfy insulating conditions at the external metamaterial unit-cell boundaries and the thermodynamic equilibrium at the back contact, considered ideal ohmic. It is highlighted that, even though both contacts can be indiscriminately represented as Au layers from an electromagnetic standpoint, suitable Au-based alloys should be used in practice to ensure ohmic conditions at the back contact [32], having, though, marginal effect on the electromagnetic analysis.

The GaAs semiconductor parameters are listed in Table I, while the carrier mobility is calculated using [38]. The Au workfunction is set equal to 5.1 eV.

REFERENCES

[1] M. Tonouchi, "Cutting-edge terahertz technology," *Nature Photon.*, vol. 1, pp. 97–105, 2007.

[2] D. M. Mittleman, "Perspective: Terahertz science and technology," *J. Appl. Phys.*, vol. 122, no. 23, 2017, Art. no. 230901.

[3] R. Kersting, G. Strasser, and K. Unterrainer, "Terahertz phase modulator," *Electron. Lett.*, vol. 36, no. 13, pp. 1156–1158, Jun. 2000.

[4] T. Kleine-Ostmann, P. Dawson, K. Pierz, G. Hein, and M. Koch, "Room-temperature operation of an electrically driven terahertz modulator," *Appl. Phys. Lett.*, vol. 84, no. 18, pp. 3555–3557, 2004.

[5] R. Degl'Innocenti, S. J. Kindness, H. E. Beere, and D. A. Ritchie, "All-integrated terahertz modulators," *Nanophotonics*, vol. 7, pp. 127–144, 2018.

[6] H.-T. Chen *et al.*, "Active terahertz metamaterial devices," *Nature*, vol. 444, pp. 597–600, 2006.

[7] H.-T. Chen *et al.*, "A metamaterial solid-state terahertz phase modulator," *Nature Photon.*, vol. 3, pp. 148–151, 2009.

[8] M. Rahm, J.-S. Li, and W. J. Padilla, "THz wave modulators: A brief review on different modulation techniques," *J. Infrared Millimeter Terahertz Waves*, vol. 34, no. 1, pp. 1–27, 2013.

[9] J. Yoon *et al.*, "GaAs photovoltaics and optoelectronics using releasable multilayer epitaxial assemblies," *Nature*, vol. 465, pp. 329–334, 2010.

[10] D. Shrekenhamer, W.-C. Chen, and W. J. Padilla, "Liquid crystal tunable metamaterial absorber," *Phys. Rev. Lett.*, vol. 110, Apr. 2013, Art. no. 177403.

[11] G. Isić, B. Vasić, D. C. Zografopoulos, R. Beccherelli, and R. Gajić, "Electrically tunable critically coupled terahertz metamaterial absorber based on nematic liquid crystals," *Phys. Rev. Appl.*, vol. 3, Jun. 2015, Art. no. 064007.

[12] B. Vasić, D. C. Zografopoulos, G. Isić, R. Beccherelli, and R. Gajić, "Electrically tunable terahertz polarization converter based on overcoupled metal-isolator-metal metamaterials infiltrated with liquid crystals," *Nanotechnology*, vol. 28, no. 12, 2017, Art. no. 124002.

[13] B. Sensale-Rodriguez *et al.*, "Extraordinary control of terahertz beam reflectance in graphene electro-absorption modulators," *Nano Lett.*, vol. 12, no. 9, pp. 4518–4522, 2012.

[14] W. Gao *et al.*, "High-contrast terahertz wave modulation by gated graphene enhanced by extraordinary transmission through ring apertures," *Nano Lett.*, vol. 14, no. 3, pp. 1242–1248, 2014.

[15] S.-F. Shi *et al.*, "Optimizing broadband terahertz modulation with hybrid graphene/metasurface structures," *Nano Lett.*, vol. 15, no. 1, pp. 372–377, 2015.

[16] D. Shrekenhamer *et al.*, "High speed terahertz modulation from metamaterials with embedded high electron mobility transistors," *Opt. Express*, vol. 19, no. 10, pp. 9968–9975, May 2011.

[17] N. Karl *et al.*, "An electrically driven terahertz metamaterial diffractive modulator with more than 20 dB of dynamic range," *Appl. Phys. Lett.*, vol. 104, no. 9, 2014, Art. no. 091115.

[18] Y. Zhang *et al.*, "Gbps terahertz external modulator based on a composite metamaterial with a double-channel heterostructure," *Nano Lett.*, vol. 15, no. 5, pp. 3501–3506, 2015.

[19] M. T. Nouman *et al.*, "Terahertz modulator based on metamaterials integrated with metal-semiconductor-metal varactors," *Sci. Rep.*, vol. 6, 2016, Art. no. 26452.

[20] Z. Zhou, S. Wang, Y. Yu, Y. Chen, and L. Feng, "High performance metamaterials-high electron mobility transistors integrated terahertz modulator," *Opt. Express*, vol. 25, no. 15, pp. 17832–17840, Jul. 2017.

[21] J. Lee *et al.*, "Ultrafast electrically tunable polaritonic metasurfaces," *Adv. Opt. Mater.*, vol. 2, no. 11, pp. 1057–1063, 2014.

[22] Y. Todorov *et al.*, "Strong light-matter coupling in subwavelength metal-dielectric microcavities at terahertz frequencies," *Phys. Rev. Lett.*, vol. 102, May 2009, Art. no. 186402.

[23] A. A. Anappara, A. Tredicucci, G. Biasiol, and L. Sorba, "Electrical control of polariton coupling in intersubband microcavities," *Appl. Phys. Lett.*, vol. 87, no. 5, 2005, Art. no. 051105.

[24] A. Benz *et al.*, "Resonant metamaterial detectors based on THz quantum-cascade structures," *Sci. Rep.*, vol. 4, 2014, Art. no. 4269.

[25] D. Palaferri *et al.*, "Patch antenna terahertz photodetectors," *Appl. Phys. Lett.*, vol. 106, no. 16, 2015, Art. no. 161102.

[26] D. Palaferri *et al.*, "Ultra-subwavelength resonators for high temperature high performance quantum detectors," *New J. Phys.*, vol. 18, no. 11, 2016, Art. no. 113016.

[27] L. Xu *et al.*, "Terahertz metasurface quantum-cascade VECSELs: Theory and performance," *IEEE J. Sel. Topics Quantum Electron.*, vol. 23, no. 6, pp. 1–12, Nov. 2017.

[28] L. Xu *et al.*, "Metasurface quantum-cascade laser with electrically switchable polarization," *Optica*, vol. 4, no. 4, pp. 468–475, Apr. 2017.

[29] Y. Todorov *et al.*, "Optical properties of metal-dielectric-metal microcavities in the THz frequency range," *Opt. Express*, vol. 18, no. 13, pp. 13886–13907, Jun. 2010.

[30] B. J. Baliga, R. Ehle, J. R. Shealy, and W. Garwacki, "Breakdown characteristics of gallium arsenide," *IEEE Electron Device Lett.*, vol. EDL-2, no. 11, pp. 302–304, Nov. 1981.

[31] M. Hudait and S. Krupanidhi, "Breakdown characteristics of MOVPE grown Si-doped GaAs Schottky diodes," *Solid-State Electron.*, vol. 43, no. 12, pp. 2135–2139, 1999.

[32] A. Baca, F. Ren, J. Zolper, R. Briggs, and S. Pearton, "A survey of ohmic contacts to III-V compound semiconductors," *Thin Solid Films*, vol. 308/309, pp. 599–606, 1997.

[33] S. Fan, W. Suh, and J. D. Joannopoulos, "Temporal coupled-mode theory for the Fano resonance in optical resonators," *J. Opt. Soc. Amer. A*, vol. 20, no. 3, pp. 569–572, Mar. 2003.

[34] J.-M. Manceau, S. Zanotto, I. Sagnes, G. Beaudoin, and R. Colombelli, "Optical critical coupling into highly confining metal-insulator-metal resonators," *Appl. Phys. Lett.*, vol. 103, no. 9, 2013, Art. no. 091110.

[35] G. Isić, and R. Gajić, "Geometrical scaling and modal decay rates in periodic arrays of deeply subwavelength terahertz resonators," *J. Appl. Phys.*, vol. 116, no. 23, 2014, Art. no. 233103.

[36] R. Ulbricht, E. Hendry, J. Shan, T. F. Heinz, and M. Bonn, "Carrier dynamics in semiconductors studied with time-resolved terahertz spectroscopy," *Rev. Mod. Phys.*, vol. 83, pp. 543–586, Jun. 2011.

[37] D. Lockwood, G. Yu, and N. Rowell, "Optical phonon frequencies and damping in AlAs, GaP, GaAs, InP, InAs and InSb studied by oblique incidence infrared spectroscopy," *Solid State Commun.*, vol. 136, no. 7, pp. 404–409, 2005.

[38] M. Sotoodeh, A. H. Khalid, and A. A. Rezazadeh, "Empirical low-field mobility model for III-V compounds applicable in device simulation codes," *J. Appl. Phys.*, vol. 87, no. 6, pp. 2890–2900, 2000.

[39] S. Sze and K. N. Kwok, *Physics of Semiconductor Devices*. Hoboken, NJ, USA: Wiley, 2007.

[40] C. Bulucea, "Breakdown voltage of diffused epitaxial junctions," *Solid State Electron.*, vol. 34, no. 12, pp. 1313–1318, 1991.

[41] P. Kovesi, "Good colour maps: How to design them," 2015, arXiv/1509.03700.

[42] G. Isić, R. Gajić, and S. Vuković, "Plasmonic lifetimes and propagation lengths in metallodielectric superlattices," *Phys. Rev. B*, vol. 89, Apr. 2014, Art. no. 165427.

[43] H.-T. Chen *et al.*, "Hybrid metamaterials enable fast electrical modulation of freely propagating terahertz waves," *Appl. Phys. Lett.*, vol. 93, no. 9, 2008, Art. no. 091117.

[44] M. A. Ordal, R. J. Bell, R. W. Alexander, L. L. Long, and M. R. Querry, "Optical properties of fourteen metals in the infrared and far infrared: Al, Co, Cu, Au, Fe, Pb, Mo, Ni, Pd, Pt, Ag, Ti, V, and W," *Appl. Opt.*, vol. 24, no. 24, pp. 4493–4499, Dec. 1985.

[45] H. A. Haus and W. Huang, "Coupled-mode theory," *Proc. IEEE*, vol. 79, no. 10, pp. 1505–1518, Oct. 1991.

[46] W. Suh, Z. Wang, and S. Fan, "Temporal coupled-mode theory and the presence of non-orthogonal modes in lossless multimode cavities," *IEEE J. Quantum Electron.*, vol. 40, no. 10, pp. 1511–1518, Oct. 2004.

[47] P. Lalanne, W. Yan, K. Vynck, C. Sauvan, and J.-P. Hugonin, "Light interaction with photonic and plasmonic resonances," *Laser Photon. Rev.*, vol. 12, no. 5, 2018, Art. no. 1700113.

[48] G. Sinatkas, A. Pitilakis, D. C. Zografopoulos, R. Beccherelli, and E. E. Kriezis, "Transparent conducting oxide electro-optic modulators on silicon platforms: A comprehensive study based on the drift-diffusion semiconductor model," *J. Appl. Phys.*, vol. 121, no. 2, 2017, Art. no. 023109.

[49] G. Sinatkas and E. E. Kriezis, "Silicon-photonic electro-optic phase modulators integrating transparent conducting oxides," *IEEE J. Quantum. Electron.*, vol. 54, no. 4, pp. 1–8, Aug. 2018.

[50] C. Crowell and S. Sze, "Current transport in metal-semiconductor barriers," *Solid State Electron.*, vol. 9, no. 11, pp. 1035–1048, 1966.

[51] V. Agranovich and Y. Gartstein, "Gallium arsenide (GaAs)," in *Handbook Series on Semiconductor Parameters*, vol. 1, M. Levinshtein, S. Rumyantsev, and M. Shur, Eds. Singapore: World Scientific, 2000.

Authors' photographs and biographies not available at the time of publication.

PAPER

Plasmonic silvered nanostructures on macroporous silicon decorated with graphene oxide for SERS-spectroscopy

View the article online for updates and enhancements.

IOP ebooks™

Bringing together innovative digital publishing with leading authors from the global scientific community.

Start exploring the collection−download the first chapter of every title for free.

Plasmonic silvered nanostructures on macroporous silicon decorated with graphene oxide for SERS-spectroscopy

K V Girel[1], A Yu Panarin[2] ⬤, H V Bandarenka[1], G Isic[3] ⬤,
V P Bondarenko[1] and S N Terekhov[2,4]

[1] Micro- and Nanoelectronics Department of BSUIR, Brovka St., 6, 220013, Minsk, Belarus
[2] B.I. Stepanov Institute of Physics NASB, Nezalezhnasti Ave., 68, 220072, Minsk, Belarus
[3] Institute of Physics Belgrade, University of Belgrade, Pregrevica 118, 11080, Zemun-Belgrade, Serbia

E-mail: s.terekhov@ifanbel.bas-net.by

CrossMark

Abstract

A method for fabricating surface-enhanced Raman scattering (SERS)-active substrates by immersion deposition of silver on a macroporous silicon (*macro*-PS) template with pore diameters and depth ranging from 500–1000 nm is developed. The procedure for the formation of nanostructured silver films in the layers of *macro*-PS was optimized. Silver particles of dimensions in the nano- and submicron-scale were formed on the external surface of the *macro*-PS immersed in the water–ethanol solution of $AgNO_3$, while the inner pore walls were covered by smaller, 10–30 nm diameter, silver nanoparticles. Upon introducing the hydrofluoric acid to the reaction mixture, the size of nanoparticles grown on the pore walls increased up to 100–150 nm. Such nanostructures were found to yield SERS-signal intensities from CuTMpyP4 analyte molecules of the same order to those obtained from silvered mesoporous silicon reported previously. The tested storage stability for the silvered *macro*-PS-based samples reached up to 8 months. However, degradation of the SERS intensity under illumination by the laser beam during spectral measurements was observed. To improve the stability of the SERS-signal a hybrid structure involving graphene oxide deposited on the top of analyte molecules adsorbed on the Ag/*macro*-PS was formed. A systematic observation of the time evolution of the characteristic peak at 1365 cm^{-1} showed that the addition of the oxidized graphene layer over the analyte results in ~2 times slower decay of the Raman intensity, indicating that the graphene coating can be used to enhance the stability of the SERS-signal from the CuTMpyP4 molecules.

Supplementary material for this article is available online

Keywords: surface-enhanced Raman scattering, silver nanoparticles, macroporous silicon, porphyrin, graphene oxide

(Some figures may appear in colour only in the online journal)

1. Introduction

Surface-enhanced Raman scattering (SERS) is of great interest since it is an extremely sensitive technique for wide applications in analytical chemistry, environmental monitoring, biomedicine, etc [1–4]. The most significant enhancement of Raman signal takes a place for analyte molecules located in the 2–10 nm gaps between nanostructures of the noble metals so-called 'hot spots', where local light field strength can exceed the incident field by many orders of magnitude [5–7]. The engineering of inexpensive nanostructures for SERS with advanced properties, such as high sensitivity and long-term stability remains an important task for experimentalists.

Silver nanostructures are the most widespread SERS-active substrates because of their superior Raman signal enhancement in comparison to other noble metals when

---

[4] Author to whom any correspondence should be addressed.

excited in the visible region. Among them nanocomposites based on silver coated porous silicon (PS) have been of intensive interest for more than a decade due to high SERS-activity while being easy to manufacture [8, 9]. The PS is an attractive template for SERS substrate preparation due to several reasons: developed surface area contributed by both its external and internal surfaces, the pore diameter and depth can be readily controlled by the regimes of PS fabrication covering ranges of micro-, meso- and macroporous materials [10]. Microporous silicon represents highly porous silicon sponges in which the pores are less than 2 nm in diameter. Mesoporous silicon (*meso*-PS) is characterized by its 2–50 nm pore diameter while its porosity (the fraction of voids in the layer) can reach 85%–90%. The pore diameter of macroporous silicon (*macro*-PS) varies in the range of several microns. The feature of this material is in the parallel cylindrical pores which are well-ordered. The porosity of macroporous silicon is rather low and typically does not exceed 20%.

Mesoporous silicon is the first material that was used to obtain SERS-active substrates by silver deposition on the internal surface of meso-pores by thermal decomposition method [8]. In this method, *meso*-PS was soaked in a silver nitrate solution after exposure to a procedure of plasma oxidation to prevent the spontaneous immersion coating of the silicon surface. The excess of the $AgNO_3$ solution was removed from the pores and the sample was then dried. Finally, the silver nitrate was thermally decomposed to silver metal and gases.

Later the attention was directed to the formation of silver nanostructures on the external surface of *meso*-PS by the immersion plating method [9]. Immersion deposition occupies a special place among the wet metal deposition techniques as it allows the formation of metallic nanoparticles on the substrate without applying external potential or additional reducing agents. The works of Giorgis *et al* [11–13], our team [14–16] and other groups [17–20] reported fabrication of quasi-ordered silver nanoarrays over meso-pores which demonstrated a high level of SERS-activity and the detection limits down to 10^{-15} M. Several studies of the SERS-active gold nanostructures deposited on the surface of *meso*-PS have also been reported [21, 22].

It should be noted that in almost all the cases mentioned above for *meso*-PS the metal deposition occurred on the top of the porous layer occluding the pores. At the same time, there was an intention to increase SERS-activity through contributions of both external and internal surfaces of PS. For this purpose, a suitable template is macroporous silicon. Several authors reported *macro*-PS based plasmonic structures for the generation of SERS-signal [23–26]. For example, sputtered gold nanoparticles (NPs) provided micromolar limit of detection for thiol molecules [23]. Gold nanothorns grown on *macro*-PS by the reduction from Au chloride solution were shown to demonstrate femtomolar detection limit of crystal violet [24]. The same order of detection limit of rhodamine 6G was achieved with the tightly packed film of Ag NPs [25]. Original SERS substrate was prepared by Kosović *et al* [27] from silvered macro–mesoporous silicon templates. They

showed high SERS sensitivity that enabled ultralow concentration detection of R6G dye molecules down to 10^{-15} M. It should be noted that the thickness of the macroporous layer in the above-mentioned studies was several times more than the pore diameters. Thus, authors considered SERS-activity contributed only by the metallic nanostructures on the external surface of *macro*-PS.

In this paper, we develop the method of immersion deposition of silver NPs on the walls of macropores. In principle such kind of silvered *macro*-PS can be considered as a system of nanovoids ('antinanoparticles' [28]). Metallic nanovoids are of interest for SERS-spectroscopy because in contrast to NPs they provide an additional enhancement of Raman signal due to localized plasmon mode of strong rim component around the nanovoid mouth and contributions from the multiple reflections inside the voids [29]. Such nanovoids should have 0.5–2 μm diameter and can be formed by several techniques, such as the nanosphere lithography [30], its combination with additional processing steps [31–33], silver films deposition on the alumina protrusion arrays [34] and other.

We propose an approach for the simple and cheap formation of plasmonic structures on the surface and into the pores of *macro*-PS, including etching of macropores in silicon wafers followed by immersion deposition of silver films onto the *macro*-PS surface. This work was initiated in [35] but we were not successful in complete pore walls covering with silver NPs at the experimental conditions used. However in the current study we optimized the regimes of silver deposition by varying the composition of the reaction mixture that allowed covering not only external surface between macropores but pore walls. The SERS-activity of the obtained silver nanostructures was tested with cationic water-soluble porphyrin CuTMPyP4 molecules and compared with the results for substrates based on the silvered *meso*-PS reported before [15].

Moreover we have modified Ag/*macro*-PS structures with thin 2D graphene oxide (GO) protective films and studied their SERS intensity behavior. While providing an excellent electromagnetic enhancement factor, some plasmonic materials (e.g. silver) are known to be chemically unstable, easily oxidizing and degrading in time, thus influencing adversely the performance of optical devices. The stability of the plasmonic nanostructures can be improved by adding a layer of graphene over the metal deposit. Experimental results suggest that the thin inert graphene layer can be used as a shield to gases, liquid and other corrosive agents. Recently Kravets *et al* showed that coating of graphene over copper and silver can protect them against oxidation and degradation [36]. In the work [37] the stability in air of devices constituted by gold and silver thin films was enhanced or by the thin layer of graphene over the plasmonic nanostructure.

Due to the volatility of the silver surface, various physical or chemical changes may occur at the metal-dielectric or metal-analyte interface, especially when illuminated by a laser beam, leading to the loss of the SERS-signal intensity. It is suggested that graphene-containing layers can also protect analyte molecules from photo-induced damage. Recently the significant role of graphene in improving the stability of the

SERS substrate, either in storage or usage, has been demonstrated [38–40]. In the current work composite structures GO/CuTMPyP4/Ag/*macro*-PS and GO/CuTMPyP4/GO/Ag/*macro*-PS were fabricated and the influence of graphene oxide on the SERS performance has been studied using micro-Raman system at high power density of laser illumination. The time evolution of the characteristic peak for CuTMPyP4 at 1365 cm^{-1} showed that the layer of oxidized graphene over the analyte molecules results in nearly two times increase of the SERS-signal stability.

2. Experimental

2.1. Chemicals and synthesis of the oxidized graphene

All chemicals (silver nitrate AgNO$_3$ (99.9999%), hydrofluoric acid HF (45%) and hydrochloric acid HCl, ethanol C$_2$H$_5$OH, hydrogen peroxide H$_2$O$_2$, ammonium hydroxide solution NH$_4$OH, dimethyl sulfoxide DMSO) were purchased from Sigma-Aldrich Co. and used without additional purification. To synthesize graphene nanoparticles, artificial graphite produced by Alfa Aesar with a particle size of 7–11 μm was used. Distilled water was used for preparation of all solutions.

Oxidized graphene was prepared using a modified procedure of Hummers [41] by chemical oxidation of synthetic graphite in three stages. At the first stage the pre-oxidized graphene was formed. Then graphene samples obtained were oxidized. At the third stage GO was isolated from the synthesis medium. Using the method of dynamic light scattering with the Zetasizer Nano SZ90 (Malvern Panalytical Ltd, UK), the average GO particle size is found to be around 130 nm.

2.2. Fabrication of porous silicon

Monocrystalline p-type silicon wafers of 12 Ω cm resistivity and (100) orientation (JSC 'Integral', Belarus) were used as initial substrates. They were cut from the silicon ingot fabricated by the Czochralski method. Prior to *macro*-PS formation the wafers were cleaned in a solution of NH$_4$OH, H$_2$O$_2$ and H$_2$O mixed in a volume ratio of 1:1:4. The native SiO$_2$ layer was removed from wafers by rinsing in 4.5% HF solution. The front face of the silicon wafers was then rendered porous to a depth of 1 μm by an electrochemical anodization in a solution of HF (45%) and DMSO mixed at the 10:46 volume ratio. The potentiostat/galvanostat AUTOLAB PGSTAT302n (Metrohm Autolab B.V., Netherlands) was used to provide anodization at galvanostatic regime at a current density of 8 mA cm^{-2}. After anodization the wafers were rinsed with deionized water and spun dry. With the above procedure macroporous silicon of pore diameters and depth varied from 0.5 to 1 μm was obtained. *Meso*-PS samples were formed in the same manner as it was reported elsewhere [15].

2.3. Silver deposition on porous silicon

Silver was deposited on the *meso*- and *macro*-PS by immersion technique. Freshly etched *meso*-PS samples were immersed in a 3 mM AgNO$_3$ solution in distilled water with dipping time from 10 to 60 min. The procedure of silver deposition on *macro*-PS was optimized by varying composition of solution (content of water, ethanol, hydrofluoric acid, AgNO$_3$) and reaction duration for 20–200 min. The silvered PS samples were rinsed with deionized water and then air-dried. After that the wafers were diced into rectangular samples with the 0.75 cm^2 surface area. To eliminate contaminants adsorbed on the high surface area of the Ag film, which give rise to strong SERS background, Ag NPs substrates were rinsed out in the 10 mM HCl solution for several seconds.

2.4. Preparation of samples for SERS

The SERS-activity of the silvered PS was studied using water-soluble cationic Cu(II)-tetrakis(4-N-methylpyridyl) porphyrin (CuTMpyP4). The samples for SERS measurements were prepared in two ways. In the first case silvered PS samples were incubated for two hours in the aqueous solution of 10^{-6} M CuTMpyP4. The GO-based composites were obtained by drop casting procedure: GO/CuTMPyP4/Ag NPs/*macro*-PS sample was precipitated from 40 μl of a drop of the CuTMpyP4 solution onto a silvered surface of *macro*-PS plate with the surface area ~40 mm^2 and allowed to air-dry, then 40 μl GO solution was added and dried. In the case of GO/CuTMPyP4/GO/Ag NPs/*macro*-PS composite an additional procedure of 40 μl GO drop casting preceded the CuTMPyP4 deposition.

To study the storage stability of the silvered *macro*-PS each sample with analyte was placed in a plastic zipper bag and kept at 21 °C for 1, 3 and 8 months. The air was sucked out of the bag before zipping.

2.5. Measurements

The morphology of the samples was studied by the scanning electron microscope (SEM) S-4800 (Hitachi High-Technologies Corporation, Japan) that provided 1 nm resolution.

SERS spectra of CuTMPyP4/AgNPs/*macro*-PS samples were recorded with a 90° scattering geometry by using DM160-MS3504I (Solar TII, Belarus) spectrometer equipped with a CCD detector SPEC10:256E (Roper Scientific, USA) cooled down to 153 K with liquid nitrogen. Wavelength of 441.6 nm was provided by He–Cd laser (JSC ≪PLASMA≫, Russia). The laser power used was typically of 8 ÷ 10 mW.

Measurements of the SERS spectra kinetics for GO-based composites were carried out by using a scanning probe Raman microscope 'NanoFlex' (Solar LS, Belarus). The source of excitation at 488.0 nm was an argon laser (Melles Griot, USA). Excitation and registration of Raman scattering was carried out through 100× objective with CCD camera Newton 970 EMCCD DU970P-BV (Andor Technology Ltd, UK).
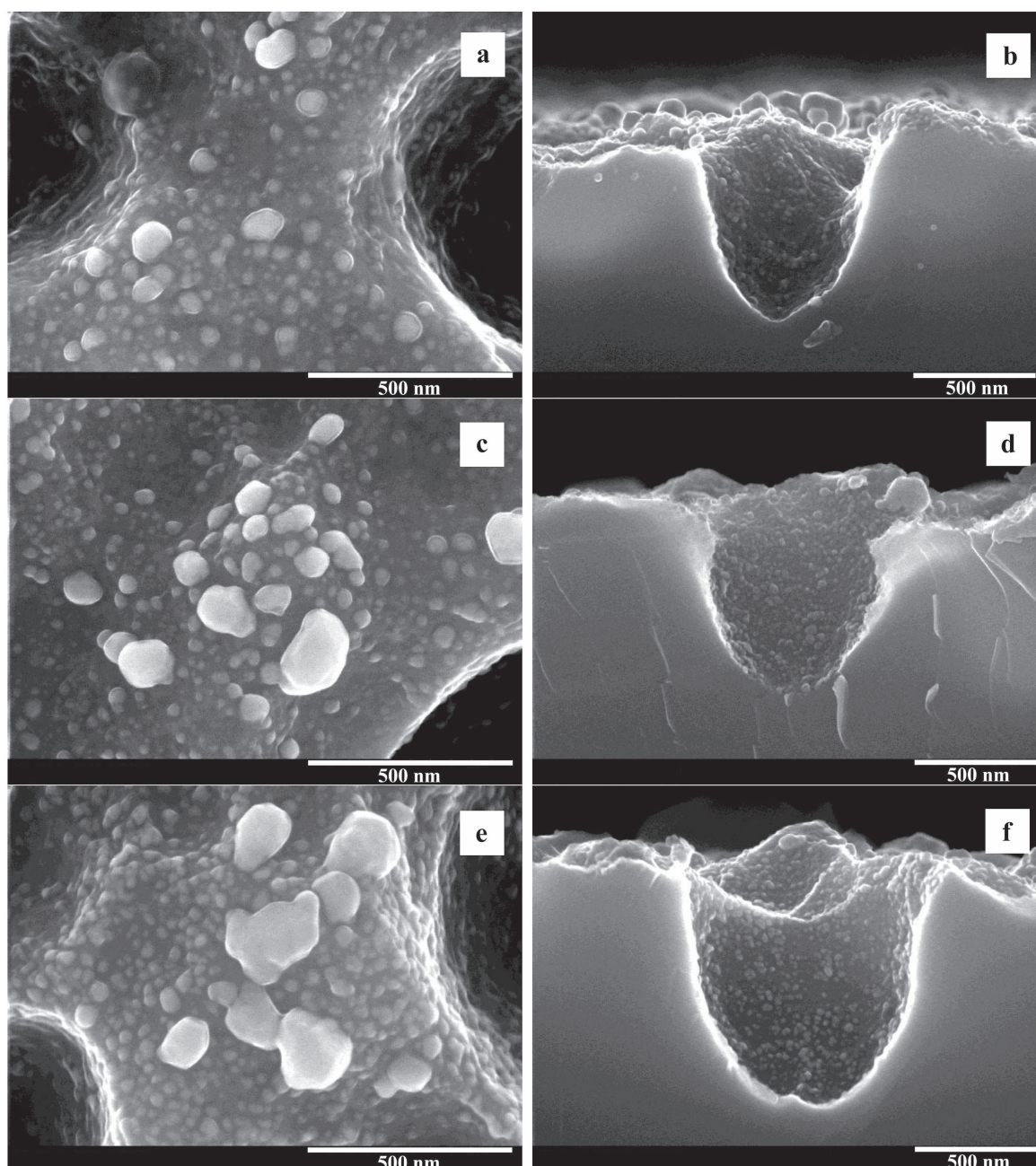
Figure 1. SEM images of (a), (c), (e) top and (b), (d), (f) cross-sectional views of the Ag/*macro*-PS samples formed by the silver immersion deposition from water–ethanol solution of 1 mM AgNO$_3$ for 40 (a), (b), 120 (c), (d) and 200 (e), (f) min.

3. Results and discussion

3.1. Morphology of the silver nanostructures

In the present work, we used anodizing regimes that provided formation of the *macro*-PS layers with pore diameters and depth varying in the range of 0.5–1 μm. Such dimensions are typical for the SERS-active nanovoids obtained by the traditional nanoengineering techniques [29, 42]. To form silver films on internal surface of PS as well as on the walls of macropores with suitable parameters, we carried out the immersion plating in the water–ethanol AgNO$_3$ solutions without of HF and in its presence gradually increasing the deposition time from 20 up to 200 min.

3.1.1. Water–ethanol (1:1) 1 mM AgNO$_3$ solution. The typical morphology of three samples of *macro*-PS formed at the Ag deposition times of 40, 120 and 200 min is shown in figure 1. SEM images for the same Ag/*macro*-PS samples obtained at lower magnification are shown in figure S1 in the supporting information, which is available online at stacks.iop.org/NANO/29/395708/mmedia. These samples were chosen since they demonstrated quite different SERS-activity. A top view images (figures 1(a), (c) and (e)) show that silver particles of nano- and submicron sizes are observed on the silicon surface between pores while they are hardly recognized on the pore walls. Cross-sectional SEM images (figures 1(b), (d) and (f)) clearly show that pore walls are also
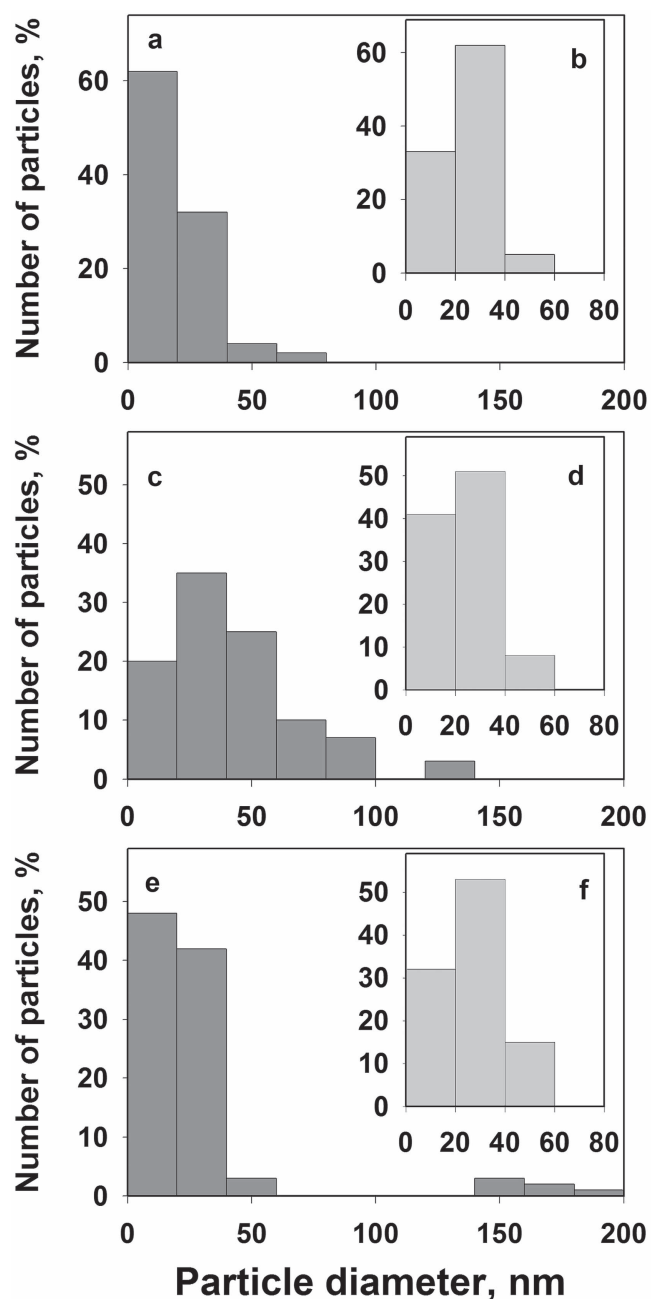
Figure 2. Size distribution histograms of Ag NPs on the silicon surface between the macropores (a), (c), (e) and on the internal surface of the macropores (b), (d), (f). Silver was deposited from water–ethanol solution of 1 mM AgNO$_3$ for 40 (a), (b), 120 (c), (d) and 200 min (e), (f).

20–40 nm. Further deposition resulted in bimodal size distribution of Ag NPs to the nanometer (less than 100 nm) and submicron (140–200 nm) ranges. The dominated sizes of Ag NPs were between a few to 20 nm.

The evaluation of Ag NPs density on the external and internal surfaces of *macro*-PS showed that the number of external particles deposited for 40 min is maximal and reaches 6×10^{10} cm^{-2}, while density of the internal NPs is twice less $(3.3 \times 10^{10}$ cm$^{-2})$. The last value is roughly saved for the both external and internal surfaces for the samples formed for 200 min when bimodal size distribution of the Ag particles takes a place. Almost twofold decrease in the whole number of NPs can be due to the coalescence of the initially growth nanoparticles. This also results in the extension of the size range to submicron-scale and its splitting to the bimodal view.

Therefore, with increase of the deposition time Ag NPs continue to coalesce while the reopened silicon surface is covered with newly nucleated particles. Therefore, with increase of the deposition time Ag NPs continue to coalesce while the reopened silicon surface is covered with newly nucleated particles. This kind of process is typical for the following conditions: (i) a flat substrate, (ii) significant mismatch of the lattice parameters of the substrate and depositing material and (iii) weak wetting of the substrate with the depositing material [43]. Indeed, the surface between pores is flat enough and the difference in the lattice parameters of the silicon and silver is of 25%. Moreover, the wetting of the substrate decreases due to oxidation of the silicon surface during the silver deposition procedure [44].

On the other hand, the sizes of Ag NPs on the pore walls are approximately constant for all stages of deposition and particles of 20–40 nm diameters are dominated (figures 2(b), (d) and (f)). The number of the internal Ag NPs was not significantly changed during the deposition process. It is also observed that an amount of silver on the pore walls is smaller than that outside the pores because the thin mesoporous layer is quickly oxidized during Ag deposition limiting supply of electrons to the silver ions for their further reduction.

We obtained the samples Ag/*macro*-PS by silver immersion deposition during different time using solution with concentration of 10 mM of AgNO$_3$ without HF. The SEM images of the samples obtained for 5, 15 and 45 min are shown in figure S2. It can be seen that even higher silver nitrate concentration in comparison to above discussed case (1 mM of AgNO$_3$) does not result in silver deposition into macropores.

3.1.2. Water–ethanol mixture with addition of hydrofluoric acid. It is known that the presence of HF in the reaction solution in which silver precipitation takes place promotes the growth of silver NPs on the silicon surface [45]. The influence of the concentration of HF on the deposition rate, the shape of silver particles and their dimensions was studied in [46]. It was shown that the higher the concentration of HF, the faster silver deposition occurs, and the larger the average diameter the silver particles will have.

Therefore, we have decided to add hydrofluoric acid to the reaction solution for the immersion plating of silver into

covered with Ag particles but their sizes belong to the nanoscaled range. An increase in silver deposition time led to the growth of the external silver NPs size while internal particles remained with nearly the same diameter (figures 1(c)–(f)). This is proved by size distribution histograms of silver particles presented in figure 2. The external surface of the *macro*-PS after 40 min deposition is covered with Ag particles of diameters ranging from a few to 80 nm where NPs smaller than 20 nm are prevalent. Immersion for 120 min led to an increase of Ag NPs diameters on the external surface of *macro*-PS up to 140 nm and shift of the prevalent size range to
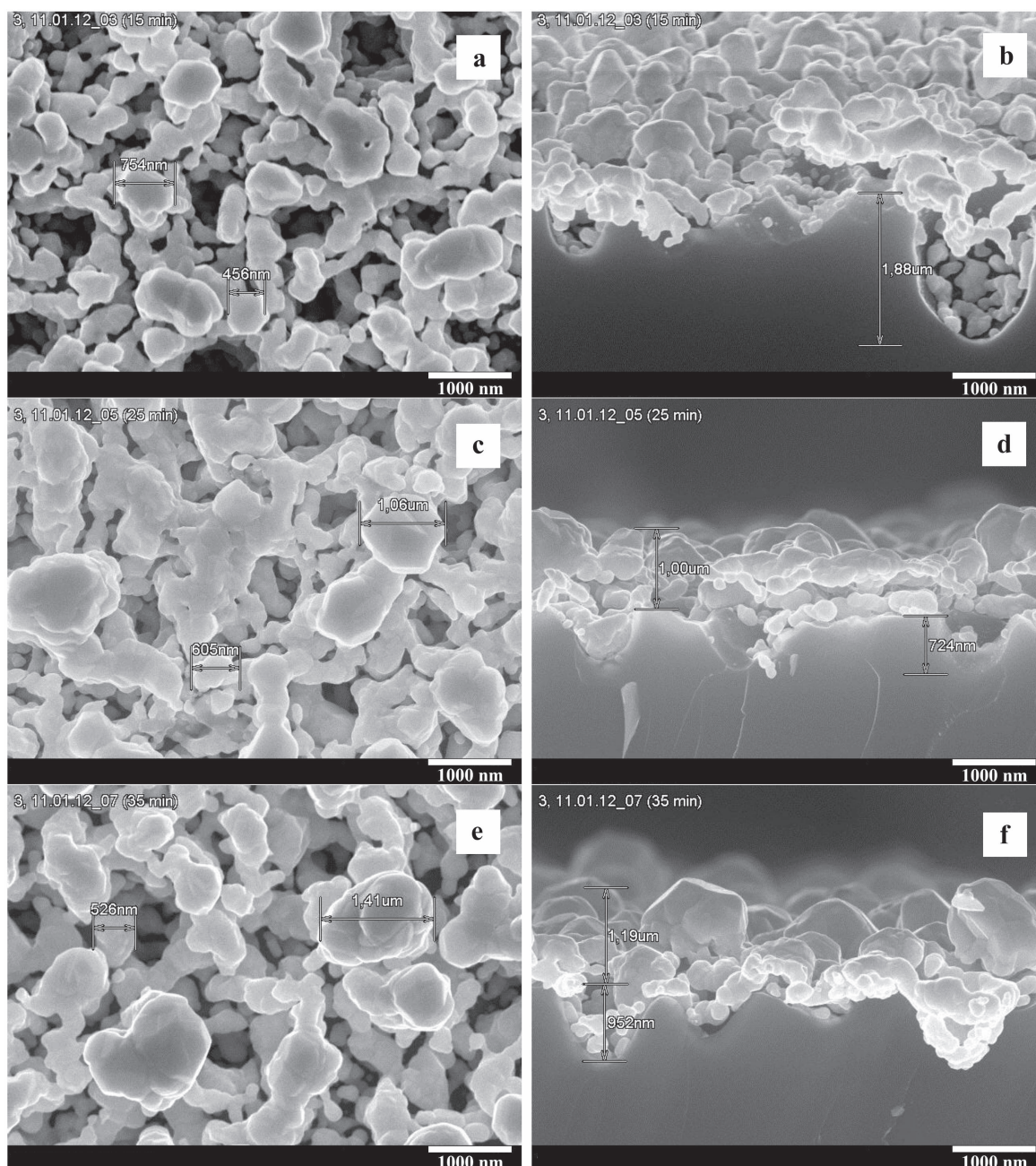
Figure 3. Plain view SEM (a), (c), (e) top and (b), (d), (f) cross-sectional images of the Ag/*macro*-PS samples formed by the silver immersion deposition for 15 (a), (b), 25 (c), (d) and 35 min (e), (f) in water–ethanol-HF solution of AgNO$_3$ at 10 mM concentration.

macropores. Thus the *macro*-PS samples were immersed in the mixture of deionized water, 1 M ethanol and 0.5 M HF. Moreover, a higher (in comparison with water–ethanol solution) concentration of AgNO$_3$ equal to 10 mM was used. Figure 3 shows SEM images of the Ag/*macro*-PS samples formed for 15, 25 and 35 min. SEM images for the same samples obtained at lower magnification are shown in figure 3S in supporting information. These samples demonstrated minimum/maximum/minimum SERS-activity, respectively (see below SERS data which are shown in figure 6(D) and section 3.2). When samples of *macro*-PS impregnated in silver nitrate solution for 15 min the external surface was covered with nanostructured silver film of densely

close-packed particles with a diameter of 100–700 nm, i.e., almost comparable to the pore diameter. At the same time, the mouths of the pores remained open. The shape of Ag NPs is irregular. Evidently it is impossible evaluate their density on the Si surface cause Ag NPs are layered on each other. There are individual particles with an average size of 200 nm on the pore walls. With increasing deposition time to 25 and 35 min much bigger silver NPs with broad size distribution and irregular shapes on the interpore surface are formed (figures 3(c)–(f)). In most cases the particles are partially coalesced, forming a fractal-like network of large islands of silver reaching sizes up to 1–1.5 μm. The number and size of silver particles inside the pores slightly increased. As can be
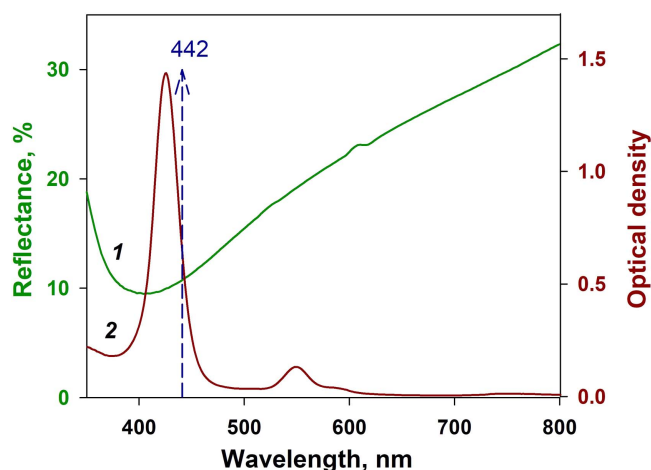
Figure 4. Reflection spectrum of the Ag/*macro*-PS sample formed by the silver immersion deposition for 25 min) in water–ethanol-HF solution of AgNO$_3$ at 1 mM concentration (1), absorption spectrum of CuTMpyP4 in water solution (2).

seen from cross-sectional image for the sample obtained in 35 min, a fairly uniform film of silver particles with a diameter of about 200 nm is formed on the walls of the pores.

Thus, the addition of hydrofluoric acid into reaction solution greatly effects the process of silver deposition on *macro*-PS that manifests itself in accelerating of the deposition speed and increasing the size and density of the Ag NPs, in particular in the formation of silver film on the pore walls, i.e. the particles decorate the inner surface of the pores in contrast to the HF-free solution.

3.2. SERS-activity of the silvered macro-PS

We examined Ag coated *macro*-PS samples for their SERS-activity using chromophore CuTMpyP4 with characteristic Raman spectrum at the concentration 10^{-6} M. The excitation wavelength was 441.6 nm, which is highly suitable for measurements since both porphyrin absorption and plasmon extinction of silver substrate are in resonance. This can be seen from figure 4 where a typical reflection spectrum of the Ag/*macro*-PS sample formed by the silver immersion deposition in AgNO$_3$ solution is characterized by a broad dip around 410 nm which can be ascribed to surface plasmon resonance of Ag NPs. The dip is broadened due to the particle polydispersity covering the excitation range. The excitation wavelength (441.6 nm), indicated by the dashed arrow, is seen to match the intense 425 nm Soret band of the CuTMpyP4 absorption spectrum. The significance of the Ag NPs plasmon resonance for the observed SERS-activity is demonstrated by the fact that no Raman signal was observed for flat silicon wafers soaked in the 10^{-6} M solution of CuTMpyP4, while all silvered *macro*-PS samples exhibited SERS-activity.

It is important that for a correct measurement of the spectral intensities it is necessary to pay special attention to the Raman setup. This is due to the morphology of the substrate surfaces, following silver deposition, is rather inhomogeneous. This is seen in the SEM images presented in figures 1 and 3. Consequently, the observed SERS intensity

across the surface can exhibit significant variations. In order to avoid errors in the determination of SERS-activity, we performed measurements with experimental setup showed in figure 5. The cylindrical lens focused the beam at the sample's surface as a spot in the form of a line of approximately 4 mm. During measurements the sample was continuously rotated. Thus obtained SERS intensity corresponds to averaged scattering of analyte molecules located within the circle of ~15 mm^2 area. Moreover, the rotating sample is less susceptible to local heating, hence the degradation of the Raman signal during the measurement is decreased.

The SERS spectra for a series of Ag/*macro*-PS samples of increasing time of silver film formation from different reaction mixture and concentrations of AgNO$_3$ were measured to reveal optimal deposition regime. Figure 6 shows the dependences of the SERS intensity on the Ag deposition time which were estimated from the amplitude of the bands at 1365 and 385 cm^{-1} in the spectrum of CuTMpyP4 adsorbed from the 10^{-6} M solution. For the samples obtained in solution that does not contain HF the SERS intensity is periodically varied depending on deposition stage at the wide time intervals scalable from 20 to 200 min (figure 6(A)). In this case the most intensive SERS spectrum was observed for the sample formed by silver deposition for 120 min. It is caused by the morphology changes of the silver deposit on the external surface of *macro*-PS (figures 1(c) and (d)). At the stage of the coalescence of primary particles the boundaries of Ag NPs are nearly connected causing a lot of hot spots. These spots are the gaps between closely spaced interacting metallic particles or NPs with sharp nanoscaled corners and edges where large enhancement of the electromagnetic field is present [47]. At the same time, only minor changes in the morphology of silver coverage on the pore walls in course of immersion are observed. Therefore, in general the variation of SERS-signal is rather small as it is presented in dependence on figure 5(A). It is well seen that the maximal intensity at 120 min is only at 1.1 times higher than the minimal level of other points.

In the presence of HF in reaction mixture the highest SERS-signal is achieved faster, i.e. for the *macro*-PS immersed in AgNO$_3$ with the 1 mM concentration maximal band intensity is observed for 60 min (figure 6(B)). When the concentration of silver nitrate increased to 3 mM the maximum of SERS enhancement reached even faster for 40 min (figure 6(C)). It is remarkable, that in both these cases time dependences demonstrate two-peak character. The maxima of the SERS-signal intensity for the samples formed in 3 mM AgNO$_3$ solution are related to the deposition during 15 and 35 min, while in a case of the 1 mM AgNO$_3$ solution they can be found at 30 and 60 min (under the same HF content). The first maximum is less intensive. This might mean that two layers of Ag NPs are formed and that SERS depends in greater extent on the growth of silver agglomerates in the second layer and the creation abundance of channels between them where the scattering cross-section of the analyte's molecules drastically increases.

It should be noted that two-peak time dependences we also observed earlier for the silvered samples prepared on the base of n-type *meso*-PS substrates [16]. These peculiarities
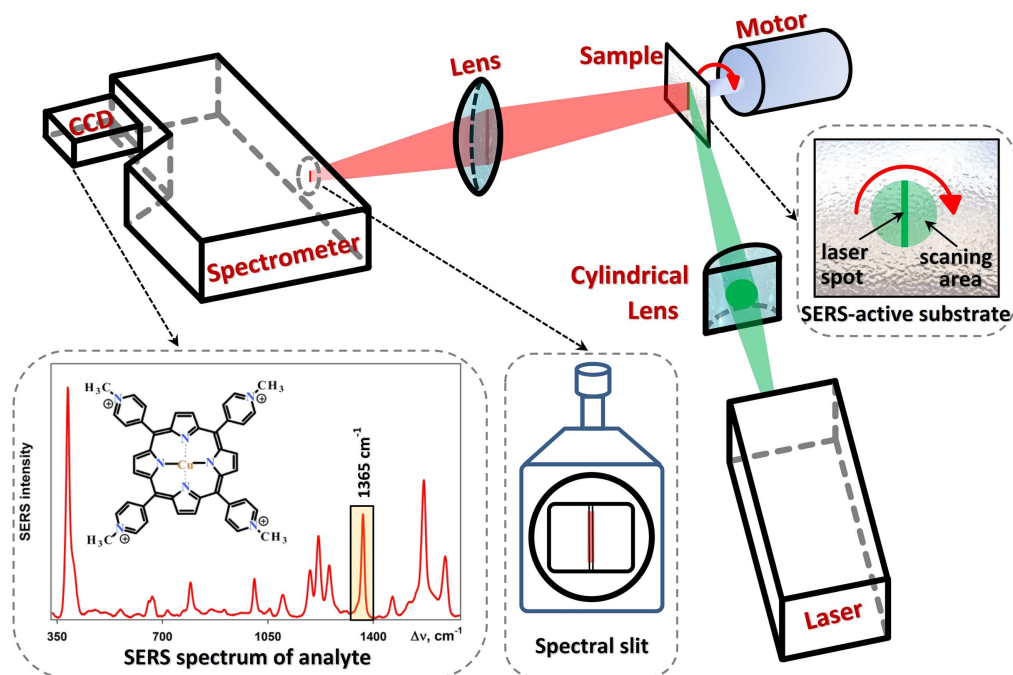
Figure 5. Schematics of the experimental setup and Raman spectrum of CuTMpyP4.

were connected with two stages of the Ag deposition process. A special parameter *effective time* has been proposed: a product of the silver salt concentration on the immersion deposition time. For different time/concentration combinations the value of *effective time* was just about constant. Silver immersion deposition in the case of *macro*-PS proceeded according to a slightly different way in contrast to *meso*-PS because we used HF additive which promoted continuous removing of passivating SiO_2 and resulting supply of the great number of electrons for the silver reduction.

Figure 6(D) shows the dependence of the SERS-signal intensity of 10^{-6} M CuTMpyP4 on the time of *macro*-PS plates soaking in 10 mM silver nitrate solution. It is seen that SERS intensity is maximal at the first 5 min. Increasing the time of $AgNO_3$ incubation to 15 min gradually decreases the spectral signal following the maximum at 20–25 min, and then SERS-activity again falls. The morphology of substrates formed at 15, 25 and 35 min exhibited coalesced NPs with highly irregular shapes and facetted forms with sharp edges that could indicate a higher probability of hot spot appearance (figure 3). The existence of many almost touching particles at the external surface and coverage by AgNPs of 150–200 nm size pore walls result in rather high level of SERS-activity for the samples prepared during 20–25 min. However, the large size of clusters due to the multitude of closely located big particles up to 1.5 μm significantly weaken the SERS effect for 35 min sample since they almost overlay macropores (figures 3 and S3(c)).

It is known that for a given excitation λ_{ex} the largest SERS intensity is reached when the SPR position is located at the middle between the excitation λ_{ex} and the wavelengths of Raman scattering, e.g. [48, 49]. Thus, in principle one could expect a somewhat different dependence of SERS intensity for different modes of CuTMpyP4. Figure 6 shows the SERS

intensity variation of two CuTMpyP4 Raman bands (385 and 1365 cm^{-1}) as a function of the time of silver immersion deposition on *macro*-PS from 1 mM (figure 6(B)), and 10 mM (figure 6(D)) $AgNO_3$ solution. The intensity variation of both the 1365 and the 385 cm^{-1} band are found to exhibit the same tendency. This result can be explained taking into account the very broad contour of SPR band (figure 4).

Comparative analysis of spectral data for all studied Ag/ *macro*-PS samples reveals nearly the same order of the SERS-activity (figure 6). The most intensive SERS-signal was observed in the case of silvered nanostructure on *macro*-PS formed in 3 mM $AgNO_3$ solution in the presence of 0.5 M HF (figure 5(C)). We also compared the level of SERS enhancement by this Ag/*macro*-PS sample with that for Ag/ *meso*-PS based substrate. Figure 5(C) shows the dependence of the intensity of CuTMpyP4 band at 1365 cm^{-1} on the time of silver immersion deposition on *meso*-PS. One can see that the obtained results for both types of substrates are comparable in terms of enhancement efficiency. However the SERS intensity from the sample based on the silvered *macro*-PS is lower in comparison with the silvered *meso*-PS. We estimated the detection limit for *macro*-PS based SERS-active substrates at the level of 10^{-10} M (see figure S4 in supporting information), while for the *meso*-PS samples it was evaluated as 10^{-11} M [16].

Finally, the storage stability of the SERS-active substrates formed by Ag deposition on the *macro*-PS for 120 min was studied. The silvered PS samples stored for 1, 3 and 8 months were rinsed in diluted HCl (HCl:H_2O = 1:9), immersed in aqueous solution of 10^{-7} M CuTMpyP4 for 2 h, then twice rinsed with distilled water and air-dried. As it can be seen from the figure S5 (see supporting information) the intensity of the SERS-signal was found to be nearly constant for the whole
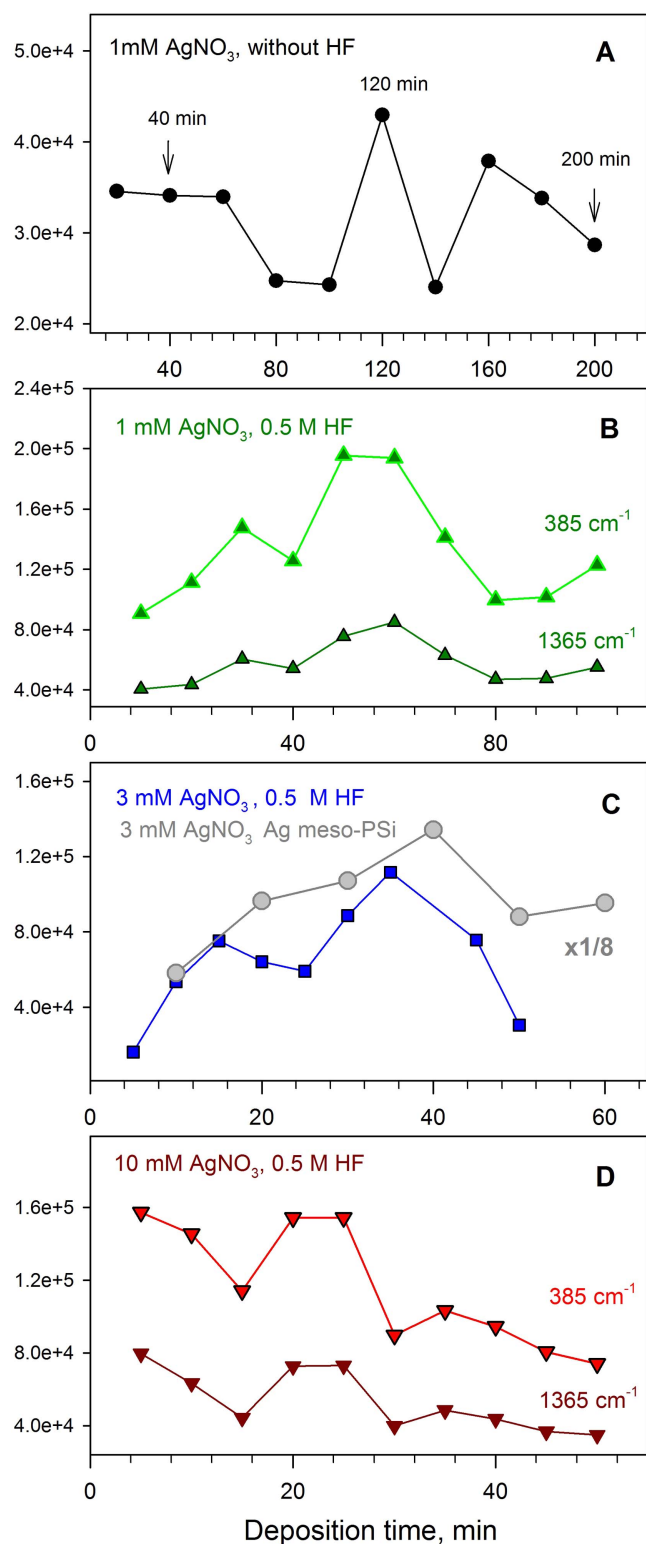
Figure 6. Dependences of the SERS intensity of the 1365 and 385 cm^{-1} bands in the spectra of 10^{-6} M CuTMpyP4 on the time of silver immersion deposition on *macro*-PS from 1 mM (A), (B), 3 mM (C) and 10 mM (D) AgNO$_3$ solution without HF (A) and in the presence 0.5 M hydrofluoric acid (B)–(D). The similar dependence for Ag/*meso*-PS sample is showed in panel (C).
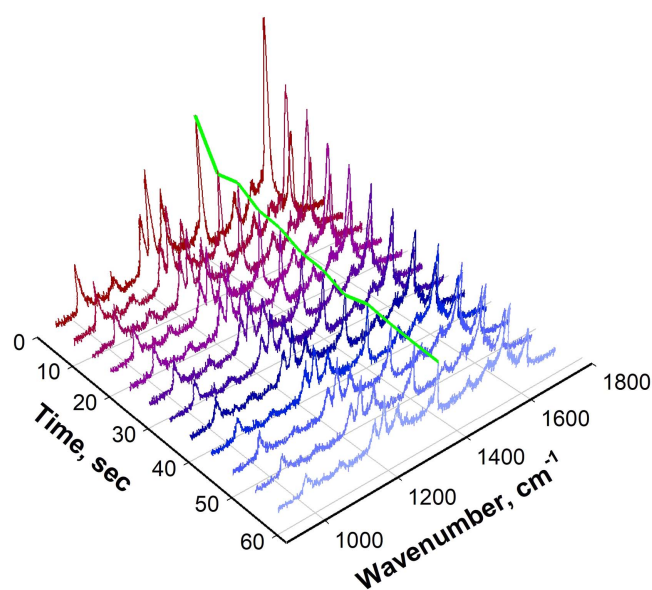

Figure 7. Degradation of SERS-signal for CuTMpyP4 at the Ag/*macro*-PS substrate without graphene oxide in the process of spectral measurements.
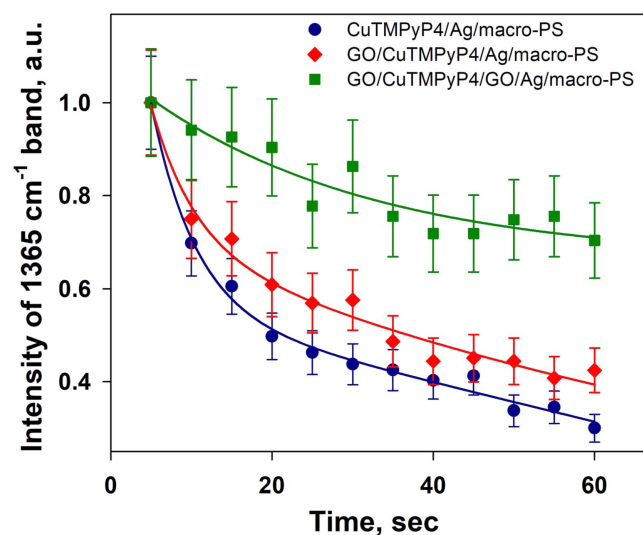

Figure 8. Normalized SERS intensity decay of CuTMpyP4 (1365 cm^{-1} peak) for three different nanostructures: CuTMPyP4/Ag/*macro*-PS (1), GO/CuTMPyP4/Ag/*macro*-PS (2) and GO/CuTMPyP4/GO/Ag/*macro*-PS (3).

storage periods fulfilling the requirements for the SERS-active substrates application [50].

3.3. Effect of the oxidized graphene on SERS-signal degradation

Although silver nanostructures are known to have a high SERS-activity, a major part of intensity enhancement can be lost due to the plasmon induced heating effect [51]. This results in reduction of spectral intensity, particularly because

9

of destruction of biological objects under analysis [52]. Moreover, silver NPs suffer from high chemical reactivity which can result in their degradation due to the reactions with atmospheric species. The decrease of the SERS performance will lower sensitivity and cause uncertainty of analysis. Therefore efforts aimed to protect silver nanostructures via depositing chemically inert layers are made [40, 53].

In principle SERS substrates based on silvered *macro*-PS meet with the same problem concerning the signal degradation. When testing the prepared samples, this problem was partially eliminated by using special experimental setup (figure 5). Nevertheless to improve the stability and repeatability of the SERS-signal we have prepared composite nanostructures by coating the silver film and analyte by graphene oxide as a protecting layer. The GO coating should provide chemical isolation of the nanoparticles from atmospheric species. Another thing, the high thermal conductivity of graphene allows swiftly dispersing the heat induced in plasmonic structure by laser excitation, thus protecting the analyte molecules from damage.

Two kinds of composite structures named as GO/CuTMPyP4/Ag/*macro*-PS (structure I) and GO/CuTMPyP4/GO/Ag/*macro*-PS (structure II) were fabricated. To study the influence of GO coating on the SERS performance the micro-Raman spectrometer was used since it gives high level of the power density from laser irradiation. While the slight detuning from the CuTMpyP4 Soret absorption band in our micro-Raman setup decreased the Raman cross-section, the SERS spectra of the fabricated samples (see figure S6 in the supporting information) was still very well resolved, thus allowing the quantitative analysis presented below. We repeatedly measured the SERS spectra at a fixed point on the substrate under laser excitation during 1 min with interval 5 s. Figure 7 shows that for the sample without graphene oxide an obvious weakening of SERS intensities (nearly three times) occurred with increasing aerobic light exposure duration. Under the same conditions, the SERS-signal on the graphene-shielded samples remained more stable. Figure 8 compares kinetics of SERS degradation for uncovered sample and for structures I and II containing GO. The data shown in figure 8 are obtained as an average over 9 spectra obtained from 3 samples measured under identical conditions at 3 randomly selected points. The time evolution of the characteristic peak for CuTMPyP4 at 1365 cm^{-1} show that the layer of the oxidized graphene over the analyte results in reducing the intensity degradation caused by photo-induced damage. For example, in the case of uncovered substrate the 1365 cm^{-1} peak intensity of CuTMpyP4 molecules within the 60 s measurement period fall off 3.2 times, while the same peak intensity for the structures I and II decreases of 2.5 and 1.4 times, respectively, as shown in figure 8. However, it should be noted, that GO coverage results in decrease of absolute level of initial SERS-signal of ~1.5 times. This may be due to the fact, that (i) GO layer by itself can absorb a part excitation light, (ii) GO covering Ag layer can shift plasmon resonance position (for both structures) and (iii) in case of structures II, the intermediate GO layer prevents a direct contact between the analyte

molecules and the plasmonic film, thus decreasing the electromagnetic enhancement.

Altogether, we can conclude that GO passivation layer on the SERS substrate based on silvered *macro*-PS has a positive impact on its properties. It provided a chemically inert surface for the substrate to prevent photo-induced SERS-signal degradation.

4. Conclusions

In this paper we have proposed a simple technique for the preparation of sensitive SERS-active substrates based on silvered macroporous silicon. By electrochemical etching of low doped p-type silicon wafers *macro*-PS templates with pore diameters and depth varying from 500–1000 nm were formed. Silver nanoparticles were deposited by the immersion plating method yielding a layer of big (up to 1500 nm) silver aggregates on the external surface of the *macro*-PS and a layer of nanoscale silver particles on the walls of the pores. The SERS performance of the obtained substrates was tested by using water-soluble porphyrin CuTMpyP4. The maximal activity was found for the samples formed by Ag deposition in the water–ethanol mixture with the addition of hydrofluoric acid. It is shown that the SERS intensity provided by the silvered *macro*-PS was nearly the same order as for the silvered *meso*-PS that we investigated earlier. A notable SERS-signal stability improvement was observed in samples with a single film of oxidized graphene deposited on top of the analyte molecules attached to the Ag/macro-PS surface. However, a further and perhaps even stronger protection against the laser-induced SERS degradation is found in samples featuring the intermediate film of GO placed between the analyte and the silver NPs.

Acknowledgments

ORCID iDs

A Yu Panarin ⓘ https://orcid.org/0000-0003-2178-7853
G Isic ⓘ https://orcid.org/0000-0002-6841-9356

References

[1] Pînzaru S C, Pavel I, Leopold N and Kiefer W 2004 Identification and characterization of pharmaceuticals using Raman and surface-enhanced Raman scattering *J. Raman Spectrosc.* **35** 338–46

[2] Reyes-Goddard J M, Barr H and Stone N 2005 Photodiagnosis using Raman and surface enhanced Raman scattering of bodily fluids *Photodiagnosis Photodyn. Ther.* **2** 223–33

[3] Kneipp J, Kneipp H and Kneipp K 2008 SERS—a single-molecule and nanoscale tool for bioanalytics *Chem. Soc. Rev.* **37** 1052–60

[4] Hering K, Cialla D, Ackermann K, Dorfer T, Moller R, Schneidewind H, Mattheis R, Fritzsche W, Rosch P and Popp J 2008 SERS: a versatile tool in chemical and biochemical diagnostics *Anal. Bioanal. Chem.* **390** 113–24

[5] Jeanmaire D L and Van Duyne R P 1977 Surface Raman spectroelectrochemistry: I. Heterocyclic, aromatic, and aliphatic-amines adsorbed on anodized silver electrode *J. Electroanal. Chem.* **84** 1–20

[6] Albrecht M G and Creighton J A 1977 Anomalously intense Raman-spectra of pyridine at a silver electrode *J. Am. Chem. Soc.* **99** 5215–7

[7] Kneipp K, Kneipp H, Itzkan I, Dasari R R and Feld M S 1999 Ultrasensitive chemical analysis by Raman spectroscopy *Chem. Rev.* **99** 2957–75

[8] Chan S, Kwon S, Koo T-W, Lee L P and Berlin A A 2003 Surface-enhanced Raman scattering of small molecules from silver-coated silicon nanopores *Adv. Mater.* **15** 1595–8

[9] Lin H H, Mock J, Smith D, Gao T and Sailor M J 2004 Surface-enhanced Raman scattering from silver-plated porous silicon *J. Phys. Chem.* B **108** 11654–9

[10] Sailor M J 2012 *Porous Silicon in Practice* 1st edn (Weinheim: Wiley) p 249

[11] Giorgis F, Descrovi E, Chiodonia A, Froner E, Scarpa M, Venturello A and Geobaldo F 2008 Porous silicon as efficient surface enhanced Raman scattering (SERS) substrate *Appl. Surf. Sci.* **254** 7494–7

[12] Virga A, Rivolo P, Frascella F, Angelini A, Descrovi E, Geobaldo F and Giorgis F 2013 Silver nanoparticles on porous silicon: approaching single molecule detection in resonant SERS regime *J. Phys. Chem.* C **117** 20139–45

[13] Novara C, Marta S D, Virga A, Lamberti A, Angelini A, Chiado A, Rivolo P, Geobaldo F, Sergo V, Bonifacio A and Giorgis F 2016 SERS-active Ag nanoparticles on porous silicon and PDMS substrates: a comparative study of uniformity and raman efficiency *J. Phys. Chem.* C **120** 16946–53

[14] Panarin A Y, Chirvony V S, Kholostov K I, Turpin P-Y and Terekhov S N 2009 Formation of SERS-active silver structures on the surface of mesoporous silicon *J. Appl. Spectrosc.* **76** 280

[15] Panarin A Y, Terekhov S N, Kholostov K I and Bondarenko V P 2010 SERS-active substrates based on n-type porous silicon *Appl. Surf. Sci.* **256** 6969–76

[16] Bandarenka H V, Girel K V, Bondarenko V P, Khodasevich I A, Panarin A Y and Terekhov S N 2016 Formation regularities of plasmonic silver nanostructures on porous silicon for effective surface-enhanced Raman scattering *Nanoscale Res. Lett.* **11** 262–72

[17] Chursanova M V, Germash L P, Yukhymchuk V O, Dzhagan V M, Khodasevich I A and Cojoc D 2010 Optimization of porous silicon preparation technology for SERS applications *Appl. Surf. Sci.* **256** 3369–73

[18] Zeiri L, Rechav K, Porat Z and Zeiri Y 2012 Silver nanoparticles deposited on porous silicon as a surface-enhanced Raman scattering (SERS) active substrate *Appl. Spectrosc.* **66** 294–9

[19] Harraz F A, Ismail A A, Bouzid H, Al-Sayari S A, Al-Hajry A and Al-Assiri M S 2015 Surface-enhanced Raman scattering (SERS)-active substrates from silver plated-porous silicon for detection of crystal violet *Appl. Surf. Sci.* **331** 241–7

[20] Mikac L, Ivanda M, Đerek V and Gotić M 2016 Influence of mesoporous silicon preparation condition on silver clustering and SERS enhancement *J. Raman Spectrosc.* **47** 1036–41

[21] Miyagawa R, Fukami K, Sakka T and Ogata Y H 2011 Surface-enhanced raman scattering from gold deposited mesoporous silicon *Phys. Status Solidi* a **208** 1471–4

[22] Sun X, Wang N and Li H 2013 Deep etched porous Si decorated with Au nanoparticles for surface-enhanced Raman spectroscopy (SERS) *Appl. Surf. Sci.* **284** 549–55

[23] Ignat T, Munoz R, Kleps I, Miu M, Obieta I and Simion M 2009 SERS active substrate based on macroporous silicon *Rom. J. Inform. Sci. Technol.* **12** 496–503

[24] Khajehpour K J, Williams T, Bourgeois L and Adeloju S 2012 Gold nanothorns-macroporous silicon hybrid structure: a simple and ultrasensitive platform for SERS *Chem Commun.* **48** 5349–51

[25] Froner E, Baschera F, Tessarolo F, Bettotti P, Pavesi L, Rossi B, Scarpa M, Mariotto G and Rigo A 2009 Hybrid nanostructured supports for surface enhanced Raman scattering *Appl. Surf. Sci.* **255** 7652–6

[26] Zhang H, Lv X, Lv C and Jia Z 2012 n-type porous silicon as an efficient surface enhancement Raman scattering substrate *Opt. Eng.* **51** 099003

[27] Kosovic M, Balarin M, Ivanda M, Derek V, Marcius M, Ristic M and Gamulin O 2015 Porous silicon covered with silver nanoparticles as surface-enhanced Raman scattering (SERS) substrate for ultra-low concentration detection *Appl. Spectrosc.* **69** 1417–24

[28] Cole R M, Mahajan S, Bartlett P N and Baumberg J J 2009 Engineering SERS via absorption control in novel hybrid Ni/Au nanovoids *Opt. Express* **17** 13299–308

[29] Kelf T A, Sugawara Y, Cole R M and Baumberg J J 2006 Localized and delocalized plasmons in metallic nanovoids *Phys. Rev.* B **74** 245415

[30] Baumberg J J, Kelf T A, Sugawara Y, Cintra S, Abdelsalam M E, Bartlett P N and Russell A E 2005 Angle-resolved surface-enhanced Raman scattering on metallic nanostructured plasmonic crystals *Nano Lett.* **5** 2262–7

[31] Kahraman M, Aydin Ö and Çulha M 2009 Size effect of 3D aggregates assembled from silver nanoparticles on surface-enhanced Raman scattering *ChemPhysChem* **10** 537–42

[32] Kahraman M and Wachsmann-Hogiu S 2015 Label-free and direct protein detection on 3D plasmonic nanovoid structures using surface-enhanced Raman scattering *Anal. Chim. Acta* **856** 74–81

[33] Kahraman M, Ozbay A, Yuksel H, Solmaz R, Demir B and Caglayan H 2018 Tunable plasmonic silver nanodomes for surface-enhanced Raman scattering *Plasmonics* **13** 785–95

[34] Lang X, Qiu T, Yin Y, Kong F, Si L, Hao Q I and Chu P K 2012 Silver nanovoid arrays for surface-enhanced Raman scattering *Langmuir* **28** 8799–803

[35] Terekhov S N, Panarin A Y, Kholostov K I, Bondarenko V P and Turpin P-Y 2009 Nanostructurated silver films on meso- and macroporous silicon layers as a substrate for surface-enhanced Raman scattering *Physics, Chemistry and Applications of Nanostructures. Reviews and Short Notes to Nanomeeting-2009* ed V I Borisenko *et al* (Singapore: World Scientific) pp 507–10

[36] Kravets V G *et al* 2014 Graphene-protected copper and silver plasmonics *Sci. Rep.* **4** 5517

[37] Del Rosso T *et al* 2017 Enhanced stability of plasmonic metal thin films by CVD grown graphene transfer *Thin Solid Films* **644** 65–70

[38] Liu Y, Hu Y and Zhang J 2014 Few-layer graphene-encapsulated metal nanoparticles for surface-enhanced Raman spectroscopy *J. Phys. Chem.* C **118** 8993–8

[39] Zhao Y, Xie Y, Bao Z, Tsang Y H, Xie L and Chai Y 2014 Enhanced SERS stability of R6G molecules with monolayer graphene *J. Phys. Chem.* C **118** 11827–32

[40] Xia M 2018 A review on applications of two-dimensional materials in surface-enhanced Raman spectroscopy *Int. J. Spectrosc.* **2018** 4861472

[41] Hummers W S and Offeman R E 1958 Preparation of graphitic oxide *J. Am. Chem. Soc.* **80** 1339–1339

[42] Coyle S, Netti M C, Baumberg J J, Ghanem M A, Birkin P R, Bartlett P N and Whittaker D M 2001 Confined plasmons in metallic nanocavities *Phys. Rev. Lett.* **87** 176801–4

[43] Oura K, Lifshits V G, Saranin A A, Zotov A V and Katayama M 2003 *Surface Science: An Introduction* (Berlin: Springer) p 443

[44] Coulthard I, Sammynaiken R, Naftel S J, Zhang P and Sham T K 2000 Porous silicon: a template for the preparation of nanophase metals and bimetallic aggregates *Phys. Status Solidi* a **182** 157–62

[45] Ye W, Shen C, Tian J, Wang C, Bao L and Gao H 2008 Self-assembled synthesis of SERS-active silver dendrites and photoluminescence properties of a thin porous silicon layer *Electrochem. Commun.* **10** 625–9

[46] Ye W, Chang Y, Ma C, Jia B, Cao G and Wang C 2007 Electrochemical investigation of the surface energy: effect of the HF concentration on electroless silver deposition onto p-Si (1 1 1) *Appl. Surf. Sci.* **253** 3419–24

[47] Michaels A M, Jiang J and Brus L 2000 Ag nanocrystal junctions as the site for surface-enhanced Raman scattering of single rhodamine 6g molecules *J. Phys. Chem.* B **104** 11965–71

[48] Haynes C L and Duyne R P V 2003 Plasmon-sampled surface-enhanced Raman excitation spectroscopy *J. Phys. Chem.* B **107** 7426–33

[49] Félidj N, Aubard J, Levi G, Krenn J R, Hohenau A, Schider G, Leitner A and Aussenegg F R 2003 Optimized surface-enhanced Raman scattering on gold nanoparticle arrays *Appl. Phys. Lett.* **82** 3095–7

[50] Natan M J 2006 Concluding remarks surface enhanced Raman scattering *Faraday Discuss.* **132** 321–8

[51] Dinish U S, Fu C Y, Kho K W, Thoniyot P, Agarwal A and Olivo M 2009 Fluctuation in surface enhanced Raman scattering intensity due to plasmon related heating effect *Proc. SPIE.* **7394** 73940T

[52] Saptarshi S R, Duschl A and Lopata A L 2013 Interaction of nanoparticles with proteins: relation to bio-reactivity of the nanoparticle *J. Nanobiotechnol.* **11** 26

[53] Ling X Y, Yan R, Lo S, Hoang D T, Liu C, Fardy M A, Khan S B, Asiri A M, Bawaked S M and Yang P 2014 Alumina-coated Ag nanocrystal monolayers as surface-enhanced Raman spectroscopy platforms for the direct spectroscopic detection of water splitting reaction intermediates *Nano Res.* **7** 132–43

SCIENTIFIC REPORTS

OPEN

Tamm plasmon modes on semi-infinite metallodielectric superlattices

Goran Isić [1], Slobodan Vuković[2,3], Zoran Jakšić [2] & Milivoj Belić[3]

We analyze the fundamental properties of optical waves referred to as Tamm plasmon modes (TPMs) which are tied to the interface of a semi-infinite two-phase metallodielectric superlattice with an arbitrary homogeneous capping medium. Such modes offer new ways of achieving high electromagnetic field localization and spontaneous emission enhancement in the vicinity of the interface in conjunction with absorption loss management, which is crucial for future applications. The homointerface, formed when the capping medium has the same permittivity as one of the superlattice constituents, is found to support a TPM whose dispersion overlaps the single-interface surface plasmon polariton (SPP) dispersion but which has a cut off at the topological transition point. In contrast, a heterointerface formed for an arbitrary capping medium, is found to support multiple TPMs whose origin can be traced by considering the interaction between a single-interface SPP and the homointerface TPM buried under the top layer of the superlattice. By carrying out a systematic comparison between TPMs and single-interface SPPs, we find that the deviations are most pronounced in the vicinity of the transition frequency for superlattices in which dielectric layers are thicker than metallic ones.

The development of nanofabrication techniques has recently enabled the experimental demonstration of various artificial materials consisting of subwavelength metallodielectric elements - metamaterials, designed to exhibit peculiar optical properties that are not present in conventional media[1]. Aimed at gaining control over light propagation, any artificial optical material must rely on a high radiation confinement and low losses in the structure composites[2]. Surface modes on metal-dielectric interfaces offer a high radiation confinement to the surface, but the presence of intrinsic dissipation in the metallic component imposes severe restrictions to their applications.

Among a variety of metamaterials that have been designed and fabricated so far, the so-called hyperbolic metamaterials (HMMs) have attracted a rapidly growing attention[3], as high quality ultrathin metal films can be grown[4] yielding metallodielectric superlattices that support electromagnetic modes with very high wavenumbers and large photonic density of states that enables unprecedented ability to access and manipulate the near-field coming from a light emitter or a scattering source[5,6]. HMMs can be composed of alternating metal and dielectric layers, of an array of metallic nanowires embedded in a dielectric and different other 2D and 3D metal-dielectrics[7].

The aim of the present paper is to investigate the fundamental properties of surface plasmon modes localized at the planar interface between an arbitrary semi-infinite medium, metal or dielectric, with a semi-infinite metallodielectric superlattice. The term superlattice is used to emphasize the periodic arrangement of alternating metal and dielectric layers. Because of the analogy with electronic states localized at crystal lattice interfaces, we refer to these surface waves as Tamm plasmon modes (TPM). Surface optical waves at an interface between a metal and a purely dielectric superlattice (i.e. dielectric Bragg mirror), here referred to as Bragg TPMs, have been considered previously[8–10]. The fact that such Tamm plasmons appear within the dielectric light cones in both s- and p-polarization, inside the band gap of the Bragg mirror, makes them interesting for applications in lasers[11], photodetectors[12], engineering of spontaneous optical emission[10] and chemical and biological refractometric sensors[13,14].

[1]Institute of Physics Belgrade, Center for Solid State Physics and New Materials, University of Belgrade, Belgrade, 11080, Serbia. [2]Institute of Chemistry, Technology and Metallurgy, Center Of Microelectronic Technologies, University of Belgrade, Belgrade, 11000, Serbia. [3]Texas A&M University at Qatar, Doha, P.O. Box 23874, Qatar. Correspondence and requests for materials should be addressed to G.I. (email: isicg@ipb.ac.rs)
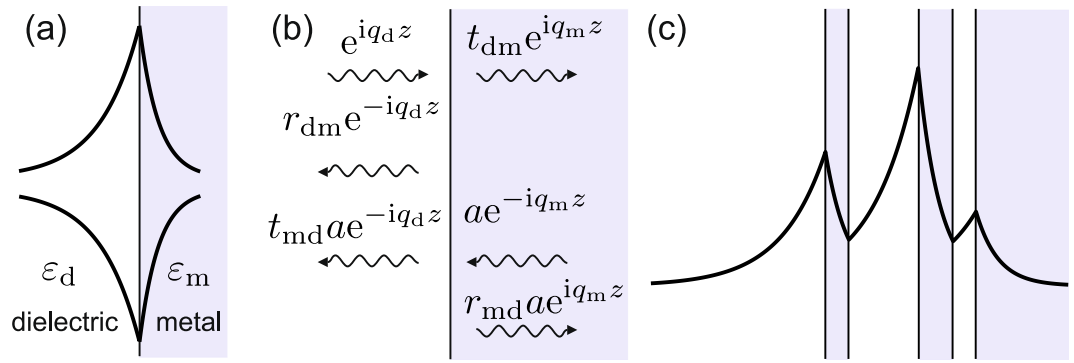
Figure 1. Schematics showing the general properties of stratified two-phase metallodielectric systems with an odd number of interfaces. (**a**) Two possible magnetic field variations which fulfill the interface boundary conditions. (**b**) Definition of Fresnel reflection and transmission coefficients. (**c**) Magnetic field of a mode fulfilling both the interface and boundary conditions at infinity.

In contrast to Bragg TPMs, the dispersion curves of metallodielectric TPMs have not been discussed systematically in literature so far. Metallodielectric TPMs are related to the traditional surface plasmon polaritons (SPPs) in that they are in-plane, p-polarized evanescent waves, but they stem from the hybridization of many single-interface SPPs of the metallodielectric superlattice and dielectric gap polaritons. The TPMs lie outside the dielectric light cone like the conventional SPPs and thus cannot escape from the flat interface, they appear when both the dielectric and metal layers are deeply subwavelength and have finite lateral group velocities. An important difference between Bragg and metallodielectric TPMs, perhaps crucial for tailoring spontaneous emission, is that the later exist even at the interface with air while the former are always buried beneath the interface with the Bragg mirror.

The current relevance of metallodielectric TPMs comes from recent reports on spontaneous emission enhancement by metallodielectric superlattices[15–17] from which it is evident that they strongly affect the photonic density of states of an interface although a systematic understanding of their role is still lacking.

We analyze the conditions for the TPM existence for both metallic and dielectric capping layers, and determine their dispersion, propagation lengths as well as the TPM resonance strength quantified by the reflection coefficient residue at the TPM pole, which is proportional to the power a point dipole placed close to the interface would emit into the mode[18]. We also analyze the predictions made within the effective medium approximation (EMA), which becomes accurate in the limit of vanishing layer thicknesses.

Two-phase stratified systems. We start with a reasoning requiring the use of single-interface boundary conditions only with minimal technical details. In spite of its deceptively simple appearance, it allows us to reach a general result regarding the existance of a particular surface mode in an arbitrary two-phase metallodielectric system and offers the explanation for some surprisingly simple properties of homointerface TPMs. A rigorous transfer-matrix-based method is then used in the remainder of the paper to confirm the general statements of this section for the particular case of a two-phase system involving a semi-infinite metallodielectric superlattice whose periodicity allows us to find closed-form solutions at the homointerface.

Starting from macroscopic Maxwell equations in which a dielectric and metallic medium are characterized by relative dielectric permittivities ε_d and ε_m, the boundary conditions imposed on a p-polarized surface wave on the planar interface between two media, with transverse wavevector components q_i ($i = d, m$), are found to imply[2]

$$\alpha_d + \alpha_m = 0, \quad \alpha_i = \frac{q_i}{\varepsilon_i}, \quad i = d, m. \tag{1}$$

Assuming that the z-axis is perpendicular to the interface and oriented towards the metallic medium, the fields of the surface wave are proportional to $\exp(-iq_d z)$ and $\exp(iq_m z)$, in the dielectric and metal medium respectively, from which it follows that the imaginary parts of both q_i must be positive in order to meet boundary conditions at infinity. This case corresponds to a magnetic field whose magnitude has a peak at the interface, as indicated by the top curve in Fig. 1(a).

However, Eq. (1) remains fulfilled if q_i are both replaced by $-q_i$, corresponding to fields growing exponentially away from the local minimum at interface, as depicted by the bottom curve in Fig. 1(a).

Introducing the Fresnel reflection and transmission coefficients as

$$r_{dm} = \frac{\alpha_d - \alpha_m}{\alpha_d + \alpha_m}, \quad t_{dm} = 1 + r_{dm}, \tag{2}$$

for incidence from the dielectric side, and

$$r_{md} = -r_{dm}, \quad t_{md} = 1 + r_{md} = 1 - r_{dm}, \tag{3}$$
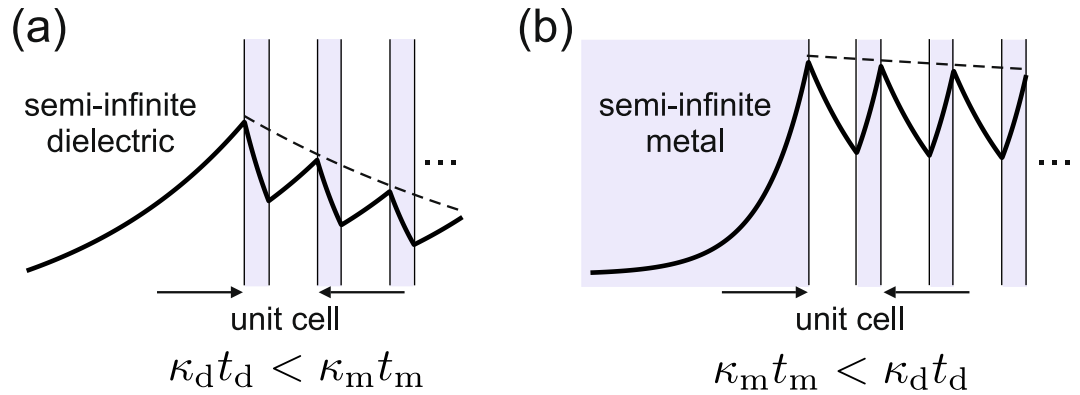
2

Figure 2. Magnetic field variation on homointerfaces for (**a**) dielectric and (**b**) metallic capping medium. The requirement that the Bloch anvelope, indicated by dashed lines, decays towards infinity on the right, yield the condition that $\kappa_d t_d < \kappa_m t_m$ and $\kappa_d t_d > \kappa_m t_m$ for (**a,b**), respectively. Note that the values of κ_d and κ_m used in panels (**a,b**) differ.

for the opposite incidence, the case of field having the peak at the interface is seen to represent the scattered field for an incoming wave from either medium, when $|r_{dm}|$ diverges, which is equivalent[19] to Eq. (1).

The analogous explanation of how the solution growing away from the interface arises, is found by assuming two waves are incident on the interface, the one from the dielectric side with unit amplitude and the other with complex amplitude a, as depicted in Fig. 1(b). By chosing $a = r_{dm}/(r_{dm} - 1)$, the fields going away from the interface cancel out when r_{dm} has a pole, leaving only the incoming components which correspond to the exponential growth away from the interface.

The significance of the latter solution to interface boundary conditions becomes apparent when additional layers with permittivities ε_d and ε_m are inserted between the semi-infinite dielectric and metal media, which means adding an even number of interfaces to the initial one. Now it is seen that if the boundary conditions at each interface are satisfied by alternating field maxima and minima, as depicted in Fig. 1(c), the boundary conditions at infinity will also be fulfilled, meaning that the obtained field will represent a surface mode of the multilayer. Therefore, any metallodielectric multilayer capped by the semi-infinite dielectric on one side and the metallic medium on the other, will have at least one surface mode whose transverse wavevector components fulfill Eq. (1), which implies that its dispersion curve is identical with the single-interface SPP dispersion curve

$$\beta_{dm} = k_0 \sqrt{\frac{\varepsilon_d \varepsilon_m}{\varepsilon_d + \varepsilon_m}}, \tag{4}$$

where β_{dm} represents the complex amplitude of the longitudinal (parallel to interfaces) wavevector component and $k_0 = \omega/c$ is the free-space wavenumber.

To see the implications of this general result for semi-infinite metallodielectric superlattices, we consider a surface wave, henceforth referred to as TPM, with a dispersion given by Eq. (4). The first condition it has to satisfy on a semi-infinite superlattice capped by a dielectric, as depicted in Fig. 2(a), is that it decays exponentially to the left, meaning that moving to the right, it has to decay in metallic layers and grow in dielectric ones. Denoting by t_i the layer thicknesses and κ_i the imaginary part of q_i, we see that the field amplitude is multiplied by $\exp(-\kappa_m t_m)$ and $\exp(\kappa_d t_d)$ in passing through the metal and the dielectric layer, respectively, meaning that passing through one unit cell, its amplitude is multiplied by $\exp(-\kappa_m t_m + \kappa_d t_d)$. The second condition imposed on this TPM is that it decays towards infinity on the right side, therefore a TPM on the dielectric-capped superlattice can exist only if

$$\kappa_d t_d < \kappa_m t_m. \tag{5}$$

Repeating the above reasoning for the metal-capped superlattice, the field amplitude is seen to be multiplied by $\exp(\kappa_m t_m - \kappa_d t_d)$ in passing each unit cell, so a TPM with dispersion given by Eq. (4) will exist if the opposite is true

$$\kappa_d t_d > \kappa_m t_m. \tag{6}$$

In the following section we show rigorously that the homointerface supports only the TPMs given by Eq. (4), in conjunction with conditions (5) or (6), depending on the capping medium. Under such circumstances, the reasoning applied in this section has a purpose of giving an intuitive explanation of several coincidences that might not have been expected. One interesting point to note here is that if the two possible homointerfaces of a given semi-infinite superlattice are considered, one being capped by the dielectric and the other by the metal constituent medium as in Fig. 2(a) and (b), at any given frequency ω only one of the conditions in Eqs. (5) or (6) can be fulfilled, so only one of them can support a TPM. This hints that in drawing the schematics in Fig. 2, different values of ω have been assumed for panels (a) and (b).
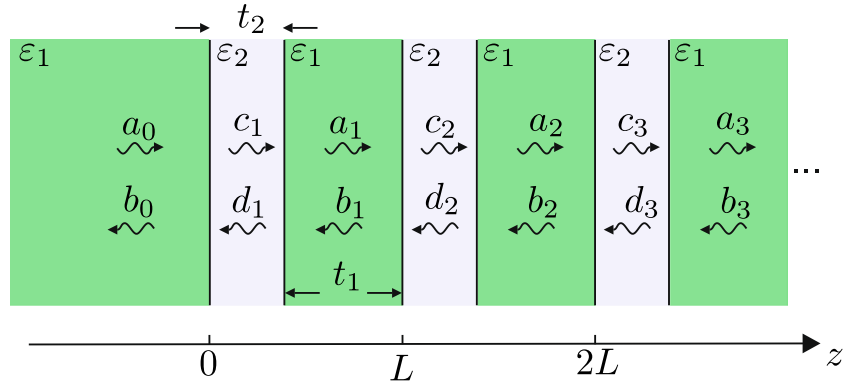
Figure 3. Schematics of the homointerface geometry used in the transfer-matrix method. The ε_1 medium extends from left infinity up to the interface at $z = 0$, after which the superlattice is formed by periodically repeating the unit cell comprising a ε_2 and ε_1 layer.

Homointerface. The general geometry of the problem is sketched in Fig. 3. The capping medium permittivity is assumed equal to one of the lattice constituents, ε_1, while the second medium permittivity is ε_2. This system will henceforth be referred to as homointerface. In determining the fields, we follow the transfer-matrix method of ref.[20] For completeness and due to some minor differences in notation, here we briefly summarize the main aspects of the method.

The trasverse field phasor F in the n-th unit cell is represented as a sum of the forward and backward propagating plane wave amplitudes, denoted by a_n and b_n in medium ε_1 and by c_n and d_n in the second medium. F corresponds to the electric or magnetic field for a s- or p-polarized wave, respectively. The wave amplitudes a_n, b_n of adjacent unit cells are related by the translation matrix

$$\begin{bmatrix} a_{n-1} \\ b_{n-1} \end{bmatrix} = T \begin{bmatrix} a_n \\ b_n \end{bmatrix}, \quad T = \begin{bmatrix} A & B \\ C & D \end{bmatrix},$$

(7)

whose elements are given by

$$A = e^{-iq_1 t_1} \left[\cos(q_2 t_2) - \frac{i}{2} \left(\frac{\alpha_2}{\alpha_1} + \frac{\alpha_1}{\alpha_2} \right) \sin(q_2 t_2) \right],$$

(8)

$$B = -e^{iq_1 t_2} \frac{i}{2} \left(\frac{\alpha_2}{\alpha_1} - \frac{\alpha_1}{\alpha_2} \right) \sin(q_2 t_2),$$

(9)

$$C = e^{-iq_1 t_2} \frac{i}{2} \left(\frac{\alpha_2}{\alpha_1} - \frac{\alpha_1}{\alpha_2} \right) \sin(q_2 t_2),$$

(10)

$$D = e^{iq_1 t_1} \left[\cos(q_2 t_2) + \frac{i}{2} \left(\frac{\alpha_2}{\alpha_1} + \frac{\alpha_1}{\alpha_2} \right) \sin(q_2 t_2) \right].$$

(11)

Here q_i represent the complex wavevector z-components, related with the longitudinal (in-plane) component β via the dispersion relation of each layer

$$q_i = \pm \sqrt{\varepsilon_i k_0^2 - \beta^2}, \quad \text{Im}\{q_i\} \geq 0,$$

(12)

with $\pm$ denoting the sign that gives q_i with a non-negative imaginary part. In case of s-polarization, $\alpha_i = q_i$ while for p-polarization $\alpha_i = q_i / \varepsilon_i$, as before.

From the above, T is seen to be unimodular for any (real or complex) ε_i or q_i. It further implies that the product of its two eigenvalues is unity, so they can be written in the form $e^{\pm iKL}$, where $L = t_1 + t_2$ and K is the Bloch wavenumber. Here we define K so that $\exp(iKL)$ corresponds to a wave propagating towards positive infinity, meaning that

$$e^{iKL} = \frac{A + D}{2} \pm \sqrt{\left(\frac{A + D}{2} \right)^2 - 1}, \quad \text{Im}\{K\} \geq 0,$$

(13)

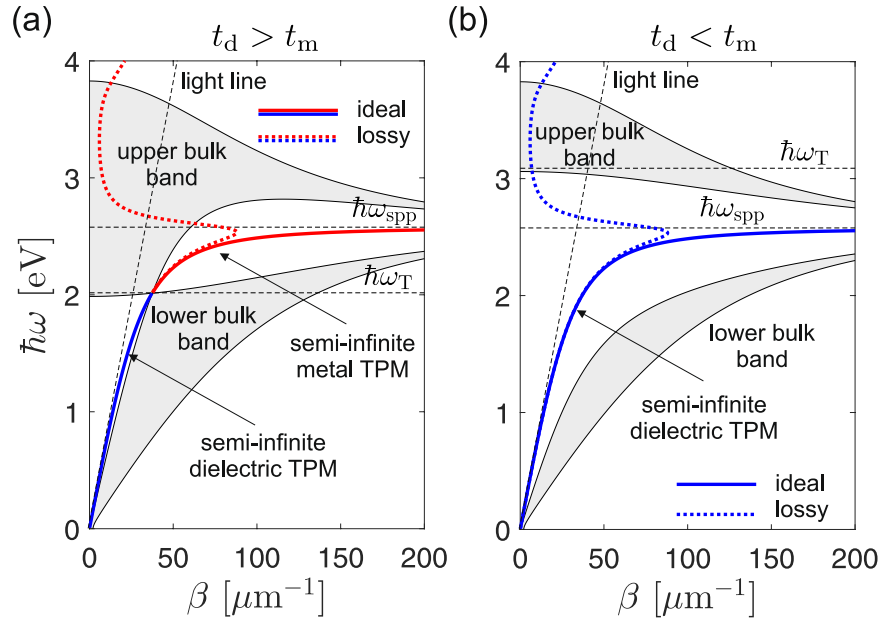where $\pm$ denotes the sign giving a non-negative imaginary part of K.

Figure 4. Bulk band structure (shading) and TPMs (thick lines) of one typical example for each the two possible band structure topologies. (**a**) $t_d > t_m$ with $\omega_T < \omega_{spp}$, leading to an intersection of the bands at ω_T. Here titanium dioxide and silver are assumed with $t_d = 20$ nm and $t_m = 10$ nm. (**b**) $t_d > t_m$ leading to $\omega_T < \omega_{spp}$ meaning that the upper and lower bulk bands do not intersect. Here $t_d = 10$ nm and $t_m = 20$ nm is assumed for titanium dioxide and silver, respectively.

Before proceeding further, the basic aspects of dissipation should be clarified. At visible and infrared frequencies, the dominant source of dissipation, by far, are intra- and inter-band electronic transitions in the metal. Therefore, we assume that the dielectric has a purely real relative permittivity $\varepsilon_d = 6.76$, corresponding to titanium dioxide, while for metal we use the silver Drude-Lorentz parametrized experimental data from ref.[21]. A convenient method[22] to treat the problem of losses is to introduce a modified dielectric function of the metal via the perturbation parameter p

$$\varepsilon_m^{(p)} = \mathrm{Re}\{\varepsilon_m\} + ip\mathrm{Im}\{\varepsilon_m\}, \quad \varepsilon_m^{(1)} \triangleq \varepsilon_m. \tag{14}$$

Setting p to unity recovers the original ε_m, while reducing it towards zero approaches smoothly the lossless case $\varepsilon_m^{(0)}$ in which the optical eigenmodes can properly be defined. The latter are thus used as a convenient scaffold on which quantities calculated with real loss are projected. The eigenmodes of a lossless infinite superlattice, henceforth referred to as bulk modes, are defined as solutions of Eq. (13) having both their eigenfrequency ω and wavevector $\mathbf{k} = (\beta, K)$ purely real.

Depending on the relative thickness of the dielectric, t_d, and metal, t_m, layers, the band structure of the infinite superlattice is known to have one of two possible topologies, corresponding to $t_d > t_m$ and $t_d < t_m$, as indicated by the shaded areas in Fig. 4(a) and (b). In this paper we carry out concrete calculations for one representative example from both classes: $t_d = 20$ nm, $t_d = 10$ nm, shown in Fig. 4(a), and $t_d = 10$ nm, $t_m = 20$ nm, in Fig. 4(b).

A general property of the $t_d > t_m$ class is that the upper and lower bulk bands intersect[23] at a frequency ω_T we shall refer to as the transition frequency. In the literature, ω_T is sometimes[15] referred to as the topological transition point since the band topology changes when crossing ω_T. It can be shown[23] that ω_T is defined by the condition

$$t_d\varepsilon_d + t_m\varepsilon_m(\omega_T) = 0, \tag{15}$$

which can alternatively be stated as

$$\varepsilon_\parallel(\omega_T) = 0, \tag{16}$$

with $\varepsilon_\parallel$ denoting the average in-plane permittivity (or the in-plane permittivity tensor component in EMA)

$$\varepsilon_\parallel = \eta\varepsilon_1 + (1 - \eta)\varepsilon_2, \quad \eta = \frac{t_1}{L}. \tag{17}$$

While it is obvious that ω_T can be engineered by varying the thickness of layers in the metallodielectric superlattice, it is interesting that its value does not depend on the actual layer thicknesses but only on their ratio t_d/t_m.

The bulk bands of the $t_d < t_m$ class are separated by $\beta_{dm}(\omega)$ which lies between them. The band edges shown by thin (black) lines in Fig. 4 correspond to solutions having $\cos(KL) = 1$ (inner boundaries) and $\cos(KL) = -1$ (outer boundaries). In a lossy system, however, there is no strict definition of band edges, but rather a continuum

of modes in the $\beta - \omega$ plane whose lifetime and propagation lengths increase rapidly around the band edges of the lossless system[22].

Having defined the bulk bands of the superlattice, we are now ready to discuss the surface modes of the semi-infinite superlattice, i.e. the TPMs. By definition, the surface mode at a planar interface must be located outside the bulk bands of both the capping medium and the superlattice, meaning that it must be represented by a point in the $\beta - \omega$ plane outside both the light line and the shaded regions in Fig. 4.

TPMs are identified as poles of the reflection coefficient r of an incoming wave from the capping layer. The reflection coefficient r for the semi-infinite superlattice is determined as the $N \to \infty$ limit of the reflection coefficient r_N of a system comprising N unit cells, such that the ε_1 medium of the N-th unit cell is semi-infinite. In that case[20], a_N, b_N are related with a_0, b_0 via T^N while r_N is defined as the ratio of b_0 and a_0 when there is no incoming wave in the N-th layer. Using the known expression[24] for T^N, we find

$$r_N = \frac{C}{A - \sin([N-1]KL)/\sin(NKL)}, \tag{18}$$

with A and C given by Eqs. (8) and (10). Remembering that K has at least an infinitesimaly small positive imaginary part, we find

$$\lim_{N \to \infty} \frac{\sin([N-1]KL)}{\sin(NKL)} = e^{iKL}, \tag{19}$$

and finally

$$r = \lim_{N \to \infty} r_N = \frac{C}{A - e^{iKL}}. \tag{20}$$

The condition for the existence of a TPM is that r diverges which happens when

$$A = e^{iKL}. \tag{21}$$

Combining Eq. (13) with Eqs. (8) and (11), the necessary condition for Eq. (21) to hold in a non-trivial case is found to be

$$\alpha_1 + \alpha_2 = 0. \tag{22}$$

Since this is equivalent with Eq. (1), a TPM can exist only in p-polarization while its in-plane wavenumber must be qual to that of the single-interface SPP $\beta_{\text{TPM}}(\omega) = \beta_{\text{md}}(\omega)$.

Combining Eqs. (21) and (22) for p-polarization gives

$$K = \frac{q_2 t_2 - q_1 t_1}{L} = -\alpha_1 \varepsilon_\| = \alpha_2 \varepsilon_\|. \tag{23}$$

Since K has a non-negative imaginary part by definition, we find that a TPM can exist on a homointerface only if

$$\text{Im}\{-\alpha_1 \varepsilon_\|\} = \text{Im}\{\alpha_2 \varepsilon_\|\} \geq 0. \tag{24}$$

For a dielectric-capped homointerface, where $\varepsilon_1 = \varepsilon_d$, Eq. (24) requires $\varepsilon_\|$ to be negative in the lossless limit, meaning that the TPM exist only for frequencies up to ω_T, as indicated by the thick solid blue curves in Fig. 4(a) and (b). In contrast, the metal-capped homointerface, where $\varepsilon_1 = \varepsilon_m$, supports a TPM only above ω_T as $\varepsilon_\|$ must be positive. As ω_T is below the surface plasmon resonance frequency ω_{spp} (the upper frequency limit for SPP propagation), only if $t_d > t_m$, a TPM on a metal-capped homointerface exists only in the $t_d > t_m$ class of superlattices, as indicated by the thick solid red line in Fig. 4(a).

Solving for Eqs. (22) and (24) with loss taken into account yields complex values for $\beta_{\text{TPM}}(\omega)$, the real part of which is drawn in Fig. 4(a) and (b) by thick dotted lines. We find that, quite generally, at any given frequency ω a TPM mode with $\beta_{\text{TPM}}(\omega) = \beta_{\text{md}}(\omega)$ exists either on the metal- or dielectric capped superlattice, which is manifested by the fact that taken together, they form the complete SPP dispersion curves $\beta_{\text{dm}}(\omega)$ in Fig. 4(a) and (b). In the lossy case, some subtleties arise regarding the inequality in Eq. (24), as indicated by the fact that the metal-capped $t_d > t_m$ homointerface is found to support a TPM above around 3.82 eV. Such modes, however, exist only formally as their lifetimes are way too short to be relevant.

The above transfer-matrix-based homointerface TPM analysis thus shows formally that the TPM eigenmodes discussed on general grounds in Section "Two-phase stratified systems" are, in fact, the only possible surface modes and that they have properties very similar to single-interface SPPs. Before proceeding with details showing the important differences between the two, we briefly look at the problem from the EMA perspective.

In EMA, the layer thicknesses t_i are assumed to be negligible relative to any length scale relevant for wave propagation, so the superlattice is described by two dielectric permittivities $\varepsilon_\|$ and $\varepsilon_\perp$, with the former having been defined previously in Eq. (17) and the latter given by

$$\varepsilon_\perp = \frac{\varepsilon_1 \varepsilon_2}{(1 - \eta)\varepsilon_1 + \eta \varepsilon_2}. \tag{25}$$

The reflection coefficient for a p-polarized wave incident from a semi-infinite medium ε_1 is

$$r_{\text{ema}} = \frac{\alpha_1 - \alpha_{\text{ema}}}{\alpha_1 + \alpha_{\text{ema}}}, \qquad \alpha_{\text{ema}} = \frac{q_{\text{ema}}}{\varepsilon_{\parallel}},$$

(26)

while the transverse wavenumber in the effective uniaxial medium is

$$q_{\text{ema}} = \pm \sqrt{\varepsilon_{\parallel} k_0^2 - \frac{\varepsilon_{\parallel}}{\varepsilon_{\perp}} \beta^2}, \qquad \text{Im}\{q_{\text{ema}}\} \geq 0.$$

(27)

The dispersion of the surface mode at the interface between ε_1 and the uniaxial medium is obtained as

$$\beta_{\text{ema}} = \pm k_0 \sqrt{\frac{\varepsilon_1 \varepsilon_{\perp} (\varepsilon_{\parallel} - \varepsilon_1)}{\varepsilon_{\parallel} \varepsilon_{\perp} - \varepsilon_1^2}}, \qquad \text{Im}\{\beta_{\text{ema}}\} \geq 0.$$

(28)

Replacing $\varepsilon_{\parallel}$ and $\varepsilon_{\perp}$ by expressions given by Eqs. (17) and (25), we find that $\beta_{\text{ema}} = \beta_{\text{dm}}$. Since the divergence of r_{ema} requires $q_{\text{ema}} = -\alpha_1 \varepsilon_{\parallel}$, a comparison with Eq. (23), shows that the perpendicular component of the wave in EMA is equal to the Bloch wavenumber

$$K = q_{\text{ema}}.$$

(29)

Therefore, EMA describes correctly not only the dispersion and condition for the existence of the TPM, but also its transverse extension into the superlattice quantified by the penetration depth

$$\delta = \frac{1}{\text{Im}\{K\}} = \frac{1}{\text{Im}\{q_{\text{ema}}\}}.$$

(30)

The overlap of complex dispersion curves $\beta_{\text{dm}}(\omega)$, $\beta_{\text{TPM}}(\omega)$ and $\beta_{\text{ema}}(\omega)$, corresponding to the single-interface SPP, TPM and the EMA surface wave, is somewhat unexpected considering that it implies an idential modal decay dynamics which is known to be determined by how is the modal energy distributed in space[22]. The fact that these three modes have a very different field variation in the direction perpendicular to the interface while sharing the same dispersion curve is, evidently, a consequence of the simple rule by which the boundary conditions in a two-phase stratified system can be fulfilled, as discussed in Section "Two-phase stratified systems", which allows the ratio of the total field energy residing in the dielectric and metal medium to remain invariant upon the insertion of an arbitrary number interfaces (as long as their total number is odd).

The manner in which the presence of a surface mode modifies the optical properties of an interface is determined by how the reflection coefficient $r(\beta)$, considered as a function over the complex β plane, behaves in the vicinity of the associated pole β_{pole}. For example, ref.[18] shows that the power emitted by a dipole located in the vicinity of a metal-dielectric interface is proportional to the residue a_{pole} of $r(\beta)$ at β_{pole}, evaluated as

$$a_{\text{pole}} = \frac{1}{2\pi i} \oint_{\gamma} \frac{r(\beta) d\beta}{\beta - \beta_{\text{pole}}},$$

(31)

where γ denotes a positively oriented contour around β_{pole} in the complex β-plane, sufficiently small so that $r(\beta)$ is analytic within it (i.e. avoiding the branch cuts associated with q_i).

The analytic expression for the single-interface SPP residue has been reported in ref.[18]

$$a_{\text{spp}} = \frac{2\varepsilon_1 \varepsilon_2}{\varepsilon_1^2 - \varepsilon_2^2} \beta_{\text{sp}}.$$

(32)

Since the homointerface TPM and the EMA surface wave dispersion curves overlap with the SPP, it is straightforward to show that their residues are given by

$$a_{\text{TPM}} = \frac{\sin(q_2 t_2 - q_1 t_1)}{\exp(i q_1 t_1) \sin(q_2 t_2)} a_{\text{spp}},$$

(33)

where q_1 and q_2 should be evaluated at β_{TPM}, and

$$a_{\text{ema}} = \left(1 + \frac{f}{1 - f} \frac{\varepsilon_1}{\varepsilon_2} \right) a_{\text{spp}},$$

(34)

respectively. The last two equations hold only if the mode exists while in case it does not, the corresponding residue is zero.

Comparing the magnitudes of a_{spp}, a_{TPM} and a_{ema} in a $t_d > t_m$ type dielectric-capped superlattice, both $|a_{\text{TPM}}|$ and $|a_{\text{ema}}|$ are seen to decrease monotonously as ω is increased towards ω_T, Fig. 5(a) (blue line). This happens because the argument of the sine function in a_{TPM} in Eq. (33) is, according to Eq. (23), proportional to $\varepsilon_{\parallel}$ and thus decreases close to zero (or becomes exactly zero in the lossless limit) at ω_T. Since $|a_{\text{ema}}|$ is the limit of $|a_{\text{TPM}}|$ for vanishing layer thicknesses (this holds by definition of EMA and is also evident by taking the $t_i \rightarrow 0$ limit of Eq. (33)) it is depicted by dotted lines and indicates the possible trend of the $|a_{\text{TPM}}|$ spectra in case the layer thicknesses are scaled down. Above ω_T, the TPM mode of the dielectric-capped homointerface disappears, meaning
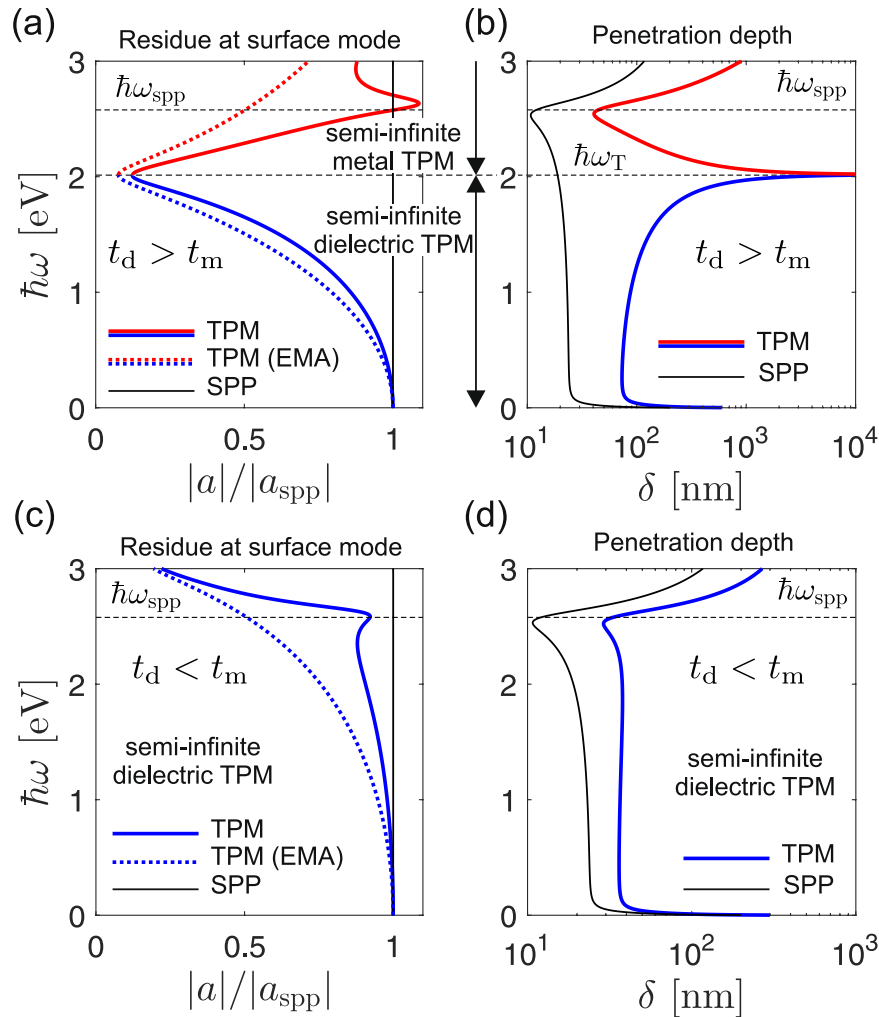
Figure 5. Left panels: residue at the TPM and SPP mode, drawn for the (**a**) $t_d > t_m$ and (**c**) $t_d < t_m$ examples, respectively. Righ panels: penetration depths into the superlattice for (**a**) $t_d > t_m$ and (**c**) $t_d < t_m$ examples, compared with the corresponding SPP penetration depth.

that $|a_{TPM}|$ drops to zero. In order to simplify Fig. 5, the curves corresponding to $|a_{TPM}| = 0$ are omitted, so in Fig. 5(a) the blue and red curves are discontinued at $\omega = \omega_T$. In the lossless limit (not shown), $|a_{TPM}|$ becomes exactly zero at ω_T.

The opposite trend of $|a_{TPM}|$ is observed for the $t_d > t_m$ type metal-capped superlattice, where $|a_{TPM}|$ starts from small values (zero in the lossless limit) at ω_T and approaches $|a_{spp}|$ as ω goes to ω_{spp}. The disappearance of the TPM resonance around ω_T is accompanied with a delocalization of the mode energy across the superlattice, as seen in Fig. 5(b). In the lossless limit, the penetration depth δ of the TPM mode diverges at ω_T, while in the real lossy case shown in Fig. 5(b), δ reaches values up to around 10 microns. The penetration depth of the single-interface SPP shown for reference (black line), varies only a bit between 20 and 30 nm over the infrared and visible frequencies, up to ω_{spp} where it has a dip.

For the $t_d < t_m$ class of superlattices, a simpler behavior is found, as depicted in Fig. 5(c) and (d). Here $|a_{TPM}|$ is only slightly below $|a_{spp}|$, while the TPM penetrates only slightly more into the superlattice, showing no pronounced spectral variations.

Figures 5(a) and (c) show that the EMA description of homointerface TPMs is not entirely accurate, after all. The fact that a_{ema} differs from a_{TPM} means that EMA does not account properly for the TPM contribution to the reflection coefficient, meaning the it will give an erroneous TPM dispersion if any additional interface is added, as it is the case with a heterointerface.

Heterointerface. A heterointerface is obtained when the capping medium permittivity ε_a differs from the permittivities ε_1, ε_2 of the two superlattice constituents, as shown in Fig. 6. The notation is chosen so that ε_1 denotes the permittivity of the top layer of the superlattice, which is shown below to play a major role in determining the types of TPMs supported by the interface. Denoting by a and b the plane wave amplitudes of the incoming and scattered wave, the heterointerface reflection coefficient r_{het} is defined as their ratio for excitation from the capping medium. Introducing the auxiliary reflection coefficient
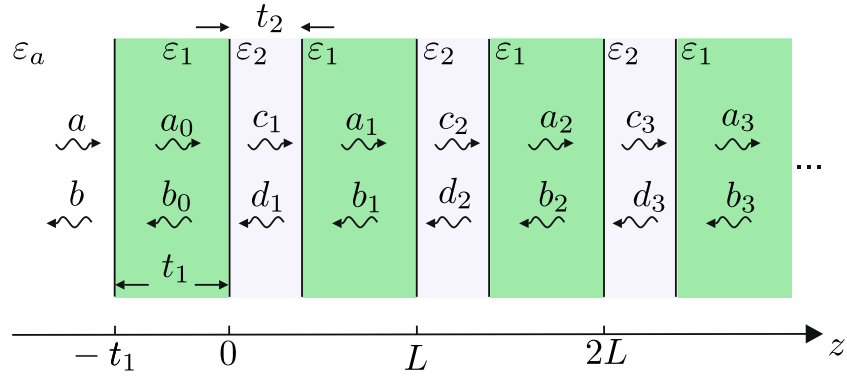
Figure 6. Schematics of the heterointerface geometry. It is obtained from the homointerface geometry in Fig. 4 by replacing the semi-infinite ε_1 medium with a semi-infinite medium ε_a extending from left infinity up to $z = -t_1$, so that the structure remains invariant for $z > -t_1$. In the text we show that the TPM properties are determined by a combined interaction of the newly added $\varepsilon_a - \varepsilon_1$ interface at $z = -t_1$ and the homointerface at $z = 0$ buried under the top ε_1 layer of the superlattice.

$$r_a = \frac{\alpha_a - \alpha_1}{\alpha_a + \alpha_1}, \tag{35}$$

which corresponds to reflection on a single interface between ε_a and ε_1, the total reflection coefficient is obtained as

$$r_{\text{het}} = \frac{r_a + r\exp(2iq_1t_1)}{1 + r_a r\exp(2iq_1t_1)}. \tag{36}$$

The condition for the existence of a TPM mode in the non-trivial case ($r_a \neq 0$ and $r \neq 0$) is that the denominator vanishes

$$1 + r_a r\exp(2iq_1t_1) = 0, \tag{37}$$

where we recognize the typical condition for a cavity resonance, with r_a and r being the mirror reflection coefficients. In ultrathin films considered here, the real part of phase $2q_1t_1$ is much below π, meaning that the heterointerface TPMs are not expected to have a Fabri-Perot character but to be formed by the modification of poles of either r_a or r, as the rapid variation of the reflection phase in their vicinity allows the condition in Eq. (37) to be satisfied.

For a given frequency ω, the complex in-plane wavenumber of a TPM fulfilling Eq. (37) will be denoted by $\beta_n(\omega)$, with $n = 1, 2, \ldots$ enumerating the existing TPMs. In contrast to the homointerface case in which only one TPM is allowed while the dependence of β_{TPM} on ω is given by an analytic expression, here multiple solutions may exist while $\beta_n(\omega)$ cannot, in principle, be expressed analytically. Therefore, we look for TPM modes by evaluating $r_{\text{het}}(\omega, \beta)$ in the $\beta - \omega$ plane[19] and use the fact that the local density of optical states $\rho(\omega, \beta)$ at the interface is proportional[25] to the imaginary part of r_{het}, so that sharp maxima of $|\text{Im}\{r_{\text{het}}\}|$ signal the presence of a TPM.

Typical r_{het} maps for $t_d > t_m$ heterointerface types are depicted in Fig. 7(a–d), with lossless single-interface $\varepsilon_d - \varepsilon_m^{(0)}$ and $\varepsilon_a - \varepsilon_m^{(0)}$ SPP dispersion curves denoted by $\beta_{\text{md}}(\omega)$ and $\beta_{\text{am}}(\omega)$ drawn for reference. In order to sharpen the map features, we compare the maps corresponding the actual silver permittivity ε_m (right panels of Fig. 7) with ones obtained by assuming reduced losses, i.e. $\varepsilon_m^{(p)}$ with $p < 1$. Here we use $p = 0.1$, as it is found to be sufficient for reliably resolving the TPM dispersion in the $\beta - \omega$ plane. As expected, the $|\text{Im}\{r_{\text{het}}\}|$ has higher values within the bands, and decreases rapidly with crossing the band edges indicated by thin (black) solid lines. The TPM modes show up as dark bands in the $\beta - \omega$ plane outside of the bulk bands.

A formal justification for relating the properties of the two maps is based on perturbation theory[22] which shows that, up to the first order, the real part of the modal wavenumber $\text{Re}\{\beta_n\}$ is independent on the perturbation parameter $g = \text{Im}\{\varepsilon_m\}/\varepsilon_m$, while $\text{Im}\{\beta_n\}$ has a linear proportionality. Therefore, the sharp maps in the left panels of Fig. 7 are used for estimating the complex β_n. The estimated value is then used as a starting guess for a Nelder-Mead minimization method[26] implemented numerically, which finds the solutions for β_n, with high accuracy, as the minima of the absolute value of the left-hand side in Eq. (37).

In the case of a metallic top layer of the $t_d > t_m$ heterointerface, two TPM modes, TPM-1 and TPM-2, are identified, as indicated by thick enumerated (red) lines in Fig. 7(b). The curves representing $\text{Re}\{\beta_1(\omega)\}$ and $\text{Re}\{\beta_2(\omega)\}$ are seen to correspond well to the sharp peaks in the vicinity of $\beta_{\text{am}}(\omega)$ and $\beta_{\text{md}}(\omega)$ curves in Fig. 7(a). At first, it might apear unusual that we do not consider the dark band in Fig. 7(a) appearing slightly above $\omega_{\text{spp,a}}$ and having a negative slope. We have found that, although formally a TPM mode, it is so far from the real β-axis that the associated propagation length is in the nanometer range, which makes it effectively indistinguishable from the air-silver surface plasmon resonance. The fact that this band appears as sharp in Fig. 7(a) as TPM-1 and TPM-2, while numerical calculations show it is dissipated much more, indicates that the perturbation picture does not
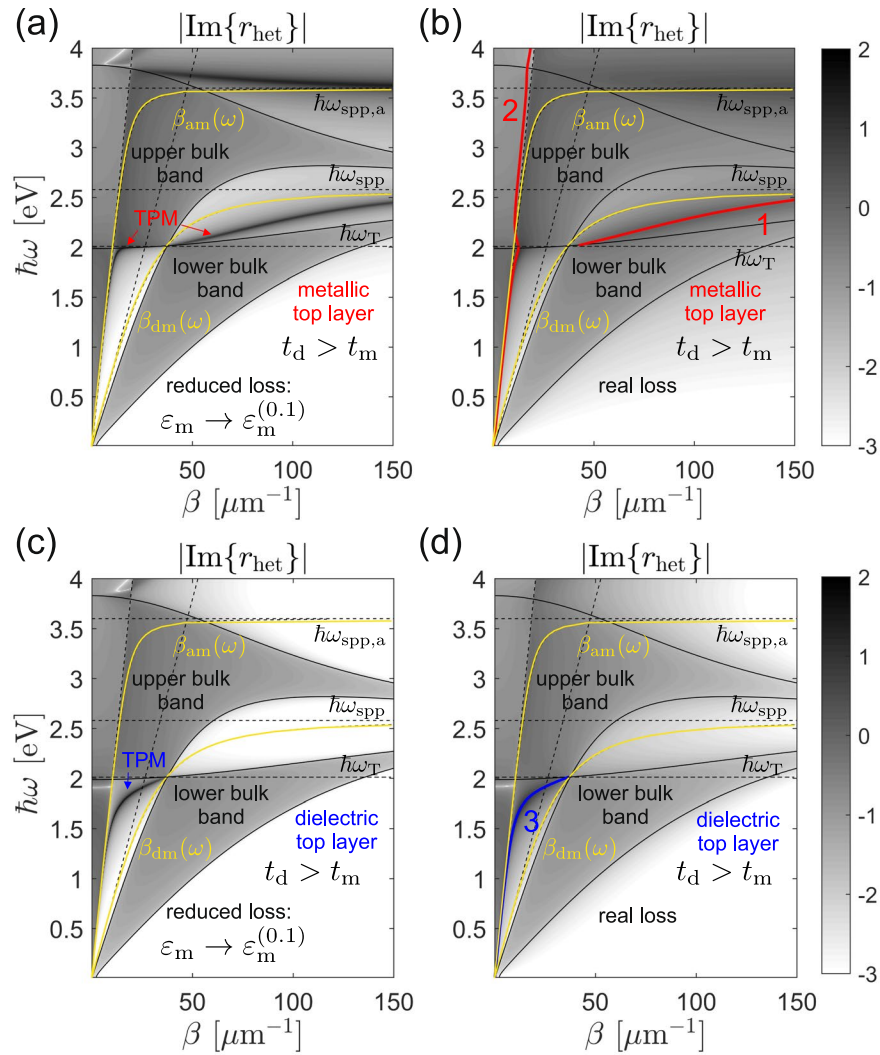
Figure 7. Maps of $|\mathrm{Im}\{r_{\mathrm{het}}\}|$ drawn in logarithmic scale with the colormap chosen so that all values outside the $(-3, 2)$ interval are saturated. Top panels are drawn for superlattices terminated by a metallic layer ($\varepsilon_1 = \varepsilon_{\mathrm{m}}$), while the bottom ones correspond to a dielectric top layer ($\varepsilon_1 = \varepsilon_{\mathrm{d}}$). Left panels: maps obtained by multiplying the imaginary part of the silver permittivity by $p = 0.1$ in order to sharpen the features and render TPMs visible. Right panels: maps obtained by taking the loss fully into account. All maps correspond to the $t_{\mathrm{d}} > t_{\mathrm{m}}$ example. The two slanted dashed lines represent the ε_a and ε_{d} light lines.

work well above the top bulk band. Indeed, in the vicinity of $\omega_{\mathrm{spp,a}}$ the real and the imaginary part of ε_{m} have comparable magnitudes, meaning that $|g|$ is not small compared to unity as required by perturbation theory[22].

The fact that TPM-1 and TPM-2 in Fig. 7(b) arise by a modification of the metal-capped homointerface TPM and the single-interface $\varepsilon_a - \varepsilon_{\mathrm{m}}$ SPP, respectively, can be shown by considering Eq. (37). Assuming first that $|r_a\mathrm{exp}(2\mathrm{i}q_1t_1)|$ is small around the $\beta_{\mathrm{TPM}}(\omega)$ pole of r, so that the $\beta_1(\omega)$ pole of r_{het} is close to $\beta_{\mathrm{TPM}}(\omega)$, r can be written as

$$r(\omega, \beta) \approx \frac{a_{\mathrm{TPM}}}{\beta - \beta_{\mathrm{TPM}}(\omega)}, \tag{38}$$

which combined with Eq. (37) yields

$$\beta_1(\omega) \approx \beta_{\mathrm{TPM}}(\omega) - a_{\mathrm{TPM}}r_a\mathrm{exp}(2\mathrm{i}q_1t_1). \tag{39}$$

This shows that if the heterointerface is obtained by gradually changing the capping permittivity from ε_1 to ε_a, the dispersion curve $\beta_1(\omega)$ gradually evolves from $\beta_{\mathrm{TPM}}(\omega)$, with a deviation increasing as r_a increases and with a factor proportional to the homointerface TPM residue a_{TPM}. Another important implication of Eq. (39) is that using EMA does not yield a correct dispersion of heterointerface TPMs because a_{ema} differs from a_{TPM}.

Repeating a similar analysis but now assuming $\beta_2(\omega)$ is in the vicinity of $\beta_{\mathrm{am}}(\omega)$, we find

$$\beta_2(\omega) \approx \beta_{\mathrm{am}}(\omega) - a_{\mathrm{spp,a}}r\mathrm{exp}(2\mathrm{i}q_1t_1), \tag{40}$$
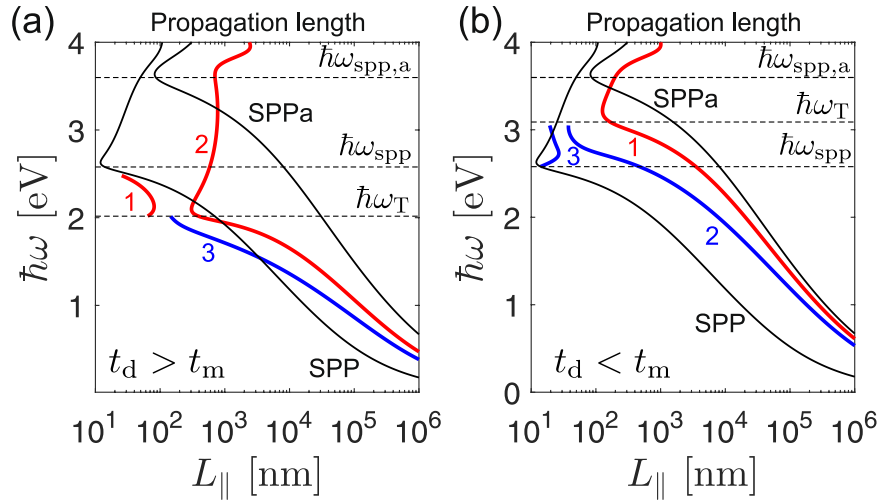
Figure 8. In-plane propagation length $L_\parallel$ for TPMs whose dispersion of $\text{Re}\{\beta_n(\omega)\}$ is drawn in (**a**) Figs 7 and (**b**) and 9. The solid lines denoted as SPP and SPPa are the $L_\parallel$ values corresponding to the $\varepsilon_d - \varepsilon_m$ and $\varepsilon_a - \varepsilon_m$ interface SPPs.
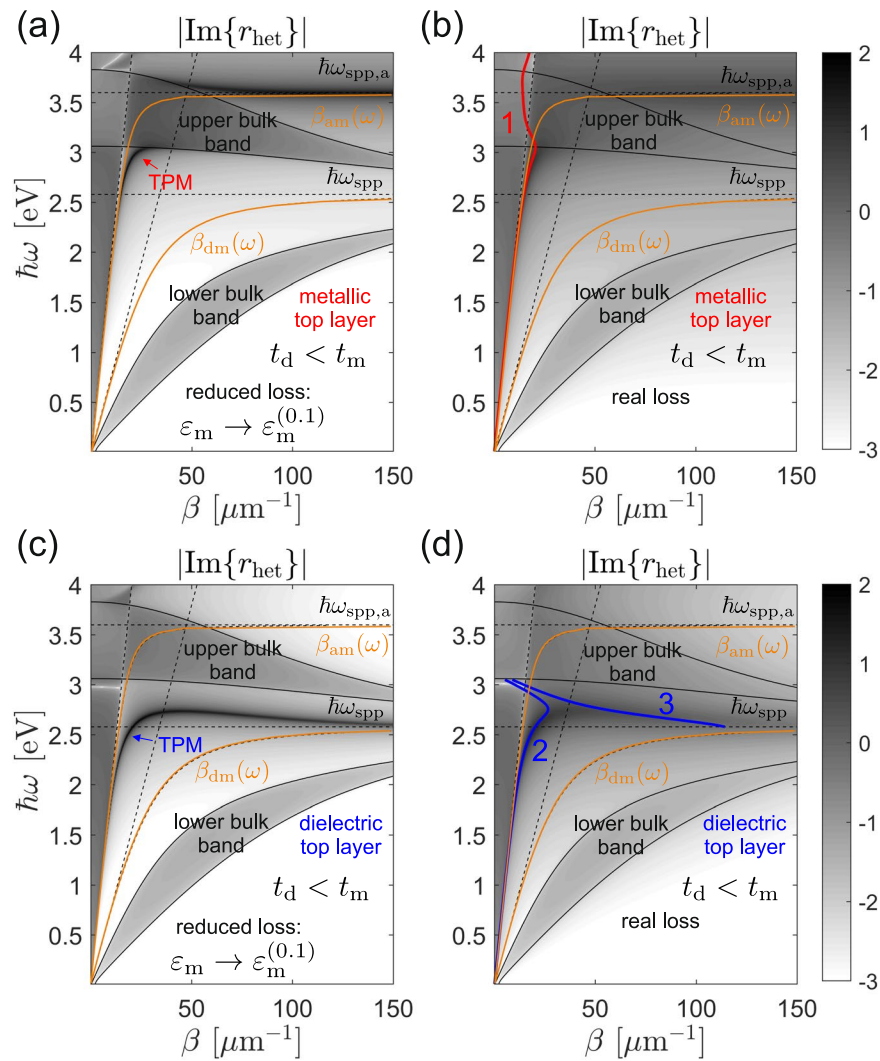

Figure 9. Maps of $|\text{Im}\{r_{het}\}|$ fully analogous to those drawn in Fig. 7, except that here the $t_d < t_m$ example is considered.
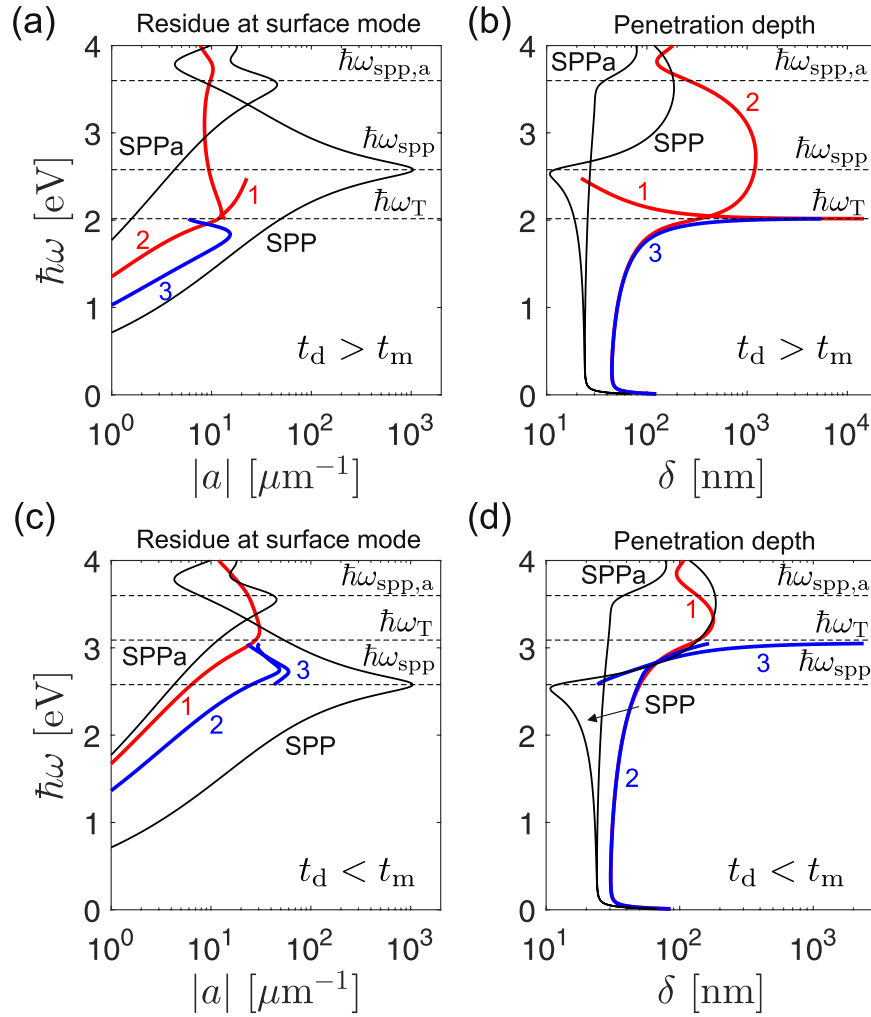
Figure 10. Left panels: residue at the TPM and SPP modes, drawn for the (**a**) $t_d > t_m$ and (**c**) $t_d < t_m$ examples, respectively. Righ panels: penetration depths into the superlattice for (**b**) $t_d > t_m$ and (**d**) $t_d < t_m$ examples, compared with the corresponding SPP penetration depth. SPP and SPPa stand for the $\varepsilon_d - \varepsilon_m$ and $\varepsilon_a - \varepsilon_m$ interface SPPs, respectively.

which shows that $\beta_2(\omega)$ will be very close to $\beta_{am}(\omega)$ if $|r\exp(2iq_1 t_1)|$ is small which e.g. is a good approximation for $t_1 = t_m = 20$ nm, or higher. Equations (39) and (40) thus allow us to classify the heterointerface TPMs into homointerface-like (TPM-1) and SPP-like (TPM-2).

The bottom two panels of Fig. 7 show the case in which the $t_d > t_m$ superlattice is terminated by the dielectric layer. Here only one solution, TPM-3, exists which evidently originates from the dielectric-capped homointerface TPM meaning it falls under the homointerface-like TPM type.

The thick TPM dispersion curves in Fig. 7 show the real part of the modal in-plane wavenumber β_n. The corresponding imaginary parts determine the lateral propagation length of the mode

$$L_{\parallel,n} = \frac{1}{\text{Im}\{\beta_n\}}. \tag{41}$$

The values obtained for the realistic (lossy) case are shown in Fig. 8(a), together with reference values corresponding to SPPs on $\varepsilon_d - \varepsilon_m$ (denoted as SPP) and $\varepsilon_a - \varepsilon_m$ (denoted as SPPa) single interfaces. At lower frequencies, both TPM-2 and TPM-3 are seen to have $L_{\parallel}$ values between the two single-interface SPP limits. As ω_T is approached, the propagation length of TPM-3 drops which is a result of the reduced group velocity, cf. the reduced slope of TPM-3 in the vicinity of ω_T in Fig. 7(d). The $L_{\parallel}$ value of TPM-2 also drops above ω_T, but here the reason is that it hybridizes with bulk modes in the superlattice and free space modes in the ε_a light cone and leaks away from the surface, cf. Fig. 7(b) where the thick (red) line denoted by 2 is seen to enter the ε_a lightcone once it enters the upper bulk band. Finally, TPM-1 is seen to have extremely low propagation lengths (below 100 nm) over the entire spectrum in which it is supported, which is the concequence of the vicinity of the SPP resonance at ω_{spp}.

Analogous r_{het} maps obtained for the $t_d < t_m$ example are plotted in Fig. 9(a–d). As here $\omega_T > \omega_{spp}$, homointerface-like TPMs appear only in the case of a dielectric top layer, as indicated by the TPM-2 and TPM-3

lines in Fig. 9(d). The shape of the TPM band indicated in Fig. 9(c) shows that the effect of replacing titanium dioxide by air as the capping medium blueshifts the homointerface TPM and deforms it so that its slope becomes zero around $\beta \approx 35\,\mu\mathrm{m}^{-1}$ and negative for larger β. This implies that at frequencies slightly above ω_{spp} there are two TPM modes, which is confirmed by the numerically found TPM-2 and TPM-3 dispersion curves in Fig. 9(d). Here it should be noted that the TPM-3 curve represents $-\mathrm{Re}\{\beta_3\}(\omega)$, i.e. the actual dispersion curve lying in the $\beta < 0$ half-space is folded to the positive sided for a compact representation, see also refs[22,23], for further discussion of this topic.

The TPM mode of the $t_{\mathrm{d}} < t_{\mathrm{m}}$ superlattice with metallic top layer is a modified $\varepsilon_a - \varepsilon_{\mathrm{m}}$ single-interface SPP, as evident from its dispersion in Fig. 9(a) and (b), where it is seen to closely follow the $\beta_{\mathrm{am}}(\omega)$ curve, up until hybridizes with modes from the upper bulk band after which the pole shifts into the ε_a light cone and starts leaking out into both the superlattice and capping layer propagating modes. The propagation lengths of the TPM modes of the $t_{\mathrm{d}} < t_{\mathrm{m}}$ example are shown in Fig. 8(b).

The resonance strength and confinement degree of heterointerface TPM modes for the considered two superlattice types is summarized in Fig. 10(a–d). Perhaps the most relevant case is that of the $t_{\mathrm{d}} > t_{\mathrm{m}}$ supperlattice with a dielectric top layer supporting TPM-3 depicted in Fig. 10(a). Similarly as its homointerface counterpart, by the perturbation of which TPM-3 is formed, the resonance strength of this mode is seen to rapidly decrease as ω_{T} is approached while it becomes delocalized across the superlattice, as seen in Fig. 10(c).

Summary and conclusion. This paper presents a systematic analysis of surface waves on two-phase semi-infinite metallodielectric superlattices. As their character is determined by the properties of the periodic arrangement of unit cells, in analogy with surface electronic states in crystals, these waves are termed Tamm plasmon modes.

It is shown that if the capping medium has the same permittivity as one of the superlattice constituents, a case referred to as the homointerface, TPM modes can exist only along the single-interface SPP dispersion curve and that there exists a critical frequency ω_{T} which represents the upper limit for the TPM existence in the dielectric- and the lower frequency limit in the metal-capped superlattice and is determined by the superlattice composition and relative layer thicknesses. This fact is particularly relevant if ω_{T} is below the SPP resonance frequency, which happens if the dielectric layers are thicker than the metal layers. Both the dielectric- and metal-capped TPMs become delocalized across the lattice when ω_{T} is approached, while the strength of the corresponding resonance, quantified by residues of the reflection coefficient at the associated poles, dies out.

The heterointerface, where the capping medium permittivity differs from that of the superlattice constituents and most relevant in practice as it includes the case of the superlattice exposed to air, is found to be exhibit a more complex behavior. We show that the heterointerface TPMs can be analyzed as resulting from either the capping-top layer interface, or an homointerface TPM located at the interface between the top layer and the rest of the superlattice. The homointerface-like TPMs, originating from the latter group, are found to also exhibit the critical behaviour around ω_{T}.

In view of the significance of the effective medium approximation for the ongoing research on hyperbolic metamaterials, we have also compared its predictions against the exact theory. Somewhat surprisingly, we find that EMA accurately describes several important aspects of homointerface TPMs with arbitrary layer thicknesses, including the critical behaviour, but that it fails entirely in the heterointerface case.

These results are important for engineering the optical properties of semi-infinite metallodielectric superlattices which have recently been receiving strong attention in connection with enhanced spontaneous emission into the bulk superlattice modes. The analysis reported here should help quantify the individual contributions of the bulk and TPM modes in the total optical density of states at the interface and thus tailor the amount of emitted light that propagates through the superlattice or stays tied at the interface, respectively.

References

1. Cai, W. & Shalaev, V. *Optical Metamaterials* (Springer, New York, 2010).
2. Maier, S. A. *Plasmonics: Fundamentals and Applications* (Springer, 2007).
3. Poddubny, A., Iorsh, I., Belov, P. & Kivshar, Y. Hyperbolic metamaterials. *Nat. Photon.* **7**, 948–957 (2013).
4. Chen, W., Thoreson, M. D., Ishii, S., Kildishev, A. V. & Shalaev, V. M. Ultra-thin ultra-smooth and low-loss silver films on a germanium wetting layer. *Opt. Express* **18**, 5124–5134 (2010).
5. Jacob, Z. *et al.* Engineering photonic density of states using metamaterials. *Appl. Phys. B* **100**, 215–218 (2010).
6. Jacob, Z., Smolyaninov, I. I. & Narimanov, E. E. Broadband purcell effect: Radiative decay engineering with metamaterials. *Appl. Phys. Lett.* **100**, 181105 (2012).
7. Ferrari, L., Wu, C., Lepage, D., Zhang, X. & Liu, Z. Hyperbolic metamaterials and their applications. *Prog. Quant. Electron.* **40**, 1–40 (2015).
8. Kaliteevski, M. *et al.* Tamm plasmon-polaritons: Possible electromagnetic states at the interface of a metal and a dielectric bragg mirror. *Phys. Rev. B* **76**, 165415 (2007).
9. Sasin, M. E. *et al.* Tamm plasmon polaritons: Slow and spatially compact light. *Appl. Phys. Lett.* **92**, 251112 (2008).
10. Gazzano, O. *et al.* Evidence for confined tamm plasmon modes under metallic microdisks and application to the control of spontaneous optical emission. *Phys. Rev. Lett.* **107**, 247402 (2011).
11. Symonds, C. *et al.* Confined tamm plasmon lasers. *Nano Lett.* **13**, 3179–3184 (2013).
12. Zhang, C., Wu, K., Giannini, V. & Li, X. Planar hot-electron photodetection with tamm plasmons. *ACS Nano* **11**, 1719–1727 (2017).
13. Zhang, W. L., Wang, F., Rao, Y. J. & Jiang, Y. Novel sensing concept based on optical tamm plasmon. *Opt. Express* **22**, 14524–14529 (2014).
14. Das, R., Srivastava, T. & Jha, R. Tamm-plasmon and surface-plasmon hybrid-mode based refractometry in photonic bandgap structures. *Opt. Lett.* **39**, 896–899 (2014).
15. Krishnamoorthy, H., Jacob, Z., Narimanov, E., Kretzschmar, I. & Menon, V. Topological transitions in metamaterials. *Science* **336**, 205–209 (2012).
16. Kidwai, O., Zhukovsky, S. V. & Sipe, J. E. Effective-medium approach to planar multilayer hyperbolic metamaterials: Strengths and limitations. *Phys. Rev. A* **85**, 053842 (2012).

17. Newman, W. D., Cortes, C. L. & Jacob, Z. Enhanced and directional single-photon emission in hyperbolic metamaterials. *J. Opt. Soc. Am. B* **30**, 766–775 (2013).
18. Ford, G. & Weber, W. Electromagnetic interactions of molecules with metal surfaces. *Phys. Rep.* **113**, 195–287 (1984).
19. Isić, G. & Gajić, R. Lifetime and propagation length of light in nanoscopic metallic slots. *J. Opt. Soc. Am. B* **31**, 393–399 (2014).
20. Yeh, P., Yariv, A. & Hong, C.-S. Electromagnetic propagation in periodic stratified media. i. general theory. *J. Opt. Soc. Am.* **67**, 423–438 (1977).
21. Rakic, A. D., Djurisic, A. B., Elazar, J. M. & Majewski, M. L. Optical properties of metallic films for vertical-cavity optoelectronic devices. *Appl. Opt.* **37**, 5271–5283 (1998).
22. Isić, G., Gajić, R. & Vuković, S. Plasmonic lifetimes and propagation lengths in metallodielectric superlattices. *Phys. Rev. B* **89**, 165427 (2014).
23. Rosenblatt, G. & Orenstein, M. Competing coupled gaps and slabs for plasmonic metamaterial analysis. *Opt. Express* **19**, 20372–20385 (2011).
24. Born, M. & Wolf, E. *Principles of optics* (Cambridge University Press, 2005).
25. Novotny, L. & Hecht, B. *Principles of Nano-Optics* (Cambridge University Press, 2012).
26. Nelder, J. A. & Mead, R. A simplex method for function minimization. *Comput. J.* **7**, 308–313 (1965).

Acknowledgements

Author Contributions

S.V. and G.I. conceived the analysis, G.I. conducted the numerical calculations, All authors discussed the results and reviewed the manuscript.

Additional Information

Competing Interests: The authors declare that they have no competing interests.

Publisher's note: Springer Nature remains neutral with regard to jurisdictional claims in published maps and institutional affiliations.

CrossMark

Subwavelength nickel-copper multilayers as an alternative plasmonic material

I. Mladenović[1] · Z. Jakšić[1] · M. Obradov[1] · S. Vuković[2] · G. Isić[2] · D. Tanasković[1] · J. Lamovec[1]

Abstract Surface plasmon polaritons (SPP) are electromagnetic waves bound by the collective oscillations of free carrier plasma to the surface of a conductor surrounded by dielectric. These waves can be localized, concentrated or manipulated simply by processing the conductor surface. The choice of a convenient conductor is quite limited by the availability of natural materials and strong absorption losses associated with free electron plasma. For this reason new alternative plasmonic materials are actively being researched and developed. Most common approaches to this problem include doping of nonmetallic materials and fabrication of metal-dielectric nanocomposite metamaterials. In this contribution we perform an analysis of the suitability of the use of the heterometallic multilayers consisting of copper and nickel. Copper is an excellent plasmonic material, but the problem is formation of natural copper oxides on the surface. Therefore for this purpose a layer of nickel is used as a protection against oxidation of copper. Laminate composite structures of alternating nanocrystalline nickel and copper films on a cold-rolled polycrystalline copper foils were fabricated by electrochemical deposition technique. We simulated the electromagnetic properties of subwavelength Cu/Ni multilayers by the 2D finite element method using realistic material parameters to assess different electromagnetic modes. Our results show that the pair Cu/Ni can be viewed as an alternative tailorable plasmonic material. It has also been shown that it is possible to fabricate plasmonic structures without applying any complex lithographic processes.

✉ I. Mladenović
   ivana@nanosys.ihtm.bg.ac.rs

1   Centre of Microelectronic Technologies, Institute of Chemistry, Technology and Metallurgy, University of Belgrade, Njegoševa 12, 11000 Belgrade, Serbia

2   Institute of Physics, University of Belgrade, Pregrevica 118, 11080 Belgrade, Serbia

⚛ Springer

1 Introduction

Plasmonic materials ensure extreme concentrations and localizations of electromagnetic fields as a consequence of the appearance of evanescent waves (surface plasmons polaritons—SPP) in the range of negative values of relative dielectric permittivity (Maier 2007). The many applications of plasmonics include ultrasensitive chemical sensors, advanced all-optical devices, enhanced photodetectors, energy harvesting devices and many others (Ozbay 2006; Anker et al. 2008; Aubry et al. 2010).

Among hurdles to a more widespread use of plasmonics are a rather limited range of available plasmonic materials (usually good metals like gold and silver) and their high absorption losses in the range of interest. This is why alternative plasmonic materials are of great interest (West et al. 2010). Besides using materials like transparent conductive oxides, highly doped semiconductors, intermetallics and similar, a possible approach is to combine a plasmonic material with lossless dielectric into mesoscopic or subwavelength nanocomposites (plasmonic crystals) (Vuković et al. 2011), thus allowing almost arbitrary tailoring of frequency dispersion in a spectral range defined by the plasma frequency.

Thin copper films are mostly used in electronic applications due to high conductivity of copper and low production costs. Together with nickel, copper is the most common choice for metallic plating (Schlesinger and Paunovic 2011). Furthermore laminar structures of alternating thin layers of copper and nickel offer excellent approach in tuning mechanical properties of metallic coatings (Lamovec et al. 2011). Several different techniques have been developed for the deposition of thin metal films for plasmonic structures (Nagpal et al. 2009) but an interesting approach for growing of metal and alloy layers is the use of electrochemical deposition technique. Electrochemical deposition (ED) technique is fully compatible with other MEMS technologies, it is a low temperature deposition technique with possibility of easy controlled deposition rate, thickness and microstructure of the metallic films (Datta and Landolt 2000).

In this contribution we consider the use of bimetallic superlattices, i.e. all-metal 1D plasmonic crystals consisting of two alternating materials with negative values of their relative dielectric permittivities as plasmonic materials with tailorable properties. Copper is a good plasmonic material, but not widely used due to surface oxidation impairing its electromagnetic properties over time. The layers of nickel, also a plasmonic material, serve a dual purpose of being a protection against copper oxidation and ensuring formation of surface waves at the alternating interfaces between the two materials. At the same time, the multilayers serve as couplers between the propagating and the surface waves. We examine the optical properties of nickel-copper multilayers numerically, utilizing the finite element program package Comsol Multiphysics and fabricate nanocrystalline Cu/Ni multilayers using an ED technique.

2 Theory

We investigate a multilayer structure with individual strata of nickel and copper, each described by its complex relative dielectric permittivity and thickness. The geometry of the heterometallic multilayer is shown in Fig. 1a). Coupling of propagating waves to bound
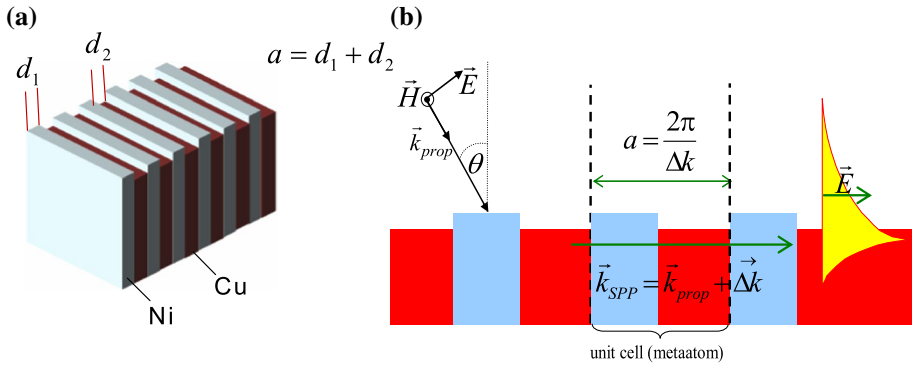
Fig. 1 a Schematic presentation of geometry of our heterometallic multilayer. Surface relief is visible at the top of structure; **b** coupling between the SPP and the TM polarized propagating wave with incident angle θ on a diffractive grating (in this case the surface relief on the Cu-Ni multilayer). Yellow area shows the intensity of the electric field of the SPP versus distance from the interface. (Color figure online)

surface modes is only possible by matching the wave vectors via refractive or diffractive elements. Impedance matching between the propagating wave (k_{prop}) and SPP (k_{SPP}) via diffraction grating (Δk) is shown in Fig. 1b). This allows for practically arbitrary tailoring of optical properties by changing geometrical properties of the grating. Diffractive grating is readily formable by selectively etching one of the two metal constituents.

We assume that the relative dielectric permittivity of each metal is well described by the lossy extended Drude model (Maier 2007):

$$\varepsilon(\omega) = \varepsilon_\infty - \frac{\omega_p^2}{\omega^2 + i\gamma\omega} \tag{1}$$

where ε_∞ is the asymptotic dielectric permittivity and $\gamma = 1/\tau$ is the characteristic frequency related to the damping of electron oscillations due to collisions, where τ is the relaxation time of the electron gas and ω_p is the plasma frequency, determined by the concentration of free carriers

$$\omega_p = \frac{ne^2}{m^*\varepsilon_0} \tag{2}$$

where n is the electron concentration, e is the free electron charge, ε_0 is the dielectric permittivity of vacuum, and m^* is the effective mass of electrons.

3 Experimental procedure

For our experiments we used a polycrystalline Cu foil (125 μm thick) as a substrate for electrodeposition of thin copper and nickel films. For each experiment samples were processed as follows: substrate preparation, electrochemical reagent preparation, electrodeposition process and microscopic analysis of samples. Prior to deposition substrate was washed, degreased and chemically polished in a mixture of acids HNO_3:H_3PO_4:$CH_3COOH = 4$: 11: 5 vol%. Copper films were electrodeposited from a sulfate bath consisting of 240 g/l CuSO4 ·5H_2O, 40.8 ml H_2SO_4 and deionized water. Process temperature and pH were

maintained at 25 °C and 0.4 respectively. We used a copper electrode with a cylindrical shape. The volume of the electrolyte was 100 ml. Nickel films were electrodeposited from a sulfamate bath consisting of 300 g/l $Ni(NH_2SO_3)_2 \cdot 4\ H_2O$, 30 g/l $NiCl_2 \cdot 6H2O$, 30 g/l H_3BO_3, 1 g/l saccharine with maintained temperature and pH values at 50 °C and 4.2, respectively. The volume of 500 ml electrolyte, magnetic stirring and pure Ni electrodes were used. Electrochemical deposition was carried out using direct current galvanostatic mode with the current density values maintained at 10 mA/cm^2 and 50 mA/cm^2. The deposition time was determined in dependence on the plating surface and the projected thickness of deposits. The electrodeposition efficiency for Cu is about 97–98%, for Ni it is a little lower. Ni and Cu films were electrodeposited separately from two different electrolytes. This technique is known as the Dual Bath Technique (DBT). (Zhang et al. 2015)

Process of revealing the geometry of the multilayer structure started with a perpendicular cut of the deposited films. The samples were embedded in a self-curing methyl methacrylate-polymer (Palavit G, Heraeus, Germany) and mechanically polished with different SiC papers and alumina powder with different grain size (1 and 0.3 μm). Rinsing solution of Na_2CO_3 was used to avoid agglomeration of the alumina powder. Finally the structures were dried in nitrogen flow.

Then, acidic solution of 1 M thiourea at 40 °C (pH = 1, achieved by adding HCl) was used for selective etching of copper layers, while nickel layers showed chemical resistance to this solution. Etching time of varies from 5 to 25 s.

4 Numerical modeling

We examined optical properties of bimetallic plasmonic crystal shown in Fig. 1. Using the finite element method. To this purpose we utilized the RF module of Comsol Multiphysics software package. Entire plasmonic crystal can be represented by its metaatom, a single pair of Ni\Cu layers and Floquet periodic boundary condition applied to the edges of the unit cell parallel to the layers. Boundary conditions correspond to dashed lines marking a grating period in Fig. 1b. Light enters simulation domain from air via an active port. We assume that the incident light is TM polarized. Dispersive properties are obtained by performing a parametric sweep of wavelengths of interest. For the needs of our simulation the plasmonic crystal is considered infinite in the direction perpendicular to the layers. The parameters of Drude model describing the relative permittivity of the metals are taken from literature. (Rakić et al. 1998).

Dispersive properties of our structure are shown in Figs. 2, 3 and 4. Reflection is calculated as ratio between total power received and emitted by the active port. What can readily be seen is that the structure exhibits rich modal behavior manifested as dips in reflection when incident light couples into plasmonic modes. When incident light fully couples into surface modes (Fig. 2) structure behaves as a perfect absorber since there is no transmission through the structure. Furthermore dispersive properties are fully tailorable by changing the thickness of individual layers.

Electric field distributions of surface modes are shown in Figs. 5, 6. Distributions are shown for three unit cells to better illustrate the response of the metamaterial as a whole. Strongest coupling is achieved for structures with Cu layers thicker than Ni layers and almost all of the incident light is localized on subwavelength scale within the channels formed by selective etching of copper as shown in Fig. 5. But since we have a bimetallic structure plasmonic modes can also be bound to the surface of Ni layers

Fig. 2 Dispersive properties of Ni/Cu plasmonic crystal for different values of layer thickness and normal incidence; Ni layer thickness is kept constant at 100 nm, Cu thickness varies from 100 nm to 400 nm
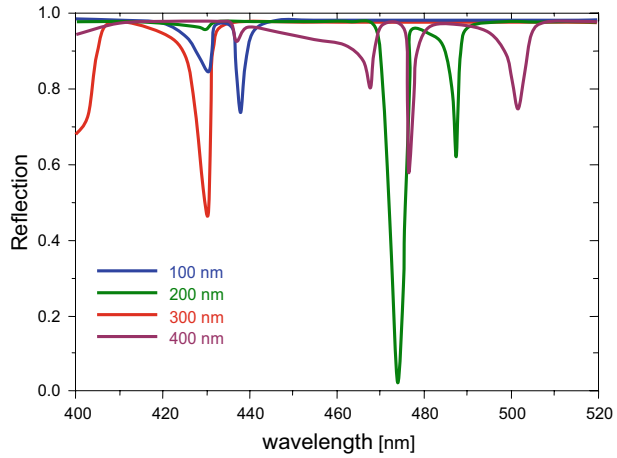
Fig. 3 Dispersive properties of Ni/Cu plasmonic crystal for different values of layer thickness and normal incidence Cu layer thickness is kept constant at 100 nm, Ni thickness varies from 100 nm to 400 nm
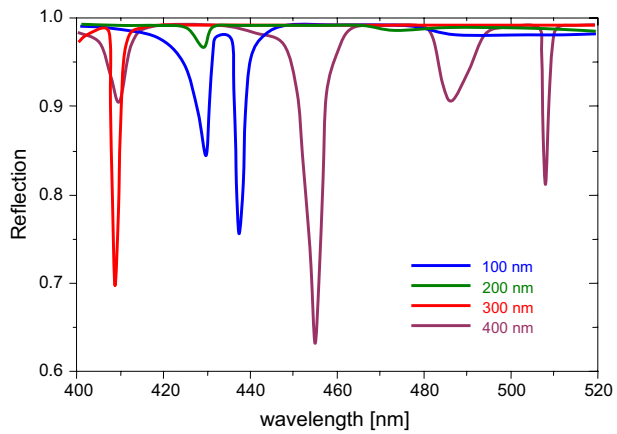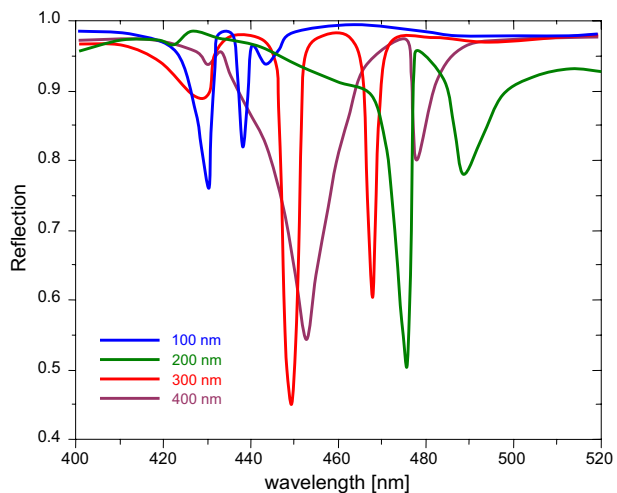
Fig. 4 Dispersive properties of Ni/Cu plasmonic crystal for different values of layer thickness at 30° incident angle. Ni layer thickness is kept constant at 100 nm, Cu thickness varies from 100 nm to 400 nm
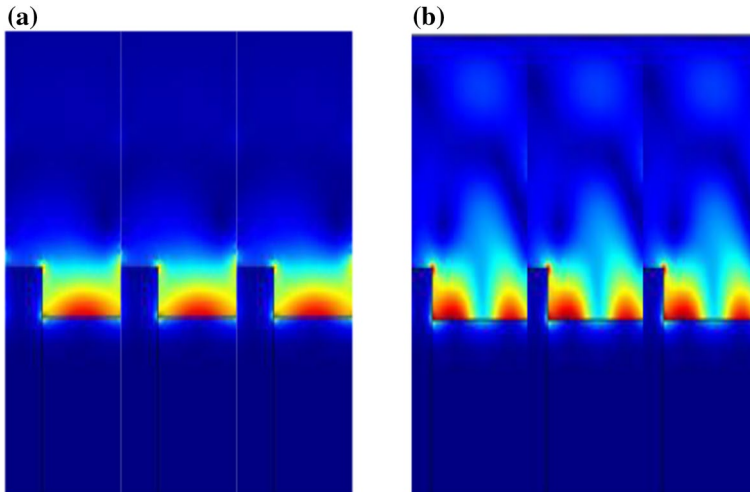
Fig. 5 Electric field distribution Ni/Cu plasmonic crystal: **a** for 100 nm/200 nm at 475 nm wavelength, normal incidence; **b** for 100 nm/400 nm at 455 nm wavelength and 30° incident angle
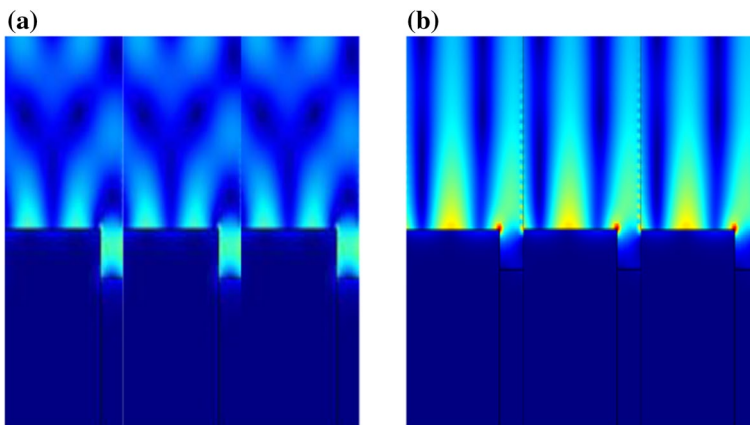

Fig. 6 Electric field distribution for 400 nm/100 nm Ni/Cu plasmonic crystal and normal incidence: **a** 410 nm wavelength; **b** 510 nm wavelength

as shown in Fig. 6 for structures with thicker Ni layers. This shows that in addition to tailoring macroscopic optical response we can also tailor transformations of the optical space simply by varying thickness of the layers. While geometrical properties of the grating define the operating range of the structure i.e. increasing the layers thickness would push operating range into infrared, material properties limit its usefulness. High absorptive loses of metals at longer wavelengths while potentially useful for far field response (absorber) would severely hamper near field response (light localization) thus depriving us of the entire aspect of potential applications.

5 Experimental results

Microstructure of copper-nickel composite fabricated using the procedure described in Sect. 3 of the paper was investigated using metallographic microscopy (Carl Zeiss microscope "Epival Interphako"). Topographic details of multilayer cross-section were investigated using Scanning Electron Microscope (SEM, JEOL JSM-6610LV). Structure consists of 21 alternating copper and nickel layers deposited on a copper substrate. The thicknesses of each layer is 1 μm.

Microstructure of the Ni/Cu multilayer before the selective etching of copper layers in thiourea solution is shown in Fig. 7a. Microstructure after etching the copper layers in acid thiourea solution for 5 s is presented in Fig. 7b. We can see that the copper

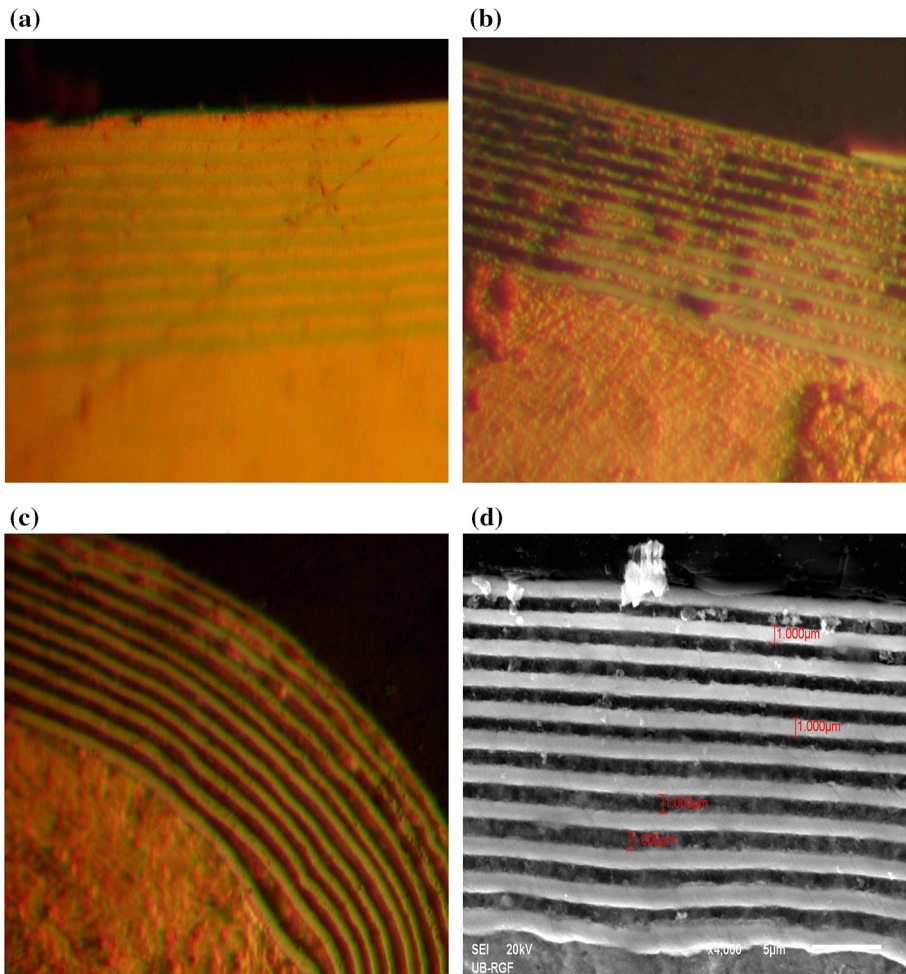**Fig. 7** Cross-section of an electrodeposited Ni/Cu multilayer, thickness 1 μm/1 μm: **a** before a selective etching of copper; **b** after 5 s etching of copper layers in thiourea solution, **c** after 25 s etching; **d** SEM image after 25 s etching

is only partially removed manifesting as islands both between nickel layers and on the copper substrate so it is necessary to increase the etching time. Results after 25 s etching process are presented in Fig. 7c. (optical image) and Fig. 7d. (SEM image). Darker bands are Cu channels while brighter bands are Ni layers (Fig. 7b, c, d). It can be seen that both Cu and Ni layers have uniform thickness. Good repeatability of the layer thickness is also observed. Layer thickness is controlled by the duration and applied current density of the ED process. The surface morphology of the substrate plays an important role in the growth of the deposits (Fig. 7c, d). Layer closest to the surface follows surface morphology and has poor uniformity but the quality of the layers improves with the number of layers. The appearance of cracks and delamination of the layers was not observed.

6 Conclusion

We simulated the electromagnetic properties of subwavelength Cu–Ni multilayers by the 2D finite element method using realistic material parameters. A rich optical behavior was obtained, as governed by the electromagnetic properties of the multilayers. We adjusted both the far field and the near field response of the structure by simply varying Cu to Ni thickness ratio. Experimentally, we fabricated 1D plasmonic crystals consisting of alternately stacked nanocrystalline Ni and Cu layers by electrodeposition on a cold-rolled copper substrate. We obtained highly parallel interfaces with thin individual strata and excellent morphology. We made use of beneficial structural properties of both Cu and Ni, while suppressing the undesirable ones. This approach offers high quality, large area, compact and low cost structures, while retaining a compatibility with the standard microfabrication and microelectronic processes. Uniformity and deposition control can be further improved by introducing more efficient mixing of electrolytes (ultrasound) and adding specific surfactants to the electrolyte, which is the direction of our further research.

References

Anker, J.N., Hall, W.P., Lyandres, O., Shah, N.C., Zhao, J., Van Duyne, R.P.: Biosensing with plasmonic nanosensors. Nat. Mater. **7**(6), 442–453 (2008)

Aubry, A., Lei, D.Y., Fernández-Domínguez, A.I., Sonnefraud, Y., Maier, S.A., Pendry, J.B.: Plasmonic light-harvesting devices over the whole visible spectrum. Nano Lett. **10**(7), 2574–2579 (2010)

Datta, M., Landolt, D.: Fundamental aspects and applications of electrochemical microfabrication. Electrochim. Acta **45**(15), 2535–2558 (2000)

Lamovec, J., Jović, V., Vorkapić, M., Popović, B., Radojević, V., Aleksić, R.: Microhardness analysis of thin metallic multilayer composite films on copper substrates. J. Min. Metall. Sect. B. **47**(1), 53–61 (2011)

Maier, S.A.: Plasmonics: Fundamentals and Applications. Springer Science + Business Media, New York (2007)

Nagpal, P., Lindquist, N.C., Oh, S.-H., Norris, D.J.: Ultrasmooth patterned metals for plasmonics and metamaterials. Science **325**(5940), 594–597 (2009)

Ozbay, E.: Plasmonics: merging photonics and electronics at nanoscale dimensions. Science **311**(5758), 189–193 (2006)

Rakić, A.D., Djurišić, A.B., Elazar, J.M., Majewski, M.L.: Optical properties of metallic films for vertical-cavity optoelectronic devices. Appl. Opt. **37**(22), 5271–5283 (1998)

Schlesinger, M., Paunovic, M.: Modern electroplating. Wiley, New York (2011)

Vuković, S.M., Jakšić, Z., Shadrivov, I.V., Kivshar, Y.S.: Plasmonic crystal waveguides. Appl. Phys. A Mater. Sci. Process. **103**(3), 615–617 (2011)

West, P.R., Ishii, S., Naik, G.V., Emani, N.K., Shalaev, V., Boltasseva, A.: Searching for better plasmonic materials. Laser Photon. Rev. **4**, 1–13 (2010)

Zhang, B., Kou, Y., Xia, Y., Zhang, X.: Modulation of strength and plasticity of multiscale Ni/Cu laminated composites. Mater. Sci. Eng. A **636**, 216–220 (2015)

Terahertz Modulation by Schottky Junction in Metal-Semiconductor-Metal Microcavities

Goran Isić[1,2,*], Georgios Sinatkas[3], *Student Member, IEEE*, Dimitrios C. Zografopoulos[4], Borislav Vasić[1],
Antonio Ferraro[4], *Member, IEEE*, Romeo Beccherelli[4], *Member, IEEE*,
Emmanouil E. Kriezis[3], *Senior Member, IEEE*, and Milivoj Belić[2]

[1]*Graphene Laboratory of Center for Solid State Physics and New Materials, Institute of Physics Belgrade,
University of Belgrade, Pregrevica 118, 11080 Belgrade, Serbia*

[2]*Texas A&M University at Qatar, Doha 23874, Qatar*

[3]*School of Electrical and Computer Engineering, Aristotle University of Thessaloniki,
Thessaloniki 52124, Greece*

[4]*Consiglio Nazionale delle Ricerche, Istituto per la Microelettronica e Microsistemi, Rome 00133, Italy*
* Tel: (38111) 3713 050, Fax: (38111) 3162 190, e-mail: isicg@ipb.ac.rs

ABSTRACT

We discuss arrays of metal-semiconductor-metal cavities as electrically tunable terahertz metasurfaces. The operation of the considered device is based on reverse biasing the Schottky junction formed between top metal strips and the n-type semiconductor buried beneath. The effective Drude permittivity of the cavity array is tuned by changing the depletion layer thickness via a gate bias applied between the strips and a back metal reflector. Combining Maxwell equations for terahertz waves with a drift-diffusion model for the semiconductor carriers into a multiphysics framework, we show that the proposed modulation concept is promising for a large part of the terahertz spectrum.

Keywords: terahertz metasurface, tunable metamaterial, terahertz modulation, Schottky junction.

1. INTRODUCTION

The development of fast electro-optic modulators for free-space terahertz waves is one of the important challenges for terahertz technology and further progress in wireless communications. Following the low modulation efficiencies found in initial experiments [1,2], which were ascribed to weak interaction of the terahertz wave with the electron system [3], recent works have mostly employed resonant metasurfaces for increasing the modulation efficiency [4-10]. In addition to semiconductors which seem to be most promising for high-speed modulation [11], graphene [12] and liquid crystal [13-15] modulators have recently been attracting attention. In contrast to existing semiconductor devices employing antenna-like elements for tuning, here [16] we consider the use of a metal-semiconductor-metal resonant cavity array, known for providing a strong light-matter interaction [17,18].
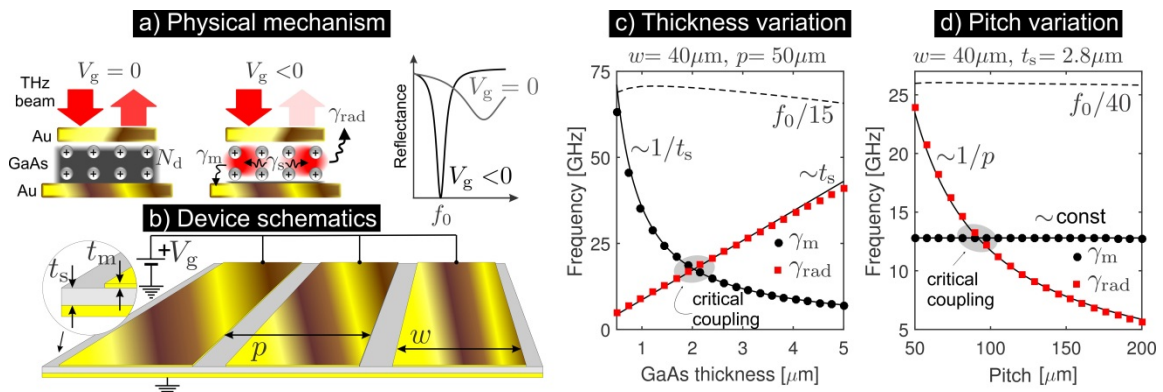

Figure 1. Schematics of a) cavity-response tuning through carrier depletion and the resulting reflectance modulation, b) real-scale device. c) and d) show the dependence of the TCMT parameters on device geometry.

2. MODULATION PRINCIPLE

The proposed device comprises an array of metal-semiconductor-metal cavities as shown in Figs. 1(a) and 1(b), whereby the semiconductor (gallium arsenide-GaAs) is highly doped and prepared to form a Schottky junction with the top electrode and an ohmic contact with the bottom one. With no bias, the free carriers inhibit the penetration of terahertz fields and strongly dissipate the fields inside the cavity through Joule heating. Upon applying a sufficiently high reverse bias, the depletion layer extends down to the bottom electrode and the cavity is able to support a resonant mode at f_0. According to a formalism known as the temporal coupled-mode theory (TCMT) [19,20], in addition to f_0, two more parameters are sufficient to fully characterize the resonant optical

response of such a cavity array: the resonant mode non-radiative decay rate γ_0 and its radiative decay rate γ_{rad}. γ_0 is the sum of all absorption mechanisms, including absorption in the metal and Joule losses by the free carriers in GaAs. However, at full cavity depletion, the Joule losses are negligible and γ_0 becomes equal to the metal absorption rate γ_m. To achieve optimal performance, in this work we aim at designing the cavities (i.e. choosing their geometrical parameters) so that $\gamma_0 \approx \gamma_{rad}$ which represents the so-called critical coupling regime and results in 100% absorption at f_0. Figures 1(c) and 1(d) show how the TCMT parameters depend on the cavity array height and pitch, with further details discussed in [16,21]. The modulation principle is thus based on having 100% absorption at high reverse bias (fully depleted and critically coupled cavity) and a rather inefficient absorption at resonance (typically 10% or less) at zero V_g, resulting from the combined detuning of the resonance and its weak coupling with the terahertz wave due to $\gamma_0 \gg \gamma_{rad}$.

For purposes of illustration, below we consider the case of a modulator designed to operate at f_0=1 THz. The cavity geometrical parameters yielding critical coupling for f_0 ranging across the terahertz range can be obtained analogously or even faster by scaling the 1 THz cavity, Fig. 2(a) [20].

The dopant concentration N_d is the final parameter affecting the device operation. Since a higher electron concentration leads to a higher resonance detuning at zero bias, N_d should be as high as possible while still allowing the full depletion of the cavity at the maximal reverse bias $-V_{g,max}$. The latter is estimated via the so-called critical field approximation whereby the junction breakdown is assumed to occur once the electric field at the junction surpasses 4×10^7 V/m, which is reasonably accurate for the doping range considered in our work [22]. The gate effect in the considered system is studied using a rigorous solid-state physics framework based on a majority-carrier solution scheme [23,24], while typical electron concentration and electric field profiles for the 1 THz geometry are shown in Figs. 2(b) and 2(c).
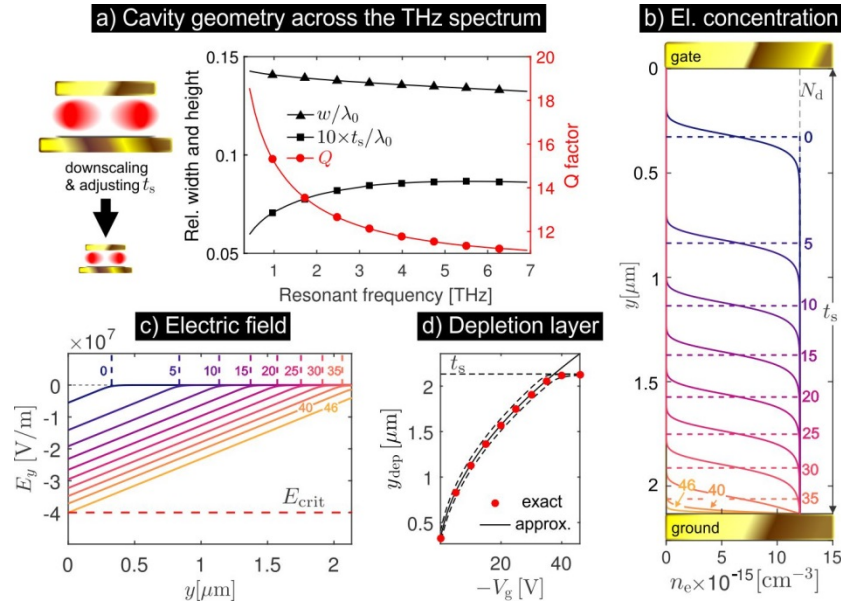

Figure 2: a) Geometrical parameters of critically coupled cavities drawn across the terahertz spectrum. The behavior of the Schottky junction under reverse bias: b) and c) electron concentration and electric field profile parameterized by V_g, d) depletion layer width as a function of V_g.

3. PROOF OF CONCEPT

We use a rigorous multiphysics framework incorporating Maxwell equations for terahertz waves and a drift-diffusion model for describing the carrier concentration $n_e(\mathbf{r})$ and mobility μ_n [25] in GaAs. The two physical models are coupled via the inhomogeneous dielectric permittivity of GaAs [26]

$$\varepsilon_s(\mathbf{r}, \omega) = \varepsilon_{opt}\left(1 - \frac{\omega_p^2(\mathbf{r})}{\omega(\omega + i\gamma_c)}\right) \qquad (1)$$

where the plasma frequency ω_p and intraband electron collision rate γ_c are given in terms of the GaAs conduction band effective mass m_c^* and unit charge q as

$$\omega_p^2(\mathbf{r}) = \frac{n_e(\mathbf{r})q^2}{\varepsilon_{opt}\varepsilon_0 m_c^*}, \qquad \gamma_c = \frac{q}{\mu_n m_c^*}. \qquad (2)$$
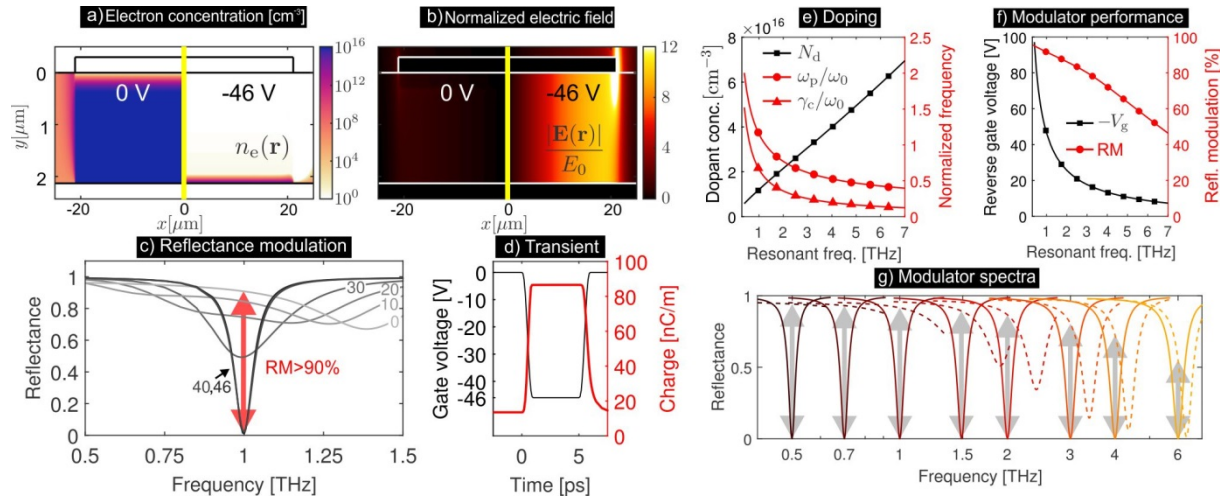
Figure 3: a)-d) Proof of concept multiphysics simulation results, showing the performance of the device operating at 1 THz. For operating frequencies across the terahertz spectrum, e),f) and g) show the required doping, modulation depth/bias voltage and modulator spectra, respectively.

The simulation results obtained for the $f_0 = 1$ THz device are shown in Figs. 3(a)-3(d). The electron concentration and electric field maps over the unit cell cross section are depicted in Figs. 3(a) and 3(b), where the unit cell mirror symmetry is exploited to show the maps corresponding to zero and maximum reverse bias ($V_{g,max} = -46$ V) in the left and right half of the unit cell, respectively. These results demonstrate a very efficient electrical switching effect, which is manifested through the voltage-dependent reflectance spectra in Fig. 3(c) (the numbers associated with curves denote $-V_g$) and the reflectance modulation RM > 90%. From the charge/discharge cycle in Fig. 3(d) and the calculated ps-order rise and fall times of the $Q(t)$ curve, we conclude that the proposed device has a very large intrinsic speed, which is a consequence of the deeply subwavelength separation of the driving electrodes.

Using the cavity geometry parameters that ensure critical coupling at full depletion from Fig. 2(a), we carry out a similar analysis for other f_0 values across the terahertz spectrum. The change of device geometry requires that the GaAs doping is adjusted as well, as shown in Fig. 3(e). The downscaling of cavity geometry required for operation at increasing frequencies, is seen to be accompanied by an approximately linear increase in the required doping (i.e. the maximum N_d value which can be fully depleted), which in turn leads to a reduction of the ω_p/ω_0 ratio responsible for permittivity tuning according to Eq. (1). This causes the gradual decrease of the modulator performance RM shown in Fig. 3(f), as additionally evidenced from several representative modulator spectra shown in Fig. 3(g).

4. SUMMARY

The very high terahertz field confinement in arrays of metal-semiconductor-metal cavities with deeply subwavelength thickness may be combined with a reversely-biased Schottky junction in or close to the reach-through regime in order to provide a modulation performance on par or even exceeding best existing devices. Considering that the deep modulation and fast response of the latter require the use of elaborate structures, we believe that the simplification offered by employing the concepts discussed in this work will be of interest for the development of novel terahertz modulators.

ACKNOWLEDGEMENTS

REFERENCES

[1]   R. Kersting *et al.*: Terahertz phase modulator, *Electron. Lett.*, vol. 36, no. 13, pp. 1156-1158, Jun. 2000.
[2]   T. Kleine-Ostmann *et al.*: Room-temperature operation of an electrically driven terahertz modulator, *Appl. Phys. Lett.*, vol. 84, no. 18, pp. 3555-3557, 2004.
[3]   R. Degl'Innocenti *et al.*: All-integrated terahertz modulators, *Nanophotonics*, vol. 7, pp. 127-144, 2018.
[4]   H.-T. Chen *et al.*: Active terahertz metamaterial devices, *Nature*, vol. 444, pp. 597-600, 2006.

[5]   H.-T. Chen *et al.*: A metamaterial solid-state terahertz phase modulator, *Nature Photon.*, vol. 3, pp. 148-151, 2009.

[6]   D. Shrekenhamer *et al.*: High speed terahertz modulation from metamaterials with embedded high electron mobility transistors, *Opt. Express*, vol. 19, no. 10, pp. 9968-9975, May 2011.

[7]   N. Karl *et al.*: An electrically driven terahertz metamaterial diffractive modulator with more than 20 dB of dynamic range, *Appl. Phys. Lett.*, vol. 104, no. 9, 2014, Art. no. 091115.

[8]   Y. Zhang *et al.*: Gbps terahertz external modulator based on a composite metamaterial with a double-channel heterostructure, *Nano Lett.*, vol. 15, no. 5, pp. 3501-3506, 2015.

[9]   M.T. Nouman *et al.*: Terahertz modulator based on metamaterials integrated with metal-semiconductor-metal varactors, *Sci. Rep.*, vol. 6, 2016, Art. no. 26452.

[10] Z. Zhou *et al.*: High performance metamaterials-high electron mobility transistors integrated terahertz modulator, *Opt. Express*, vol. 25, no. 15, pp. 17832-17840, Jul. 2017.

[11] M. Rahm *et al.*: THz wave modulators: A brief review on different modulation techniques, *J. Infrared Millimeter Terahertz Waves*, vol. 34, no. 1, pp. 1-27, 2013.

[12] B. Sensale-Rodriguez *et al.*: Extraordinary control of terahertz beam reflectance in graphene electro-absorption modulators, *Nano Lett.*, vol. 12, no. 9, pp. 4518-4522, 2012.

[13] D. Shrekenhamer *et al.*: Liquid crystal tunable metamaterial absorber, *Phys. Rev. Lett.*, vol. 110, Art. no. 177403, Apr. 2013.

[14] G. Isic *et al.*: Electrically tunable critically coupled terahertz metamaterial absorber based on nematic liquid crystals, *Phys. Rev. Appl.*, vol. 3, Art. no. 064007, Jun. 2015.

[15] B. Vasic *et al.*: Electrically tunable terahertz polarization converter based on overcoupled metal-isolator-metal metamaterials infiltrated with liquid crystals, *Nanotechnology*, vol. 28, no. 12, Art. no. 124002, 2017.

[16] G. Isic *et al.*: Electrically tunable metal-semiconductor-metal terahertz metasurface modulators, *IEEE J. Sel. Top. Quant.*, vol. 25, no. 3, Art. no. 8500108, 2019.

[17] Y. Todorov *et al.*: Strong light-matter coupling in subwavelength metal-dielectric microcavities at terahertz frequencies, *Phys. Rev. Lett.*, vol. 102, Art. no. 186402, May 2009.

[18] Y. Todorov *et al.*: Optical properties of metal-dielectric-metal microcavities in the THz frequency range, *Opt. Express*, vol. 18, no. 13, pp. 13886-13907, Jun. 2010.

[19] S. Fan *et al.*: Temporal coupled-mode theory for the Fano resonance in optical resonators, *J. Opt. Soc. Amer. A*, vol. 20, no. 3, pp. 569-572, Mar. 2003.

[20] G. Isic and R. Gajic: Geometrical scaling and modal decay rates in periodic arrays of deeply subwavelength terahertz resonators, *J. Appl. Phys.*, vol. 116, no. 23, Art. no. 233103, 2014.

[21] G. Isic *et al.*: Plasmonic lifetimes and propagation lengths in metallodielectric superlattices, *Phys. Rev. B*, vol. 89, Art. no. 165427, Apr. 2014.

[22] C. Bulucea: Breakdown voltage of diffused epitaxial junctions, *Solid State Electron.*, vol. 34, no. 12, pp. 1313-1318, 1991.

[23] G. Sinatkas *et al.*: Transparent conducting oxide electro-optic modulators on silicon platforms: A comprehensive study based on the drift-diffusion semiconductor model, *J. Appl. Phys.*, vol. 121, no. 2, Art. no. 023109, 2017.

[24] G. Sinatkas and E.E. Kriezis: Silicon-photonic electro-optic phase modulators integrating transparent conducting oxides, *IEEE J. Quantum. Electron.*, vol. 54, no. 4, pp. 1-8, Aug. 2018.

[25] M. Sotoodeh *et al.*: Empirical low-field mobility model for III-V compounds applicable in device simulation codes, *J. Appl. Phys.*, vol. 87, no. 6, pp. 2890-2900, 2000.

[26] D. Lockwood *et al.*: Optical phonon frequencies and damping in AlAs, GaP, GaAs, InP, InAs and InSb studied by oblique incidence infrared spectroscopy, *Solid State Commun.*, vol. 136, no. 7, pp. 404-409, 2005.

МОДИФИКАЦИЯ ПОВЕРХНОСТИ ПЛАЗМОННЫХ НАНОСТРУКТУР ДЛЯ СПЕКТРОСКОПИИ ГИГАНТСКОГО КОМБИНАЦИОННОГО РАССЕЯНИЯ БИОМОЛЕКУЛ

Б.В. Ранишенко[1), Г. Исич[2), П. Мойзес[3), С.Н. Терехов[4), А.Ю. Панарин[4)
[1)*Институт физико-органической химии НАН Беларуси,
ул. Сурганова 13, 220072 Минск, Беларусь, ranishenka@gmail.com*
[2)*Институт физики Белграда, Университет Белграда, Сербия, isicg@ipb.ac.rs*
[3)*Карлов университет, Прага, Чехия, mojzes@karlov.mff.cuni.cz*
[4)*Институт физики им. Б.И. Степанова НАН Беларуси,
пр. Независимости 68, 220072 Минск, Беларусь,
a.panarin@ifanbel.bas-net.by, s.terekhov@ifanbel.bas-net.by*

Методом адсорбционной иммобилизации сформированы плазмонные покрытия на поверхности стеклянных подложек, которые характеризуются высокой однородностью и эффективностью усиления сигнала гигантского комбинационного рассеяния (ГКР). С использованием различных неорганических и органических реагентов осуществлена обработка наноструктурированных серебряных пленок для улучшения адсорбции разно-заряженных молекул-аналитов. Показано, что путем предварительной модификации плазмонных покрытий полиэтиленимином можно увеличить сигнал ГКР для катионного порфирина в 3-3,5 раза. В свою очередь, использование модификаторов поверхности на основе меркаптопропионовой кислоты и ионов металла не позволяют полностью компенсировать отрицательный заряд наночастиц серебра и, следовательно, улучшить адсорбцию на них анионных аналитов.

Ключевые слова: плазмоника; наночастицы серебра; гигантское комбинационное рассеяние.

SURFACE MODIFICATION OF PLASMONIC NANOSTRUCTURES FOR SERS SPECTROSCOPY OF BIOMOLECULES

B.V. Ranishenka[1), G. Isić[2), P. Mojzes [3), S.N. Terekhov[4), A.Yu. Panarin[4)
[1)*Institute of Physical Organic Chemistry NAS Belarus,
13 Surganov Str., 220072 Minsk, Belarus, ranishenka@gmail.com*
[2)*Institute of Physics Belgrade, University of Belgrade, Belgrade, Serbia, isicg@ipb.ac.rs*
[3)*Charles University, Prague 2, CZ-12116, Czech Republic, mojzes@karlov.mff.cuni.cz*
[4)*B.I. Stepanov Institute of Physics NAS Belarus, 68 Nezavisimosti Ave., 220072 Minsk, Belarus,
a.panarin@ifanbel.bas-net.by, s.terekhov@ifanbel.bas-net.by*

Plasmon coatings on the surface of glass substrates, which are characterized by high homogeneity and the efficiency of amplification of the SERS signal, were formed by the adsorption immobilization method. Method of surface of the SERS-active substrates modification by various inorganic and organic compounds to improve the adsorption of both positively and negatively charged analyte molecules was developed. It was shown that preliminary modification of plasmon coatings by mercaptopropionic acid and metal ions (Au and Cu) could not completely compensate the negative charge of silver nanoparticles and, thus couldn't improve the adsorption of the anionic analytes. At the same time, the presence of positively charged copper ions in the solution contained anionic labeled oligonucleotide upon its adsorption on the surface of the SERS-active substrate allows a significant increase in the signal of Raman scattering of the analyte. The use of a surface modification based on polyethylenimine allows increasing of the SERS signal for cationic porphyrin by 3-3.5 times.

Key words: plasmonics; silver nanoparticles; surface enhanced Raman scattering.

Введение

Гигантское комбинационное рассеяние (ГКР) является уникальным методом колебательной спектроскопии, который позволяет получать детальную информацию о структуре исследуемых соединений при предельно низких концентрациях. Благодаря высокой чувствительности и специфичности спектроскопия ГКР находит широкое применение во многих аналитических приложениях, таких, например, как биомедицинская диагностика, детектирование и идентификация следовых количеств веществ, вплоть до регистрации одиночных молекул и клеток [1].

Упомянутые выше достоинства метода ГКР обеспечиваются с помощью специальных металлических наноструктурированных материалов, так называемых ГКР-активных субстратов, с характер-

ными размерами шероховатостей в диапазоне 10-100 нм. Таким образом, важным условием практической реализации метода ГКР является наличие доступных, воспроизводимых, высокочувствительных ГКР-активных субстратов, как правило, состоящих из наноструктур благородных металлов. Разработке методик формирования массивов металлических нанообъектов с заданными параметрами (формой, размером, расстоянием между наночастицами (НЧ), степенью упорядоченности) в настоящее время уделяется большое внимание [2].

Следует отметить, что создание новых плазмонных материалов не является единственным путем для расширения сфер применения спектроскопии ГКР. Одним из главных условий эффективной реализации данного метода является необходимость обеспечения практически непосредствен-

13-я Международная конференция «Взаимодействие излучений с твердым телом», 30 сентября - 3 октября 2019 г., Минск, Беларусь
13th International Conference "Interaction of Radiation with Solids", September 30 - October 3, 2019, Minsk, Belarus

485

ного контакта между молекулами аналита и поверхностью металла. Это связано с тем, что эффект ГКР является короткодействующим, и, удаление исследуемой молекулы всего на несколько нанометров приводит к значительному падению сигнала комбинационного рассеяния. Как правило, плазмонные структуры обладают избыточным поверхностным зарядом и, следовательно, заряд молекул аналита играет ключевую роль в процессе их сорбции на поверхность ГКР-активного субстрата. Следует отметить, что большинство биологически важных молекул, или их фрагментов, обладают катионными или анионными свойствами. В этой связи, разработка методов модификации плазмонных пленок, с целью увеличения их сродства с заряженными аналитами является важной задачей для расширения круга аналитических приложений спектроскопии ГКР.

Методика эксперимента

Образцы ГКР активных субстратов были получены методом адсорбционной иммобилизации [3]. В качестве подложек использовалось стандартное предметное стекло, поверхность которого ковалентно модифицировали полиэтиленимином (PEI) с молекулярной массой 25000 г/моль. Наночастицы серебра были синтезированы по методике [4] (концентрация серебра 27 мг/л) и переведены путем диализа в 2.5 мМ цитратный буфер. Стеклянные пластинки выдерживались в растворе наночастиц серебра, на протяжении 24 ч. Готовые ГКР-активные субстраты тщательно отмывались дистиллированной водой. Все образцы после химической модификации поверхности наночастиц серебра также промывались дистиллированной водой и высушивались на воздухе.

Размер коллоидных наночастиц серебра определялся методом динамического рассеяния света с помощью прибора Malvern Zetasizer Nano SZ90 (Malvern Panalytical Ltd, United Kingdom).

Для проверки эффективности усиления сигнала ГКР в качестве соединения-аналита использовались катионный порфирин Cu(II)-5,10,15,20-тетракис(4-N-метилпиридиний) порфирин (CuT-MpyP4) и анионный олигонуклеотид с красителем BHQ1: 5'CCTGCGATCTCTCTATCCAG[BHQ1]3' (oligo-BHQ). Нанесение аналитов на образцы осуществлялось методом капельного осаждения раствора с концентрацией 10^{-6} M.

Регистрация спектров гигантского комбинационного рассеяния производилась с помощью модульного КР-спектрометра оснащенного спектрографом Spex 270M (Jobin Yvon) и ПЗС детектором, охлаждаемым жидким азотом (Princeton Instruments). Источником возбуждения служил He-Cd лазер ($\lambda_{возб.}$ = 441.6нм) с мощностью порядка 2 мВт. Точность определения колебательных частот не выходила за пределы ±1 см$^{-1}$.

Результаты и их обсуждение

Методом просвечивающей электронной микроскопии (TEM) была изучены структурные свойства синтезированных наночастиц серебра. Анализ микрофотографий (см. рис. 1(1)) показывает, что для них характерна достаточно низкая полидисперсность по размеру и форме. Доминирующее

количество наночастиц серебра имеет квазисферическую форму и размер в диапазоне 40 ± 5 нм.

В качестве основы для формирования плазмонных пленок серебра были взяты стеклянные пластинки. Приготовление образцов тонких плазмонных пленок из наночастиц серебра на поверхности стеклянных подложек осуществлялось методом адсорбционной иммобилизации. С помощью данного метода можно формировать плазмонные покрытия (см. рис. 1(2)), обладающие высокой однородностью и воспроизводимостью спектрального сигнала от образца к образцу, что позволяет производить сравнение интенсивности спектров ГКР аналита при обработке стеклянных подложек различными реагентами.

Как было отмечено ранее, электростатическое взаимодействие наноструктурированного серебра с молекулами аналита является одним из ключевых факторов, влияющих на эффективность усиления сигнала ГКР. Исходные НЧ серебра имеют отрицательный заряд (дзета-потенциал около -35 мВ). Принимая во внимание молекулярную массу ПЭИ на поверхности стеклянной подложки, была произведена оценка толщины слоя полимера, которая составила около 10 нм. Таким образом, можно заключить, что для НЧ серебра с размером частиц около 50 нм большая часть поверхности металла остается свободной от полимера и обладает, предположительно теми же свойствами, что и НЧ в растворе (т.е. отрицательно заряжена). Природа отрицательного заряда на поверхности серебра может быть обусловлена как наличием наночастицах слоя молекул стабилизатора, так и тонкой оксидной пленки.
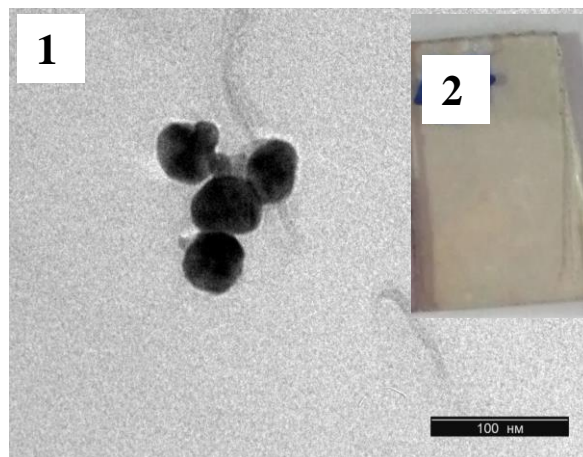

Рис. 1. Микрофотография наночастиц серебра (1) и фотография образца ГКР-активного субстрата (2)

Fig. 1. TEM-image of silver nanoparticles (1) and photo of SERS-active substrate (2)

Из литературы известно, что обработка плазмонной поверхности неорганическими солями может существенным образом повлиять на интенсивность сигнала ГКР [5]. Механизм действия различных химических реагентов, однако, до сих пор остается предметом для изучения. С целью изучения влияния различных модификаторов поверхности плазмонных структур на эффективность усиления интенсивности комбинационного рассеяния,

13-я Международная конференция «Взаимодействие излучений с твердым телом», 30 сентября - 3 октября 2019 г., Минск, Беларусь
13th International Conference "Interaction of Radiation with Solids", September 30 - October 3, 2019, Minsk, Belarus

486

были приготовлены ГКР-активные субстраты с различной химической обработкой и типом аналита. Модификация наноструктурированной поверхности серебра осуществлялась как ионами металлов (Au и Cu), так и органическими соединениями (меркаптопропионовой кислотой и полиэтиленимином).

На рис. 2(1) представлен спектр ГКР катионного порфирина CuTMpyP4 осажденного на поверхность плазмонной пленки из НЧ серебра с диаметром около 50 нм, сформированной методом адсорбционной иммобилизации без воздействия дополнительных химических реагентов. Такие наноструктуры характеризуются высокой эффективностью усиления сигнала ГКР для положительно-заряженного аналита, а также достаточно хорошей однородностью сигнала по поверхности образца. В тоже время, практически не удалось зарегистрировать сигнал ГКР для отрицательно-заряженного олигонуклеотида с красителем BHQ1. Такое поведение хорошо согласуется с предположением об электростатической природе адсорбции молекул аналита на поверхность металлических плазмонных структур.

Наиболее часто используемыми модификаторами поверхности ГКР-активных субстратов при работе с биологически важными молекулами являются соединения, содержащие тиоловые группы [6]. На рис. 2(2) приведен спектр ГКР катионного порфирина для образца, приготовленного путем обработки подложки меркаптопропионовой кислотой (MPA) (0,1 мг/мл раствор в воде) в течение 10 мин. Видно, что происходит уменьшение интенсивности сигнала комбинационного рассеяния примерно в 2 раза по сравнению со стандартным ГКР-активным субстратом (без модификации поверхности). При этом интенсивность ГКР для анионного аналита oligo-BHQ увеличивается незначительно. Скорее всего, это связано с тем, что меркаптопропионовая кислота, взаимодействуя посредством тиольной группы с поверхностью НЧ, экспонирует отрицательно-заряженные карбоксильные группы на поверхность НЧ. При этом значительного уменьшения общего отрицательного заряда серебряных частиц не происходит, а падение сигнала ГКР для катионного аналита связано с увеличением расстояния между ним и плазмонной поверхностью. В целом использование такой модификации поверхности целесообразно в случае положительно-заряженных биологически важных молекул, которые разрушаются при прямом контакте с серебром.

Для того чтобы уменьшить отрицательный заряд плазмонной наноструктры был использован ряд химических реагентов содержащих ионы металлов, которые способны к взаимодействию с поверхностью НЧ серебра.

На рис. 2(3) представлен спектр ГКР катионного CuTMpyP4 осажденного на поверхность ГКР-активного субстрата, обработанную раствором HAuCl₄ (150 мкМ) в течение 10 мин. В этом случае также происходит значительное уменьшение интенсивности сигнала комбинационного рассеяния примерно в 1,5-2 раза по сравнению с немодифицированным ГКР-активным субстратом. Вероятно, это связано с изменением резонансных условий лазерного возбуждения за счет того, что при заме-

щении ионами золота атомов серебра на поверхности НЧ полоса поверхностного плазмонного резонанса смещается в длинноволновую область спектра. Можно также заключить, что при модификации поверхности посеребренных субстратов ионами золота не происходит значительного изменения для нее общего отрицательного заряда. Это подтверждается незначительным увеличением сигнала ГКР для анионного олигонуклеотида.
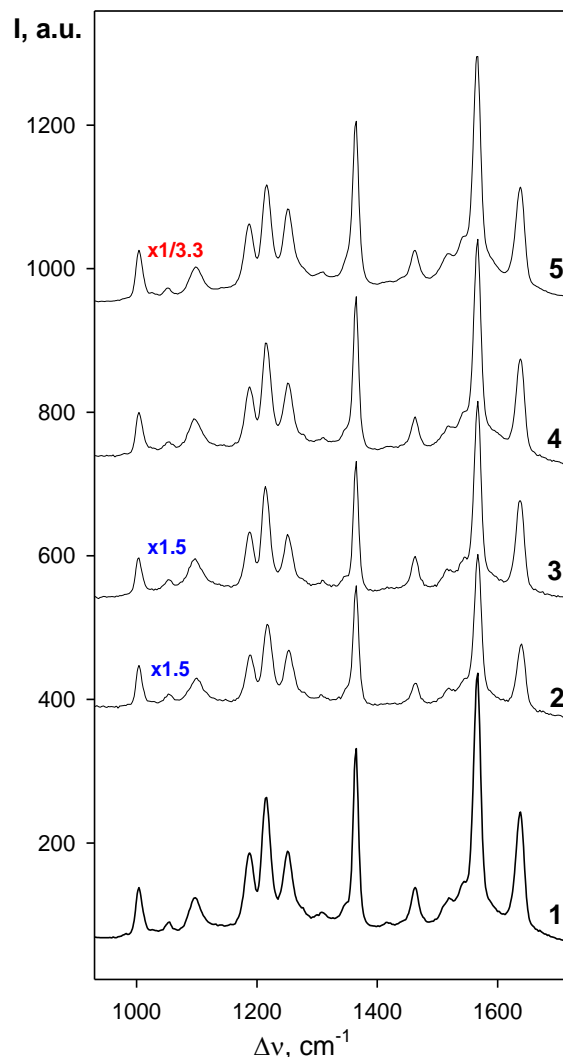

Рис. 2. Спектры ГКР CuTMpyP4 на плазмонной пленке (1) - без модификации поверхности и модифицированной: (2) - MPA, (3) - HAuCl₄, (4) - CuSO₄, (5) - PEI

Fig. 2. SERS spectra of CuTMpyP4 on plasmonic film (1) – without surface modification and modified with: (2) - MPA, (3) - HAuCl₄, (4) - CuSO₄, (5) - PEI

Также была проведена обработка поверхности ГКР-активного субстрата водным раствором сульфата меди (время обработки 10 мин; концентрация реагента 5 мг/мл). Ионы меди, являясь двухзарядными, способны эффективно экранировать отрицательный заряд НЧ. Оказалось, что при такой модификации поверхности плазмонной структуры интенсивность спектра ГКР, как для катионного, так и анионного аналитов практически совпадает с интенсивностью спектров данных аналитов на немо-

13-я Международная конференция «Взаимодействие излучений с твердым телом», 30 сентября - 3 октября 2019 г., Минск, Беларусь
13th International Conference "Interaction of Radiation with Solids", September 30 - October 3, 2019, Minsk, Belarus

487

дифицированном ГКР-активном субстрате. Скорее всего, в этом случае ионы меди могут десорбироваться или подвергаться гидролизу в процессе отмывки образцов. Для проверки этого предположения на стандартный немодифицированный ГКР-активный образец был нанесенным анионый олигонуклеотид в присутствии ионов меди в растворе (концентрация сульфата меди 10 мМ). При этом наблюдалось значительное увеличение сигнала ГКР для анионного аналита. Вероятно, в этом случае взаимное отталкивание отрицательнозаряженных аналита и НЧ серебра нейтрализуется присутствием положительно-заряженных ионов меди, которые служат связывающим агентом и, таким образом, обеспечивают подходящее расположение молекул вблизи поверхности плазмонной пленки.

Также была осуществлена модификация плазмонной поверхности полимером путем выдерживания образцов в водном растворе, содержащем разветвленный PEI с молекулярной массой 25000 г/моль (концентрация 0,1 мг/мл; время выдерживания 20 мин). Полиэтиленимин был выбран в качестве вещества, способного эффективно адсорбироваться на поверхности серебра и являющегося слабым основанием. Благодаря своей основной природе полимер может экранировать отрицательный заряд на НЧ. На рис. 2(5) представлен спектр ГКР катионного CuTMpyP4, осажденного на поверхность ГКР-активного субстрата модифицированного PEI. Обработка плазмонной поверхности полиэтиленимином приводит к значительному в 3-3,5 раза увеличению сигнала ГКР красителя. Рост интенсивности комбинационного рассеяния может быть обусловлен способностью полиэтиленимина образовывать дополнительные связи с аналитом и, таким образом, увеличивать количество молекул катионного порфирина вблизи наноструктурной поверхности серебра. Кроме того, мы предполагаем, что полиэтиленимин, будучи слабым основанием, не способен полностью компенсировать отрицательный заряд НЧ. Отсутствие сигнала ГКР для олигонуклеотида подтверждает это предположение.

Заключение

Методом адсорбционной иммобилизации сформированы плазмонные покрытия на поверхности стеклянных подложек, которые характеризуются высокой однородностью и эффективностью усиления сигнала ГКР. Была осуществлена модификация поверхности наночастиц серебра ионами металлов и органическими соединениями для улучшения адсорбции как положительно- так и отрицательно-заряженных молекул-аналитов. Показано, что предварительная модификация плазмонных покрытий MPA и ионами металла не позволяют полностью компенсировать отрицательный заряд серебряных наночастиц и улучшить адсорбцию анионного олигонуклеотида. В тоже время, присутствие положительно-заряженных ионов меди в растворе oligo-BHQ при его адсорбции на поверхность ГКР-активного субстрата позволяет значительно увеличить сигнал комбинационного рассеяния аналита. В свою очередь, использование модификатора поверхности на основе полиэтиленимина позволяет увеличить сигнал ГКР для катионного порфирина в 3-3,5 раза.

Библиографические ссылки / References

1 Kneipp K., Wang Y., Kneipp H., Perelman L.T., Itzkan L., Dasari R.R., Feld M.S. Single Molecule Detection Using Surface-Enhanced Raman Scattering (SERS). *Phys. Rev. Lett.* 1997; 78: 1667–1670.
2 Fan M., Andrade G.F.S., Brolo A.G. A review on the fabrication of substrates for surface enhanced Raman spectroscopy and their applications in analytical chemistry. *Analytica Chimica Acta* 2011; 693: 7-25.
3 Grabar K.C., Freeman R.G., Hommer M.B., Natan M.J. Preparation and Characterization of Au Colloid Mono-layers *Anal. Chem.* 1995; 67(4): 735-743
4 Fabrikanos Von A., Athanassiou S., Lieser, K.H. Darstellung stabiler Hydrosole von Gold und Silber durch Reduktion mit Äthylendiamintetraessigsäure. *Z. Naturforsch.* 1963; 18B: 612-617.
5 Koo T.W., Chan S., Sun L., Su X., Zhang J., Berlin A.A. Specific chemical effects on surface-enhanced Raman spectroscopy for ultra-sensitive detection of biological molecules. Appl Spectrosc. 2004; 58(12):1401-1407.
6 Mosier-Boss P.A. Review of SERS Substrates for Chemical Sensing. *Nanomaterials* 2017; 7(6): 142.

13-я Международная конференция «Взаимодействие излучений с твердым телом», 30 сентября - 3 октября 2019 г., Минск, Беларусь
13th International Conference "Interaction of Radiation with Solids", September 30 - October 3, 2019, Minsk, Belarus

488

Electrically tunable solid-state terahertz metamaterial absorbers

D. C. Zografopoulos[1], **G. Isić**[2,3], **B. Vasić**[2], **A. Ferraro**[1], **G. Sinatkas**[4], **E. E. Kriezis**[4],
R. Gajić[2], **and R. Beccherelli**[1]

[1]Consiglio Nazionale delle Ricerche, Istituto per la Microelettronica e Microsistemi (CNR-IMM), Rome 00133, Italy
[2]Center for Solid State Physics and New Materials, Institute of Physics Belgrade, University of Belgrade, Pregrevica 118, 11080 Belgrade, Serbia
[3] Texas A&M University at Qatar, P.O. Box 23874, Education City, Doha, Qatar
[4]Department of Electrical and Computer Engineering, Aristotle University of Thessaloniki, 54124 Thessaloniki, Greece
dimitrios.zografopoulos@artov.imm.cnr.it

Abstract – **This work presents the design of electrically tunable solid-state metamaterial absorbers in the terahertz spectrum. The proposed devices consist of a metal-insulator-metal resonant cavity formed between a subwavelength metal stripe grating and a back metal reflector. The dielectric spacing between the metallic parts is occupied by a deeply subwavelength layer of n-doped GaAs. By reverse biasing the Schottky junction formed at the interface between GaAs and the top metal grating, the thickness of the associated carrier depletion zone is controlled and, hence, the GaAs complex permittivity profile in the resonant cavities. Optimized structures are derived based on the mechanism of critical coupling, achieving amplitude modulation of the reflected terahertz wave with low insertion losses and theoretically infinite extinction ratio.**

I. Introduction

In the last years, significant research effort has been dedicated to terahertz (THz) science, thanks to numerous envisaged applications in technologically relevant sectors, such as wireless communications, safety, material characterization or quality control, and bioengineering. The engineering of the THz systems needed to deploy such novel technological paradigms relies among others on the availability of frequency-tunable components, capable of controlling the amplitude and phase of the propagating THz waves. Various approaches have been thus far employed using materials whose electromagnetic properties can be dynamically controlled, such as thermally tunable phase-change materials [1] or electrically tunable liquid crystals [2, 3] and semiconductors [4, 5].

The latter approach relies on the electrical control of a reverse biased Schottky junction formed at the interface of resonating metallic elements, e.g. split-ring resonators, and a bulk n-doped GaAs substrate, which is depleted in the vicinity of the junction. Although a validated approach, its efficiency is limited by the fact that the tunable region lies in the substrate and thus it cannot fully overlap with the electromagnetic hot-spot of the metasurface resonators. Here, we design a solid-state terahertz metamaterial absorber that works in reflection as an amplitude modulator. Although it is based on the same principle of reverse biasing a Schottky junction, the depletion layer can almost entirely overlap with the electromagnetic hot-spot volume and maximize the tuning effect, thanks to the extremely subwavelength thickness of the employed metal-insulator-metal resonating cavities. The carrier distribution is solved by means of the drift-diffusion model, seamlessly coupled with terahertz wave propagation studies in a single finite-element method platform [6, 7]. Through a careful design exploiting the mechanism of critical coupling, the modulator exhibits theoretically infinite extinction ratio and low insertion losses.

II. Solid-state tunable terahertz metamaterial absorbers

The layout of the proposed tunable terahertz metamaterial absorber is shown in Fig. 1. A layer of n-doped GaAs is grown [8] on a metal back-reflector supported by a dielectric substrate. A grating of metal stripes is patterned

on top of the GaAs layer, creating a periodic arrangement of metal-insulator-metal resonant cavities. Schottky and ohmic junctions are suitably formed at the GaAs/metal grating and GaAs/metal back-reflector interfaces, respectively [5]. When the junction is unbiased, a thin carrier depletion layer is formed, which occupies a small fraction of the cavity. By reverse biasing the junction, the thickness of the depletion layer is adjusted, modulating the GaAs complex permittivity in the resonant cavities. The device is designed to operate for a single (TM) polarization, although it can be extended to dual-polarization by considering, e.g., a 2D grating of metallic patches.
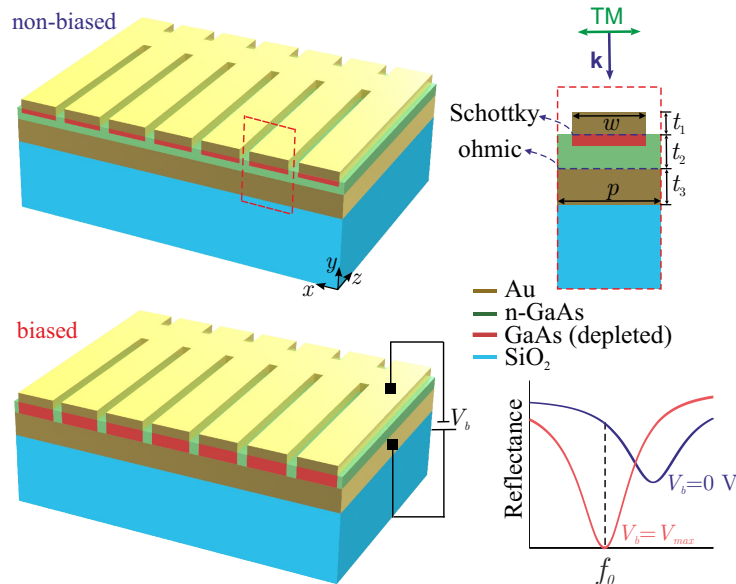

Fig. 1: Layout of the investigated solid-state tunable terahertz metamaterial absorber. The application of an electrical bias at the Schottky junction at the interface between the top Au electrodes and the GaAs layer controls the carrier depletion zone inside the resonant metal-insulator-metal cavity. By proper design, the device is critically-coupled at the target frequency in the biased case, thus achieving high modulation depth and extinction ratio.

In the biased case, which corresponds to a fully depleted cavity, GaAs is dielectric and the resonator is designed such that the critical coupling condition is reached, in order to achieve complete absorption of the impinging THz wave at the design resonance frequency f_0. At rest, the real permittivity of the n-doped GaAs layer is lower, while significant losses also arise, in accordance with the Drude model for doped semiconductors [6]. This leads to the broadening of the reflectance spectrum $R(f)$ and its shift towards higher frequencies, thus modulating the amplitude at f_0. By rigorously solving for the voltage-dependent carrier distribution and the THz wave propagation, a series of optimized devices are derived in the one to few THz range, below the GaAs phonon resonances emerging at 8 THz. To maximize the modulation depth, the bias voltage varies from zero up to the limiting value related to the dielectric breakdown of GaAs. Figure 2 shows the key parameters for the optimally designed modulators.
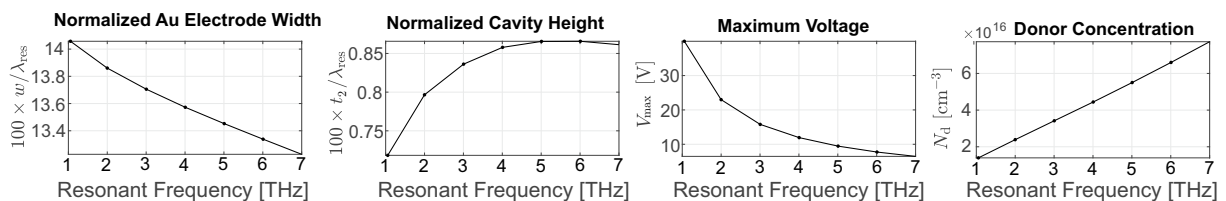

Fig. 2: Optimized design parameters for modulation in the 1-7 THz range.

The performance of these optimized structures is evaluated in Fig. 3. The modulation depth of the THz wave, namely $R(f_0)$ at $V_b = 0$ V, varies from 92% to 53%, whereas the extinction ratio in all cases is, theoretically, infinite, owing to the zero reflectance of the biased state, which stems from the critical coupling condition.
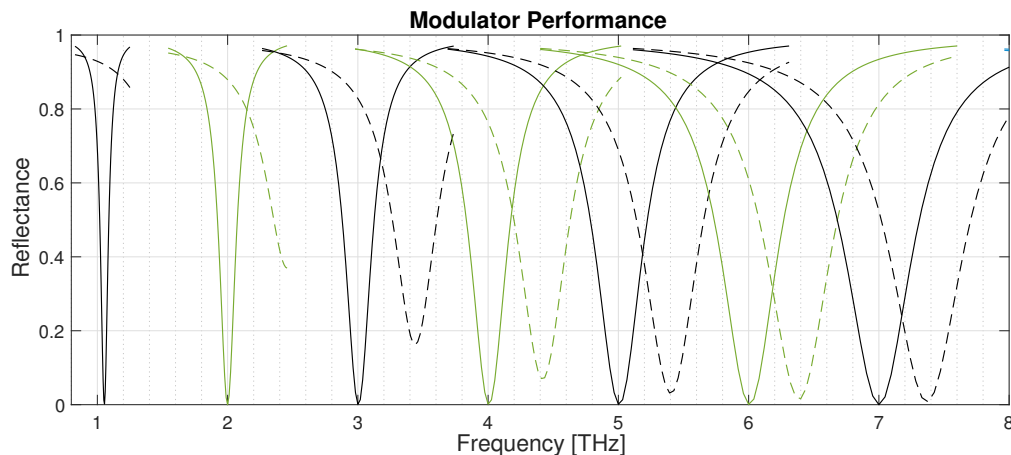
Fig. 3: Amplitude modulation for optimized structures working at 1 to 7 THz, according to the parameters of Fig. 2. Solid and dashed lines correspond to operation at maximum and zero bias voltage, respectively.

III. Conclusion

A new class of solid-state electrically-tunable terahertz metamaterial absorbers is presented, based on the electrical control of the carrier depletion layer in metal-GaAs-metal resonant cavities with a reverse biased Schottky junction. Optimized structures are derived, which operate as amplitude modulators at THz frequencies, exhibiting both low insertion losses and theoretically infinite extinction ratio.

Acknowledgement

References

[1] Q.-Y. Wen, H.-W. Zhang, Q.-H. Yang, Z. Chen, Y. Long, Y.-L. Jing, Y. Lin, and P.-X. Zhang, "A tunable hybrid metamaterial absorber based on vanadium oxide films," *J. Phys. D*, vol. 45, art. no. 235106, 2012.

[2] G. Isić, B. Vasić, D. C. Zografopoulos, R. Beccherelli, and R. Gajić, "Electrically tunable critically coupled terahertz metamaterial absorber based on nematic liquid crystals," *Phys. Rev. Applied*, vol. 3, art. no. 064007, 2015.

[3] B. Vasić, D. C. Zografopoulos, G. Isić, R. Beccherelli, and R. Gajić, "Electrically tunable terahertz polarization converter based on overcoupled metal-isolator-metal metamaterials infiltrated with liquid crystals," *Nanotechnology*, vol. 28, art. no. 124002, 2017.

[4] O. Paul, C. Imhof, B. Lgel, S. Wolff, J. Heinrich, S. Höfling, A. Forchel, R. Zengerle, R. Beigang, and M. Rahm, "Polarization-independent active metamaterial for high-frequency terahertz modulation," *Opt. Express*, vol. 17, no. 2, pp. 819-827, 2009.

[5] H.-T. Chen, W. J. Padilla, M. J. Cich, A. K. Azad, R. D. Averitt, and A. J. Taylor, "A metamaterial solid-state terahertz phase modulator," *Nature Photon.*, vol. 3, pp. 148–151, 2009.

[6] G. Sinatkas, A. Pitilakis, D. C. Zografopoulos, R. Beccherelli, and E. E. Kriezis, "Transparent conducting oxide electro-optic modulators on silicon platforms: A comprehensive study based on the drift-diffusion semiconductor model," *J. Appl. Phys.*, vol. 121, art. no. 023109, 2017.

[7] D. C. Zografopoulos, G. Sinatkas, E. Lotfi, L. A. Shahada, M. A. Swillam, E. E. Kriezis, and R. Beccherelli, "Amplitude modulation in infrared metamaterial absorbers based on electro-optically tunable conducting oxides," *Appl. Phys. A*, vol. 124, art. no. 105, 2018.

[8] J. Yoon, S. Jo, I. S. Chun, I. Jung, H.-S. Kim, M. Meitl, E. Menard, X. Li, J. J. Coleman, U. Paik, and J. A. Rogers, "GaAs photovoltaics and optoelectronics using releasable multilayer epitaxial assemblies," *Nature*, vol. 465, pp. 329–333, 2010.

Copper-Nickel heterometallic multilayer composites for plasmonic applications

Ivana Mladenović, Zoran Jakšić, *Senior Member, IEEE*, Marko Obradov,
Slobodan Vuković, Goran Isić, Jelena Lamovec

Abstract— **Plasmonics and optical metamaterials offer possibilities for numerous applications in different fields, from transformation optics and chemical sensing to merging the beneficial properties of electronic and optical circuits. Crucial for their function are interfaces between materials of which one has to exhibit negative value of relative dielectric permittivity due to the existence of free electron plasma. However, the choice of convenient materials is rather limited and their performance is severely impaired by strong absorption losses. This is the reason why alternative plasmonic media are currently of an increasing interest. In this contribution we consider one such medium, the heterometallic multilayer consisting of copper and nickel. Copper is an excellent plasmonic material, but needs protection against surface oxidation, a role fulfilled by nickel layers which simultaneously form interfaces supporting surface waves. We describe our proposed heterometallics and consider their electromagnetic properties and experimental fabrication. *Ab initio* numerical simulations were done using the finite element method for Cu-Ni multilayers on a copper substrate. Laminate composite structures of alternately electrodeposited nanocrystalline Ni and Cu films on cold-rolled polycrystalline copper substrates were fabricated. Highly-densified parallel interfaces can be obtained by depositing layers at a very narrow spacing. Our results show that Cu-Ni pairs are a viable alternative to conventional plasmonic media, while the electrodeposition approach offers acceptable structural and electromagnetic parameters with large area and good uniformity at a low cost.**

Index Terms — **Plasmonics; Heterometallics; Optical Multilayers; Copper-Nickel Films; Electrodeposition**

I. INTRODUCTION

FROM the electromagnetic point of view, the existence of interfaces between materials with different relative dielectric permittivity and/or relative magnetic permeability results in a wealth of different electromagnetic modes supported by such structures. The simplest case is a contact between two semi-infinite uniform materials, one of them with negative relative permittivity (i.e. having free electrons as charge carriers) and the other with positive permittivity. If electron plasma frequency coincides with or is sufficiently near to the electromagnetic wave frequency, a new mode appears defined by the resonant oscillations of electrons. It is p-polarized and bound to the interface between the two materials, exponentially decaying in both perpendicular directions – the surface plasmon polariton (SPP). More complex composites introduce a wealth of new modes. The branch of electromagnetic optics making use of the resonant properties of free electrons is called plasmonics [1, 2]. The existence of the SPPs and similar surface phenomena ensures extreme localizations of fields in subwavelength volumes [3,4].

More generally, the possibility to design electromagnetic modes at will opens the gate to arbitrary tailoring and transforming the optical space. This is called transformation optics [5], and plasmonics ensures its use in the optical frequency range. Various applications include chemical and biological sensors [6], circuits that merge compactness of electrical circuitry with high frequencies of all-optical devices [7], superabsorbers and superlenses, super-resolution lithography [8], to name just a few.

One of the problems with the use of materials with free electron plasma are their high absorption losses caused by intra- and inter-band electronic transitions. Another is related with the available operating frequency ranges. These are some of the reasons why alternative plasmonic materials are constantly being sought after. The most common choice for plasmonics are gold and silver, both offering excellent conductivity and the possibility to be processed using the standard microsystem techniques. Other proposed materials include transparent conductive oxides, heavily doped semiconductors, intermetallics, etc. [9, 10]

Copper is one of the materials with properties very convenient for plasmonics. A problem is that exposed to atmosphere it quickly oxidizes, which can impair the performance of nanometer-thick structures used in plasmonics or even completely remove any desirable effects. In spite of this, copper is sometimes used in plasmonics, combined with some means to protect its surface.

Here we report on the design and fabrication of alternating copper-nickel multilayers, where nickel serves a dual purpose of ensuring multiple plasmonic interfaces with copper and providing protection against environmental influences.

Ivana Mladenović is with Centre of Microel. Technologies, Institute of Chemistry, Technology and Metallurgy, University of Belgrade, Njegoševa 12, 11000 Belgrade, Serbia (e-mail: ivana@nanosys.ihtm.bg.ac.rs).

Zoran Jakšić is with Centre of Microelectronic Technologies, Institute of Chemistry, Technology and Metallurgy, University of Belgrade, Njegoševa 12, 11000 Belgrade, Serbia (e-mail: jaksa@nanosys.ihtm.bg.ac.rs).

Marko Obradov is with Centre of Microel. Technologies, Institute of Chemistry, Technology and Metallurgy, University of Belgrade, Njegoševa 12, 11000 Belgrade, Serbia (e-mail: marko.obradov@nanosys.ihtm.bg.ac.rs).

Slobodan Vuković is with Centre of Microel. Technologies, Institute of Chemistry, Technology and Metallurgy, University of Belgrade, Njegoševa 12, 11000 Belgrade, Serbia (e-mail: svukovic@nanosys.ihtm.bg.ac.rs).

Goran Isić is with Center for Solid State Physics and New Materials, Institute of Physics Belgrade, University of Belgrade, Pregrevica 118, 11080 Belgrade, Serbia (e-mail: isicg@ipb.ac.rs).

Jelena Lamovec is with Centre of Microel. Technologies, Institute of Chemistry, Technology and Metallurgy, University of Belgrade, Njegoševa 12, 11000 Belgrade, Serbia (e-mail: jejal@nanosys.ihtm.bg.ac.rs).
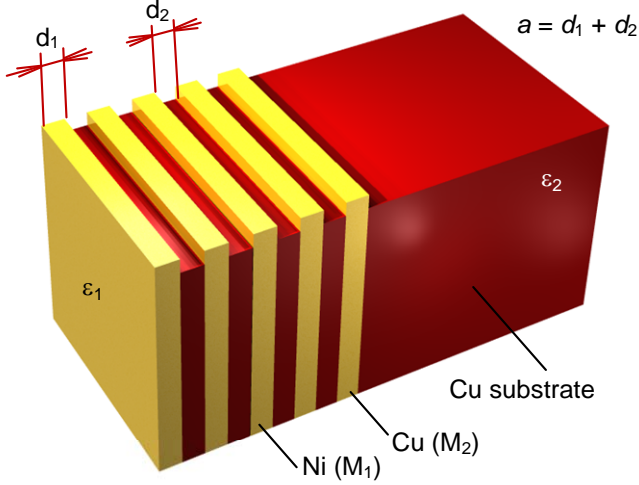
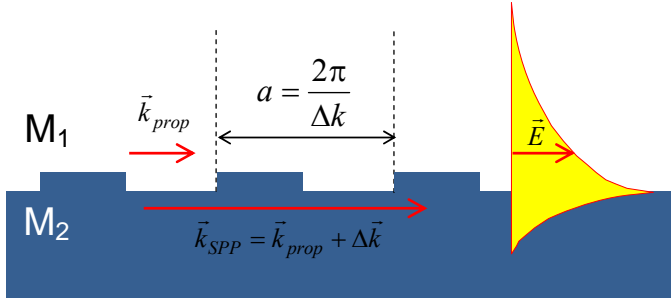Fig. 1. Geometry of our heterometallic multilayer. Surface relief is visible at the top of the structure.

Fig. 2. Coupling between the SPP and the propagating beam on a diffractive grating (in this case the surface relief on the Cu-Ni multilayer). M_1 and M_2 denote nickel and copper (metal 1 and metal 2), respectively. Yellow area shows the intensity of the electric field of the SPP versus distance from the interface.

II. THEORY

We investigate a multilayer structure with alternating strata of two different materials (metals M_1 and M_2,) each of them uniform and homogenous, each described by its complex relative dielectric permittivity ($\varepsilon_1(\omega) = \varepsilon'_1 + \varepsilon''_1$ and $\varepsilon_2(\omega) = \varepsilon'_1 + \varepsilon''_2$) and by its thickness ($d_1$ and d_2). We assume that the relative magnetic permeabilities of the both constituents $\mu_1(\omega)$ and $\mu_2(\omega)$ are equal to 1 since we consider the optical frequency range.

The geometry of the heterometallic multilayer is shown in Fig. 1. The multilayer is deposited onto a copper substrate. We assume that the relative dielectric permittivity of each metal is well described by the lossy extended Drude model [1]

$$\varepsilon_j(\omega) = \varepsilon_{\infty j} - \frac{\omega_{pj}^2}{\omega^2 + i\gamma_j\omega}, \quad j = 1,2 \qquad (1)$$

where ω_p is the plasma frequency of the electron plasma, ε_∞ is the asymptotic dielectric permittivity and $\gamma = 1/\tau$ is the characteristic frequency related to the damping of electron oscillations due to collisions, where τ is the relaxation time of the electron gas.

Since both M_1 and M_2 are plasmonic materials, the multilayer structure shown in Fig. 1 represents the general case of finite one-dimensional, two-material plasmonic crystal [11, 12]. We denote the electromagnetic wave propagation perpendicular to the multilayer surface by the Bloch wave vector $\vec{q}$. The propagation of a surface wave along an interface between the two different materials M_1 and M_2 is described by the plasmonic wave vector $\vec{k}$. We denote the number of the layer pairs by N, and the total thickness of a single layer pair by $a = d_1 + d_2$.

We proceed by writing the spectral dispersion relation connecting the frequency and the wave vector within the given structure. The usual way to obtain the dispersion of a finite plasmonic crystal is to utilize the transfer matrix method [13–15]. The dispersion relation is obtained as

$$\frac{1}{2}(T_{11} - T_{22}) = -\cot g(Nqa)\sin(qa) , \qquad (2)$$

$$\frac{1}{2}(T_{11} + T_{22}) = \cos(qa) , \qquad (3)$$

where T_{11} and T_{22} are the diagonal transfer matrix elements. Written for the electromagnetic waves outside the light cone and for S-polarized waves these elements are

$$T_{11} = \exp(i\,\kappa_m d_{m1})\Big[\cosh(\kappa_{m2}a - \kappa_{m2}d_{m1}) -$$
$$- \frac{1}{2}\left(\frac{\kappa_{m2}}{\kappa_{m1}} - \frac{\kappa_{m1}}{\kappa_{m2}}\right)\sinh(\kappa_{m2}a - \kappa_{m2}d_{m1})\Big] , \qquad (4)$$

$$T_{22} = \exp(-i\,\kappa_m d_{m1})\Big[\cosh(\kappa_{m2}a - \kappa_{m2}d_{m1}) +$$
$$+ \frac{1}{2}\left(\frac{\kappa_{m2}}{\kappa_{m1}} - \frac{\kappa_{m1}}{\kappa_{m2}}\right)\sinh(\kappa_{m2}a - \kappa_{m2}d_{m1})\Big] . \qquad (5)$$

whereas for P-polarized waves outside the light cone

$$T_{11} = \exp(i\,\kappa_m d_{m1})\Big[\cosh(\kappa_{m2}a - \kappa_{m2}d_{m1}) -$$
$$- \frac{1}{2}\left(\frac{\kappa_{m2}\varepsilon_{m1}}{\kappa_{m1}\varepsilon_{m2}} - \frac{\kappa_{m1}\varepsilon_{m2}}{\kappa_{m2}\varepsilon_{m1}}\right)\sinh(\kappa_{m2}a - \kappa_{m2}d_{m1})\Big] , \qquad (6)$$

$$T_{22} = \exp(-i\,\kappa_m d_{m1})\Big[\cosh(\kappa_{m2}a - \kappa_{m2}d_{m1}) +$$
$$+ \frac{1}{2}\left(\frac{\kappa_{m2}\varepsilon_{m1}}{\kappa_{m1}\varepsilon_{m2}} - \frac{\kappa_{m1}\varepsilon_{m2}}{\kappa_{m2}\varepsilon_{m1}}\right)\sinh(\kappa_{m2}a - \kappa_{m2}d_{m1})\Big] . \qquad (7)$$

These equations are also applicable for the waves inside the light cone, but in this case hyperbolic functions in T_{11}, T_{22} should be replaced with the corresponding regular trigonometric functions.

The next point of interest is the surface relief visible on the top of the sample in Fig. 1. An idealized view of the obtained profile is shown in Fig. 2. The existence of the relief is convenient to ensure coupling between SPPs and a propagating interrogation beam without a need to utilize inconvenient external beam couplers needed for the conventional plasmonic structures.

It is well known that to couple propagating and surface waves one needs to impart additional momentum Δk to the propagating wave [1]. One of the methods of coupling is the use of a diffractive grating [2]. In our case the heterometallic multilayer itself represents such a grating. Technologically the necessary relied can be produced in a simple way by selectively etching the copper part of the heterometallic layer.

The well-known relation between the diffractive grating constant $a = d_1 + d_2$ and the wave vector of the diffracted mode is

$$\Delta k = \pm m \frac{2\pi}{a} , \qquad (8)$$

where m is an integer. Thus matching is obtained if

$$\vec{\kappa} = \vec{q} + \Delta \vec{k} , \qquad (9)$$

where the propagating mode is

$$q = \frac{\omega}{c} \sin \theta . \qquad (10)$$

here ω is the angular frequency, c is the speed of light in the medium above the plasmonic surface and θ is the incident angle of the propagating mode.

III. NUMERICAL

We examined the scattering of a plane wave incident on the structure in Fig. 1 using the finite element method. To this purpose we utilized the RF module of Comsol Multiphysics software package. The modeled structure consisted of four nickel layers and three copper layers deposited on a copper substrate. For the purpose of our simulation the substrate was assumed sufficiently thick to be considered infinite. The structure was surrounded by air.

Our simulations calculated the scattered waves as a perturbation caused when our structure is introduced into a background electromagnetic field described by a propagating plane wave. Since the background medium is homogenous (air) it is possible to set the background field by simply using the analytic expression for the plane wave. The entire domain was encased in a perfectly matched layer (PML) acting as a perfect absorber and preventing unwanted internal reflections by collecting scattered radiation. The total field representing the optical response of the structure was calculated as a superposition of the scattered and the background fields.

Figs. 3 and 4 show examples of the incident wave coupling with the plasmonic modes of our structure for oblique incidence. Fig. 3 shows a d_1=100nm, d_2=300nm structure for 750 nm incident radiation. A selectivity of light localization in the copper channels is observed when changing the angle of incidence from 30º to 60º. Coupling of the incident wave with the surface modes on the copper substrate is shown in Fig. 4 for a 60º incident angle. The frequency and the strength of the coupling are both dependent on the grating period. We observed a blue shift of the resonant wavelength from 850 nm to 670 nm when the thickness of the layers was changed from d_1=100 nm, d_2=300 nm to d_1=200 nm, d_2=500 nm.
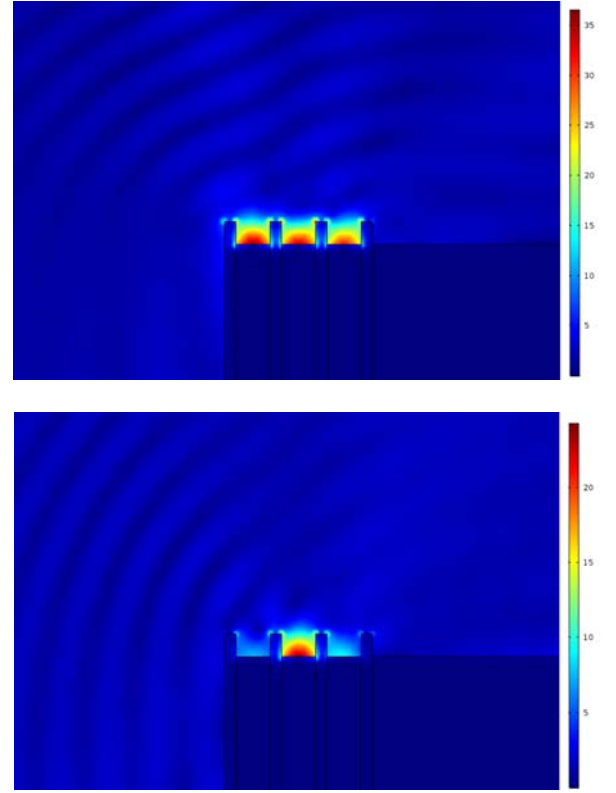

Fig. 3. Total electric field intensity for d_1=100 nm, d_2=300 nm structure at 750 nm for: a) 30º incident angle and b) 60º incident angle.
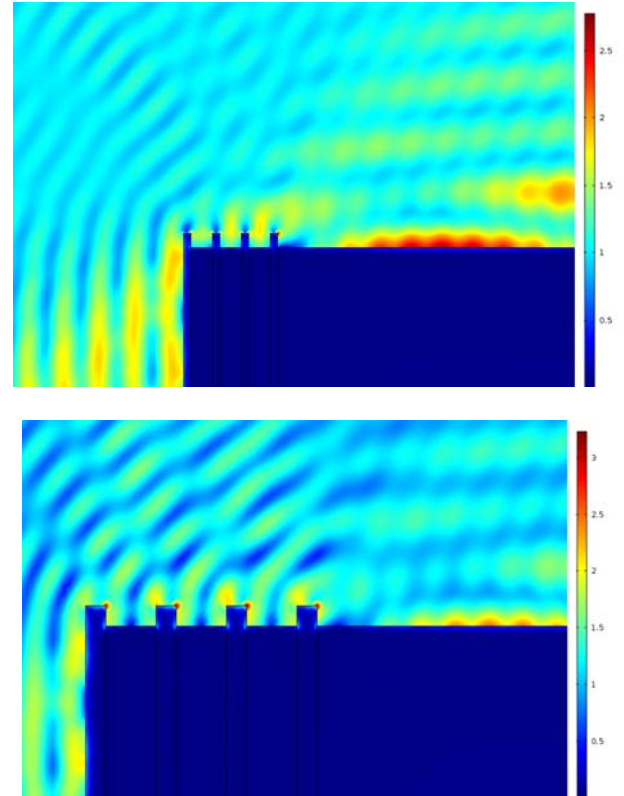

Fig. 4. Total electric field intensity for: a) d_1=100 nm, d_2=300 nm structure at 670 nm and 60º incident angle; b) d_1=200 nm, d_2=500 nm structure at 850 nm and 60º incident angle.

IV. EXPERIMENTAL

For our experiments we used electrochemical deposition since it is fully compatible with MEMS technologies and offers a high controllability of the deposition rate, thickness and residual stress in Ni and Cu deposits [16, 17].

The substrate for electrodeposition of Ni and Cu thin films was a 125 μm thick copper foil. Prior to deposition, the substrate was degreased and chemically polished in acid mixture.

Electrochemical deposition was carried out using direct current galvanostatic mode with the current density values maintained at 10 mA/cm^2 and 50 mA/cm^2. The deposition time was determined in dependence on the plating surface and the projected thickness of deposits.

Ni and Cu films were electrodeposited separately from two different electrolytes. This technique is known as the Dual Bath Technique (DBT).

Copper films were electrodeposited from a sulfate bath consisting of 240 g·l^{-1} CuSO$_4$ × 5H$_2$O (1M CuSO$_4$), 40.8 ml H$_2$SO$_4$ (0.77 M H$_2$SO$_4$) and deionized water. The process temperature and pH were maintained at 25ºC and 0.4, respectively. Nickel films were electrodeposited from a sulfamate bath consisting of 300 g·l^{-1} Ni(NH$_2$SO$_3$)$_2$ · 4 H$_2$O, 30 g·l^{-1} NiCl$_2$ · 6H$_2$O, 30 g·l^{-1} H$_3$BO$_3$, 1 g·l^{-1} saccharine with maintained temperature and pH values at 50ºC and 4.2, respectively.

The microstructure of the laminate composite structures was investigated by metallographic microscopy (Carl Zeiss microscope "Epival Interphako") . The topographic details of the cross-section of the multilayer composite were investigated by Scanning Electron Microscope (SEM, JEOL JSM-T20).

The process of revealing the geometry of the multilayer structure started with a perpendicular cut of the deposited films. The samples were embedded in self-curing methyl methacrylate-polymer (Palavit G, Heraeus, Germany) and mechanically polished with different SiC papers and alumina powder with different grain size (1 μm and 0.3 μm). Rinsing solution of Na$_2$CO$_3$ was used to avoid the agglomeration of alumina powder. Finally the structures were dried in nitrogen flow.

The revealed microstructure of the Ni and Cu layers with different strata thickness, before sacrificial etching of copper layer in thiourea solution, is shown in Fig. 5 (total film thickness 75 μm), and in Fig. 6 (total film thickness 25 μm). The acid solution of 1 M thiourea at 40°C (pH = 1, achieved by adding HCl) was used for selective etching of copper layers and the substrate, while the nickel layers remained chemically stable.

In Fig. 7, the result of the etching process of the copper layers in acid thiourea solution is presented. The released nickel layers are clearly visible.
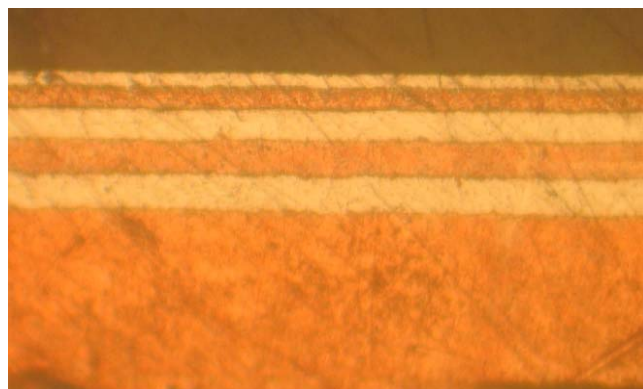

Fig. 5. Optical image of the cross-section of an electrodeposited Ni-Cu-Ni multilayer, thickness 20 μm/20 μm/20/10/5 μm, before a selective etching copper film. The current density for both film was 50 mA/cm^2
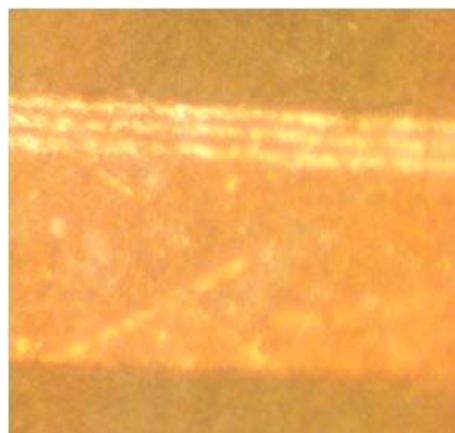

Fig. 6. Optical image of the cross-section of an electrodeposited Ni-Cu-Ni multilayer, thickness of the single film is 5 μm, number of layer is 5.
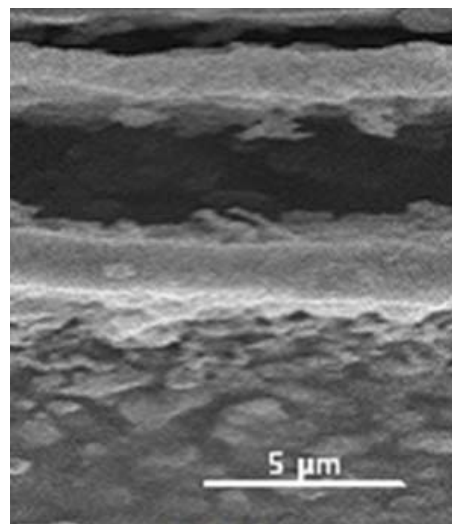

Fig. 7. SEM image of the cross-section of an electrodeposited Ni-Cu-Ni multilayer, thickness 2 μm/5 μm/2 μm.

V. Conclusion

We analyzed the applicability of Cu-Ni laminar composites as an alternative plasmonic material. It is shown that beneficial properties of 2D copper layers can be used while suppressing the undesired ones by the use of nickel. The obtained structures serve a dual purpose as a plasmonic platform and simultaneously a diffractive coupler between propagating and surface modes. Among the advantages of the utilized approach are its low cost and its high controllability over large areas, the possibility to deposit layer on non-flat structures, as well as its compatibility with the standard MEMS procedures. Our further work will consider the use of alternative substrates, as well as different other heterometallic and, more generally, heteroplasmonic platforms.

References

[1] S. A. Maier, *Plasmonics: Fundamentals and Applications*, Springer Science+Business Media, New York, NY, 2007.

[2] H. Raether, *Surface plasmons on smooth and rough surfaces and on gratings*, Springer Verlag, Berlin-Heidelberg, Germany, 1986.

[3] W. L. Barnes, A. Dereux, and T. W. Ebbesen, "Surface plasmon subwavelength optics," *Nature,* vol. 424, no. 6950, pp. 824-830, 2003.

[4] J. A. Schuller, E. S. Barnard, W. Cai, Y. C. Jun, J. S. White, and M. L. Brongersma, "Plasmonics for extreme light concentration and manipulation," *Nature Mater.*, vol. 9, no. 3, pp. 193-204, 2010.

[5] J. B. Pendry, D. Schurig, D. R. Smith, Controlling Electromagnetic Fields, *Science,* 312, (2006), 1780-1782.

[6] I. Abdulhalim, M. Zourob, and A. Lakhtakia, "Surface plasmon resonance for biosensing: A mini-review," *Electromagnetics,* vol. 28, no. 3, pp. 214-242, 2008.

[7] E. Ozbay, "Plasmonics: Merging Photonics and Electronics at Nanoscale Dimensions," *Science,* vol. 311, no. 5758, pp. 189-193, 2006.

[8] N. Fang, H. Lee, C. Sun, and X. Zhang, "Sub-diffraction-limited optical imaging with a silver superlens," *Science,* vol. 308, no. 5721, pp. 534-537, 2005.

[9] A. Boltasseva, H. A. Atwater, Low-Loss Plasmonic Metamaterials, *Science,* 331, (2011), 290-291.

[10] P. R. West, S. Ishii, G. V. Naik, N. K. Emani, V. Shalaev, A. Boltasseva, Searching for better plasmonic materials, *Laser & Photon. Rev,* (2010), 1-13.

[11] S. M. Vuković, Z. Jakšić, I. V. Shadrivov, Y. S. Kivshar, Plasmonic crystal waveguides *Appl. Phys. A,* 103, (2011), 615-617.

[12] S. M. Vuković, Z. Jakšić, J. Matovic, Plasmon modes on laminated nanomembrane-based waveguides, *J. Nanophotonics,* 4, (2010), 041770.

[13] M. Born, E. Wolf, *Principles of Optics*, 7th ed., Cambridge University Press, Cambridge 1999.

[14] P. Yeh, A. Yariv, C.-S. Hong, Electromagnetic propagation in periodic stratified media. I. General theory, *J. Opt. Soc. Am.,* 67, (1977), 423-438.

[15] P. Yeh, *Optical Waves in Layered Media*, Wiley VCH, Weinheim 1988.

[16] J. Lamovec, V. Jović, D. Randjelović, R. Aleksić, V. Radojević, "Analysis of the composite and film hardness of electrodeposited nickel coatings on different substrates", *Thin Solid Films*, 516 (23), pp. 8646-8654, (2008).

[17] J. Lamovec, V. Jović, M. Vorkapić, B. Popović, V. Radojević, R. Aleksić, "Microhardness analysis of thin metallic multilayer composite films on copper substrates", *Journal of Mining and Metallurgy, Section B: Metallurgy*, 47 (1), pp. 53-61, 2011.

Tailorable Effective Optical Response of Dual-metal Plasmonic Crystals

M. Obradov, J. Lamovec, I. Mladenović, Z. Jakšić, S. Vuković,
G. Isić, D. Tanasković

Abstract - The main problems with plasmonics for devices are connected with its very nature implying the need to use free electron conductors, mostly good metals like silver or gold. The choice of natural materials and thus their operating ranges, as defined by their plasma frequency, is rather limited. Also, absorption losses in good conductors are quite high. Because of that alternative plasmonic materials are of increasing interest. In this contribution we consider the possibility to design plasmonic crystals incorporating a pair of plasmonic materials (all-metal plasmonic crystals). For the sake of technological simplicity, we limit ourselves to one-dimensional structures with a pair of alternating layers with subwavelength periodicity. Such structures behave as strongly anisotropic effective media tailorable by design. In other words, instead of considering waveguiding in usual IMI (insulator-metal-insulator) and MIM (metal-insulator-metal) we investigate MMM (metal -metal -metal) and generally PPP (plasmonic-plasmonic-plasmonic) structures. For the plasmonic material pair we choose copper and nickel. The properties of Cu as a plasmonic material are excellent, however it oxidizes when exposed to atmosphere. Besides serving as the second plasmonic material, Ni also protects Cu layers against corrosion. Electromagnetic simulations to obtain optical properties of our all metal plasmonic crystal were performed using the finite element method.

I. INTRODUCTION

Plasmonics is a branch of electromagnetic optics dealing with evanescent fields in nanostructures containing conductive materials with free electron plasma [1]. High localizations of electromagnetic near fields in subwavelength volumes is achieved via the bound surface modes at the conductor insulator interface [2]. Moreover unconventional nature of these plasmonic modes allows for practically arbitrary tailoring and transformation of the optical space [3]. As such plasmonic structures can posses macroscopic electromagnetic parameters rarely found in nature in addition to intricate spatial field distributions.

M. Obradov, J. Lamovec, I. Mladenović, Z. Jakšić, S. Vuković and D. Tanaskovićare are with the Centre of Microel. Technologies, Institute of Chemistry, Technology and Metallurgy, University of Belgrade, Njegoševa 12, 11000 Belgrade, Serbia (e-mail: marko.obradov@nanosys.ihtm.bg.ac.rs

G. Isić is with the Institute of Physics Belgrade, Center for Solid State Physics and New Materials, University of Belgrade, Belgrade 11080, Serbia (e-mail: isicg@ipb.ac.rs)

Numerous fields of practical use of plasmonics include ultrasensitive chemical and biological sensors (down to a single molecule of analyte)[4], superconcentrators and superabsorbers, cloaking devices, enhnancement of photodetectors and many others [5, 6]. Particularly interesting feature of plasmonics is a possibility to fabricate integrated circuits merging the dimensions of VLSI with THz operating frequencies and low dissipation of all-optical devices[7].

Perhaps the most limiting factor in using the materials with free electron plasma are their high absorption losses due to carrier plasma relaxation. Furthermore most natural plasmonic materials are metals which due to their extremely high carrier concentrations have fixed plasmonic properties creating a problem with the available operating frequency ranges. As such alternative plasmonic materials like transparent conductive oxides or heavily doped semiconductors are constantly being investigated with intention to overcome these problems usually by changing the doping levels or deposition techniques [8, 9]. However, metals like gold, silver, aluminium etc. are easily available and posses numerous technological advantages including the possibility to be processed using the standard well developed microsystem techniques.

Copper is one of the natural plasmonic materials with highly developed processing techniques. Unfortunately when directly exposed to the environment copper very quickly oxidizes. While this can have beneficial effect for other uses of copper it also causes copper to lose all of its plasmonic properties. One of the means of protecting the copper from oxidations are lamellar structures in combination with some other metal [10]. Metal commonly chosen for protection of copper because of their matching mechanical properties is nickel [11].

II. THEORY

We examine a multilayer structure with alternating strata of two different metals. Each layer is described by its complex relative dielectric permittivity and by its geometrical properties. Relative dielectric permittivity of each metal is well described by the lossy extended Drude model [1]

$$\varepsilon(\omega) = \varepsilon_{\infty} - \frac{\omega_p^2}{\omega^2 + i\gamma\,\omega}, \qquad (1)$$

where ω_p is the plasma frequency of the electron plasma, ε_∞ is the asymptotic dielectric permittivity and $\gamma = 1/\tau$ is the characteristic frequency related to the damping of electron oscillations due to collisions, where τ is the relaxation time of the electron gas.

Interface between dielectric and metal supports surface plasmon polaritons (SPP). Dispersion relation of SPPs is given as [1]:

$$\beta = k_0 \sqrt{\frac{\varepsilon_d \varepsilon_m}{(\varepsilon_d + \varepsilon_m)}} \quad , \qquad (2)$$

$$\omega_{spp} = \frac{\omega_p}{\sqrt{1 + \varepsilon_d}} \quad , \qquad (3)$$

where β is SPP propagation constant, and ε_d and ε_m are complex dielectric permittivities of dielectric and metal respectively, ω_{spp} is surface plasmon polariton frequency and ω_p is the plasma frequency of the metal.

In case of a single metallic layer with thickness a surrounded by dielectric two SPP states on both sides of the layer couple splitting single state into even ω_+ and odd ω_- states.

$$\omega_+ = -\frac{\omega_p}{\sqrt{1 + \varepsilon_d}} \sqrt{1 + \frac{2\varepsilon_d e^{-2\beta a}}{1 + \varepsilon_d}},$$

$$\omega_- = -\frac{\omega_p}{\sqrt{1 + \varepsilon_d}} \sqrt{1 - \frac{2\varepsilon_d e^{-2\beta a}}{1 + \varepsilon_d}}. \qquad (4)$$

In the case of multiple alternating layers splitting of states leads to forming of bands similar to the electrons propagating in periodic potential of crystal lattice. The geometry of the heterometallic multilayer is shown in Fig. 1. The multilayer is deposited onto a copper substrate. The multilayer structure shown in Fig. 1 is the general case of finite one-dimensional, two-material plasmonic crystal [12, 13].
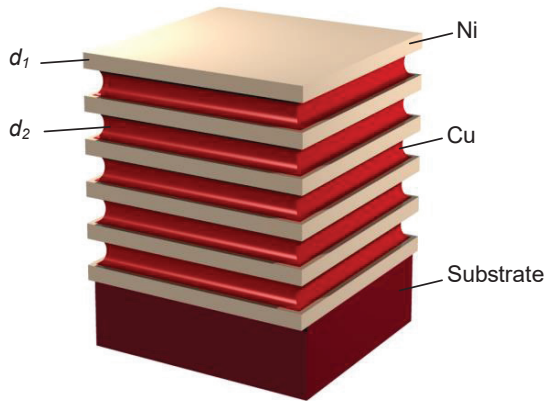

Fig. 1. Schematics of a finite Cu-Ni 1D plasmonic crystal deposited on a copper substrate.

Propagation of electromagnetic wave in direction perpendicular to the multilayer surface is described by the Bloch wavevector q. Real values of Bloch wavevector denote allowed bands and imaginary values denote forbidden bands. The propagation of a surface wave parallel to the layers along an interface between two materials is described by the plasmonic wavevector k. Number of the layer pairs is N, and the total thickness of a single layer pair is $a = d_1 + d_2$.

Dispersion relation of plasmonic crystal can be obtained from Bloch periodic condition utilizing the transfer matrix method [14, 15].

$$\frac{1}{2}(T_{11} - T_{22}) = -\cot g(Nqa)\sin(qa) \ , \qquad (5)$$

$$\frac{1}{2}(T_{11} + T_{22}) = \cos(qa) \ , \qquad (6)$$

where T_{11} and T_{22} are the diagonal transfer matrix elements. Written for the electromagnetic waves outside the light cone and for TE polarization these elements are

$$T_{11} = \exp(i\kappa_1 d_1)\left[\cosh(\kappa_2 a - \kappa_2 d_1) - \frac{1}{2}\left(\frac{\kappa_2}{\kappa_1} - \frac{\kappa_1}{\kappa_2}\right)\sinh(\kappa_2 a - \kappa_2 d_1)\right] \ , \qquad (7)$$

$$T_{22} = \exp(-i\kappa_1 d_1)\left[\cosh(\kappa_2 a - \kappa_2 d_1) + \frac{1}{2}\left(\frac{\kappa_2}{\kappa_1} - \frac{\kappa_1}{\kappa_2}\right)\sinh(\kappa_2 a - \kappa_2 d_1)\right] \ . \qquad (8)$$

whereas for TM polarization outside the light cone

$$T_{11} = \exp(i\kappa_1 d_1)\left[\cosh(\kappa_2 a - \kappa_2 d_1) - \frac{1}{2}\left(\frac{\kappa_2 \varepsilon_1}{\kappa_1 \varepsilon_2} - \frac{\kappa_1 \varepsilon_2}{\kappa_2 \varepsilon_1}\right)\sinh(\kappa_2 a - \kappa_2 d_1)\right] \ , \qquad (7)$$

$$T_{22} = \exp(-i\kappa_1 d_1)\left[\cosh(\kappa_2 a - \kappa_2 d_1) + \frac{1}{2}\left(\frac{\kappa_2 \varepsilon_1}{\kappa_1 \varepsilon_2} - \frac{\kappa_1 \varepsilon_2}{\kappa_2 \varepsilon_1}\right)\sinh(\kappa_2 a - \kappa_2 d_1)\right] \ . \qquad (8)$$

These equations can be modified for the waves inside the light cone, only in this case hyperbolic functions in T_{11}, T_{22} should be replaced with the corresponding regular trigonometric functions.

III. RESULTS AND DISCUSSION

We examined optical properties of plasmonic crystals described in Fig. 1. using Finite Element Method. To achieve this we used the RF module of Comsol Multiphysics software package. We considered finite plasmonic crystal consisting of three nickel and two copper layers on a copper substrate. We assumed that the structure was surrounded by air. Incident light is TM polarized. Parameters for Drude model describing relative permittivity of the metals are taken from literature [16].
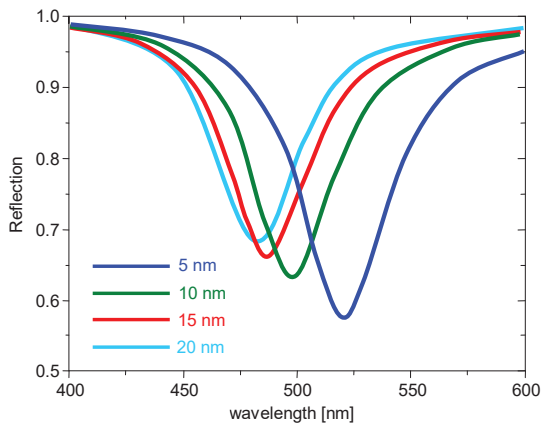
124

Fig. 2. Dispersive properties of Otto configuration coupling of incident light to SPP on plasmonic crystal surface depending on Ni layer thickness.

First we utilize Otto configuration with glass prism to couple incident light to SPP on the surface of the plasmonic crystal. We keep all of the parameters of the calculation the same and only vary the thickness of the nickel layers from 5nm to 20nm. Thickness of the copper layers is 10nm. Since excitation of SPP is achieved under condition of total internal reflection (TIR) when coupling occurs significant dip in the reflection is observed as shown in Fig. 2. What can readily be observed is that by changing the thickness of the Ni layers we change the effective parameters of the multilayer. Plasmonic crystal behaves as a single metallic material with tunable plasma frequency. Spatial field distributions of SPP are shown in Fig.3 for 5/10nm Ni/Cu plasmonic crystal.
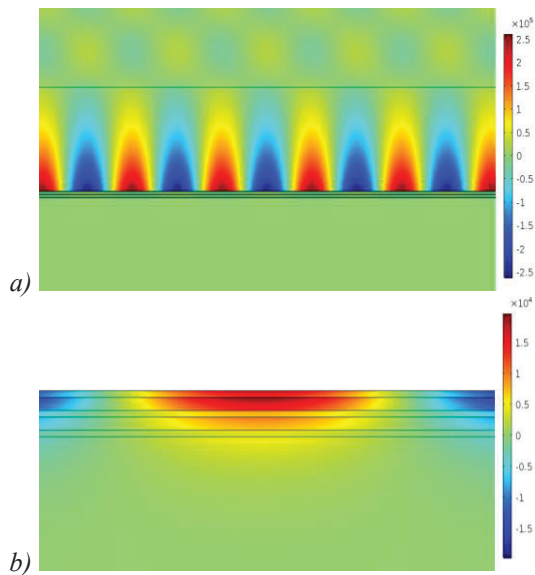

Fig. 3. Field distribution of SPP at 520nm resonant wavelength: a) on plasmonic crystal surface and b) within the plasmonic crystal.

Furthermore we investigate dispersive properties of our plasmonic crystal under direct illumination without any

couplers. In Fig.4 are shown dispersive properties of 10/10nm Ni/Cu plasmonic crystal for different incident angles.
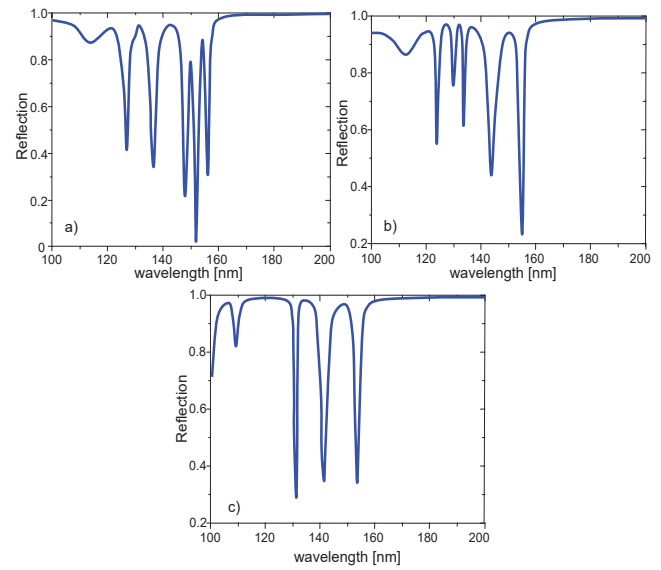

Fig. 4. Dispersive properties finite Ni/Cu plasmonic crystal for different incident angles: a) 15º; b) 30º and c)45º.
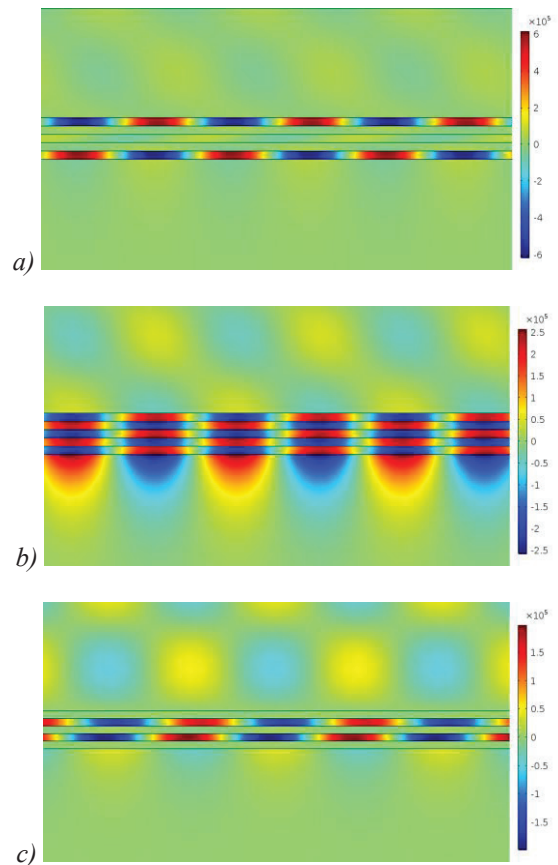

Fig. 5. Field distribution for 45º incident angle at different resonant wavelengths: a) 130nm; b) 140nm and c)150nm.

From Fig. 4 can readily be seen the existence of the allowed and forbidden band. States in the allowed band are

125

clustered together and spread apart with the increase in the angle of incidence. Of particular interest are states in 130nm to 160nm band where nickel has negative permittivity and copper has positive permittivity, but unlike most commonly seen cases which argue for high contrast between the materials here we have the case of very weak confinement i.e. the difference between relative permittivities is only a fraction of unity. What we observe as shown in Fig.5 is very high light localization on subwalength scale within the layers.

IV. CONCLUSION

Our investigations show that the effective properties of the Cu-Ni plasmonic crystal are continually tailorable by simple tuning of the thickness of the two building materials thus offering an alternative to the conventional plasmonic media. Furthermore our research demonstrates that MMM (metal -metal -metal) structures support plasmonic modes in weak confinement regime that can be excited using a propagating wave. These plasmonic modes are highly localized in individual strata of the crystal with excellent spectral selectivity of the layers. From technological point of view we have an added benefit that the techniques already developed and tested for tuning mechanical and chemical properties of metallic lamellar structures are perfectly aligned with our approach to utilize all-metal plasmonic crystals for their optical properties. An obvious direction for further research is the consideration of other plasmonic material pairs, including metal-transparent conductive oxide-metal structures.

ACKNOWLEDGEMENT

REFERENCES

[1] S. A. Maier, *Plasmonics: Fundamentals and Applications*, Springer Science+Business Media, New York, NY, 2007.

[2] H. Raether, *Surface plasmons on smooth and rough surfaces and on gratings*, Springer Verlag, Berlin-Heidelberg, Germany, 1986.

[3] J. B. Pendry, D. Schurig, and D. R. Smith, "Controlling Electromagnetic Fields," *Science,* 2006 vol. 312, no. 5781, pp. 1780-1782.

[4] I. Abdulhalim, M. Zourob, and A. Lakhtakia, "Surface plasmon resonance for biosensing: A mini-review," *Electromagnetics,* 2008, vol. 28, no. 3, pp. 214-242.

[5] W. L. Barnes, A. Dereux, and T. W. Ebbesen, "Surface plasmon subwavelength optics," *Nature,* 2003, vol. 424, no. 6950, pp. 824-830.

[6] M. Obradov, Z. Jakšić, and D. Vasiljević-Radović, "Suppression of noise in semiconductor infrared detectors using plasmonics," *Journal of Optics,* 2014, vol. 16, no. 12, pp. 125011.

[7] E. Ozbay, "Plasmonics: Merging Photonics and Electronics at Nanoscale Dimensions," *Science,* 2006, vol. 311, no. 5758, pp. 189-193.

[8] P. R. West, S. Ishii, G. V. Naik, N. K. Emani, V. Shalaev, and A. Boltasseva, "Searching for better plasmonic materials," *Laser & Photon. Rev*, 2010, pp. 1-13.

[9] A. Boltasseva, and H. A. Atwater, "Low-Loss Plasmonic Metamaterials," *Science,* 2011, vol. 331, no. 6015, pp. 290-291.

[10] J. Lamovec, V. Jović, M. Vorkapić, B. Popović, V. Radojević, and R. Aleksić, "Microhardness analysis of thin metallic multilayer composite films on copper substrates," *Journal of Mining and Metallurgy, Section B: Metallurgy,* 2011, vol. 47, no. 1, pp. 53-61.

[11] J. Lamovec, V. Jović, D. Randjelović, R. Aleksić, and V. Radojević, "Analysis of the composite and film hardness of electrodeposited nickel coatings on different substrates," *Thin Solid Films,* 2008, vol. 516, no. 23, pp. 8646-8654.

[12] S. M. Vuković, Z. Jakšić, I. V. Shadrivov, and Y. S. Kivshar, "Plasmonic crystal waveguides " *Appl. Phys. A,* 2011, vol. 103, no. 3, pp. 615-617.

[13] S. M. Vuković, Z. Jakšić, and J. Matovic, "Plasmon modes on laminated nanomembrane-based waveguides," *J. Nanophotonics,* 2010, vol. 4, pp. 041770.

[14] P. Yeh, *Optical Waves in Layered Media*, Wiley VCH, Weinheim, 1988.

[15] P. Yeh, A. Yariv, and C.-S. Hong, "Electromagnetic propagation in periodic stratified media. I. General theory," *J. Opt. Soc. Am.,* 1997, vol. 67, no. 4, pp. 423-438.

[16] A. D. Rakić, A. B. Djurišić, J. M. Elazar, and M. L. Majewski, "Optical properties of metallic films for vertical-cavity optoelectronic devices," *Appl. Opt.,* 1998, vol. 37, no. 22, pp. 5271-5283.

Analysis of the ellipsometric spectra of nanometer thick polyelectrolyte layers on silicon wafers with thermally grown silicon dioxide

Goran Isić[1,2], Stanko Nedić[1], Borislav Vasić[1], Uroš Ralević[1], Sonja Aškrabić[1]

(1) *Institute of Physics Belgrade, University of Belgrade, Pregrevica 118, 11080 Belgrade, Serbia*

(2) *Texas A&M University at Qatar, PO Box 23874 Education City, 23874 Doha, Qatar*

Contact: G. Isić (isicg@ipb.ac.rs)

Abstract. The layer-by-layer deposition method involves a successive deposition of polyanions and polycations onto a desired surface, usually by repeated immersion in aqueous solutions of the polyelectrolytes. Since its advancement in the early 1990s, it has become widespread as a cheap and versatile means for ultrathin polymer film preparation [1].

Here we consider multilayers of cationic poly(allylamine hydrochloride) (PAH) and anionic poly(sodium 4-styrenesulfonate) (PSS) molecules deposited on top of commercially produced dry thermal silicon dioxide layers (target thickness of 285 nm) grown over a lightly Boron-doped crystalline silicon wafer, which serve as well-known substrates for the accurate optical characterization of PAH/PSS multilayers. The bare substrate, substrate after base piranha functionalization and, finally, substrate with the number of PAH/PSS bilayers ranging from 1 to 4, were carefully measured by variable-angle spectroscopic ellipsometry (VASE) [2, 3].

In this work, we analyze the obtained VASE spectra to determine the dielectric function of the polyelectrolyte films of different thicknesses. First, the spectra of bare substrates are fitted to several models with different parameters, involving the Sellmeier function for the silicon dioxide permittivity, the interfacial layer between silicon and silicon dioxide and the layer thicknesses, in order to determine the minimal value of the test (error) function that can be achieved for a given model [4, 5]. The fitting involved the least squares minimization of the vector of residuals (difference between measured and model spectra) achieved using 3 different algorithms, (i) Trust Region Reflective, (ii) dogleg and (iii) Levenberg-Marquardt, implemented in the scipy.optimize package of the SciPy Python library [6]. In the second step, the VASE spectra of samples with various number of polyelectrolyte bilayers are fitted to several models involving the Cauchy's function for the refractive index of the polyelectrolyte layers and their thicknesses, assuming the dielectric functions and layer thicknesses of the underlying substrate are known. The layer thicknesses inferred from VASE spectra are then compared with thicknesses directly measured by atomic force microscopy.

REFERENCES

[1] G. Decher, Science 277 (1997), 1232.
[2] H. Fujiwara, *Spectroscopic Ellipsometry - Principles and Applications*, John Wiley & Sons, Tokyo (2007).
[3] J. J. Iturri Ramos, S. Stahl, R. P. Richter, S. E. Moya, Macromolecules **43** (2010), 9063.
[4] C. M. Herzinger, B. Johs, W. A. McGahan, J. A. Woollam, W. Paulson, J. Appl. Phys. **83** (1998), 3323.
[5] M. M. Jakovljević et al., Nanotechnology **31** (2020), 435708.
[6] http://docs.scipy.org/doc/scipy/reference/generated/scipy.optimize.least_squares.html (access.: 14.02.2022)

Characterization of ultrathin dielectric films prepared via layer-by-layer polyelectrolyte deposition on thermally oxidized silicon wafers

Stanko Nedic[1], Sonja Aškrabić[1], Borislav Vasić[1], Goran Isić[1,2], Uroš Ralević[1]

(1) *Institute of Physics Belgrade, University of Belgrade, Pregrevica 118, 11080 Belgrade, Serbia*

(2) *Texas A&M University at Qatar, PO Box 23874 Education City, 23874 Doha, Qatar*

Contact: S. Nedic (snedic@ipb.ac.rs)

Abstract. Seminal work by Decher et al. in the 1990s introduced the layer-by-layer deposition of oppositely charged polyelectrolytes [1-3]. This versatile deposition technique has since attracted considerable interest owing to its ability to modulate polyelectrolyte multilayer film properties at the nanoscale [4].

In this work, we study layer-by-layer polyelectrolyte deposition by alternately immersing thermally oxidized silicon wafer substrates into successive aqueous solutions of cationic poly(allylamine hydrochloride) (PAH) and anionic poly(sodium 4-styrenesulfonate) (PSS) polyelectrolytes with intermediate rinsing steps [5]. The surface functionalization (SF) of the substrates was performed by dipping them into the NH_4OH/H_2O_2 base piranha mix for 2 hours at 50°C, thus creating an OH^- terminated surface prior to exposing the samples to the positively charged PAH.

Due to the polyelectrolyte multilayer film thickness at the nanometer scale, their characterization requires highly sensitive techniques such as atomic force microscopy (AFM) and variable-angle spectroscopic ellipsometry (VASE). Both techniques verified the presence of polyelectrolyte multilayer films. Particularly, the SF and PAH/PSS bilayer thicknesses were established by AFM scratching, whereas VASE measurements demonstrated consistent shifts in the most prominent $\tan\Psi$ peak resulting in an increase in the peak's wavelength shift with the increasing number of PAH/PSS bilayers.

Finally, the refractive indices of polyelectrolyte multilayer films of different thicknesses (consisting of 1-4 PAH/PSS bilayers) in the wavelength range of 200-800 nm are determined from the obtained VASE spectra for bare substrates, substrates after surface functionalization, and substrates with one to four polyelectrolyte bilayers.

REFERENCES

[1] G. Decher, J.-D. Hong, *Makromol. Chem. Macromol. Symp.* **46** (1991), 321-327.
[2] G. Decher, J. D. Hong, *Ber. Bunsen-Ges.* **95** (1991), 1430-1434.
[3] G. Decher, J. D. Hong, J. Schmitt, *Thin Solid Films* **210-211** (1992), 831-835.
[4] F. X. Xiao, M. Pagliaro, Y. J. Xu, B. Liu, *Chem. Soc. Rev.* **45** (2016), 3088-3121.
[5] P. T. Hammond, *Adv. Mater.* **16** (2004), 1271-1293.

Nanoscopy of transition metal dichalcogenide based van der Waals heterostructures fabricated by the wet and dry transfer methods

Uroš Ralević[1], Borislav Vasić[1], Sonja Aškrabić[1], Stanko Nedić[1], Goran Isić[1,2]

(1) Institute of Physics Belgrade, Pregrevica 118, 11080 Belgrade, Serbia

(2) Texas A&M University of Qatar, PO Box 23874 Education City, 23874 Doha, Qatar

Contact: U. Ralević (uros@ipb.ac.rs)

Abstract. The research of two-dimensional (2D) crystals beyond graphene has led to a new idea of stacking these atomically thin layers one on top of the other into the so-called van der Waals heterostructures (VdWhs) [1]. The combination of different 2D crystals into a VdWh gives rise to new electronic and optical properties, while preserving the intrinsic properties of the constituent crystals [2]. This paired with the vast choice of currently available 2D crystals, renders VdWhs as an interesting prospect for various applications in the fields of electronics to optoelectronics [2].

In this work we investigate VdWhs produced from 2D transition metal dichalcogenides (WS_2, WSe_2, MoS_2 and $MoSe_2$), which are considered to be strong candidates for applications in the field of optoelectronics [2]. The fabrication of VdWhs was done by using the wet and dry variants of the transfer method [3]. The structural and optical properties of the VdWhs fabricated by these methods were thoroughly investigated by atomic force microscopy, Raman spectroscopy and photoluminescence spectroscopy. The analysis of the results obtained from the afore mentioned characterization techniques shows that VdWhs have low amount of surface contaminants, unmodified crystal structure, high and uniform photoluminescence intensity. The VdWhs are found to have interlayer contaminants which are accumulated in pockets of different shapes. In fact, achieving clean interfaces is one of the main challenges of the transfer methods.

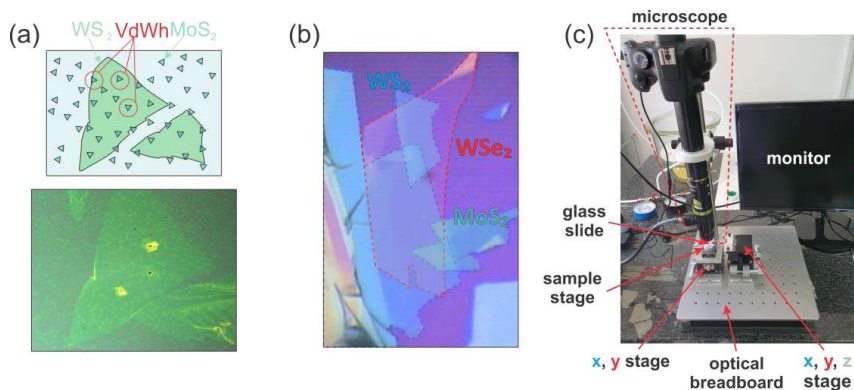Figure 1. (a) MoS2 / WS2 VdWh. (b) WSe2 / WS2 / MoS2 VdWh. (c) Dry transfer setup

REFERENCES

[1] K.S. Novoselov et al, Sicence 353 (2016), aac9439-1
[2] Y. Liu et al, Nat.Rev.Mater. 1 (2016), 16042
[3] R. Frisenda et al, Chem. Soc. Rev. 47 (2018), 53

Determination of refractive index of ultrathin dielectric films prepared via layer-by-layer polyelectrolyte deposition

S. Nedić[1], S. Aškrabić[1], B. Vasić[1] and G. Isić[1]

[1] *Institute of Physics Belgrade, University of Belgrade, Belgrade, Serbia*

e-mail:snedic@ipb.ac.rs

In this work, layer-by-layer polyelectrolyte deposition has been studied by alternately immersing the Si/SiO_2(300 nm) substrates into successive aqueous solutions of cationic poly(allylamine hydrochloride) (PAH) and anionic poly(sodium 4-styrenesulfonate) (PSS) polyelectrolytes with intermediate rinsing steps [1]. Base piranha approach was adopted for the surface functionalization (SF) of the substrates by dipping them into the NH_4OH/H_2O_2 mix for 2 h at 50°C in order to create an OH^- terminated surface prior to exposing the samples to the positively charged PAH.

Due to their thickness at the nanometer scale, the characterization of polyelectrolyte multilayer films requires highly sensitive techniques such as spectroscopic ellipsometry (SE) and atomic force microscopy (AFM). Both techniques verified the presence of polyelectrolyte multilayer films. Particularly, SE measurements demonstrated consistent shifts in the most prominent $\tan\Psi$ peak resulting in an increase in the peak's wavelength shift with the increasing number of bilayers (Figure 1), whereas the SF and PAH/PSS bilayer thicknesses were established by AFM scratching and are approximately ~0.5 nm and ~1.1-1.4 nm, respectively.

The empirical Cauchy model can be used for approximation of the real part of the refractive index within spectral regions for which the material has very low or non-existing absorption [2]. Furthermore, complex refractive index of a layer in a multilayer structure can be extracted by direct inversion when the thickness of the layer is known. In accordance with this, the thicknesses of the polyelectrolyte multilayer films established by AFM were used to calculate the complex refractive indices. Finally, direct inversion and parametric fitting based on the Cauchy model have been utilized in order to fully determine the real and imaginary parts of the refractive index of ultrathin polyelectrolyte multilayer films in the wavelength range of 200-800 nm.

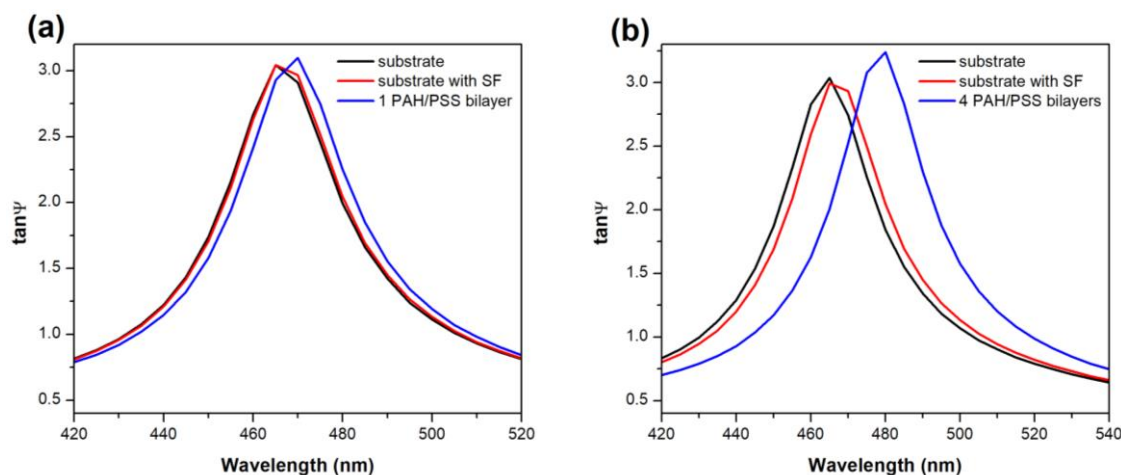Figure 1. Experimentally measured ellipsometric spectra of two different Si/SiO_2(300 nm) substrates with SF and (a) one, and (b) four PAH/PSS bilayers.

REFERENCES

[1] P. T. Hammond, "Form and function in multilayer assembly: New applications at the nanoscale," Adv. Mater. 16, 1271-1293 (2004).

[2] H. G. Tompkins, E. A. Irene, "Handbook of Ellipsometry,"William Andrew Publishing - Springer (2005).

Light absorption in two-dimensional crystals covered by randomly distributed plasmonic nanoparticles

G. Isić[1,2], U. Ralević[1] and M. R. Belić[2]

[1]*Institute of Physics Belgrade, University of Belgrade, Belgrade, Serbia*
[2]*Texas A&M University at Qatar, Doha, Qatar*
e-mail:isicg@ipb.ac.rs

The discovery of many thermodynamically stable two-dimensional crystals attainable, amongst others, by the mechanical exfoliation method [1] has, since the 2000s, been inspiring the investigation of a range of electronic and, more recently, optoelectronic systems featuring such atomically thin layers either individually or stacked into so-called van der Waals heterostructures. In case of van der Waals heterostructure photovoltaics [2], light trapping strategies gain in significance as the active layer thickness is typically two orders of magnitude smaller than the wavelength.

We pursue ways to increase the light absorption efficiency using plasmonic nanoparticles randomly distributed on top of two-dimensional crystals [3]. To study the light absorption in disordered systems, we employ Smuthi [4,5], an open-source T-matrix based Python package for simulating light scattering on particles embedded in arbitrary layered systems. In numerical simulations, we assume that a number N_p of nanoparticles is arranged over a square area A with a uniform distribution. As macroscopic clusters (such that $A \sim 1$ mm^2 or more) are way too large to simulate numerically, our method relies on simulating sufficiently large (typically $N \sim 100$) ensembles of smaller randomly generated clusters and estimating the absorption enhancement of a macroscopic system from the ensemble average. In the example shown in Fig. 1, we study how the nanoparticle concentration n affects the observed enhancement and find that, typically, the enhancement grows with increasing n, but, somewhat unexpectedly, only to a certain point after which it starts to decrease.
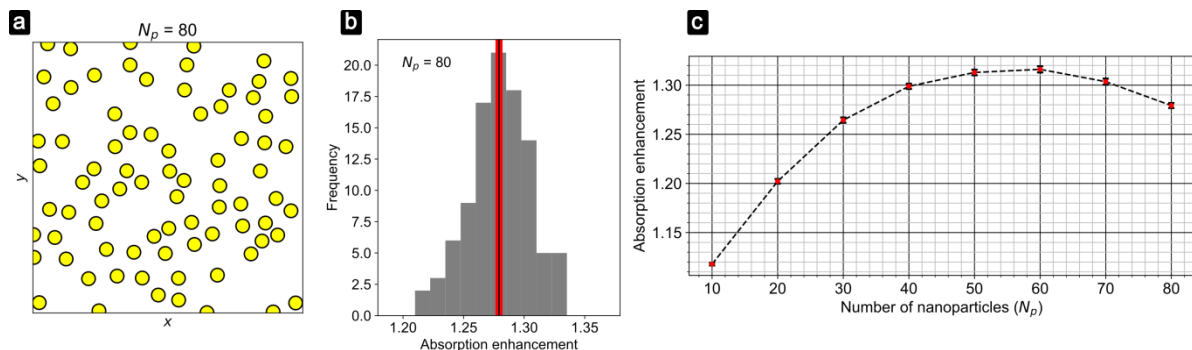
Figure 1. Absorption enhancement at $\lambda = 550$ nm in a 1 nm layer of MoS_2 sitting on top of a gold film (a) A typical cluster of 80 gold 100 nm nanoparticles randomly distributed over an area of 2 x 2 μm^2. (b) Absorption enhancement histogram obtained by simulating 100 randomly generated clusters. The vertical black line represents the ensemble mean, while the mean error is indicated by the red band. (c) Absorption enhancement (ensemble mean) as a function of the number of nanoparticles with $A = 4 \ \square$m^2. The mean error is indicated by error bars which are hardly visible on this scale.

REFERENCES
[1] K. S. Novoselov, D. Jiang, F. Schedin, T. J. Booth, V. V. Khotkevich, S. V. Morozov, A. K. Geim, PNAS **102**, 10451 (2005)
[2] D. Jariwala, A. R. Davoyan, J. Wong, H. A. Atwater, ACS Photonics 4, 2962 (2017)
[3] http://pv-waals.com
[4] SMUTHI Available: https://smuthi.readthedocs.io [Accessed June 22, 2021]
[5] Amos Egel: "Accurate optical simulation of disordered scattering layers for light extraction from organic light emitting diodes", Dissertation, Karlsruhe, DOI: 10.5445/IR/1000093961 (2018)

Optical properties of surface plasmon polaritons launched via metallic groves

U. Ralević[1], G.Isić[1,2]

[1]*Institute of Physics Belgrade, University of Belgrade, Belgrade, Serbia*
[2]*Texas A&M University at Qatar, Doha, Qatar*
e-mail: uros@ipb.ac.rs

The optical properties of surface plasmon polaritons (SPPs) including field enhancement, subwavelength field confinement, and high sensitivity to the structure of the dielectric/metal interfaces where they exist have been exploited for numerous applications ranging from sensors to optical integrated circuits [1]. One of the key requirements for building a SPP based device is a controllable and efficient conversion of the free-space light to the SPPs. In the last two decades, isolated nano-sized slits and grooves perforated in metal films have been utilized as efficient SPP launchers in novel, compact SPP based devices, where high density of integration, amongst other properties, plays an important role [2].

In this work we investigate the SPPs launched on a metal grove using finite element method numerical simulations. In particular, we study the effects of various parameters such as grove shape and the incident angle on the properties of launched SPPs and the launching efficiency. The launching efficiency of the SPPs exhibits maxima (minima) whenever the scattering into SPPs is in constructive (destructive) interference with the scattering arising via the groove mode excitation. The extremal points position is found to be dependent on the groove shape and virtually independent on the incident angle. We show that the rotation of the plane of incidence modifies the SPP wavevector by introducing an offset between the amplitude and phase fronts of the launched SPP. The former becomes slanted with respect to the Poynting vector, while the latter remains perpendicular to it.

REFERENCES
[1] W.L. Barnes, A. Dereux, T.W. Ebbesen, Nature 424, 824 (2003)
[2] H. J. Lezec, A. Degiron, E. Devaux, R. A. Linke, L. Martin-Moreno, F. J. Garcia-Vidal, T. W. Ebbesen, Science 297, 820 (2002)

"Point-by-point" inversion vs. parametrized fitting of ultrathin film's dielectric function measured by rotating polarizer ellipsometry

<u>M. M. Jakovljević</u>[1], S. Aškrabić[1], M. Artemyev[2], A. V. Prudnikau[2], A. V. Antanovich[2], G. Isić[1], B. Vasić[1], U. Ralević[1], Z. Dohčević-Mitrović[1] and R. Gajić[1]

[1] *Center for Solid State Physics and New Materials, Institute of Physics, Belgrade, Serbia*
[2] *Research Institute for Physical Chemical Problems of the Belarusian State University, Belarus*
[3] *Texas A&M University at Qatar, Doha, Qatar*
e-mail: milka@ipb.ac.rs

With the emergence of nanotechnology, spectroscopic ellipsometry (SE) got an important role in optical characterization of ultra-thin nanostructured films [1]. Using this technique, various relevant characteristics such as film thickness, surface roughness and optical functions can be determined, but only by proper modeling of the near-surface region of multilayer samples.

In this work, we investigated the extraction of optical properties of ultrathin (~5 nm) films composed of a single layer of core-shell CdSe-CdS nanoplatelets on SiO_2(85 nm)/Si(bulk) substrate. The ellipsometric spectra were measured using SE in rotating polarizer ellipsometry (RPE) configuration. We compared two standard approaches for SE thin film analysis: "point-by-point" inversion and model based (parametrized) data fitting [2]. While the model based data fitting is quite effective in the case where the shape of film's dielectric function is easy to anticipate, one should be careful with analysis of nanometer scaled film thicknesses. Since they are very thin, reasonable goodness of fit could be misleading. On the other hand, "point-by-point" inversion suffers from the fact that the neighbouring wavelengths do not support each other, eventually leading to lack of Krammers-Kroning consistency [3]. It also strongly depends on measurement precision and sensitivity which is critical in RPE configuration in case of Δ being close to 0 or 180° [4]. For both approaches, pre-knowledge about the underlying substrate is essential. Having all this in mind, the combination of both "point-by-point" inversion and parametrized fitting should be applied.

REFERENCES
[1] M. Losurdo, K. Hingerl, *Ellipsometry at Nanoscale*, Springer, (2013).
[2] H. Fujiwara, *Spectroscopic Ellipsometry: Principles and applications*, John Wiley & Sons, Ltd, (2007).
[3] H. Tompkins, J. Hilfiker, *Spectroscopic Ellipsometry: Practical Application to Thin Film Characterization*, Momentum Press Engineering, (2016).
[4] D. E. Aspnes, J. Opt. Soc. Am. 64, 639 (1974).

Liquid crystal based tunable metasurfaces for beam steering at terahertz frequencies

<u>B. Vasić</u>[1], G. Isić[1,2], R. Gajić[1], R. Beccherelli[3] and D. C. Zografopoulos[3]

[1]*Graphene Laboratory of Center for Solid State Physics and New Materials, Institute of Physics Belgrade, University of Belgrade, Belgrade, Serbia*
[2]*Texas A&M University at Qatar, Doha, Qatar*
[3]*Consiglio Nazionale delle Ricerche, Istituto per la Microelettronica e Microsistemi, Rome, Italy*
e-mail: bvasic@ipb.ac.rs

Metasurfaces are artificial, planar, and periodic electromagnetic structures consisting of subwavelength resonators which strongly enhance light-matter interaction. Therefore, metasurfaces are an excellent choice for making compact and fast tunable photonic devices in a broad window of the electromagnetic spectrum, including terahertz (THz) frequencies as well [1]. Gradient metasurfaces belong to a special class characterized by a spatially inhomogeneous phase response providing novel opportunities for beam steering and wavefront shaping [2]. Here we examine tunable metasurfaces with inhomogeneous phase profiles as efficient beam steering devices at THz frequencies. The considered structures are based on metal-insulator-metal (MIM) cavities, where the top layer consists of a metallic ribbon array separated from the bottom ground plane by a thin layer of a highly-birefringent nematic liquid crystal (LC) [3, 4], which serves as an electrically tunable element. The resulting change of the LC refractive index provides spectral shifting of the metasurface resonance and large phase shift of the reflected field at the desired frequency.

In order to achieve tunable beam steering, we designed metasurfaces based on periodic arrays of MIM cavities taken as building blocks, where the spatially varying phase profile, either binary or linear, is provided by spatially inhomogeneous and tunable LC refractive index. The metasurface with the binary phase profile consists of spatial zones with a phase shift either 0° or 180° and it operates as a beam splitter. The reflection angle of the first diffraction order is adjusted by changing the period of the supercell composed of individually-controlled MIM cavities, which provide the binary phase profile of the grating. At the same time, by suitably selecting the binary phase-shift values, the tunable grating enables the equal redistribution of the reflected power between the first diffraction order and the back-scattered zeroth order. Finally, we demonstrate that a gradient metasurface consisting of subunit cells with a discretized linear phase profile ranging from 0° to 270° behaves as a blazed grating. Tunable beam steering is then achieved by modifying the period of the linear phase spatial profile, which determines accordingly the reflection angle of the diffracted terahertz beam.

REFERENCES
[1] H.-T. Chen et al., Nature 444, 597 (2006).
[2] N. Yu et al., Science 334, 333 (2011).
[3] G. Isić et al., Phys. Rev. Appl. 3, 064007 (2015).
[4] B. Vasić et al., Nanotechnology 28, 124002 (2017).

Surface plasmon polariton launching by light scattering on grooves in metal films

U. Ralević[1], G. Isić[1,2], M. Falkner[3] and R. Gajić[1]
[1]*Graphene Laboratory of Center for Solid State Physics and New Materials,*
Institute of Physics Belgrade, University of Belgrade, Serbia
[2]*Texas A&M University at Qatar, Doha, Qatar*
[3]*Institute of Applied Physics, Abbe Center of Photonics, Friedrich-Schiller-Universität Jena, Germany*
e-mail: uros@ipb.ac.rs

Surface plasmon polaritons (SPPs) are electromagnetic surface waves which propagate at a metal-dielectric interface. The optical properties of SPPs such as subwavelength field confinement, field enhancement and high sensitivity to the composition and structure of the surface have been exploited for numerous applications ranging from sensors to optical integrated circuits [1]. Many of the numerous applications of the SPPs require efficient and controllable methods for conversion of the free-space light to SPPs [2]. In order to achieve SPP launching in such a way, the transverse momentum of the free-space light has to be matched to that of a SPP. The momentum matching is traditionally done by using a prism or a metallic grating. However, these bulky elements are not convenient for applications demanding high density of integration, as it is the case with the SPP based integrated optics. As an alternative to prisms and metallic gratings, structures such as nano-sized slits and grooves perforated in metal films have been proposed recently as promising candidates for novel compact SPP based devices [3].

In the process of light scattering on a groove in a metal film only a fraction of the incident wave is converted to SPPs. Here we investigate the SPP launching efficiency in the 600 nm - 900 nm wavelength range, using finite element based numerical simulations under the assumption that a plane wave is incident on the groove. We study the influence of the groove shape, incident angle, angle between the plane of incidence and the groove axis (the azimuth angle) and the polarization of the incident wave on the launching efficiency and the character of the launched SPPs. We find that the SPP launching efficiency exhibits minima (maxima) whenever the scattering into SPPs is in destructive (constructive) interference with the scattering arising via the groove mode excitation. The spectral position of these extremal points strongly depends on the groove shape and the azimuth angle, while it is virtually independent on the incident angle. We show that the rotation of the plane of incidence modifies the SPP wavevector resulting in an offset between their amplitude and phase fronts. The former becomes slanted with respect to the Poynting vector, while the latter remains perpendicular to it.

REFERENCES
[1] W. L. Barnes, A. Dereux, T. W. Ebbesen, Nature 424, 824 (2003).
[2] J. Lin et al., Science 340, 331 (2013).
[3] H. J. Lezec et al., Science 297, 820 (2002).

Plasmonic defect states in metallodielectric superlattices

G. Isić[1,2], S. Vuković[2,3], Z. Jakšić[3] and M. Belić[2]
[1]Institute of Physics Belgrade, University of Belgrade, Belgrade, Serbia
[2]Texas A&M University at Qatar, Doha, Qatar
[3]Center of Microelectronic Technologies, Institute of Chemistry, Technology and Metallurgy,
University of Belgrade, Belgrade, Serbia
e-mail: isicg@ipb.ac.rs

The recent progress in depositing high-quality ultrathin metal layers, with thickness well below the light penetration depth [1], has allowed the fabrication of metallodielectric superlattices with properties very similar to hyperbolic homogeneous media [2]. The latter are characterized by a very large photonic density of states (PDOS) [3] and thus considered promising for the development of novel light sources [4].

In a boundless metallodielectric superlattice, the PDOS consists exclusively of bulk-like plasmonic states, formed through a strong hybridization of surface plasmon polaritons of many individual metal-dielectric interfaces comprising the superlattice [5]. So far, however, semi-infinite superlattices have been more relevant in practice as quantum emitters have typically been deposited on top of metallodielectric layers [6]. The superlattice-homogeneous medium interface introduces two additional types of states into which photons may be emitted: far-field and Tamm plasmon modes [7], which causes a strong spatial variation of the PDOS composition [8].

Here the problem of a single-defect in an otherwise boundless metallodielectric superlattice is considered. It is relevant for emitters embedded into the superlattice, which has been suggested [4] as a measure for further increasing PDOS. The considered defects take the form of a slightly different layer thickness or a local permittivity deviation, so that the system may be regarded as a combination of two semi-infinite superlattices interacting through a common capping layer. We investigate the conditions leading to the formation of transversally localized plasmonic defect states, study their dispersion and field distribution and evaluate their contribution to the total PDOS. The results we obtained show that the total PDOS is significantly increased in comparison to a defect-free case, which is of great interest for quantum well-based light-emitting devices and infrared detectors.

REFERENCES
[1] W. Chen et al., Opt. Express 18, 5124 (2010).
[2] A. Poddubny et al., Nat. Photonics 7, 948 (2013)
[3] L. Novotny, B. Hecht, *Principles of Nano-Optics*, Cambridge University Press, 2012.
[4] W. D. Newman, C. L. Cortes, Z. Jacob, J. Opt. Soc. Am. B 30, 766 (2013).
[5] G. Isić, R. Gajić, S. Vuković, Phys. Rev. B 89, 165427 (2014).
[6] H. Krishnamoorthy et al., Science 336, 205 (2012).
[7] G. Isić et al., Sci. Rep. 7, 3746 (2017).
[8] G. Isić et al., *Spontaneous emission into Tamm plasmons on hyperbolic metamaterial interfaces*, submitted (2019).

Surface enhanced Raman spectroscopy of thiacyanine coated silver nanoparticle clusters

U. Ralević[1], G. Isić[1], B. Laban[2], D. Vasić Anićijević[3], V. Vodnik[3], U. Bogdanović[3], V. Vasić[3], V. M. Lazović[1] and R. Gajić[1]

[1]*Institute of Physics Belgrade, University of Belgrade,*
Belgrade, Serbia
[2]*Faculty of Natural Sciences and Mathematics, University of Priština,*
Kosovska Mitrovica, Serbia
[3]*Vinča Institute of Nuclear Sciences,University of Belgrade,*
Belgrade, Serbia
e-mail:uros@ipb.ac.rs, isicg@ipb.ac.rs

Metallic nanoparticles are known for their remarkable ability to confine and enhance the electromagnetic fields incident upon them. These nanoobjects have thus been successfully utilized as a platform for enhancing the intensity of light scattered from analyte molecules residing in their close vicinity. A perfect example is surface enhanced Raman spectroscopy (SERS) in which the confined, strong electromagnetic fields transfer the electromagnetic energy to the analyte thereby increasing the magnitude of the analyte phonon-modulated dipole moment and consequently its Raman scattering efficiency [1]. The SERS enhancement factors depend on various factors such as the topology of the metallic nanoobjects, and can be as high as 10^{11} [1]. Large enhancement factors render SERS a very versatile technique which can be used for detection of extremely small amounts of analyte adsorbed on the surface of metallic nanoobjects [2] as well as for studies on a single molecule level [3].

Here we investigate silver nanoparticle clusters deposited on an insulating substrate as a platform for SERS, using confocal Raman microspectroscopy and a finite element based numerical analysis. The analysis of SERS enhancement based on rigorous numerical simulations of Maxwell equations for the case of plane wave scattering on random silver nanoparticle clusters, shows that the highest field enhancement factors are reached at collective nanoparticle plasmon resonances and become redshifted in elongated clusters with an increasing number of particles. From an inspection of electromagnetic field distribution on nanoparticle surfaces, a conclusion is reached that at least 90% of the total enhancement originates from nanogaps between adjacent nanoparticles, implying that the SERS experiments are sensitive only to adsorbates located in these gaps. The latter conclusion is used to aid the experimental SERS study of the thiacyanine (TC) dye adsorption on the surface of silver nanoparticle clusters. By analyzing the SERS spectra of TC dye coated nanoparticle clusters, we find that the adsorption of this particular dye is strongly influenced by the capping anions which are initially conformed on the surface of the nanoparticles.

REFERENCES
[1] M. Kerker, D.-S. Wang, H. Chew, Surface enhanced Raman scattering (SERS) by molecules adsorbed at spherical particles, Appl. Opt. 19 3373 (1980).
[2] Y. Kitahama, Y. Tanaka, T. Itoh, M. Ishikawa, Y. Ozaki, Identification of thiacyanine J–aggregates adsorbed on single silver nanoaggregates by surface–enhanced Raman scattering and emission spectroscopy, Bull. Chem. Soc. Jpn. 82 1126 (2009).
[3] A. B. Zrimsek, N. L. Wong, R. P. Van Duyne, Single Molecule Surface-Enhanced Raman Spectroscopy: A Critical Analysis of the Bianalyte versus Isotopologue Proof, J. Phys. Chem. C 120 5133 (2016).

Influence of graphene and two-dimensional materials on electromagnetic enhancement in silver nanoparticle clusters

U. Ralević[1], A. Panarin[2] and G. Isić[1]
*[1]Graphene Laboratory of Center for Solid State Physics and New Materials, Institute of Physics Belgrade,
University of Belgrade, Belgrade, Serbia
[2]B. I. Stepanov Institute of Physics,
National academy of sciences of Belarus, Minsk, Belarus*
e-mail: isicg@ipb.ac.rs

Since its discovery in the 1970s, surface-enhanced Raman scattering (SERS) has become indispensable in analytic applications of Raman spectroscopy involving trace concentrations of analyte. It is well established that SERS enhancement factors above 10^{10} can be reached if the analyte molecules are deposited into the electromagnetic "hotspots" formed in metal nanoparticle gaps or crevices, allowing single-molecule detection. While several mechanisms are known to contribute to the overall enhancement, the dominant contribution to large enhancement factors is known to be of the electromagnetic nature, scaling approximately as the fourth degree of the local electric field enhancement.

Silver nanoparticles deposited on appropriately chosen substrates are amongst most frequently used SERS substrates because the plasmonic properties of silver at visible frequencies are superior to other metals. However, silver is prone to oxidation in ambient conditions, especially when illuminated by a strong laser beam, leading to stability issues when attempting to use it in SERS substrates [1]. In addition to improved stability, a passivation of the silver surface by ultrathin dielectric layers has been shown [2] to be beneficial as a way to functionalize the surface. Recent studies [3,4] have indicated that graphene, as a two-dimensional material which combines atomic thickness with mechanical robustness, might be an ideal protection layer for silver nanoparticle SERS substrates.

Here we employ rigorous finite-element based numerical simulations of light scattering on silver nanoparticle clusters deposited on a substrate, in order to determine the electromagnetic SERS enhancement factor provided by the nanoparticle cluster. While it is evident that graphene or a similar absorbing two-dimensional cover layer [5] reduces this factor, our aim is to determine and understand the magnitude of this reduction, in order to help optimize the use of graphene in novel silver nanoparticle SERS substrates.

REFERENCES
[1] A. Yu. Panarin, I. A. Khodasevich, O. L. Gladkova, S. N. Terekhov, Appl. Spectrosc. 68, 297 (2014).
[2] X. Zhang, J. Zhao, A. V. Whitney, J. W. Elam, R. P. Van Duyne, J. Am. Chem. Soc. 128, 10304 (2006).
[3] W. Xu, J. Xiao, Y. Chen, Y. Chen, X. Ling, J. Zhang, Adv. Mater. 25, 928 (2013).
[4] W. G. Xu, X. Ling, J. Q. Xiao, M. S. Dresselhaus, J. Kong, H. X. Xu, Z. F. Liu, J. Zhang, Proc. Natl. Acad. Sci. USA 109, 9281 (2012).
[5] U. Ralević, G. Isić, B. Vasić, R. Gajić, J. Phys. D: Appl. Phys. 47, 335101 (2014).

Spontaneous emission into Tamm plasmon modes on semi-infinite metallodielectric superlattices

G. Isić[1], Z. Jakšić[2], S. Vuković[2]
*[1]Center for Solid State Physics and New Materials, Institute of Physics Belgrade,
University of Belgrade, Belgrade, Serbia
[2]Center of Microelectronic Technologies, Institute of Chemistry, Technology and Metallurgy,
University of Belgrade, Serbia*
e-mail: isicg@ipb.ac.rs

An optical medium is said to be hyperbolic if the principal values of its dielectric permittivity tensor differ in sign, implying a hyperboloid equifrequency surface. As the photonic density of states (PDOS) and the associated spontaneous emission rate of quantum emitters are known to be proportional to the area of the equifrequency surface, hyperboloid media exhibit very large Purcell factors, infinite in the local approximation. In nature, a hyperboloid behavior occurs in certain crystals at mid and far infrared frequencies and is usually associated with vibrational resonances.

In recent years [1], periodic stacks of ultrathin metal and dielectric layers, here referred to as metallodielectric superlattices, have been considered as artificial media exhibiting a hyperboloid behavior up to visible freuqencies. As visible and infrared wavelengths are many times longer than the period, the main optical properties of a superlattice can be understood by approximating it by a uniaxial homogeneous medium. A more rigorous microscopic picture [2] shows that the unusual properties are a consequence of the transparency of individual layers which allows a hybridization of surface plasmon polaritons (SPPs), supported by each metal-dielectric interface, and the formation of Bloch SPPs delocalized across the superlattice.

Here we consider the spectral characteristics of PDOS at the interface between a semi-infinite metallodielectric superlattice and a homogeneous medium. We discuss the conditions leading to the appearance of surface modes referred to as Tamm plasmons and their contribution to the surface PDOS, aiming to discriminate the efficiency of a quantum emitter placed near the surface. Coupling of the emitted radiation with Tamm and Bloch plasmons improves the interpretation of recent experiments by Krishnamoorthy et al. [3]. We show how the classical results for emission into surface plasmons [4] are modified in case of Tamm plasmons, explain the factors influencing the magnitude of the relative contribution of Tamm plasmons to the total PDOS and its critical behavior in the vicinity of the topological transition frequency between hyperbolic and elliptical regime.

REFERENCES
[1] A. Poddubny, I. Iorsh et al., Nat. Photon. 7, 958-967 (2013).
[2] G. Isić, R. Gajić, S. Vuković, Phys. Rev. B 89, 165427 (2014).
[3] H. N. S. Krishnamoorthy, Z. Jacob et al., Science 336, 205-209 (2012).
[4] G. W. Ford, W. H. Weber, Phys. Rep. 113, 195-287 (1984).

Film-coupled silver nanoparticles on flat and periodically corrugated aluminium substrates

G. Isić[1], U. Ralević[1], S. Aškrabić[1a], S. Graovac[1], S. Savić-Šević[2], A. Mikhailov[3], A. Antanovich[3], A. Prudnikau[3], M. Artemyev[3], I. Fabijanić[4], V. Janicki[4], B. Okorn[4], J. Sancho-Parramon[4] and R. Gajić[1]

[1]*Graphene Laboratory of* [1a]*Center for Solid State Physics and New Materials, Institute of Physics Belgrade,*
University of Belgrade, Belgrade, Serbia
[2]*Photonics Center, Institute of Physics Belgrade,*
University of Belgrade, Belgrade, Serbia
[3]*Research Institute for Physical Chemical Problems,*
Belarusian State University, Minsk, Belarus
[4]*Ruđer Bošković Institute,*
Zagreb, Croatia
e-mail: isicg@ipb.ac.rs

The strong scattering of light by noble metal nanoparticles has, since ancient times, been utilized in various ways, from Roman stained glass to modern day hCG pregnancy tests. At optical frequencies, both the "lightning rod effect" associated with nanometer geometric features and the excitation of collective charge oscillations known as localized surface plasmons (LSPs) contribute to the formation of strong and highly localized electric field "hotspots" at the nanoparticle surface. Understanding the "hotspot" formation mechanism and its attributes such as resonant wavelength, excitation efficiency or spatial confinement, as well as mastering the technology to efficiently produce LSP systems with desired properties, has been at the focus of plasmonics and nanooptics in the past decade and motivated by the perspective of producing a new generation of ultrasensitive spectroscopic sensors [1] or controlling the photon generation by quantum emitters [2]. A significant recent development has been realized by the use of the layer-by-layer polyelectrolite deposition technique [2,3], providing cheap means to produce dielectric layers the thickness of which can be controlled with subnanometer precision.

Here we report on a comprehensive study of optical properties of silver nanospheres or nanocubes separated from a flat or periodically corrugated aluminium substrate by a few nanometer thick layer of oxide and several polyelectrolite layers. Combining theoretical methods based on the mixed representation of the Dyadic Green function for the electric field, numerical simulations employing the finite element method, various colloidal synthesis protocols for silver nanoparticle generation, holographic generation of periodically corrugated surfaces, electron beam deposition of aluminium films, layer-by-layer polyelectrolite deposition, spectrophotometry, spectroscopic ellipsometry, Raman spectroscopy and atomic force microscopy, we investigate the properties of surface plasmon polaritons of the aluminum surface [4] and their role in the formation of LSPs highly localized in tiny gaps between the nanoparticle and aluminium substrate.

REFERENCES
[1] L. Rodriguez-Lorenzo, R. A. Alvarez-Puebla, I. Pastoriza-Santos, S. Mazzucco, O. Stephan, M. Kociak, L. M. Liz-Marzan, F. J. Garcia de Abajo, J. Am. Chem. Soc. 131, 4616 (2009).
[2] O. Kulakovich, N. Strekal, A. Yaroshevich, S. Maskevich, S. Gaponenko, I. Nabiev, U. Woggon, M. Artemyev, Nano Lett. 2, 1449 (2002).
[3] J. J. Mock, R. T. Hill, A. Degiron, S. Zauscher, A. Chilkoti, D. R. Smith, Nano Lett. 8, 2245 (2008).
[4] D. Gerard, S. K. Gray, J. Phys. D: Appl. Phys. 48, 184001 (2015).

Subwavelength nickel-copper multilayers as an alternative plasmonic material

Ivana Mladenović[1], <u>Zoran Jakšić</u>[1], Marko Obradov[1], Slobodan Vuković[1],
Goran Isić[2], Dragan Tanasković, Jelena Lamovec[1]
[1] *Center of Microelectronic Technologies, Institute of Chemistry, Technology and Metallurgy,*
University of Belgrade, Serbia
[2]*Institute of Physics,*
University of Belgrade, Serbia
e-mail: jaksa@ nanosys.ihtm.bg.ac.rs

Plasmonic materials ensure extreme concentrations and localizations of electromagnetic fields as a consequence of the appearance of evanescent waves (surface plasmons polaritons) in the range of negative values of relative dielectric permittivity near the plasma frequency [1]. The many applications of plasmonics include ultrasensitive chemical sensors, advanced all-optical devices, enhanced photodetectors, energy harvesting devices and many others [2].

Among hurdles to a more widespread use of plasmonics are a rather limited range of available plasmonic materials (usually good metals like gold and silver) and their high absorption losses in the range of interest. This is why alternative plasmonic materials are of large interest [3]. Besides using materials like transparent conductive oxides, highly doped semiconductors, intermetallic and similar, a possible approach is to combine a plasmonic material with lossless dielectric into mesoscopic or subwavelength nanocomposites (plasmonic crystals) [4], thus allowing almost arbitrary tailoring of frequency dispersion in a spectral range defined by the plasma frequency.

In this contribution we consider numerically and experimentally the use of bimetallic superlattices, i.e. all-metal plasmonic crystals consisting of two alternating materials with negative values of their relative dielectric permittivities. We use the copper-nickel multilayers. Copper is a good plasmonic material, but not widely used due to surface oxidation impairing its electromagnetic properties over time. The layers of nickel, also a plasmonic material, serve a dual purpose of being a protection against copper oxidation and ensuring formation of surface waves at the alternating interfaces between the two materials. At the same time, the multilayers serve as couplers between the propagating and the surface waves.

We simulated the electromagnetic properties of subwavelength Cu-Ni multilayers by the 2D finite element method using realistic material parameters. We adjusted the response by simply varying Cu to Ni thickness ratio. A rich optical behavior was obtained, as governed by the electromagnetic properties of the multilayers. Experimentally, we fabricated 1D plasmonic crystals consisting of alternately stacked nanocrystalline Ni and Cu layers by electrodeposition on a cold-rolled copper substrate [5]. We obtained highly parallel interfaces with thin individual strata and excellent morphology. We made use of beneficial structural properties of both Cu and Ni, while suppressing the undesirable ones. The approach offers high quality, large area, compact and low cost structures, while retaining a compatibility with the standard microfabrication and microelectronic processes.

REFERENCES
[1] S. A. Maier, Plasmonics: Fundamentals and Applications, Springer New York, NY, (2007).
[2] W. L. Barnes, A. Dereux, T. W. Ebbesen, Nature 424, 824 (2003).
[3] P. West, S. Ishii, G. Naik, N. Emani, V. Shalaev, A. Boltasseva, Laser & Photon. Rev, 1 (2010).
[4] S. M. Vuković, Z. Jakšić, I. V. Shadrivov, Y. S. Kivshar, Appl. Phys. A, 103, 615 (2011).
[5] J. Lamovec, V. Jović, D. Randjelović, R. Aleksić, V. Radojević, Thin Solid Films, 516, 8646 (2008).